



Numerical simulations of supersonic turbulent wall-bounded flows

Ouissem Ben Nasr

► To cite this version:

Ouissem Ben Nasr. Numerical simulations of supersonic turbulent wall-bounded flows. Other [cond-mat.other]. INSA de Rouen, 2012. English. NNT: 2012ISAM0008 . tel-01059805

HAL Id: tel-01059805

<https://theses.hal.science/tel-01059805>

Submitted on 2 Sep 2014

HAL is a multi-disciplinary open access archive for the deposit and dissemination of scientific research documents, whether they are published or not. The documents may come from teaching and research institutions in France or abroad, or from public or private research centers.

L'archive ouverte pluridisciplinaire **HAL**, est destinée au dépôt et à la diffusion de documents scientifiques de niveau recherche, publiés ou non, émanant des établissements d'enseignement et de recherche français ou étrangers, des laboratoires publics ou privés.

THÈSE

présentée en vue de l'obtention du titre de

Docteur

de

L’Institut National des Sciences Appliquées de Rouen

Discipline : Mécanique

Spécialité : Mécanique des Fluides

par

OUISSEM BEN NASR

NUMERICAL SIMULATIONS OF SUPERSONIC TURBULENT WALL-BOUNDED FLOWS

ETUDE NUMÉRIQUE DES TRANSFERTS PARIETAUX EN ECOULEMENTS TURBULENTS SUPERSONIQUES

Soutenue le 16 Mai 2012

Membres du jury

Rapporteurs :

FRANÇOISE BATAILLE

Professeur des Universités, Université de Perpignan

PAOLA CINNELLA

Professeur des Universités, Arts et Métiers, ParisTech

Examinateurs :

GABI BEN-DOR

Professeur à l’Université de Ben-Gurion, Israël

ANNE-SOPHIE MOURONVAL

Ingénieur de recherche, Ecole Centrale Paris

SANDRINE PALERM

Ingénieur expert, CNES - Direction des Lanceurs, Paris

ASHWIN CHINNAYYA

Maître de Conférences, Université de Rouen

Directeur de thèse :

ABDELLAH HADJADJ

Professeur des Universités, INSA de Rouen

A mes parents,

A ma soeur,

A mes deux frères.

Avant-propos

Cette thèse a été réalisée au laboratoire CORIA (COmplexe de Recherche Inter- professionnel en Aérothermochimie), Unité Mixte de Recherche 6614 du CNRS, de l'Université et de l'INSA de Rouen.

Je tiens, en premier lieu, à remercier Messieurs Abdelkrim BOUKHALFA, directeur du CORIA, et Jean-Louis BILLOËT, directeur de l'INSA de Rouen, de m'avoir accueilli au sein de la structure.

Cette thèse a bénéficié d'une bourse BRI co-financée par le Centre National d'Études Spatiales (Direction des Lanceurs) et la Région Haute Normandie. Je tiens à les remercier sincèrement pour leur soutien financier.

Je tiens à témoigner de ma profonde et sincère gratitude à Monsieur Abdellah HADJADJ de m'avoir encadré durant ces trois années de thèse. Faisant toujours preuve d'une grande disponibilité et d'une grande gentillesse, il a su m'encourager dans mes travaux de recherche et me soutenir tout au long de la thèse. J'ai pour lui une grande estime et un profond respect. Merci Abdellah!

Je tiens également à témoigner de ma sincère gratitude à Madame Sandrine PALERM pour le suivi technique de mes travaux, pour les discussions fructueuses durant les réunions d'avancement et pour le soutien financier qu'elle m'a apporté à la fin de la thèse.

Je suis très reconnaissant envers Mesdames Françoise BATAILLE et Paola CINNELLA d'avoir accepté la tâche de rapporter mon travail. Je tiens également à remercier Monsieur Gabi BEN-DOR d'avoir présidé le jury, et Mademoiselle Anne-Sophie MOURONVAL et Monsieur Aschwin CHINNAYYA de leur présence en qualité d'examineurs.

Je suis particulièrement reconnaissant envers Monsieur Arnab CHAUDHURI pour les innombrables discussions que nous avons eues, ainsi que les relectures de mon manuscrit de thèse. Faisant toujours preuve de disponibilité et de gentillesse, il n'a jamais hésité à m'aider.

Je suis très reconnaissant au personnel du CRIHAN (Centre Régional Informatique de HAute-Normandie) pour la qualité de l'assistance et des moyens informatiques qu'ils ont mis à ma disposition, et qui ont permis de finir mon travail dans les meilleures conditions. Je souhaite également remercier le GENCI, plus particulièrement l'IDRIS (Institut du développement et des ressources en in-

formatique Scientifique) et le CINES (Centre Informatique National de l'Enseignement Supérieur), pour l'assistance et les moyens de calculs qu'ils ont mis à ma disposition.

Je remercie tout le personnel du service informatique du CORIA et de l'INSA de Rouen, et plus particulièrement Messieurs Guillaume EDOUARD et Philippe WENDER, pour leurs services.

Je remercie également Mesdames Isabelle LEBON et Valérie THIEURY pour leur aide afin de faciliter mes démarches administratives, ainsi que Mademoiselle Nathalie FOUET pour son aide à la bibliothèque du CORIA.

Un tiens à remercier sincèrement mes plus proches amis qui m'ont soutenu tout au long de cette aventure : Lahcène, Khaled, Memdouh, Saïd, Zakaria, Lamia, Idris, Arnab, Subbu, Micheline, Fon, Adel, Nourreddine, Dounia, Cherifa, Amine, Aliou et Alexandre. Merci à vous tous!

Je tiens à remercier sincèrement ma tante Jamila et son époux Mahjoub pour leur soutien durant mes études de Master.

Enfin, je remercie de tout mon cœur mes parents, ma soeur et mes deux frères pour leur affection, leur encouragement et leur soutien inconditionnels. Cette thèse leur est dédiée.

Abstract

This work deals with high-fidelity numerical simulations of wall-heat transfers in three-dimensional supersonic turbulent boundary layers. This configuration represents a basic element towards full characterization of complex unsteady turbulent flows occurring in rocket nozzles. A spatially-evolving supersonic turbulent boundary layer over adiabatic and cold walls at $M_\infty = 2$ and up to $\text{Re}_\theta \approx 2600$ are investigated. The large-eddy simulations (LES) modeling issue is assessed by comparing the performance of three standard subgrid-scale (SGS) models. The numerical methodology is based on a high-order *split-centered* scheme to discretize the convective fluxes of the Navier-Stokes equations, and is found to highly overcome the dissipative character of the standard shock-capturing WENO scheme. For the adiabatic case, the consistency and the accuracy of the simulations are evaluated using direct numerical simulations (DNS) taken from the literature, and turbulence statistics up to the fourth-order are reported. It is demonstrated that all SGS models require a comparable minimum grid-refinement in order to capture accurately the near-wall turbulence. Overall, the models exhibit correct behavior when predicting the dynamic properties, but show different performances for the temperature distribution in the near-wall region, even for cases with satisfactory energy resolution of more than 80%. For the isothermal case, a highly cooled case is studied using a well-refined LES, and the effect of the wall condition is highlighted by comparing the results to their adiabatic counterparts. It is found that the compressibility effects are not enhanced due to the wall cooling. As expected, the total-temperature fluctuations are not negligible in the near-wall region. The study shows that the anti-correlation linking both velocity and temperature fields, derived from the Morkovin's hypothesis, is not satisfied.

Keywords: Large-eddy simulation, Supersonic boundary layer, SGS modeling, Cold-wall boundary layer, heat transfer, Strong Reynolds Analogy, Compressibility effects.

Résumé

Cette thèse traite des transferts pariétaux dans les écoulements turbulents supersoniques via la simulation des grandes échelles turbulentes. Des couches limites adiabatique et refroidie évoluant à Mach $M_\infty = 2$ et à Reynolds $Re_\theta \approx 2600$ sont considérées. Les simulations numériques utilisent un schéma *split-centered* d'ordre élevé pour la discrétisation des flux convectifs. A l'évidence, ce schéma présente un caractère peu dissipatif comparé aux schémas à capture de chocs de type WENO. Les résultats obtenus sont comparés aux simulations numériques directes (DNS) disponibles dans la littérature. Des études détaillées de la topologie de l'écoulement proche paroi ont été effectuées grâce, notamment, aux analyses des champs instationnaires et aux traitements statistiques d'ordre élevé. Plusieurs modèles de sous-maille ont été testés et validés. Il a été montré que ces modèles exigent un minimum de raffinement de maillage afin de capturer les structures les plus énergétiques présentes en proche paroi. Bien que les modèles présentent un comportement similaire pour les grandeurs aérodynamiques, ils montrent des performances différentes pour la distribution de la température à la paroi. Ceci est vrai même pour les cas où l'énergie de sous-maille résolue dépasse 80 % de l'énergie totale. Pour le cas d'une paroi refroidie, l'effet de la condition de paroi est mis en évidence via des comparaisons avec le cas adiabatique. Il a été montré que la compressibilité de l'écoulement n'est pas modifiée par la condition à la paroi. Comme prévu, les fluctuations de température totale ne sont pas négligeables dans la région proche-paroi. Dans ce cas, l'anti-corrélation reliant les champs de vitesse et de température, basée sur l'hypothèse de Morkovin, n'est pas satisfaite.

Mots Clé: Couche limite supersonique, Transferts pariétaux, Paroi refroidie, Analogie forte de Reynolds, Effets de compressibilité, Modélisation sous maille.

Contents

Avant-propos	iii
Contents	ix
1 Introduction	1
1.1 Context of the study	1
1.2 Heat transfer in supersonic nozzles	3
1.3 Supersonic turbulent boundary layers	5
1.3.1 Adiabatic case	6
1.3.2 Isothermal case	8
1.4 Summary	15
2 Équations Mathématiques et Schémas Numériques	17
2.1 Équations mathématiques et modèles de sous-maille	17
2.1.1 Système d'équations filtrées	18
2.1.2 Modélisation de sous-maille	19
2.1.2.1 Concept de la modélisation fonctionnelle	19
2.1.2.2 Modélisation du tenseur des contraintes de sous-maille	20
2.1.2.3 Modélisation du flux de chaleur de sous-maille	25
2.1.2.4 Simulation aux grandes échelles Implicite	26
2.2 Schémas numériques	27
2.2.1 Traitement des flux convectifs	27
2.2.1.1 Schéma WENO (<i>Weighted Essentially Non-Oscillatory</i>)	27
2.2.1.2 Schéma WENO-BWO (<i>Large Bande Optimisé</i>)	30

2.2.1.3	Schéma centré conservatif <i>split-centered (Skew-Symmetric)</i>	32
2.2.2	Traitements des termes visqueux	35
2.2.3	Avancement en temps	36
2.2.4	Conditions aux limites	37
2.2.4.1	Conditions de parois, de borne supérieure et de sortie	37
2.2.4.2	Conditions d'entrée turbulente	38
2.2.5	Conventions	42
2.2.6	Notations	43
2.3	Conclusion	43
3	Adiabatic Supersonic Turbulent Boundary layer	45
3.1	Flow conditions and simulation parameters	45
3.2	Flow Organization	48
3.3	Turbulence Statistics	51
3.3.1	Auto-Correlation Coefficients	51
3.3.2	Wall properties	51
3.3.3	First- and second-order statistics	55
3.4	Subgrid scale analysis - On evaluating grid resolution	66
3.4.1	Near-wall asymptotic behavior of the SGS viscosity	66
3.4.2	Ratio of turbulent kinetic energy	68
3.4.3	Subgrid scale dissipation	68
3.4.4	Subgrid scale activity	73
3.5	Thermodynamic properties and <i>Strong Reynolds Analogy</i>	76
3.6	Instantaneous scatter plots	83
3.7	Turbulence behavior	90
3.7.1	Anisotropy invariants map	90
3.7.2	Skewness and flatness factors	91
3.7.3	Near-wall asymptotic behavior	94
3.8	Turbulent energy dissipation rate	100
3.9	Conclusion	101

4 Isothermal Supersonic Turbulent Boundary Layer	105
4.1 Nearly-adiabatic wall Conditions	105
4.1.1 Flow conditions and simulation parameters	105
4.1.2 Wall properties	106
4.1.3 Near-wall asymptotic behavior	106
4.1.4 Turbulence statistics	109
4.1.5 Scatter plots	111
4.2 LES of cold-wall supersonic turbulent boundary layer	113
4.2.1 Flow properties	114
4.2.2 Flow organization	117
4.2.3 Near-wall asymptotic behavior	117
4.2.4 Turbulence statistics	117
4.2.5 Scatter plots	128
4.2.6 Conclusion	131
5 Conclusions & perspectives	135
List of Figures	139
List of Tables	147
Bibliography	149

Chapter 1

Introduction

1.1 Context of the study

The use of advanced space propulsion devices, such as optimized rocket nozzles, has been the subject of several conceptual design studies. Indeed, rocket engine nozzles are one of the most important components of the propulsion system which need a careful design in order to fully expand and accelerate the hot gases emitted by the combustion process into exhaust gases. Since most of the energy released in the combustion chamber should be converted into kinetic energy, the performance of the nozzle, in terms of thrust and specific impulse, should be well optimized for any flight regime. Indeed, the first-stage rocket engine should operate, not only at high altitude regime, but also at ground level especially during start-up and shutdown phases. Furthermore, due to the minimal duration of the atmospheric flight compared to the total duration of the launch, the first stage engines are optimized for low external pressures. However, when operating at ground level (ignition and first lift-off phase), the rocket nozzle encounters strong instabilities due to side-loads which are generated by boundary layer separation. This phenomena is prejudicial for the mechanical behavior of the structure and can cause damage or complete loss of the engine.

In addition to the aerodynamics loads, there exists a significant difference in temperature between the hot combustion gases and the cooled walls of the engine. This inevitably leads to strong wall-heat fluxes and extreme temperature gradients through the combustion chamber and subsequently the nozzle walls. To remedy this problem, various cooling techniques have been developed and used in the past, such as ablative, radiation, gas-turbine dump and film cooling (Suslov *et al.*, 2010) [96].

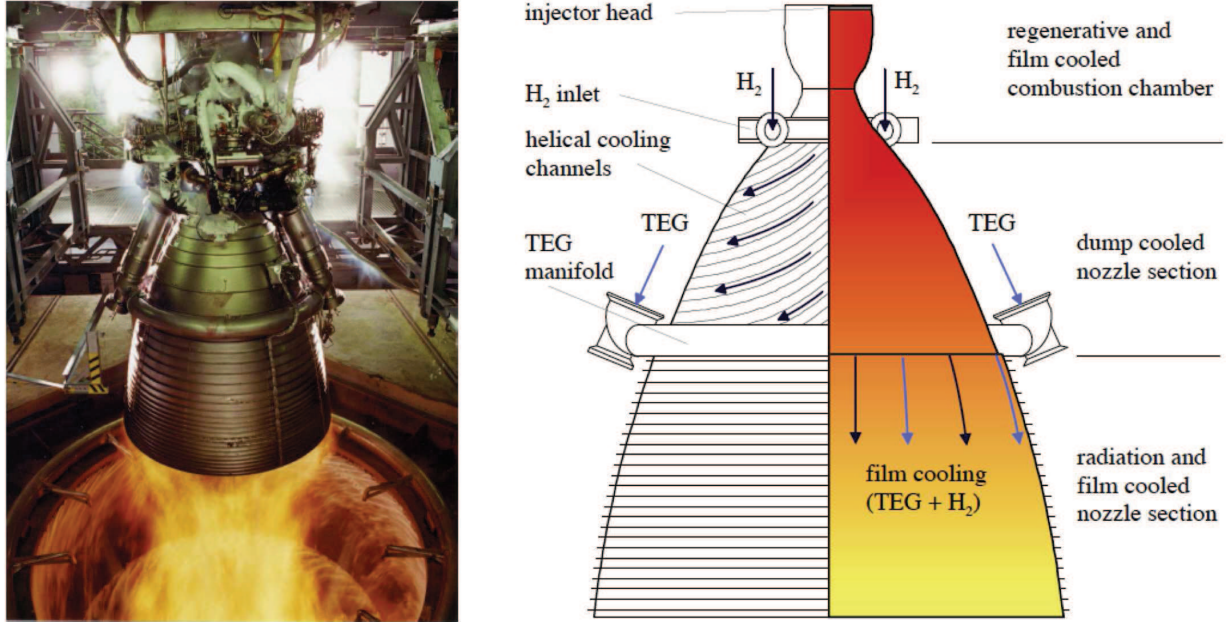


Figure 1.1: *Vulcain II* engine, at the P5 test bench in DLR Lampoldshausen, Germany (left); Nozzle geometry with the dump cooling design (right). (Suslov *et al.*, 2010) [96].

In the dump cooling, for instance, the liquid Hydrogen LH₂ at the exit of the turbine passes through cooling channels within the coating material, and is dumped at the end of the skirt of the nozzle through supersonic outlets. However, in the film cooling, part of the Liquid Hydrogen (LH₂) and the Turbine Exhaust Gas (TEG) is injected into the nozzle, at a specific cross section. This method can either be used alone for small engine nozzles with low heat fluxes, or simultaneously with cooling channels, to the lower section of the nozzle, as the *Vulcain II* engine for instance. The TEG film-injection at a relatively low temperature reduces the convective heat transfer between the hot gas and the inner surface of the nozzle.

Fig. 1.1 shows an example of the *Vulcain II* engine during a hot gas run on the P5 test bench at the DLR center in Lampoldshausen, Germany. The *Vulcain II* is a first-stage liquid propellant LOX/H₂ gas generator engine. Its vacuum thrust is about 1350 kN, with a mass flow of 320 kg/s and a specific vacuum impulse ISP of 433 s. The upper part of the structure features Liquid Hydrogen dump cooling, delivering a mass flow of 3 kg/s. The coolant flows through rectangular helical channels. At a nozzle expansion ratio of $\Sigma = A_e/A_{th} = 32$ (where A_e is the exit section and A_{th} is the throat area), Hydrogen-film is injected into the nozzle at supersonic speed in the

flow direction. Downstream of the injection point, Hydrogen develops a cooling film that protects the lower nozzle section from heat impact of the accelerated hot combustion gases. In addition to Hydrogen, the turbine exhaust gases (TEG) are also injected with a mass flow rate of about 10 kg/s at almost the same position. To provide equal circumferential coolant distribution, the TEG is guided by two pipes from the upper part of the engine along side the upper nozzle part to a manifold ring arranged before the coolant injection (Suslov *et al.*, 2010) [96].

1.2 Heat transfer in supersonic nozzles

The convective heat transfer in supersonic nozzles has not been frequently investigated through experimental studies. The available experiments mainly investigated heat transfer in conical convergent-divergent type nozzles, focusing on comparison between experimental data and available theoretical correlations. The focus was in the validity of Nusselt-type correlations, used for predicting heat transfer coefficients in canonical flows (such as pipe flows) which have been discussed and used for predicting heat transfer in the convergent as well as in the supersonic part of the nozzle.

Among others, experimental results of convective heat transfer, subjected to large variations in pressure gradients in conical nozzles, are presented by Back *et al.* (1964) [4]. The 2.5 Mach convergent-divergent nozzle has a half-angle of 30° for the convergent and a half-angle of 15° for divergent. At the inlet, the imposed stagnation pressure ranged from 5.5 to 17.2 bar, the total temperature from 570 to 1110 K, and the thicknesses of the considered dynamic boundary layers at the inlet between 5% and 25% of the radius of the nozzle inlet. The used gas is a compressed air, heated by internal combustion of methanol. The mass flow ratio (mixture of methanol/air) is taken sufficiently small (even for the largest total temperature case) so that the combustion products can be assumed to air. The results show that the heat transfer coefficient reaches its maximum just upstream of the throat (region where the mass flow rate reaches its maximum value) and that a reduction of this coefficient occurs downstream of the separation zone, which appears in the case of a low total pressure. It was also observed a reduction of 10% of the heat transfer coefficient between the lowest and highest studied boundary layer thicknesses.

This result was also observed by Bartz (1963) [7] under different boundary layer thickness and wall conditions, who presented a theoretical analysis of a convergent-divergent flow using the available skin-friction and heat-transfer coefficient calculation theories.

Interesting works on the convective heat transfer in supersonic nozzles were also conducted by Back *et al.* (1966 [3], 1967 [5], 1968 [6]). Among them, measurements of heat transfer from a hot air flow in a conical supersonic water cooled convergent-divergent type nozzle, were carried out (Back *et al.*, 1967) [5]: the nozzle has a convergent and divergent half-angle of 45° and 15° respectively, an area ratio Σ equal to 6.6 and a ratio of radius of the throat to radius of throat-curvature equal to 0.625. The ratio of the gas wall-temperature to the total temperature T_w/T_r (where T_r is the recovery temperature, nearly equal to the adiabatic wall-temperature) ranges from 0.3 to 0.7. Different turbulent boundary layer thicknesses δ_{in} were imposed at the inlet of the nozzle (where $H = \delta_{in}^*/\theta_{in}$ is the shape factor) is slightly less than 0.5. At the inlet, the dynamic boundary layer has a thickness of 45% of the radius of the nozzle inlet, and is slightly thinner than the thermal boundary layer. Reynolds numbers based on the momentum thickness at the nozzle inlet θ_{in} vary between 3000 and 18000. The results showed that the heat transfer coefficient along the nozzle depends on the structure of the boundary layer at the inlet, and on the way the boundary layer is affected by the acceleration of the flow. It was also reported that the heat transfer coefficient increases through the convergent, reaching its maximum downstream of the nozzle throat, to decrease again in the divergent. At low Reynolds number, the thinnest boundary layer is laminar along the nozzle, and the heat-transfer coefficient in the region near the throat seems unaffected by the the boundary layer thickness.

Boldmann *et al.* (1966) [10] presented experimental velocity and temperature profiles of the boundary layers, heat-transfer, and turbulence measurements for a conical nozzle configuration with a cylindrical approach section operating with air at a nominal total temperature and pressure of 540 K and 20 bar, respectively. Experimental heat-transfer coefficients were compared to values determined by Nusselt-type pipe flow correlation. It was concluded that the experimental heat-transfer coefficients could not be correlated by the Nusselt-type pipe flow correlation, where the predicted values of the heat-transfer coefficient were significantly higher by about 70% than the experimental values in the throat region of the nozzle. It was also noted that the heat-transfer coefficients were essentially unaltered even with the higher levels of turbulence intensity, and the maximum heat-transfer coefficient occurred slightly upstream of the geometric throat.

An experimental study of the effect of wall-cooling on the mean structure of a turbulent boundary layer in low-speed gas flow were presented by Back *et al.* (1970) [2]. The study is interesting in a way to highlight the single effect of wall-cooling on the dynamics of the considered flow. The

flow evolved at a Mach number of 0.06 and the Reynolds numbers Re_θ varied from 1500 to 36000. Wall-temperature to freestream temperature ratio T_w/T_∞ spanned a range extending from 0.4 to 1. Semi-empirical analysis, based on supersonic-flow measurements by Coles (1961) [16] and Spalding & Chi (1964) [92] were used to compare the obtained data. Experimental results were obtained at two different inlet conditions, based on the transition to a turbulent state of the upstream boundary layer: natural or forced transition. In this investigation, the ratio of the thermal to the velocity boundary layer thickness δ_t/δ was assumed to be the same as the ratio of energy thickness to momentum thickness ϕ/θ . It was concluded that under forced transition, the ratio of displacement thickness to momentum thickness $H = \delta^*/\theta$ (H is the shape factor) was reduced. The effect of wall-cooling was to increase the friction velocity above that of the adiabatic case (20% at $T_w/T_\infty = 0.5$). It was also reported that the measured velocity and temperature profiles were in fair agreement with Coles' (1961) transformation theory [16], and indicated a wakelike behavior in the outer part of the layer.

1.3 Supersonic turbulent boundary layers

For high-speed flows, the kinetic energy of the motion is a considerable fraction of the total energy of the fluid (which is not necessarily true for low-speed flows) which yields to an important amount of viscous dissipation in the mean energy balance within the boundary layer. Morkovin (1961) [67] showed that '*in non-hypersonic boundary layers [...] the entropy (total-temperature) mode is very small for conventional rates of heat transfer*' (Bradshaw, 1977) [11], and announced that at moderate Reynolds numbers '*the essential dynamics of these shear flows will follow the incompressible pattern*' (Smits & Dussauge, 1996) [89]. In fact, for an adiabatic compressible turbulent boundary layer, and due to viscous heating, compressibility effects arise mainly from the large change in the fluid properties : '*a density gradient caused by the dissipative heating near the no-slip wall is the primary effect of increasing the mean flow Mach number*' (Lele, 1994) [58]. It is then commonly concluded that adiabatic supersonic turbulent boundary layers at moderate Mach numbers (typically $M \leq 5$) can be studied using the same models as low-speed flows, as long as the variations in the mean flow properties are accounted for. Based on this, it follows some interesting results, including mean velocity and fluctuations scalings, and a specific formulation of the Reynolds analogy, namely the SRA (*Strong Reynolds Analogy*).

1.3.1 Adiabatic case

Adiabatic supersonic turbulent boundary layers were first investigated through experiments (for a data compilation, see Fernholz & Finley (1977) [29]) mainly in order to validate the Morkovin's hypothesis. One of the main conclusions that follow the hypothesis is that the total temperature fluctuations are very weak within the boundary layer. Hence, velocity and temperature fluctuations are perfectly anti-correlated, and the Strong Reynolds Analogy linking the velocity and temperature fields is nearly equal to 1.

Recently, highly resolved direct numerical simulations (DNS) and large-eddy simulations (LES) helped getting more insight into the topic. Guarini *et al.* (2000) [38] studied an adiabatic compressible boundary layer at Mach number $M = 2.5$ and Reynolds number based on the momentum thickness $Re_\theta = 1577$, using DNS. In their simulation, it was assumed that the boundary layer grows slowly in the streamwise direction such as the turbulence can be treated as approximately homogeneous in this direction. The flow was then considered homogeneous in both streamwise and spanwise directions. It was concluded that the total temperature fluctuations were of the same order as the temperature fluctuations. The under-estimation of the R_{uT} correlation compared to the experimental values seemed to be due to a difference of about a factor of 2 in the magnitude of the total temperature fluctuations. The modified SRA relation derived by Huang *et al.* (1995) [43] was found to give a better agreement with the numerical data, compared to Gaviglio's (1987) relation [33].

Maeder *et al.* (2000) [63] made DNS of zero-pressure gradient adiabatic supersonic turbulent boundary layers at Mach numbers 3, 4.5 and 6 and a Reynolds number $Re_\theta \approx 3000$. An extended temporal approach, where the streamwise direction is supposed periodic, was used. It was concluded that the compressibility effects on the turbulence statistics are small up to a Mach number of about 5, and that the total temperature fluctuations cannot be neglected, even for a Mach number of 3. The dilatational dissipation correlations were also found to be small throughout the considered Mach number range. Verifying the Morkovin's hypothesis, the structure parameter had approximately the same value for compressible and incompressible boundary layers.

Pirozzoli *et al.* (2004) [76] performed DNS of a supersonic turbulent boundary layer over an adiabatic wall at Mach number 2.25 and $Re_\theta \approx 4000$. For the turbulent inflow condition, a generic laminar boundary layer profile is prescribed at the inlet, and a blowing/suction method forced

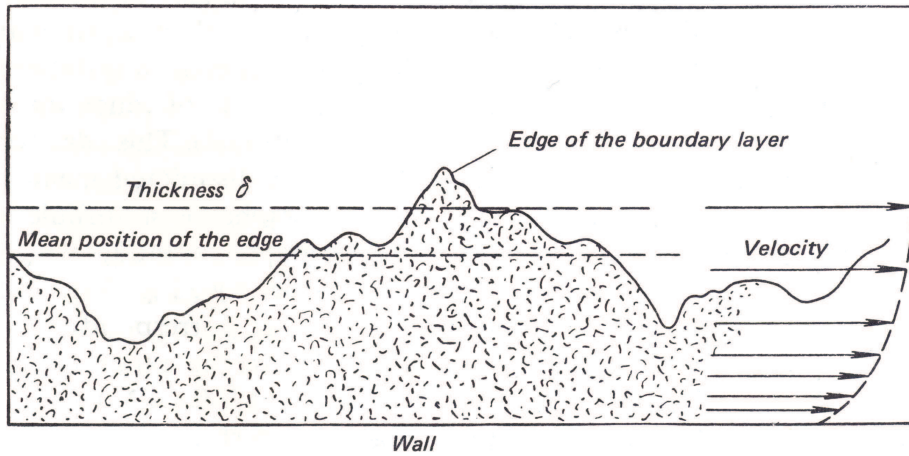


Figure 1.2: General diagram of a turbulent boundary layer on a flat plate (Schlichting, 1979 [82]).

the flow to transit to a fully turbulent state. It was reported that the total temperature was not uniform throughout the boundary layer, and that the total temperature fluctuations were non-negligible across the boundary layer. Linking the velocity and the temperature fluctuations, it was shown that u' and T' are not perfectly anti-correlated, reaching a maximum of 0.85. The turbulent Prandtl number was not equal to unity, varying between 0.7 and 0.8 in the outer part of the boundary layer.

Lagha *et al.* (2011) [55] studied compressible turbulent boundary layers with freestream Mach numbers ranging from 2.5 to 20 using DNS. A modified recycling/rescaling procedure was used to prescribe a fully turbulent inflow condition. It was shown that the zero-pressure gradient supersonic turbulent boundary layers exhibit close similarities to incompressible boundary layers, and that the incompressible results can correctly describe the main compressible turbulence statistics, as long as the density variation is taken into account.

Duan *et al.* (2011) [24] simulated turbulent boundary layers at Mach numbers ranging from 3 to 12, with Re_θ ranging from 3000 up to 11350. With regards to the Morkovin's scaling, the DNS study showed that the van Driest transformation for the mean streamwise velocity well collapse different results with the incompressible references.

More recently, Pirozzoli & Bernardini (2011) [74] investigated supersonic turbulent boundary layers at Mach number $M = 2$ and moderate Reynolds numbers up to $Re_\tau \approx 1120$, using highly

resolved DNS. An extended domain in the streamwise direction, up to $L_x = 100\delta_{in}$, was used in order to achieve a fully turbulent state of the flow, in order to ensure a better prediction of the turbulent statistics. Comparison of the velocity statistics up to the fourth-order showed nearly exact agreement with incompressible data, provided the momentum thickness Reynolds number matched, and provided the mean velocity and the velocity fluctuations were scaled according to the mean density variation. It was also found that an energy peak emerges in the logarithmic region of the boundary layer, associated with the appearance of large and streaky structures, referred to as *superstructures*. As expected for the range of the considered Mach number, compressibility effects were found to be weak. Again, the negligible total temperature fluctuations assumption is found to be violated, and the $-R_{uT}$ correlation reached its maximum in the buffer layer.

1.3.2 Isothermal case

The previous conclusions are ‘*certainly reasonable for supersonic flows without mass and heat sources.*’ (Smits & Dussauge, 2006) [88]. However, for an isothermal-wall boundary layer, the applicability of the Morkovin’s hypothesis and the following assumptions are, at first sight, debatable. The number of studies investigating supersonic turbulent boundary layers over heated/cooled walls are limited. Early investigations dealt with theoretical calculations of flow properties, such as the skin-friction C_f and the heat transfer C_h coefficients, and theoretical calculations of the flow properties.

Hopkins & Inouye (1971) [41] reviewed available theories, namely Sommer & Sort (1956) [91], Spalding & Chi (1964) [92], Van-Driest II (1956) [102] and Coles (1961) [16] theories, for predicting turbulent skin-friction and heat-transfer coefficients on flat plates at supersonic and hypersonic Mach numbers. Considered flows evolved over adiabatic as well as non-adiabatic cold walls ($0.3 \leq T_w/T_r \leq 1$) and covered a wide range of supersonic and hypersonic Mach numbers ($1.5 \leq M \leq 5.8$). They suggested that the van-Driest II theory should be used to predict the best approximations of these quantities.

Cook & Richards (1977) [17] extended the Hopkins & Inouye’s (1971) [41] study with highly cold-walls ($T_w/T_r \leq 0.3$) at lower supersonic Mach numbers ($1.5 \leq M \leq 1.8$), and found that van-Driest II theory [102] predicts with better certainty heat transfer, but was found to be less confident for predicting skin friction for the range of the considered variables.

Huang *et al.* (1993) [42] presented a theoretical method for calculating skin-friction coeffi-

lients and mean velocity profiles for compressible turbulent boundary layers with isothermal and adiabatic walls. For the logarithmic region of the mean velocity profiles, the incompressible law-of-the-wall, transformed using the van-Driest theory [101], is adopted. The transformation reads $u^c = \sqrt{B} [\arcsin(\frac{A+u}{D}) - \arcsin(\frac{A}{D})]$ with $A = q_w/\tau_w$, $B = 2C_{p_\infty}T_w/\text{Pr}_t$ and $D = \sqrt{A^2 + B}$. This equation has been extended to the outer and the viscous layers. Results reported that skin friction seems to be predicted nearly as well as using the van-Driest II theory for the range of the considered Mach numbers, while it shows lower results compared to the same theory for strongly cooled walls.

Experimental investigations of supersonic turbulent boundary layers over heated/cooled walls are limited to measurements of the basic quantities, such as mean velocity and temperature profiles, temperature fluctuations, shear stress profiles, etc.

Among others, Gran *et al.* (1974) [37] experimentally studied Mach 4 supersonic turbulent boundary layers subjected to adverse and favorable pressure gradients, and with constant temperature wall $T_w/T_r = 0.5$. They found that the van-Driest transformed velocity profiles showed good agreement with low-speed results. They also studied the response of zero pressure gradient high-speed boundary layers to a near step change in the wall temperature. Two cases were analyzed: a *step-down* case which consists of an initially adiabatic turbulent boundary layer flowing onto a cooled wall, and a *step-up* case that consists of an initially cooled boundary layer flowing onto a wall with nearly the recovery temperature. They reported that the thermal boundary layer thickness, δ_T , varies considering the direction of the wall temperature change ($\delta_T \sim x$ for the *step-up* case, and $\delta_T \sim x^{1/2}$ for the *step-down* one).

Laderman (1978) [53] reported experimental results concerning mean flow properties of a Mach 3 turbulent boundary-layer with negligible pressure gradient, and with T_w/T_r ratio ranging from 0.54 to 0.94. He reported that the law-of-the-wake expression correctly correlates the measured mean velocity profiles, and that the turbulent transport properties (turbulent shear stress, mixing length and eddy viscosity) are found to be in good agreement with previous compressible adiabatic flows. These properties were indirectly extracted from the time-averaged conservation equations using the measured mean flow profiles. With decreasing heat transfer, it was observed that the experimental total temperature-velocity profiles did not agree well with the linear Crocco's [105] relation.

Furthermore, Laderman & Demetriades (1979) [54] extended the study to account for the turbulent transport properties using hot-wire anemometry measurements of the shear stresses of a Mach

3 boundary layer at $\text{Re}_\theta \simeq 3500$, with T_w/T_r ratios of 0.94 and 0.71. The normalized shear stress distributions, τ/τ_w , is found to be independent of the Mach number and the wall-temperature, for the considered range of wall-temperature ($0.4 \leq T_w/T_r \leq 1.0$).

Gaviglio (1987) [33] and Rubesin (1990) [79] proposed two different modifications of the SRA, called respectively GSRA and RSRA, to better account for the wall-heat transfer.

Dupont (1990) [26] studied experimentally the effect of strong wall-heating on the fluctuating field of a flat plate supersonic turbulent boundary layer. It was concluded that two combined but distinct mechanisms influence the total temperature production: the first is related to compressibility effects, and the second is due to the large temperature gradient originated from the heating. The Reynolds shear stress was found to remain unaffected by the wall-heating, and the velocity-temperature correlation was found to be constant, and close to -0.8 .

Audiffren (1993) [1] studied the influence of wall-heating on the characteristics of a turbulent boundary layer at Mach 2.25 and $\text{Re}_\theta \approx 5000$. It was reported that, except the inner region ($y/\delta < 0.2$), there is no significant increase in the fluctuating Mach number. It was also concluded that the wall-heating was governed by some specific parameters, like the density ρ and the friction velocity, u_τ , for the dynamic field, and the friction temperature, T_τ , for the thermal field. It was found that the wall-heating has the effect of increasing the boundary layer thickness, and that the intensity of static and total temperatures increase as well. Finally, it was reported that the Reynolds shear stress $\langle u'v' \rangle$ did not undergo notable changes with wall-heating, and that the skewness and the flatness factors were also not influenced by the wall-heating.

Debièvre *et al.* (1997) [21] investigated the effect of a step change in the wall-temperature on a turbulent boundary layer in a supersonic flow at Mach number of 2.3 with a wall-to-recovery temperature ratio T_w/T_r taken as 1.0, 1.5 and 2.0. The aim of their study was to describe the development of the boundary-layer flow to the new condition at the wall. A deviation from Crocco's law was observed in the outer part of the boundary layer, and the temperature field seems to have had a little effect on the velocity field in the same region. It was also reported that the correlation between the velocity and the temperature fluctuations appears unaffected by the wall-heating.

On the other hand, numerical studies dealing with supersonic wall-bounded flows involving isothermal walls mainly focused on studying canonical problems, such as turbulent channel flows and flat-plate boundary layers.

Coleman *et al.* (1995) [15] simulated a compressible turbulent flow, at Mach numbers of 1.5

and 3 and Reynolds number $\text{Re}_\theta \approx 3000$, in a plane channel with cold walls using DNS. Results are found to agree well with the incompressible data, when the scaling accounts for the mean property variations. It was also concluded that, even if the assumption, which states that the instantaneous total temperature remains constant, is approximately satisfied, the van-Driest transformation is found to be overall very successful. The isothermal-wall flow is strongly influenced by sharp gradients of the mean density and temperature, to the point that most of ρ' and T' are the result of solenoidal mixing of density and temperature by the turbulence.

Huang *et al.* (1995) [43] exploited DNS results of two supersonic fully developed channel flows between very cold isothermal walls developed by Coleman *et al.* (1995) [15]. They concluded that the compressibility effects due to turbulent fluctuations might not be as strong as at a given M_t in boundary layers, and that when turbulent heat fluxes are scaled by the mean density variation $\langle \rho \rangle / \rho_w$, the profiles collapse onto the corresponding incompressible curves. A new formulation of the SRA, named HSRA, was also proposed and it seemed better accounting for the effect of the isothermal condition on the turbulence.

Lechner *et al.* (2001) [57] studied a Mach 1.5 supersonic turbulent channel flow at $\text{Re}_\theta \approx 3000$, where the results were compared to Coleman *et al.* (1995) [15]. It was reported that the density fluctuations were produced by the mean density gradient in the wall-layer and peak there. In the wall-layer, the temperature fluctuations were observed to be perfectly correlated with the density fluctuations. In this specific case of cooling, and by analyzing the scatter plots of the different thermodynamic fluctuations, it was concluded that the temperature fluctuations were conditioned by sweeps and ejections. In fact, sweeps (respectively ejections) carry positive (respectively negative) temperature fluctuations. The total temperature fluctuations reached maximum values of about 10% of the mean total temperature in the wall layer, and were due to temperature, velocity and kinetic energy fluctuations. In the core region, they were reduced by a factor of 3.

Morinishi *et al.* (2004) [66] compared two compressible turbulent channel flows at Mach 3 and $\text{Re}_\theta \approx 3000$, with cold/cold walls and cold/adiabatic walls. The main objective of the study was to reveal the effects of the cold-wall boundary conditions on the dynamic of the flow. They reported that the semi-local scaling provided a universal profile for the Reynolds shear stress, while no universal scaling was found for the turbulent heat flux. It was reported that the Morkovin's hypothesis was not applicable to the asymptotic behavior in a region very near from the wall.

Foysi *et al.* (2004) [31] studied compressibility effects and turbulence scaling in a supersonic

channel flow with cold isothermal walls using DNS, at a Mach number up to $M \approx 3.5$ and $\text{Re}_\tau \approx 1030$. When comparing their results to incompressible data, it was observed that the inner scaling with $y^+ = yu_\tau/\nu_w$ fails. The use of the semi-local scaling $y^* = y/\delta_\nu^*$ (with $\delta_\nu^* = \langle \nu \rangle / u_\tau^*$ and $u_\tau^* = \sqrt{\tau_w / \langle \rho \rangle}$, τ_w is the wall-friction) used by Huang *et al.* (1995) [43] improved collapsing the results, even if this improvement is partial. The outer scaling, using $\langle \rho \rangle R_{ij} / \tau_w$ (where R_{ij} is the Reynolds stress tensor) versus y/H (H being the height of the channel) seems collapsing all studied cases in a region sufficiently far from the wall.

An extension of the study by Morinishi *et al.* (2004) [66] was made by Tamano and Morinishi (2006) [98] of compressible turbulent channel flows between adiabatic and/or isothermal walls at Mach numbers of 1.5. By analyzing the temperature variance transport equation, they found that the compressibility effects were not negligible near the low-temperature wall. The skewness and flatness factors, $S(u')$ and $F(u')$, were found to agree well with incompressible data, which did not depend on the thermal boundary conditions. The Morkovin's hypothesis seemed to be correct for higher-order turbulence statistics of u' . However, $S(v')$ and $F(v')$ did not agree with incompressible data, due to the compressibility effects.

Additional studies were reported by Liu & Pletcher (2007) [60] on compressible turbulent boundary layers using DNS. Four cases were considered : two of them were related to turbulent boundary layers with Reynolds number $\text{Re}_\theta \approx 2000$ at Mach number $M \approx 0.06$ with a heated wall at $T_w/T_\infty = 1.58$, and the two others concerned adiabatic supersonic turbulent boundary layers with $\text{Re}_\theta \approx 2000$ and at $M = 1.8$, where the wall-temperature to freestream temperature ratio $T_w/T_\infty = 1.58$. It was concluded that the similarity laws could be approximately satisfied if the density-weighted transformation was applied. Even with the weak wall-temperature, T_w , the friction velocity, u_τ , of the heated case seemed to be larger than that of the supersonic case. Using the local scaling $u_\tau^{local} = u_\tau \sqrt{\langle \rho \rangle / \rho_w}$ and $y^+ = yu_\tau^{local} / \langle \nu \rangle$ (where $\langle \rho \rangle$ and $\langle \nu \rangle$ are the local properties), it was observed that the magnitude and the location of the maximum $u_{rms}^* = u_{rms} / u_\tau^{local}$ agreed well with the incompressible data. The streamwise component of the velocity fluctuations, u_{rms}^* , of the heated-wall case appeared to nearly coincide with the distribution of an isothermal incompressible turbulent boundary layer. The Reynolds shear stress, $-\langle u'v' \rangle$, plotted against y^+ using local properties, showed good agreement with the corresponding incompressible results. The subsonic flow with heat transfer was found to have a larger density compared to the supersonic flow throughout the boundary layer. The turbulent Mach number, M_t , had a very small value for

the $M = 0.06$ subsonic case ($M_t \leq 0.02$ for the inner part of the boundary layer), while it showed a larger value, which reached a peak of ≈ 0.25 for the adiabatic supersonic case.

Gosh *et al.* (2008) [36] made DNS and LES to investigate compressibility effects of a supersonic pipe flow at Mach number $M \approx 1.5$ (based on the ratio of the bulk velocity to the speed of sound at wall-temperature) and with an isothermal wall boundary condition. Although studying supersonic pipe flows is different from supersonic plane channel or boundary layer flows, due to the effects of wall curvature and the non-zero pressure-gradient, interesting conclusions can be learned from such studies. It was observed that, near the wall, the density and temperature showed strong negative correlation, while in the core region, there were no mean density and temperature gradients. This was also confirmed by a strong pressure-density correlation in the core region, and a nearly zero-value near the wall. In particular, it was also concluded that the Morkovin's hypothesis held for most statistics of the flow, and that the van-Driest transformation could be used for the mean velocity profile. A scaling, using local mean density and viscosity (*i.e.* semi-local scaling) was found to nearly collapse the peak locations of the velocity fluctuations, but not the peak magnitudes. As it is known, the mean density decreases with increasing Mach number, which leads to the decrease of the pressure-strain correlations, and then increase the Reynolds stress anisotropy.

Duan *et al.* (2010) [23] performed DNS of supersonic turbulent boundary layers at Mach number 5 and with T_w/T_r ranging from 0.18 to 1. One of the main conclusions of the study was that decreasing the wall-temperature increased the compressibility effects. The streamwise velocity distributions normalized using the van-Driest transformation collapsed with the incompressible results, and the *r.m.s* of the velocity fluctuations scaled using the Morkovin's scaling held also for the adiabatic profiles. The Walz's equation (White, 1991) [105] did not hold for the wall temperature varying cases, and the mismatch increased as the temperature decreased. The R_{uT} correlation remained about the same, except near the wall. The modified SRA relation given by Huang *et al.* (1995) [43] gave better results compared to the *standard* SRA and to other modified relations. It was also shown that the Prandtl number was nearly constant and insensitive to the wall cooling. For the budget of the turbulent kinetic energy, the semi-local scaling correctly collapsed profiles. It was reported also that the wall cooling has the effect of increasing the length and the coherence of the turbulent structures.

Lagha *et al.* (2011) [55] showed that the streak length in terms of x/δ decreased when Re_τ increased. It was also concluded that in an isothermal simulation with cold wall, the wall-parallel

plane streaks were longer, whereas for a hot wall, they were shorter (in comparison with the adiabatic case).

In terms of large-eddy simulation, few works relying on either explicit or implicit LES of wall-bounded flows were reported. Among others, Spyropoulos & Brais dell (1998) [94] reported LES of spatially evolving supersonic turbulent boundary layer at Mach number $M = 2.25$. A second- as well as a fourth-order accurate upwind biased finite differences schemes were used for the convective fluxes. In terms of wall-units, all considered grids had resolutions ranging between $59 \leq \Delta x^+ \leq 88$ for the streamwise direction, $0.77 \leq \Delta y_{min}^+ \leq 0.97$ for the wall-normal direction and $11.4 \leq \Delta z^+ \leq 42.1$ for the spanwise direction. It was concluded that a decrease of about 20% of the computed skin-friction is found when lower order schemes are employed, mainly a third order upwind scheme for the convective terms and second order for the viscous terms. Because of the low considered Mach number, the modeling of the isotropic part of the shear stresses was not found to have a considerable effect on the skin-friction coefficient, C_f . The insufficient amount of turbulent transport was attributed to the use of the dynamic Smagorinsky model, in which the eddy viscosity is computed using the smallest resolved scales.

Supersonic flat-plate boundary layers have been investigated by Yan *et al.* (2002) [107] using monotonically integrated large-eddy simulation (MILES) approach. In this simulation, the numerical dissipation induced by the scheme substitutes to the SGS eddy viscosity, mimicking from an energetic view-point the action of SGS terms on the flow dynamics. The simulated flows evolved at freestream Mach numbers of 2.88 and 4. An adiabatic as well as an isothermal case with $T_w/T_r = 1.1$ were performed. In terms of wall-units, grid resolutions were $\Delta x^+ = 18$, $\Delta y_{min}^+ = 1.5$ and $\Delta z^+ = 6.5$. It was reported that the mean streamwise velocity profiles using the van-Driest transformation were in good agreement with the viscous sublayer linear approximation and law-of-the-wall ($u_{vd}^+ = 2.5 \log y^+ + 5.7$). The distributions of the streamwise Reynolds stresses scaled by $\langle \rho \rangle$ and τ_w , were found to be very similar except close to the wall, and showed good agreement in the outer region of the boundary layer ($y/\delta > 0.2$). The peak magnitude in the near-wall region ($y/\delta < 0.2$) was supported by experimental and DNS results, although its location was not consistent with the reference data. The Reynolds shear stresses of both cases showed good agreement with the reference solutions. Finally, the turbulent Prandtl number Pr_t was found to be in good agreement with the experimental value of 0.89.

Brun *et al.* (2008) [12] performed LES of fully turbulent compressible isothermal channel flows

at $\text{Re}_\theta \approx 3000$ and $\text{Re}_\theta \approx 4880$, with Mach numbers varying in the range $0.3 \leq M \leq 5$. Mesh refinement was used in the near-wall region so that the flow was solved in a DNS sense, while the SGS model acted mainly in the core region of the channel. A new integral scaling for wall-bounded flows (denoted $y^{c+} = \int_0^{y^+} \mu_w / \langle \mu \rangle \, dy^+$) was presented and used to improve both the wall-unit definition and the van-Driest transformation. Both viscosity/conductivity and density effects were accounted for in the proposed scaling. Based on the present integral scaling, it was shown that a relative universality of the wall-layer property exists. A new constant $c = 1/\text{Pr}_m$ (Pr_m is the mixing Prandtl number) for the modified Strong Reynolds Analogy, as proposed by Huang *et al.* (1995) [43], was also proposed. It was shown that accounting for the Pr_m in the modified SRA yielded a good fit of the results. It was finally concluded that it is possible to deduce the turbulent properties of non-hypersonic boundary layers from the incompressible law-of-the-wall with equivalent integral Re_τ^c numbers.

1.4 Summary

With regards to heat and fluid flows in supersonic nozzles, it has been shown in the reviewed experimental studies, that the intensity of heat transfer in such systems depends on many factors such as gas flow rate, compressibility, nozzle dimensions and chemical reactions.

Nowadays, with the progress achieved in computer sciences and numerical flow simulations, space system designers, especially those in charge of rocket nozzles, are eager to introduce high-fidelity numerical simulations in their design chains. More fundamental research towards basic studies such as near-wall turbulence is therefore needed.

The objective of this work is then to understand, through well-resolved numerical simulations, the governing flow parameters and the near-wall turbulence behavior of wall-bounded flows, such as those occurring in supersonic aerodynamics. The influence of the wall-heat transfer on the dynamics of such flows is of primordial interest.

From the previous review, it can be retained that both experimental and numerical investigations do agree with the fact that, for relatively low heated/cooled walls at moderate Mach numbers, the mean velocity profiles hold for the incompressible data as long as the van-Driest transformation is applied. However, the velocity fluctuations profiles does not universally scale with the incompressible counterparts when the *standard* Morkovin scaling is used. Consequently alternative

scaling laws must be applied, whether near-wall region or far-from-wall region is studied (Morinishi *et al.*, 2004 [66], Foysi *et al.*, 2004 [31]). Also, the *original* SRA seems to fail linking velocity and temperature fluctuations, and the modified SRA relations, better accounting for the isothermal condition, are preferred (Cebeci & Smith, 1978 [13]; Gaviglio, 1987 [33]; Rubesin, 1990 [79]; Huang *et al.*, 1995 [43]). In terms of flow organization, near-wall streaks are found to be more coherent when decreasing the wall temperature (Coleman *et al.*, 1995 [15]; Duan *et al.*, 2010 [23]), and the Morkovin's hypothesis gives good agreement for predicting those structures (Morinishi *et al.*, 2004 [66]; Lagha *et al.*, 2011 [55]).

The present manuscript is organized as follows: after the introduction, the governing equations as well as the numerical strategy are presented in Chapter 2. Chapter 3 is dedicated to the LES study of an adiabatic supersonic turbulent boundary layer at $M = 2$ and $Re_\tau = 245$. The obtained results are compared to experimental as well as DNS data. Chapter 4 is an attempt to study a cold-wall supersonic turbulent boundary layer at a fixed Mach number $M = 2$. The influence of the strong wall-cooling is highlighted through a comparison with the adiabatic reference. Finally, the main conclusion along with some perspectives are drawn in Chapter 5.

Chapter 2

Équations Mathématiques et Schémas Numériques

2.1 Équations mathématiques et modèles de sous-maille

La Simulation aux Grandes Echelles (SGE) ou *Large-Eddy Simulation* (LES) repose sur l'hypothèse d'une séparation *totale* entre les grandes échelles (résolues) et les petites structures, appelées structures de sous-maille (modélisées) d'un écoulement turbulent. Lorsqu'il s'agit d'une modélisation explicite, cette séparation est effectuée en utilisant un opérateur de filtre passe-bas, appliqué au système d'équations gouvernant l'écoulement.

Si φ représente la variable à filtrer, \mathcal{G} l'opérateur filtre et $\overline{\Delta}$ la largeur du filtre appliquée, la variable filtrée $\overline{\varphi}(\mathbf{x})$ s'écrit:

$$\overline{\varphi}(\mathbf{x}) = \mathcal{G} * \varphi = \int_D G(\mathbf{x} - \boldsymbol{\xi}, \overline{\Delta}) \varphi(\boldsymbol{\xi}) \, d\boldsymbol{\xi} \quad (2.1)$$

où $*$ représente le produit de convolution à travers le domaine D et $\mathbf{x} = (x_1, x_2, x_3) = (x, y, z)$ représente les coordonnées cartésiennes d'un point.

Le filtre est construit de sorte à respecter la propriété suivante:

$$\int_D G(\mathbf{x} - \boldsymbol{\xi}, \overline{\Delta}) \, d\boldsymbol{\xi} = 1 \quad (2.2)$$

Dans les écoulements à densité variable, il est d'usage d'utiliser le filtre de Favre, basé sur la densité moyenne du fluide. Cet opérateur est défini tel que $\tilde{\varphi} = \overline{\rho\varphi}/\overline{\rho}$, considérant que chaque variable peut être décomposée en une partie résolue $\tilde{\varphi}$ (basse fréquence) et une partie modélisée φ'' (haute fréquence), de sorte à avoir $\varphi = \tilde{\varphi} + \varphi''$. Ainsi, la relation entre opérateur de Favre et de Reynolds

s'écrit:

$$\bar{\varphi} - \tilde{\varphi} = \overline{\varphi''} = -\frac{\overline{\rho' \varphi'}}{\bar{\rho}} = -\frac{\overline{\rho' \varphi''}}{\bar{\rho}} \quad (2.3)$$

avec $\varphi = \mathbf{U}$ ou T , avec $\mathbf{U} = (u_1, u_2, u_3) = (u, v, w)$ est le vecteur vitesse et T est la température.

2.1.1 Système d'équations filtrées

Le système d'équations de Navier-Stokes compressibles filtrées s'écrit sous une forme conservative:

$$\left. \begin{aligned} \frac{\partial \bar{\rho}}{\partial t} + \frac{\partial \bar{\rho} \tilde{u}_i}{\partial x_i} &= 0 \\ \frac{\partial \bar{\rho} \tilde{u}_i}{\partial t} + \frac{\partial \bar{\rho} \tilde{u}_i \tilde{u}_j}{\partial x_j} + \frac{\partial \bar{p}}{\partial x_i} - \frac{\partial \check{\sigma}_{ij}}{\partial x_j} &\approx -\frac{\partial \tau_{ij}}{\partial x_j} \\ \frac{\partial \bar{\rho} \check{E}}{\partial t} + \frac{\partial (\bar{\rho} \check{E} + \bar{p}) \tilde{u}_j}{\partial x_j} - \frac{\partial \tilde{u}_i \check{\sigma}_{ij}}{\partial x_j} + \frac{\partial \check{q}_j}{\partial x_j} &\approx -\frac{1}{\gamma - 1} \frac{\partial (\bar{p} u_j - \bar{p} \tilde{u}_j)}{\partial x_j} - \tilde{u}_j \frac{\partial \tau_{ij}}{\partial x_j} \end{aligned} \right\} \quad (2.4)$$

où $\bar{\rho}$, \bar{p} et \tilde{u}_i représentent respectivement les champ résolus de densité, de pression et de vitesse. L'équation d'état, l'énergie totale, le cisaillement visqueux et le flux de chaleur résolus s'écrivent:

$$\left. \begin{aligned} \bar{p} &= \bar{\rho} r \tilde{T} \\ \bar{\rho} \check{E} &= \frac{\bar{p}}{\gamma - 1} + \frac{1}{2} \bar{\rho} \tilde{u}_i \tilde{u}_i \\ \check{\sigma}_{ij} &= \tilde{\mu} \left(\frac{\partial \tilde{u}_j}{\partial x_i} + \frac{\partial \tilde{u}_i}{\partial x_j} \right) - \frac{2}{3} \tilde{\mu} \left(\frac{\partial \tilde{u}_k}{\partial x_k} \right) \delta_{ij} \\ \check{q}_j &= -\frac{\tilde{\mu} C_p}{Pr} \frac{\partial \tilde{T}}{\partial x_j} \end{aligned} \right\} \quad (2.5)$$

avec $\tilde{\mu}$ la viscosité dynamique résolue, obéissant à la loi de Sutherland et Pr est le nombre de Prandlt pris égal à 0.72 (pour l'air, avec $\gamma = C_p/C_v = 1.4$).

Contrairement aux symboles $\overline{(.)}$ et $\widetilde{(.)}$, le symbol $(\check{.)}$ ne représente pas une opération de filtrage, mais signifie que la quantité est calculée à partir d'une variable primitive filtrée. Ainsi, \check{E} se réfère à l'énergie totale résolue, qui n'est pas égale à l'énergie totale filtrée.

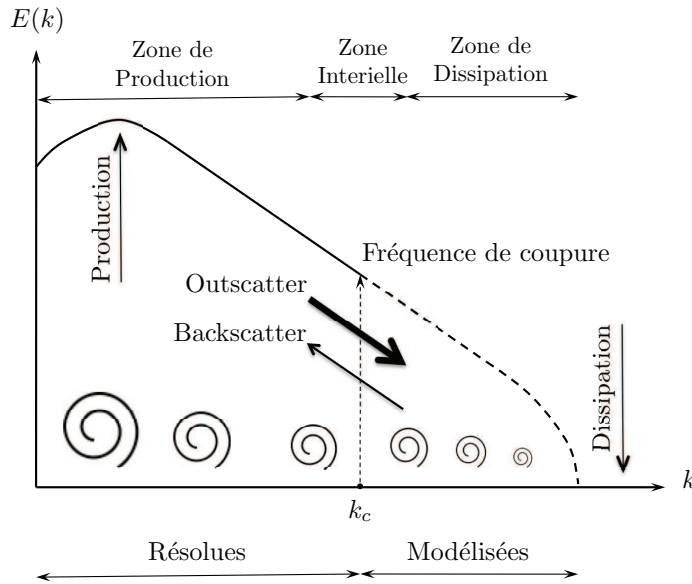


Figure 2.1: Spectre d'énergie typique dans un écoulement turbulent homogène.

2.1.2 Modélisation de sous-maille

2.1.2.1 Concept de la modélisation fonctionnelle

Le concept de base de l'approche LES repose sur le fait que l'action des échelles de sous-maille (isotropes et présentant un comportement universel) sur les échelles résolues (anisotropes avec un comportement moins déterministe) est principalement une action énergétique dissipative. De ce fait, un modèle de sous-maille agit essentiellement afin de dissiper l'énergie résolue par les grandes structures de l'écoulement. Dans notre étude, la contribution des échelles de sous-maille est considérée en utilisant une approche fonctionnelle explicite, en introduisant une viscosité turbulente reproduisant les effets des échelles de sous-maille sur la turbulence.

Un spectre typique d'une turbulence homogène, tel que représenté sur la Fig. 2.1, comprend une zone de production, une zone intercale dans laquelle l'énergie est transférée depuis les grandes structures vers les plus petites (*Outscatter*), et une zone de dissipation d'énergie.

En effet, les grandes structures d'un écoulement turbulent (associées aux faibles nombres d'ondes) extraient l'énergie cinétique depuis le champ moyen. Ces structures, qui sont initialement relativement épaisse, vont s'aplatir créant de fines structures tourbillonnaires instables qui,

en s'enroulant elles-mêmes, génèrent de petites structures (associées aux grands nombres d'ondes) sous formes de filaments. D'un point de vue énergétique, cela résulte en un transfert direct de l'énergie depuis les grandes structures vers les plus petites, jusqu'à ce que la viscosité moléculaire dissipe toute l'énergie cinétique en énergie interne (Garnier *et al.*, 2009) [32].

La modélisation des termes de sous-maille consiste donc à modifier le système d'équations régissant l'écoulement d'une manière à y intégrer les effets désirés de dissipation ou de production d'énergie.

Dans la présente étude, plusieurs modèles de sous-maille sont utilisés pour modéliser l'action des petites structures sur la turbulence : le modèle de Smagorinsky utilisant la procédure dynamique (noté DSM) proposé par Germano *et al.* (1991) [34] et Lilly (1991) [59] et étendu au cas compressible par Moin *et al.* (1991) [65], le modèle de structures cohérentes (*Coherent Structures*, noté CSM) introduit par Kobayashi (2005) [50], et le modèle WALE (*Wall-Adapting Local Eddy-viscosity*) proposé par Nicoud et Ducros (1999) [68]. Afin de mieux quantifier la contribution des modèles de sous-maille, une approche implicite (*Implicit Large-eddy simulation*, notée ILES) est aussi utilisée, dans laquelle la dissipation induite par les schémas numériques et le maillage utilisé imite, d'un point de vue énergétique, l'action du modèle de sous-maille sur les grandes structures de la turbulence.

2.1.2.2 Modélisation du tenseur des contraintes de sous-maille

Le tenseur des contraintes de sous-maille, τ_{ij} , dans l'équation (2.4) est défini comme:

$$\tau_{ij} = \bar{\rho} (\widetilde{u_i u_j} - \widetilde{u}_i \widetilde{u}_j) \quad (2.6)$$

Il est modélisé en utilisant une formulation fonctionnelle, moyennant l'introduction d'une viscosité turbulente. Cela se traduit par :

$$\tau_{ij} - \frac{1}{3} \tau_{kk} \delta_{ij} = -2\mu_{sgs} \widetilde{S}_{ij} - \frac{1}{3} \widetilde{S}_{kk} \delta_{ij} \quad (2.7)$$

où μ_{sgs} est la viscosité turbulente de sous-maille, et $\widetilde{S}_{ij} = 1/2 (\partial \widetilde{u}_i / \partial x_j + \partial \widetilde{u}_j / \partial x_i)$ est le tenseur du taux de déformation des échelles résolues.

La viscosité turbulente, μ_{sgs} , est généralement modélisée sous la forme:

$$\mu_{sgs} = \bar{\rho} C_s \Delta^2 |\widetilde{S}| \quad (2.8)$$

où $|\tilde{S}| = \sqrt{2\tilde{S}_{ij}\tilde{S}_{ij}}$ est le second invariant du tenseur de déformation, et C_s est la constante du modèle, souvent déterminée dynamiquement.

Pour les écoulements compressibles, Yoshizawa (1986) [108] propose un modèle de fermeture pour la partie isotrope du tenseur de sous-maille, τ_{kk} , défini par:

$$\tau_{kk} = 2\bar{\rho}C_I\Delta^2|\tilde{S}| \quad (2.9)$$

La constante du modèle C_I est, soit résolue dynamiquement en utilisant la procédure dynamique, soit prise constante dans le modèle CSM, égale à 0.005 (Moin *et al.*, 1991) [65].

Sauf mention, la partie isotrope du tenseur de sous-maille, τ_{kk} , ne sera pas modélisée pour les deux modèles CSM et WALE. Spyropoulos & Blaisdell (1998) [94], dans une étude LES d'une couche limite supersonique, ont montré que la contribution de la partie isotrope du tenseur SGS représente moins de 8% de la pression dynamique, même pour le cas d'un maillage relativement lâche. Ils ont donc conclus que ce terme peut être négligé.

Modèle de Smagorinsky dynamique

A cause des limites du modèle de Smagorinsky (1963) [86] dans l'étude d'écoulements turbulents pariétaux, notamment son comportement assez dissipatif dans les régions de fortes contraintes, ainsi que son comportement asymptotique incorrect dans la région de proche paroi, des améliorations, essentiellement dans la détermination des constantes, ont été apportées au modèle.

Dans la procédure dynamique du modèle de Smagorinsky, les paramètres du modèles C_s et C_I sont calculés à partir du champ résolu. Ainsi, un filtre *test*, noté $(\hat{\cdot})$, dont la largeur est supérieure à la taille du *filtre-maillage*, est appliqué aux quantités filtrées. Si $\hat{\Delta}$ représente la taille du filtre *test* et Δ la taille du *filtre-maillage*, il est d'usage de prendre $\hat{\Delta}/\Delta = 2$ (Fig. 2.2).

En effet, pour les deux niveaux de filtrage (*test* et *maillage*), il est communément supposé que les tenseurs τ_{ij} et \mathcal{T}_{ij} (voir Eq. 2.10) sont modélisés en utilisant la même constante C_s , ce qui revient à dire que C_s garde une valeur constante dans l'intervalle $[k_{test}, k_c]$ du spectre d'énergie. Par analogie à τ_{ij} , le filtre *test*, appliqué au tenseur des contraintes de sous-maille, s'écrit:

$$\mathcal{T}_{ij} = \widehat{\rho u_i u_j} - \frac{\widehat{\rho u_i} \widehat{\rho u_j}}{\widehat{\rho}} \quad (2.10)$$

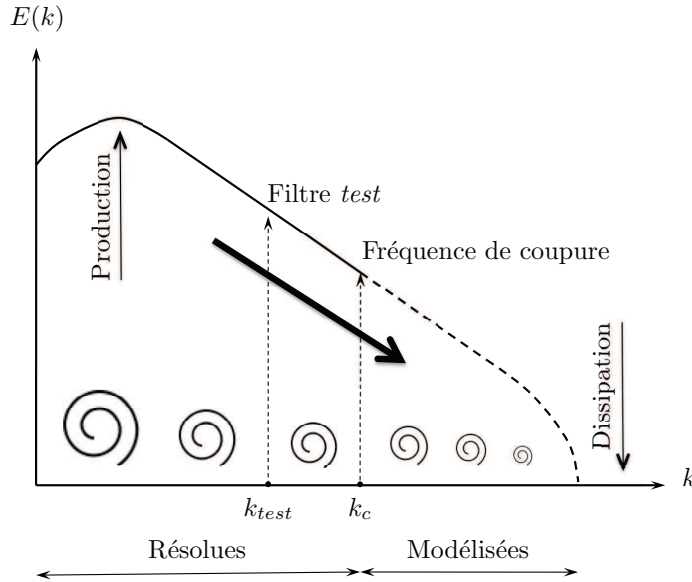


Figure 2.2: Spectre d'énergie de l'approche Dynamique du modèle de Smagorinsky.

D'après (2.6) et (2.10), le tenseur de Léonard $\mathcal{L}_{ij} = \mathcal{T}_{ij} - \widehat{\tau}_{ij}$, est défini comme:

$$\mathcal{L}_{ij} = \widehat{\rho \tilde{u}_i \tilde{u}_j} - \frac{\widehat{\rho} \widehat{\tilde{u}_i} \widehat{\tilde{u}_j}}{\widehat{\rho}} \quad (2.11)$$

Dans ce qui suit, on note:

$$\begin{aligned} \widehat{\tilde{S}_{ij}^*} &= \widehat{\tilde{S}_{ij}} - \frac{1}{3} \widehat{\tilde{S}_{kk}} \delta_{ij} \\ \mathcal{L}_{ij}^{Cs} &= \mathcal{L}_{ij} - \frac{1}{3} \mathcal{L}_{kk} \delta_{ij} \end{aligned} \quad (2.12)$$

Par analogie au modèle de fermeture du tenseur des contraintes de sous-maille, τ_{ij} , il est possible d'écrire:

$$\left. \begin{aligned} \mathcal{T}_{ij} - \frac{1}{3} \mathcal{T}_{kk} \delta_{ij} &= -2\widehat{\rho} C_s \widehat{\Delta}^2 |\widehat{\tilde{S}}| \widehat{\tilde{S}_{ij}^*} \\ \mathcal{T}_{kk} &= 2C_I \widehat{\Delta}^2 \widehat{\rho} |\widehat{\tilde{S}}|^2 \end{aligned} \right\} \quad (2.13)$$

Utilisant l'expression du tenseur de Léonard (2.11) et le système d'équations précédent (2.13),

cela donne:

$$\begin{aligned}\mathcal{L}_{ij}^{C_s} &= C_s \underbrace{\left[-2\widehat{\Delta}^2 \widehat{\rho} |\widehat{\tilde{S}}| \widehat{\tilde{S}}_{ij}^* + 2\Delta^2 \left(\widehat{\overline{\rho}} |\widehat{\tilde{S}}| \widehat{\tilde{S}}_{ij}^* \right) \right]}_{\mathcal{M}_{ij}^{C_s}} = C_s \mathcal{M}_{ij}^{C_s} \\ \mathcal{L}_{kk} &= C_I \underbrace{\left[-2\widehat{\Delta}^2 \widehat{\rho} |\widehat{\tilde{S}}|^2 + 2\Delta^2 \left(\widehat{\overline{\rho}} |\widehat{\tilde{S}}|^2 \right) \right]}_{\mathcal{M}_{ij}^{C_I}} = C_I \mathcal{M}_{ij}^{C_I}\end{aligned}\quad (2.14)$$

Une méthode de moindre carré est utilisée pour résoudre le système (2.14) et retrouver C_s et C_I (Germano *et al.*, 1991) [34]:

$$C_s = \frac{\mathcal{L}_{ij}^{C_s} \mathcal{M}_{ij}^{C_s}}{\mathcal{M}_{ij}^{C_s} \mathcal{M}_{ij}^{C_s}} \quad C_I = \frac{\mathcal{L}_{kk}}{\mathcal{M}_{kk}^{C_I}} \quad (2.15)$$

Les constantes retrouvées possèdent, néanmoins, deux propriétés mathématiques contraignantes:

- Elles peuvent prendre des valeurs négatives, ce qui implique que le modèle possède un caractère anti-dissipatif. Cette caractéristique est souvent interprétée comme la manifestation d'un transfert d'énergie depuis les petites structures vers les grandes (*Backscatter*).
- Elles ne sont pas bornées, et peuvent prendre des valeurs très larges, voire infinies.

Pour éviter toute instabilité numérique résultant de la procédure mathématique utilisée, C_s et C_I sont moyennées dans la direction homogène de l'écoulement:

$$C_s = \frac{\langle \mathcal{L}_{ij}^{C_s} \mathcal{M}_{ij}^{C_s} \rangle_H}{\langle \mathcal{M}_{ij}^{C_s} \mathcal{M}_{ij}^{C_s} \rangle_H} \quad C_I = \frac{\langle \mathcal{L}_{kk} \rangle_H}{\langle \mathcal{M}_{kk}^{C_I} \rangle_H} \quad (2.16)$$

et bornées dans les intervalles $[0, 0.08]$ and $[0, 0.02]$, respectivement, afin d'éviter toute valeur abérante due à une faible valeur du dénominateur.

Cependant, cette procédure de moyenne des constantes C_s et C_I à tendance à réduire le caractère universel du modèle, et à limiter ainsi ses capacités d'auto-adaptation, car cette opération suppose l'existence d'au moins une direction homogène.

Modèle de structures cohérentes

Dans le modèle de structures cohérentes, le paramètre C_s est calculé dynamiquement, utilisant une fonction basée sur les structures tourbillonnaires résolues, tirant profit du fait que ces dernières sont reliées à la dissipation de sous-maille (Kobayashi, 2005) [50]. En effet, le modèle est basé sur l'hypothèse que le taux de dissipation de l'énergie, ε , est localisé autour d'un ensemble de tourbillons finement résolus, et que le transfert d'énergie entre les échelles résolues et les échelles de sous-maille se situe aux alentours de cet ensemble.

Le paramètre du modèle est défini par:

$$C_s = C_{csm} |F_{cs}|^{3/2} \quad (2.17)$$

où C_{csm} est une constante du modèle (prise égale à 1/30 dans cette étude) et F_{cs} est la fonction de structures cohérentes, définie comme:

$$F_{cs} = \frac{\tilde{Q}}{\tilde{E}} \quad (2.18)$$

\tilde{Q} and \tilde{E} sont respectivement le tenseur du second invariant résolu et la norme d'un tenseur de gradient de vitesses résolues, donnés par:

$$\begin{aligned} \tilde{Q} &= \frac{1}{2} (\tilde{\mathcal{W}}_{ij} \tilde{\mathcal{W}}_{ij} - \tilde{\mathcal{S}}_{ij} \tilde{\mathcal{S}}_{ij}) \\ \tilde{E} &= \frac{1}{2} (\tilde{\mathcal{W}}_{ij} \tilde{\mathcal{W}}_{ij} + \tilde{\mathcal{S}}_{ij} \tilde{\mathcal{S}}_{ij}) \end{aligned} \quad (2.19)$$

avec $\tilde{\mathcal{S}}_{ij}$ et $\tilde{\mathcal{W}}_{ij}$ sont le tenseur du taux de déformation des échelles résolues et le tenseur de vorticité des échelles résolues, respectivement. Il s'en suit que:

$$\tilde{Q} = -\frac{1}{2} \frac{\partial \tilde{u}_j}{\partial x_i} \frac{\partial \tilde{u}_i}{\partial x_j} \quad \tilde{E} = \frac{1}{2} \frac{\partial \tilde{u}_j}{\partial x_i} \frac{\partial \tilde{u}_j}{\partial x_i} \quad (2.20)$$

Il est à noter que $-1 \leq F_{cs} \leq 1$. Il en résulte que le paramètre du modèle est borné ($0 \leq C_s \leq 0.05$) et possède une variance faible. Le modèle est donc par définition stable, ce qui évite des opérations de moyenne et de limitation de valeurs. Le modèle peut être donc utilisé même pour des géométries complexes ne présentant pas forcément de directions homogènes.

Le modèle a été précédemment testé sur des configurations à la fois canoniques et complexes, incluant des simulations de turbulence homogène et de canaux turbulents, et a montré des résultats acceptables en comparaison avec des références expérimentales et des données DNS (Kobayashi *et al.*, 2008 [51]; Kobayashi, 2010 [49]; Onodera *et al.*, 2011 [69]).

Modèle WALE *Wall-Adapting Local Eddy-viscosity*

Le modèle WALE, proposé par Nicoud et Ducros (1999) [68], calcule la viscosité turbulente, μ_{sgs} , en utilisant les invariants du tenseur de gradient de vitesses résolus. La viscosité turbulente y est définie comme:

$$\mu_{sgs} = \bar{\rho} \Delta^2 C_w^2 \frac{(\tilde{\mathcal{S}}_{ij}^* \tilde{\mathcal{S}}_{ij}^*)^{3/2}}{(\tilde{\mathcal{S}}_{ij} \tilde{\mathcal{S}}_{ij})^{5/2} + (\tilde{\mathcal{S}}_{ij}^* \tilde{\mathcal{S}}_{ij}^*)^{5/4}} \quad (2.21)$$

avec

$$\tilde{\mathcal{S}}_{ij}^* = \frac{1}{2} (\tilde{g}_{ij}^2 + \tilde{g}_{ji}^2) - \frac{1}{3} \tilde{g}_{kk}^2 \delta_{ij} \quad \tilde{g}_{ij}^2 = \tilde{g}_{ik} \tilde{g}_{kj} \quad (2.22)$$

C_w est une constante du modèle, prise égale à 0.5 (Nicoud et Ducros, 1999 [68]) et $\tilde{g}_{ij} = \partial \tilde{u}_i / \partial x_j$.

Tout comme le modèle précédent, le modèle WALE présente l'avantage de reproduire le bon comportement asymptotique en y^{+3} de la viscosité de sous-maille μ_{sgs} à la paroi (Garnier *et al.*, 2009 [32]).

2.1.2.3 Modélisation du flux de chaleur de sous-maille

Pour la modélisation du flux de chaleur, il est communément supposé que le transfert d'énergie depuis les échelles résolues vers les échelles de sous-maille est proportionnel au gradient de température résolue (Eidon, 1985 [27]; Garnier *et al.*, 2009 [32]). Le flux de chaleur de sous-maille est donc modélisé, par analogie au tenseur des contraintes de sous-maille, en utilisant une formulation de type viscosité turbulente. Il s'écrit:

$$\frac{1}{\gamma - 1} \frac{\partial (\bar{p} \bar{u}_j - \bar{p} \tilde{u}_j)}{\partial x_j} = - \frac{\mu_{sgs} C_p}{\text{Pr}_{sgs}} \frac{\partial \tilde{T}}{\partial x_j} \quad (2.23)$$

Dans cette étude, le nombre de Prandtl turbulent, Pr_{sgs} , est pris constant et égal à 0.9.

2.1.2.4 Simulation aux grandes échelles Implicite

En plus de l'opération *explicite* de filtrage, deux autres formes de filtres - *implicites* - sont associées aux simulations LES:

- En utilisant un maillage ne permettant pas de résoudre les plus fines échelles de l'écoulement étudié, une opération de filtrage, appelé *filtre-maillage*, est implicitement appliquée au système d'équations. En effet, du fait de la distribution spatiale des noeuds du maillage, une séparation entre les petites et les grandes structures de l'écoulement est implicitement générée, puisque des informations, qui sont plus petites qu'une certaine échelle associée à la résolution du maillage, ne peuvent être calculées.
- Etant donné que les schémas numériques utilisés induisent une erreur qui est dépendante de l'échelle calculée, ils introduisent donc une distinction entre les échelles suffisamment résolues et celles qui le sont moins. Une deuxième opération de filtrage est ainsi implicitement appliquée par le biais du schéma numérique utilisé, où l'erreur commise par l'approximation des opérateurs de dérivés tend à modifier la solution calculée (Garnier et al., 2009 [32]). Cette erreur se voit cependant minimiser avec l'utilisation de schémas numériques d'ordre élevés suffisamment précis.

En plus, à cause de la présence de forts gradients dans les écoulements supersoniques, des schémas numériques, robustes mais quelque peu dissipatifs - localement du moins - sont utilisés. Cette dissipation numérique intrinsèque, inhérente à ce type de schémas et qui imite d'un point de vue énergétique l'action des échelles de sous-maille sur la turbulence, peut être considérée comme une viscosité turbulente implicitement introduite par un modèle de sous-maille. Ce concept est appelé ILES, ou *Implicit large-eddy simulation*. Cette approche de modélisation des écoulements turbulents est intéressante dans la mesure où elle permet de quantifier la réelle contribution du modèle de sous-maille sur la turbulence en comparant les résultats ILES aux calculs LES explicites. Il est à noter que cette manière d'utiliser la dissipation numérique comme un modèle SGS repose sur l'hypothèse qui stipule que l'action des échelles de sous-maille sur les échelles résolues est strictement une action dissipative.

Le gros inconvénient de cette méthode c'est qu'elle ne permet pas un contrôle directe de la quantité d'énergie de sous-maille dissipée, puisque celle-ci dépend fortement du schéma de discréétisation spatiale utilisée.

2.2 Schémas numériques

Dans ce travail, les équations de Navier Stokes compressibles 3D sont résolues à l'aide du code CHOC-WAVES¹. Il s'agit d'un solveur compressible parallèle DNS/LES mono- et multi-espèces, utilisant une forme de résolution type différences finies. Pour des raisons de simplicité, la version mono-espèce du code, utilisant l'air, supposé un gaz parfait, est utilisée par la suite.

2.2.1 Traitement des flux convectifs

Dans les écoulements supersoniques en présence de forts gradients et/ou de discontinuités de contact, l'utilisation de schémas numériques suffisamment robustes dans les régions de forts gradients ou proche d'une discontinuité (telle qu'une onde de choc) mais précis dans les régions de turbulence, est primordiale.

2.2.1.1 Schéma WENO (*Weighted Essentially Non-Oscillatory*)

Les schémas ENO (*Essentially Non-Oscillatory*) sont basés sur l'idée de déterminer le flux numérique à partir d'une reconstruction d'ordre élevée sur un seul stencil adaptatif sélectionné pour éviter au maximum l'interpolation à travers les discontinuités. Ces schémas souffrent, néanmoins, de problème de convergence vers une solution stationnaire, ainsi que d'une perte de précision (Pirozzoli, 2010) [72]. Les schémas WENO (*Weighted Essentially Non-Oscillatory*), qui viennent remédier aux limites des schémas ENO, sont basés sur l'idée d'une construction d'un flux numérique d'ordre élevé à partir d'une combinaison linéaire convexe d'une reconstruction pondérée de polynômes d'ordre plus faible (*stencils*). La pondération des *stencils* a pour but de maximiser la précision du schéma dans les régions dites *lisses*, tout en annulant l'effet du stencil adaptatif près de la discontinuité.

Dans le code CHOC-WAVES, plusieurs variantes du schéma WENO sont disponibles, tels que le schéma WENO classique de Jiang & Shu (1996) [45], le schéma WENO à large bande de Martin *et al.* (2006) [64] ou encore le schéma Mapped-WENO de Henrick *et al.* (2005) [40]. Ces schémas peuvent être utilisés soit à l'ordre 3 ($r = 2$) ou à l'ordre 5 ($r = 3$), la précision du schéma étant en $2r - 1$.

¹Compressible High-Order Code using Weno AdaptiVE Stencils, ©Abdellah Hadjadj & Collaborateurs, CORIA 2012.

Pour la description de la méthode de calcul du schéma WENO, une équation de conservation scalaire unidimensionnelle est utilisée:

$$\frac{\partial u}{\partial t} + \frac{\partial f(u)}{\partial x} = 0 \quad (2.24)$$

Le flux caractéristique $f(u)$ est décomposé en une partie positive et une partie négative:

$$f(u) = f^+(u) + f^-(u) \quad (2.25)$$

Les deux flux présentant des vitesses de propagation non-négative et non-positive, respectivement:

$$\frac{df^+(u)}{du} \geq 0 \quad \frac{df^-(u)}{du} \leq 0 \quad (2.26)$$

Cette décomposition s'effectue selon le schéma de Lax-Friedrichs, qui s'écrit:

$$f^\pm(u) = \frac{1}{2} (f(u) \pm \alpha u) \quad (2.27)$$

où $\alpha = \max_u |f'(u)|$ est la plus grande valeur sur une ligne de maillage concernée. Le flux numérique à l'interface $f_{i+1/2}$ est également décomposé:

$$f_{i+1/2} = f_{i+1/2}^+ + f_{i+1/2}^- \quad (2.28)$$

Ainsi, comme indiqué sur la Fig. (2.3), le flux $f_{i+1/2}^+$ (respectivement $f_{i+1/2}^-$) est reconstruit en utilisant une interpolation des flux f_i^+ (respectivement f_i^-) sur les trois stencils $S = \{S_1, \dots, S_3\}$.

Le schéma WENO utilise une combinaison convexe des trois flux suivants afin d'obtenir la précision maximale dans les régions à faibles gradients:

$$\left\{ \begin{array}{lcl} f_{i+1/2}^{+(1)} & = & \frac{2}{6} f_{i-2}^+ - \frac{7}{6} f_{i-1}^+ + \frac{11}{6} f_i^+ \\ f_{i+1/2}^{+(2)} & = & -\frac{1}{6} f_{i-1}^+ + \frac{5}{6} f_i^+ + \frac{2}{6} f_{i+1}^+ \\ f_{i+1/2}^{+(3)} & = & \frac{2}{6} f_i^+ + \frac{5}{6} f_{i+1}^+ - \frac{11}{6} f_{i+2}^+ \end{array} \right. \quad (2.29)$$

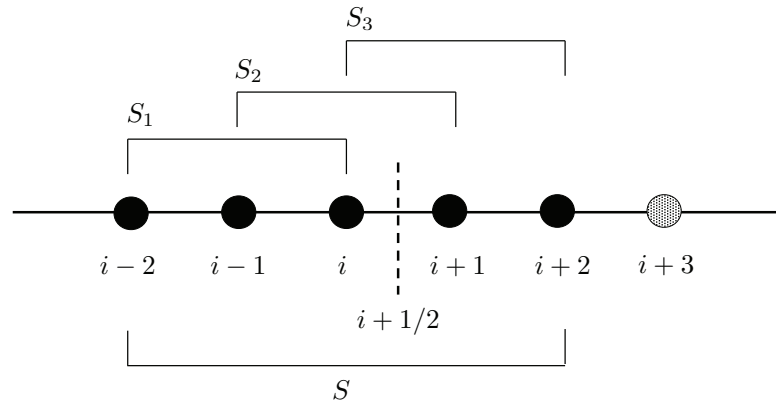


Figure 2.3: Choix des stencils pour la reconstruction des flux dans le cas du schéma WENO du 5^{ème} ordre.

Enfin, le flux numérique à l'interface à l'ordre 5 est calculé comme suit:

$$f_{i+1/2} = \sum_{l=1}^r w_l^+ f_{i+1/2}^{+(l)} \quad (2.30)$$

Les coefficients de pondération non-linéaire sont définis par:

$$w_l^+ = \frac{\alpha_l^+}{\sum_{l=1}^r \alpha_l^+} \quad \alpha_l^+ = \frac{d_l^+}{(\epsilon + \beta_l^+)^2} \quad (2.31)$$

$d_l^+ = d_l^- = d_l$ sont les poids qui permettent d'obtenir une précision optimale du schéma WENO (5 dans notre cas):

$$d_1 = 1/10 \quad d_2 = 6/10 \quad d_3 = 3/10 \quad (2.32)$$

ϵ est un nombre très faible qui permet d'éviter la division par zéro ($\epsilon = 10^{-6}$; Jiang & Shu (1996) [45]), et β_l^+ sont les indicateurs qui permettent de diminuer les poids des *stencils* contenant la discontinuité. Ils sont définis comme la somme des normes de toutes les dérivées des polynômes

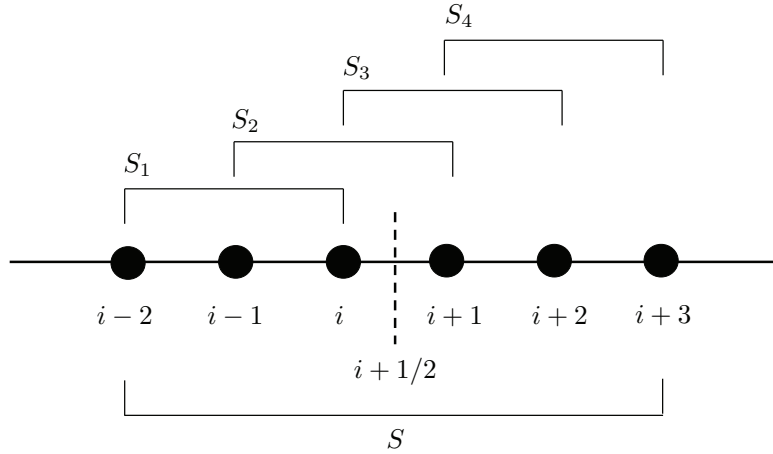


Figure 2.4: Choix des stencils pour la reconstruction des flux dans le cas du schéma WENO du 5^{ème} ordre à Large Bande optimisé.

d'interpolation, et s'écrivent:

$$\left\{ \begin{array}{lcl} \beta_1^+ & = & \frac{13}{12} (f_{i-2}^+ - 2f_{i-1}^+ + f_i^+)^2 + \frac{1}{4} (f_{i-2}^+ - 4f_{i-1}^+ + f_i^+)^2 \\ \beta_2^+ & = & \frac{13}{12} (f_{i-1}^+ - 2f_i^+ + f_{i+1}^+)^2 + \frac{1}{4} (f_{i-1}^+ - 4f_i^+ + f_{i+1}^+)^2 \\ \beta_3^+ & = & \frac{13}{12} (f_i^+ - 2f_{i+1}^+ + f_{i+2}^+)^2 + \frac{1}{4} (f_i^+ - 4f_{i+1}^+ + f_{i+2}^+)^2 \end{array} \right. \quad (2.33)$$

La partie négative du flux numérique WENO, $f_{i+1/2}^-$, est calculée en suivant exactement la même procédure, remplaçant f^+ par f^- .

2.2.1.2 Schéma WENO-BWO (*Large Bande Optimisé*)

Un des inconvénients du schéma WENO classique est sa dissipation numérique relativement importante, surtout dans les régimes de forte turbulence, où les indicateurs β_l ne sont pas strictement nuls. Pour remédier, en partie, à ce problème, un schéma à large bande optimisé a été proposé par Martin *et al.* (2006) [64]. Ce schéma comporte quatre stencils $S = \{S_1, \dots, S_4\}$ introduits de manière à limiter le décentrement, en rendant le plus symétrique possible le calcul du flux numérique à l'interface $i + 1/2$ (voir Fig. 2.4).

Les flux numériques à l'interface s'écrivent donc:

$$\left\{ \begin{array}{lcl} f_{i+1/2}^{+(1)} & = & \frac{2}{6}f_{i-2}^+ - \frac{7}{6}f_{i-1}^+ + \frac{11}{6}f_i^+ \\ f_{i+1/2}^{+(2)} & = & -\frac{1}{6}f_{i-1}^+ + \frac{5}{6}f_i^+ + \frac{2}{6}f_{i+1}^+ \\ f_{i+1/2}^{+(3)} & = & \frac{2}{6}f_i^+ + \frac{5}{6}f_{i+1}^+ - \frac{1}{6}f_{i+2}^+ \\ f_{i+1/2}^{+(4)} & = & \frac{11}{6}f_i^+ - \frac{7}{6}f_{i+1}^+ + \frac{2}{6}f_{i+2}^+ \end{array} \right. \quad (2.34)$$

Le flux numérique à l'interface est calculé ($n = 4$):

$$f_{i+1/2} = \sum_{l=1}^n w_l^+ f_{i+1/2}^{+(l)} \quad (2.35)$$

Les coefficients de pondération non-linéaire sont définis par:

$$w_l^+ = \frac{\alpha_l^+}{\sum_{l=1}^n \alpha_l^+} \quad \alpha_l^+ = \frac{d_l^+}{(\epsilon + \beta_l^+)^2} \quad \text{avec } \alpha_4^+ = \min_{1 \leq l \leq n} (\alpha_l^+) \quad (2.36)$$

d_l^+ sont les poids optimaux proposés par Martin *et al.* (2006) [64]:

$$\begin{aligned} d_1^+ &= 0.094647545896 & d_2^+ &= 0.428074212384 \\ d_3^+ &= 0.408289331408 & d_4^+ &= 0.068988910311 \end{aligned} \quad (2.37)$$

et les indicateurs de décentrement s'écrivent donc:

$$\left\{ \begin{array}{lcl} \beta_1^+ & = & \frac{13}{12} (f_{i-2}^+ - 2f_{i-1}^+ + f_i^+)^2 + \frac{1}{4} (f_{i-2}^+ - 4f_{i-1}^+ + f_i^+)^2 \\ \beta_2^+ & = & \frac{13}{12} (f_{i-1}^+ - 2f_i^+ + f_{i+1}^+)^2 + \frac{1}{4} (f_{i-1}^+ - 4f_i^+ + f_{i+1}^+)^2 \\ \beta_3^+ & = & \frac{13}{12} (f_i^+ - 2f_{i+1}^+ + f_{i+2}^+)^2 + \frac{1}{4} (f_i^+ - 4f_{i+1}^+ + f_{i+2}^+)^2 \\ \beta_4^+ & = & \frac{13}{12} (f_{i+1}^+ - 2f_{i+2}^+ + f_{i+3}^+)^2 + \frac{1}{4} (f_{i+1}^+ - 4f_{i+2}^+ + f_{i+3}^+)^2 \end{array} \right. \quad (2.38)$$

Une dernière procédure d'optimisation est aussi implémentée, en appliquant un limiteur aux coefficients de pondérations non-linéaires w_l^+ qui, selon la nature de l'écoulement (présence de choc ou de forte turbulence), permettant d'ajuster localement la précision du schéma. Le limiteur agit ainsi essentiellement dans les régions loin des instabilités, afin de limiter un tant soit peu la dissipation numérique dans ces endroits (Chaudhuri *et al.*, 2011) [14].

2.2.1.3 Schéma centré conservatif *split-centered (Skew-Symmetric)*

Il est bien connu que, même en absence d'ondes de choc, l'utilisation d'approximations centrées en différences finies, présentent des instabilités lorsqu'elles sont utilisées à des viscosités très faibles, voir nulles, ce qui est le cas des équations hyperboliques. Pour les écoulements sans discontinuités, plusieurs méthodes existantes permettent d'assurer la stabilité des schémas numériques. Pour une revue détaillée des différentes méthodes existantes, le lecteur peut se référer à l'article de Pirozzoli (2010) [72].

Une des méthodes connues, est l'utilisation de la forme fractionnée (*splitted*) des dérivées dans les termes convectifs des équations de Navier-Stokes. Cette méthode se base sur l'idée d'écrire les termes convectifs sous une forme du type '*skew-symmetric*'. Cependant, les approximations obtenues ne peuvent être écrites dans une forme localement conservative, c'est-à-dire sous la forme d'une divergence telle qu'elles sont présentées dans l'équation (2.40). Partant de ces constats, Pirozzoli (2010) [72] propose une approximation localement conservative des termes convectifs des équations de Navier Stokes compressibles, s'écrivant sous la forme:

$$\frac{\partial \rho u_k \varphi}{\partial x_k} \quad (2.39)$$

où φ est un scalaire générique, réduit à l'unité pour l'équation de continuité, au vecteur vitesse u_i ($i = 1, 2, 3$) pour l'équation de quantité de mouvement, et à l'enthalpie $H = \frac{\gamma}{\gamma-1} \frac{p}{\rho} + \frac{u^2}{2}$ pour l'équation de l'énergie totale.

Principe de base de la formulation

On cherche ici une approximation conservative de type différences finies des termes convectifs qui s'écrit sous la forme²:

$$\left. \frac{\partial \rho u_k \varphi}{\partial x_k} \right|_{x=x_j} \approx \frac{1}{h} \left(\hat{f}_{i+1/2} - \hat{f}_{i-1/2} \right) \quad (2.40)$$

où $\hat{f}_{i+1/2}$ est le flux numérique.

La forme fractionnée de l'équation (2.40), s'écrit :

$$\frac{\partial \rho u \varphi}{\partial x} = \frac{1}{2} \frac{\partial \rho u \varphi}{\partial x} + \frac{1}{2} \varphi \frac{\partial \rho u}{\partial x} + \frac{1}{2} \rho u \frac{\partial \varphi}{\partial x} \quad (2.41)$$

²Le développement numérique qui suit est repris de l'article de Pirozzoli (2010) [72].

ou encore :

$$\frac{\partial \rho u \varphi}{\partial x} = \frac{1}{2} \frac{\partial \rho u \varphi}{\partial x} + \frac{1}{2} u \frac{\partial \rho \varphi}{\partial x} + \frac{1}{2} \rho \varphi \frac{\partial u}{\partial x} \quad (2.42)$$

En remplaçant les opérateurs de dérivées continues dans (2.41) et (2.42) par leurs formulations différences finies, cela donne :

$$\left. \frac{\partial f g}{\partial x} \right|_{x=x_j} \approx D_s(fg)_j \equiv \frac{1}{2} D(fg)_j + \frac{1}{2} f_j Dg_j + \frac{1}{2} g_j Df_j \quad (2.43)$$

où D_s représente l'approximation discrète de la forme fractionnée du terme convectif, Df_j représente l'approximation discrète de la dérivée première de f au noeud x_j , et $f = \rho u$, $g = \varphi$ ou $f = \rho \varphi$, $g = u$ dans le cas de la forme fractionnée (2.41) ou (2.42), respectivement.

Une approximation centrée standard de la dérivée première s'écrit:

$$Df_j = \sum_{l=1}^L a_l D^l f_j \quad (2.44)$$

tel que

$$D^l f_j = \frac{1}{h} (f_{j+l} - f_{j-l}) \quad (2.45)$$

Dans le cas simple d'une approximation au second ordre, ce qui correspond à $L = 1$, on obtient:

$$\hat{f}_{i+1/2} = \frac{1}{4} (f_j + f_{j+l}) (g_j + g_{j+l}) \quad (2.46)$$

Alors qu'une approximation conservative de (2.40) s'écrit:

$$\hat{f}_{i+1/2} = \frac{1}{2} (f_j g_j + f_{j+l} g_{j+l}) \quad (2.47)$$

Si on considère un seul terme (D^l) de (2.44), remplacé dans (2.43), cela donne:

$$D_s^l(fg)_j = \frac{1}{2} D^l(fg)_j + \frac{1}{2} (f)_j D^l(g)_j + \frac{1}{2} (g)_j D^l(f)_j \quad (2.48)$$

ou encore:

$$D_s^l(fg)_j = \frac{2}{h} \left((\widetilde{f, g})_{j,l} - (\widetilde{f, g})_{j-l,l} \right) \quad (2.49)$$

tel que:

$$\widetilde{(f, g)}_{j,l} = \frac{1}{4} (f_j + f_{j+l}) (g_j + g_{j+l}) \quad (2.50)$$

est un opérateur de moyenne discret à deux variables.

Il est à noter que l'équation (2.48) n'est pas écrite sous la forme conservative (2.40). Moyennant un petit développement, elle peut être réécrite telle que:

$$D_s^l(fg)_j = \frac{1}{4} \left(\hat{f}_{i+1/2}^l - \hat{f}_{i-1/2}^l \right) \quad (2.51)$$

avec:

$$\hat{f}_{i+1/2}^l = 2 \sum_{m=0}^{l-1} \widetilde{(f, g)}_{j-m, l} \quad (2.52)$$

Le flux total est ensuite obtenu en assemblant les flux partiels (2.52) à partir de l'expression (2.44):

$$\hat{f}_{i+1/2} = \sum_{l=1}^L a_l \hat{f}_{i+1/2}^l \quad (2.53)$$

On obtient ainsi:

$$\hat{f}_{i+1/2} = 2 \sum_{l=1}^L a_l \sum_{m=0}^{l-1} \widetilde{(\rho u, \varphi)}_{j-m, l} \quad (2.54)$$

et

$$\hat{f}_{i+1/2} = 2 \sum_{l=1}^L a_l \sum_{m=0}^{l-1} \widetilde{(\rho \varphi, u)}_{j-m, l} \quad (2.55)$$

avec (2.54) qui correspond à la forme (2.41), l'expression (2.55) à celle (2.42), et $a_l = a_1 = 1/2$.

Ecriture généralisée

Pour les écoulements présentant de fortes variations de densité, et en développant le produit triple dans le terme à droite de l'équation (2.40), il est possible d'obtenir une forme généralisée du flux, se présentant sous la forme:

$$\frac{\partial \rho u \varphi}{\partial x} = \alpha \frac{\partial \rho u \varphi}{\partial x} + \beta \left(u \frac{\partial \rho \varphi}{\partial x} + \rho \frac{\partial u \varphi}{\partial x} + \varphi \frac{\partial \rho u}{\partial x} \right) + (1 - \alpha - 2\beta) \left(\rho u \frac{\partial \varphi}{\partial x} + \rho \varphi \frac{\partial u}{\partial x} + u \varphi \frac{\partial \rho}{\partial x} \right) \quad (2.56)$$

Dans le cas d'une écriture sous la forme (2.56), une approximation conservative semi-discretne ne peut être obtenue qu'à des conditions spécifiques. En particulier lorsque $\alpha = \beta = 1/4$

(Pirozzoli, 2010) [72]. En suivant la même approche décrite précédemment, il vient que:

$$\hat{f}_{i+1/2} = 2 \sum_{l=1}^L a_l \sum_{m=0}^{l-1} (\widetilde{\rho, u, \varphi})_{j-m, l} \quad (2.57)$$

tel que

$$(\widetilde{f, g, h})_{j,l} = \frac{1}{8} (f_j + f_{j+l}) (g_j + g_{j+l}) (h_j + h_{j+l}) \quad (2.58)$$

avec les constantes a_l sont données dans les tableau 2.1.

Ordre	$i = 1$	$i = 2$	$i = 3$	$i = 4$
L=1	$a_1 = 1/2$			
L=2	$a_1 = 8/12$	$a_2 = -1/12$		
L=3	$a_1 = 45/60$	$a_2 = -9/60$	$a_3 = 1/60$	
L=4	$a_1 = 672/840$	$a_2 = -168/840$	$a_3 = -840$	$a_4 = 3/840$

Table 2.1: Coefficients des schémas centrés du 2^{ème} au 8^{ème} ordre.

En comparaison avec les formes (2.54) et (2.55) des flux numériques, il est à noter que dans la forme (2.58), l'effet de la variation de densité est bien pris en compte, et ceci indépendamment des deux autres variables u et φ .

Dans la suite du travail, et sauf mention contraire, le schéma centré *split-centered* du 6^{ème} ordre est utilisé.

2.2.2 Traitement des termes visqueux

Dans le code CHOC-WAVES, les flux visqueux sont approximés à l'aide d'un schéma centré d'ordre 4 à 5 stencils, dans lequel la dérivée $(\partial F_v / \partial x)_{i,j,k}$ s'écrit:

$$\left. \frac{\partial F_v}{\partial x} \right|_{i,j,k} = \frac{F_{v_{i-2,j,k}} - 8F_{v_{i-1,j,k}} + 8F_{v_{i+1,j,k}} - F_{v_{i+2,j,k}}}{12\Delta x} + \mathcal{O}(\Delta x^4) \quad (2.59)$$

Les composantes du flux F_v contiennent des dérivés du type $\partial() / \partial x$, $\partial() / \partial y$ et $\partial() / \partial z$. Dans les directions normale (y) et d'envergure (z) de l'écoulement, le calcul des dérivées est approximé par une formulation centrée. Dans la direction longitudinale (x), le calcul des dérivées se fait à l'aide

de différentes formulations d'ordre 4 sur un stencil réduit $S = \{i-2, i-1, i, i+1, i+2\}$, ce qui donne:

$$\begin{aligned} \frac{\partial u}{\partial x} \Big|_{i-2,j,k} &= \frac{-25u_{i-2,j,k} + 48u_{i-1,j,k} - 36u_{i,j,k} + 16u_{i+1,j,k} - 3u_{i+2,j,k}}{12\Delta x} + \mathcal{O}(\Delta x^4) \\ \frac{\partial u}{\partial x} \Big|_{i-1,j,k} &= \frac{-3u_{i-2,j,k} - 10u_{i-1,j,k} + 18u_{i,j,k} - 6u_{i+1,j,k} + u_{i+2,j,k}}{12\Delta x} + \mathcal{O}(\Delta x^4) \\ \frac{\partial u}{\partial x} \Big|_{i+1,j,k} &= \frac{-u_{i-2,j,k} + 6u_{i-1,j,k} - 18u_{i,j,k} + 10u_{i+1,j,k} + 3u_{i+2,j,k}}{12\Delta x} + \mathcal{O}(\Delta x^4) \\ \frac{\partial u}{\partial x} \Big|_{i+2,j,k} &= \frac{3u_{i-2,j,k} - 16u_{i-1,j,k} + 36u_{i,j,k} - 48u_{i+1,j,k} + 25u_{i+2,j,k}}{12\Delta x} + \mathcal{O}(\Delta x^4) \end{aligned} \quad (2.60)$$

Il est à noter que les flux de sous-maille sont également évalués en utilisant le même schéma de discétisation.

2.2.3 Avancement en temps

Les schémas d'intégration temporelle implémentés dans le code sont principalement des algorithmes explicites du type TVD Runge-Kutta. Ces schémas obéissent à une restriction sur l'incrémentation temporel qui doit être suffisamment faible, compte tenu du caractère instationnaire des écoulements étudiés. Dans cette étude, un schéma Runge-Kutta d'ordre 3 est choisi. La procédure d'intégration se fait en 3 étapes comme suit:

$$\left\{ \begin{array}{l} U^{(1)} = U^n + \Delta t \mathcal{L}(U^n) \\ U^{(2)} = \frac{1}{4} [3U^n + U^{(1)} + \Delta t \mathcal{L}(U^{(1)})] \\ U^{n+1} = \frac{1}{3} [U^n + 2U^{(2)} + 2\Delta t \mathcal{L}(U^{(2)})] \end{array} \right. \quad (2.61)$$

où Δt est le pas de temps, U^n est la valeur de la variable U à l'instant n , et $U^{(k)}$ sont les valeurs intermédiaires de U ($k = 1, 2$). Le critère de stabilité sur le pas de temps s'écrit:

$$\Delta t = \mathcal{CFL} \cdot \min(\Delta t_x, \Delta t_y, \Delta t_z) \quad (2.62)$$

avec:

$$\Delta t_x = \min \left[\frac{\Delta x}{|u| + c}, \frac{1}{2} \frac{\Delta x^2}{\gamma (\mu/Pr + \mu_{sgs}/Pr_{sgs})} \right] \quad (2.63)$$

Le premier terme du membre à droite correspond à un temps convectif, alors que le second représente

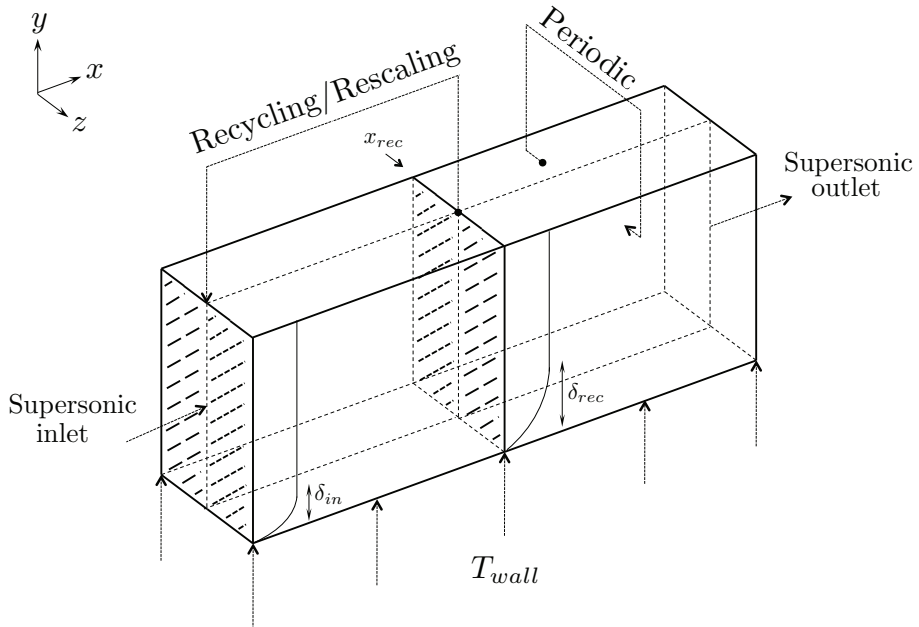


Figure 2.5: Domaine de calcul et conditions aux limites de la configuration étudiée.

un temps de diffusion (laminaire et turbulent). Le nombre de Courant-Friedrichs-Lowy (\mathcal{CFL}) doit être inférieur à l'unité pour assurer la stabilité globale du schéma. Dans le travail qui suit, $\mathcal{CFL} = 0.9$.

2.2.4 Conditions aux limites

Les conditions aux limites sont satisfaites en imposant des valeurs finies sur les cellules fantômes (*Ghost cells*) se trouvant en dehors du domaine de calcul. En fonction de la condition physique à satisfaire, les variables conservatives du système d'équations régissant l'écoulement sont définies dans ces mailles. L'ensemble des conditions imposées dans cette étude est présenté sur la Fig. (3.1).

2.2.4.1 Conditions de parois, de borne supérieure et de sortie

La condition de paroi adiabatique (*Adiabatic no-slip boundary condition*) est satisfaite en imposant une condition de gradient nul pour la température ainsi que toutes les composantes de la vitesse. Pour la condition de paroi isotherme, la même condition est imposée pour les composantes du

vecteur vitesse, et une valeur de température T_w est fixée à la paroi à travers l'équation d'énergie. A la sortie du domaine, une condition de sortie supersonique est définie, alors qu'une condition de bord libre est appliquée en haut du domaine.

2.2.4.2 Conditions d'entrée turbulente

La génération de conditions d'entrée, turbulente et instationnaire, demeure une des principales difficultés lors de la réalisation d'une DNS ou d'une LES. Ces conditions doivent être dépendantes du temps, ainsi que suffisamment précises pour décrire l'état turbulent de l'écoulement. Il est ainsi inévitable de spécifier des fluctuations réalistes, qui soient en cohérence avec l'écoulement moyen. Cette étape s'avère délicate à traiter, vu la sensibilité des équations de Navier-Stokes aux conditions aux limites. Dans cette étude, nous nous intéressons à une turbulence pleinement développée, dont les grandeurs moyennes sont supposées être moins sensibles aux variations des conditions d'entrée. Dans le cadre spécifique des simulations DNS ou LES spatio-temporelles de couches limites turbulentes, plusieurs méthodes sont proposées dans la littérature :

- La solution la plus simple consiste à imposer un profil laminaire à l'entrée et d'y superposer des fluctuations aléatoires afin que s'effectue une transition naturelle vers la turbulence. Cette approche, utilisée entre autre par Pirozzoli *et al.* (2004) [76] dans le cas d'une DNS de couche limite supersonique, a donné des résultats probants. Son coût reste prohibitif puisqu'une grande partie du domaine de calcul est consacrée à la transition de la couche limite vers un état pleinement turbulent.
- Il est également possible d'imposer, en entrée du domaine, des profils de quantités moyennes, auxquelles on superpose un bruit blanc. Cette méthode pose le problème de générer des fluctuations qui ne vérifient que statistiquement les propriétés turbulentes réelles de l'écoulement, ce qui conduit à une atténuation inévitable des fluctuations introduites à l'entrée. Elle nécessite également l'emploi de grands domaines de calculs afin que ces fluctuations se réorganisent en grandeurs réalistes, ce qui induit un coût de calcul important.
- Par ailleurs, il existe des techniques alternatives à celles déjà citées, utilisant une approche de génération de la turbulence dite synthétique. Cette approche est intéressante à condition de disposer de quelques données statistiques expérimentales ou issues de calculs DNS.

Elle consiste à imposer à l'entrée du domaine un champ moyen de vitesse et d'y superposer des fluctuations aléatoires filtrées, qui sont corrélées avec des propriétés statistiques d'ordre élevées données, connues au préalable à partir de données expérimentales ou de simulations DNS (Jarrin *et al.*, 2008 [44]).

Une méthode alternative, bien adaptée à ce type d'écoulement, est proposée par Lund *et al.* (1998) pour la simulation LES de couches limites turbulentes, dans laquelle l'écoulement produit ses propres conditions d'entrée, à partir d'un processus de renormalisation du profil de vitesse, situé à une station suffisamment éloignée de la sortie du domaine de calcul. Cette technique présente l'avantage de réduire le domaine de calcul et, de ce fait, le coût de la simulation. Une extension de cette méthode au cas compressible a aussi été proposée par Urban & Knight (2001) [100], Stolz & Adams (2003) [95], Sagaut *et al.* (2004) [80] et récemment par Pirozzoli *et al.* (2010) [75].

Méthode du filtre digital

Récemment proposée par Klein *et al.* (2004) [48], cette méthode a néanmoins montré certaines limites, puisqu'elle est significativement lourde en terme de temps de calcul. En effet, à chaque pas de temps, la méthode requiert de corrérer un ensemble de plans de données aléatoires de taille $(N_x \times N_y \times N_z)$.

Une deuxième méthode, toujours utilisant l'approche du filtre digital, proposée par Xie & Castro (2008) [106], reprend les mêmes bases que la méthode de Klein *et al.* (2004) [48], sauf qu'au lieu de filtrer et de corrérer un ensemble tridimensionnel de données, la méthode génère et filtre seulement un ensemble bidimensionnel de plans de données aléatoires, corrélé ensuite avec l'ensemble des plans de données du dernier pas de temps. Cette méthode présente l'avantage d'être performante et moins gourmande en termes de ressources informatique que la méthode originale de Klein *et al.* (2004) [48]. Ceci-dit, des tests on montré que ces méthodes de filtre digital requièrent une longueur minimale de $14\delta_{in}$ dans la direction longitudinale du domaine pour permettre à la turbulence de se développer proprement et pleinement.

Pour une revue détaillée de la procédure du filtre digital et son extension au cas d'étude de couche limites supersoniques, le lecteur peut se référer aux travaux de thèse de Touber (2010) [99] sur l'interaction onde de choc/couche limite supersonique.

Méthode de recyclage/renormalisation

Dans notre étude, la condition d'entrée turbulente est prescrite en utilisant la méthode de recyclage/renormalisation décrite par Pirozzoli *et al.* (2010) [75], originalement proposée par Lund *et al.* (1998) [62]. La méthode consiste à recycler les fluctuations de vitesses et de densité à partir d'une station dite de recyclage notée x_{rec} , et à les introduire à l'entrée du domaine, après une procédure de renormalisation des quantités, afin de prendre en compte l'épaisseur de la couche limite.

Les profils d'entrée de vitesses, de densité et de pression s'écrivent:

$$\left\{ \begin{array}{lcl} \tilde{u}(0, y, z, t) & = & u'(0, y, z, t) + \langle \tilde{u}(y) \rangle \\ \tilde{v}(0, y, z, t) & = & v'(0, y, z, t) + \langle \tilde{v}(y) \rangle \\ \tilde{w}(0, y, z, t) & = & w'(0, y, z, t) \\ \bar{\rho}(0, y, z, t) & = & \rho'(0, y, z, t) + \langle \bar{\rho}(y) \rangle \\ \bar{p}(0, y, z, t) & = & p_\infty \end{array} \right. \quad (2.64)$$

Les profils moyens génériques de vitesses et de densité sont introduits à l'entrée du domaine de calcul, et seules les fluctuations sont recyclées à partir de la station x_{rec} . Le fait de figer les profils moyens et de ne recycler que les fluctuations permet un meilleur contrôle des grandeurs caractéristiques de la couche limite à l'entrée du domaine, notamment l'épaisseur de la couche limite δ_{in} et la vitesse de frottement $u_{\tau_{in}}$. Ceci conduit à une meilleure stabilité des calculs et à la réduction du temps de convergence statistique, en comparaison avec la méthode originale de Lund *et al.* (1998) [62].

Le profil de vitesse moyenne longitudinale est défini en utilisant la vitesse moyenne transformée au sens de van-Driest (Guarini *et al.*, 2000 [38]; Bernardini, 2009 [8]):

$$\tilde{u}_{vd}^+ = \begin{cases} \frac{1}{\kappa} \log(1 + \kappa y^+) + C_1 \left(1 - e^{-\frac{y^+}{\eta_1}} - \frac{y^+}{\eta_1} e^{-b y^+} \right) + \Phi(y/\delta) & y < \delta \\ \tilde{u}_{vd_\infty}/u_\tau & y \geq \delta \end{cases} \quad (2.65)$$

où

$$\Phi(y/\delta) = \frac{1}{\kappa} \left[\left(\frac{y}{\delta} \right)^2 - \left(\frac{y}{\delta} \right)^3 + 6\Pi \left(\frac{y}{\delta} \right)^2 - 4\Pi \left(\frac{y}{\delta} \right)^3 \right]$$

et $\kappa = 0.41$, $C = 5.1$, $\pi = 0.20$, $C_1 = C - \log 1/\kappa$, $\eta_1 = 11$ et $b = 0.33$. La pression est supposée uniforme p_∞ à l'entrée du domaine, et les profils de densité et de température sont définis en utilisant la formule de Crocco-Busemann (White, 1991 [105]):

$$\frac{\rho_w}{\langle \bar{\rho} \rangle} = \frac{\langle \tilde{T} \rangle}{T_w} = 1 + \left(\frac{T_{aw}}{T_w} - 1 \right) \frac{\langle \tilde{u} \rangle}{u_\infty} - r \frac{\gamma - 1}{2} M_\infty^2 \frac{T_\infty}{T_w} \left(\frac{\langle \tilde{u} \rangle}{u_\infty} \right)^2 \quad (2.66)$$

où r est le facteur de recouvrement (pris égal à 0.89), et T_{aw} est la température adiabatique de la paroi (supposée égale de la température de recouvrement, T_r), définie par:

$$T_{aw} \simeq T_r = T_\infty \left(1 + r \frac{\gamma - 1}{2} M_\infty^2 \right) \quad (2.67)$$

Dans la première partie de l'étude de la couche limite supersonique adiabatique, les profils moyens utilisés, à savoir $\langle \tilde{u} \rangle$, $\langle \tilde{v} \rangle$ et $\langle \bar{\rho} \rangle$, correspondent aux données issus du calcul DNS de Pirozzoli & Bernardini (2011) [74].

La renormalisation des fluctuations est réalisée en divisant la couche limite en une région interne (désignée par la coordonnée y^+) et une région externe (désignée par la variable $\eta = y/\delta$), et est définie comme suit:

$$\begin{cases} u'_i|^{inn}(0, y^+, z, t) &= \psi u'_i(x_{rec}, y^+, z + L_z/2, t) \\ u'_i|^{out}(0, \eta, z, t) &= \psi u'_i(x_{rec}, \eta, z + L_z/2, t) \\ \rho'|^{inn}(0, y^+, z, t) &= \rho'(x_{resc}, y^+, z + L_z/2, t) \\ \rho'|^{out}(0, \eta, z, t) &= \rho'(x_{resc}, \eta, z + L_z/2, t) \end{cases} \quad (2.68)$$

Le paramètre de renormalisation ψ , prenant en compte l'évolution de la densité à la paroi entre l'entrée et la station de recyclage, est défini par (Pirozzoli *et al.*, 2010) [75]:

$$\psi = \frac{u_{\tau, in}}{u_{\tau, rec}} \sqrt{\frac{\bar{\rho}_{w, in}}{\bar{\rho}_{w, rec}}} \quad (2.69)$$

Dans la direction d'envergure, les fluctuations sont recyclées à partir d'une position $z + L_z/2$ (voir Eq. 2.68) afin d'éviter l'introduction de toute information faussée (périodicité du champ injecté) à l'entrée du domaine, pouvant résulter d'une condition de quasi-périodicité (Pirozzoli *et al.*, 2010) [75].

A l'extérieur de la couche limite ($\eta > 1$), un bruit blanc est superposé aux fluctuations de vitesses, avec:

$$u'_i \Big|_{\eta>1} (0, \eta, z, t) = 0.1 u_\infty e^{-2(\eta-1)} \quad (2.70)$$

Une moyenne pondérée spatialement est définie, en utilisant les deux profils issus des régions interne et externe de la couche limite, afin de garantir une transition douce entre ces deux régions. Ainsi:

$$\varphi = \varphi^{inn} [1 - W(\eta)] + \varphi^{out} W(\eta) \quad (2.71)$$

avec W est la fonction de pondération:

$$W(\eta) = \frac{1}{2} \left(1 + \frac{\tanh\left(\frac{\alpha(\eta-b)}{\eta(1-2b)+b}\right)}{\tanh(\alpha)} \right) \quad (2.72)$$

où $\alpha = 4$ et $b = 0.2$.

Initialisation des calculs

Afin de minimiser le temps d'établissement d'un régime pleinement turbulent où la couche limite atteint un état d'équilibre, le calcul est initialisé, comme l'a fait auparavant Chaudhuri *et al.* (2010) [14], en utilisant la méthode du filtre digital basée sur la procédure de Klein *et al.* (2004) [48]. La méthode consiste à imposer, dans tout le domaine, des profils moyens de vitesses, de température et de pression, en y superposant des corrélations statistiques à partir de perturbations réalistes en utilisant les profils de fluctuations de vitesses obtenus *via* une DNS. Ici, les données DNS de Bernardini & Pirozzoli (2011) [9] sont utilisées. Cette méthode présente l'avantage de définir, avant le lancement du calcul, des champs moyen et fluctuant réalistes, qui sont déjà plus ou moins corrélées entre-eux.

2.2.5 Conventions

Dans ce qui suit, et sauf mention contraire, seule la partie résolue d'une quantité φ donnée est prise en compte dans la discussion des résultats. Ce qui implique que $\tilde{\varphi}_i \equiv \varphi_i$ et $\tilde{\varphi}'_i \equiv \varphi'_i$.

2.2.6 Notations

Dans ce qui suit, chaque quantité moyenne présentée est obtenue suite à une moyenne temporelle sur la période d'échantillonnage (\mathcal{T}_s) et une intégration spatiale dans la direction homogène de l'écoulement (z). Elle est notée $\langle \varphi \rangle$, et est définie comme:

$$\langle \varphi(x, y) \rangle = \frac{1}{L_z} \frac{1}{\mathcal{T}_s} \int_{L_z} \int_{\mathcal{T}_s} \varphi(x, y, z, t) \, dt \, dz \quad (2.73)$$

2.3 Conclusion

Dans ce chapitre, les équations mathématiques qui régissent les écoulements étudiés ont été présentées. La modélisation de sous-maille, basée sur une formulation fonctionnelle, a été brièvement décrite à travers les différents modèles de sous-maille implémentés dans le code CHOC-WAVES. Pour les flux convectifs, le schéma *split-centered* est utilisé dans la suite du travail. Ce schéma présente l'avantage d'être suffisamment robuste pour l'étude d'écoulements supersoniques sans discontinuités, mais surtout moins dissipatif comparé aux schémas WENO. Enfin, la méthode de recyclage/renormalisation a été également présentée, et sera utilisée tout au long de cette étude.

Le prochain chapitre traitera de la validation des différentes méthodes numériques et modèles de sous-maille à travers l'étude LES d'une couche limite supersonique turbulente à Mach $M = 2$.

Chapter 3

Adiabatic Supersonic Turbulent Boundary layer

This chapter concerns large-eddy simulations of a supersonic turbulent boundary layer evolving over an adiabatic flat-plate. The study focuses mainly on the mean flow as well as statistical characteristics of the boundary layer. First, an assessment of the LES results is presented in order to check the proper convergence of the statistics and the conformity of the structure of the flow as a canonical zero-pressure gradient turbulent boundary layer. The obtained results in terms of mean and fluctuating quantities are compared to the recent DNS data of Pirozzoli & Bernardini (2011) [74], as well as to experimental results available in the literature. The issue of the sub-grid scale modeling through the SGS models' dissipation has also been addressed in order to get more insight into the modeling behavior.

3.1 Flow conditions and simulation parameters

The incoming boundary layer is spatially evolving at a Mach number $M = 2$ and Reynolds numbers $\text{Re}_{\tau_{in}} = \rho_w u_{\tau_{in}} \delta_{in} / \mu_w \approx 245$ (where $u_{\tau_{in}}$ is the friction velocity, δ_{in} is the inflow boundary layer thickness) and $\text{Re}_{\theta_{in}} = \rho_{\infty} u_{\infty} \theta_{in} / \mu_{\infty} \approx 1150$ (θ_{in} is the momentum thickness at the inlet). The computational domain has a size of $L_x \times L_y \times L_z = 106 \delta_{in} \times 9.13 \delta_{in} \times 3.18 \delta_{in}$ in the streamwise (x), wall-normal (y) and spanwise (z) directions, respectively. One should note that the domain was reduced by a factor of 3 compared to the DNS reference (Bernardini & Pirozzoli, 2011 [9]; Pirozzoli & Bernardini, 2011 [74]) mainly due to computational cost issues.

As shown in table 3.1, different grid resolutions are used with uniformly spaced grid in the streamwise and spanwise directions, and clustered grid in the wall-normal direction according to

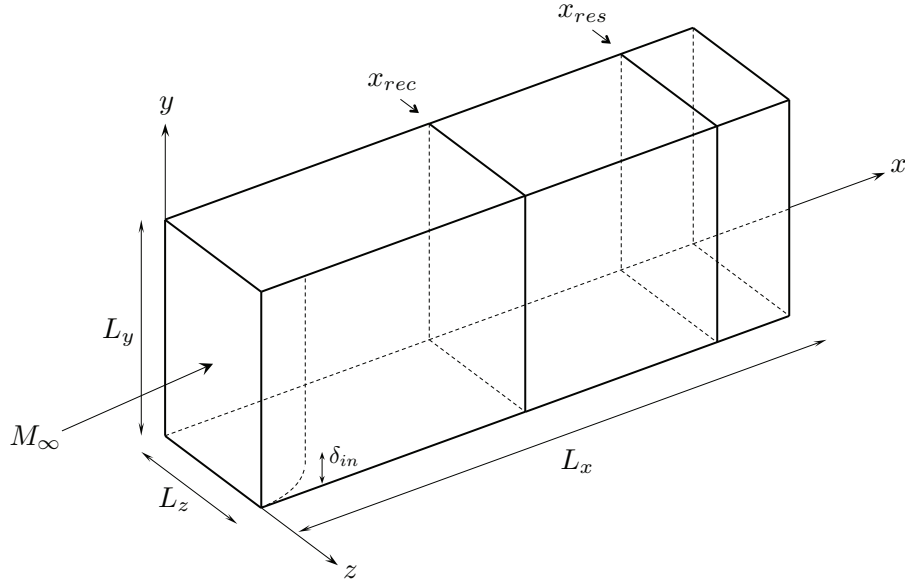


Figure 3.1: Computational domain size.

$y_j = d_y \sinh(\eta_j)$ (Toubal, 2010) [99], where $d_y = L_y / \sinh(\beta_y)$, L_y is the total height of the domain, β_y is the grid stretching parameter, and $\eta_j = \beta_y(j - 1)/(N_y - 1)$. The flowfield is initialized using a digital filter procedure based on Klein's method (Klein *et al.*, 2004) [48] where the *r.m.s.* velocity profiles are extracted from the DNS of Bernardini and Pirozzoli (2011) [9]. A series of ≈ 140 characteristic times, $\tau_c = \delta_{in}/u_\infty$ is achieved to sweep the initial transient flowfield. Then, turbulence statistics are sampled and extracted each time step from time series covering $\tau \approx 300\tau_c$. By plotting the time evolution of the main boundary layer statistics, such as the boundary layer thickness and the friction velocity, this sampling time is judged to be sufficient to reach a statistical convergence of the considered quantities.

A reference simulation (*e.g.* LES-P2 case) is performed over about 40 hours using 64 processors, for a total of about 2560 CPU hours.

The First-half of the domain is used for the recycling/rescaling procedure, and only the second-half of the domain is fully dedicated to extract and analyze the results. In the latter part of the domain, Reynolds number Re_τ is ranging from 510 to 640 (which corresponds to Re_θ from 2090 to 2900).

Tables 3.2 and 3.3 reports statistical properties of the considered test-cases at a given downstream station $x_{res} \simeq 84.8\delta_{in}$, which corresponds to $\text{Re}_\tau \approx 580$.

Case	N_x	N_y	N_z	Δx^+	Δy_{min}^+	Δz^+	β
DNS	4160	221	440	5.7	0.7	4.9	—
LES-L1	1152	180	96	22.7	0.95	8.19	4.85
LES-L2	768	180	96	35.8	1.00	8.60	4.85
LES-N2	768	180	64	35.8	1.00	12.9	4.85
LES-P2	768	90	64	35.9	1.24	12.9	5.45
LES-Q2	768	90	48	35.4	1.22	16.9	5.45
LES-R2	512	90	48	56.0	1.28	17.9	5.45
LES-S2	768	45	64	36.2	1.29	13.0	5.85

Table 3.1: Grid resolution sensitivity study using the CSM model. Subscript (+) denotes the normalization by the friction velocity, with $y^+ = y\rho_w u_\tau / \mu_w$.

Case	Re_τ	Re_θ	$10^3 C_f$	δ^*/δ	$10^2 \theta/\delta$	H	T_w/T_∞	M_τ	$\sqrt{\langle p'^2_w \rangle} / \tau_w$
DNS	583.9	2865.9	2.53	0.259	8.50	2.96	1.717	0.0712	2.62
DSM	584.4	2423.2	2.78	0.245	8.56	2.86	1.620	0.0745	2.89
CSM	590.7	2597.5	2.98	0.282	9.08	3.11	1.666	0.0773	3.40
WALE	572.1	2560.8	2.94	0.297	9.03	3.29	1.664	0.0767	3.10
ILES	567.1	2542.0	2.94	0.301	8.97	3.36	1.703	0.0767	3.45

Table 3.2: Boundary layer properties using LES-P2 grid for different subgrid models. $Re_\tau = \rho_w u_\tau \delta / \mu_w$; $Re_\theta = \rho_\infty u_\infty \theta / \mu_\infty$; $C_f = 2\tau_w / \rho_\infty u_\infty^2$; $H = \delta^*/\theta$; $M_\tau = u_\tau / (\gamma R T_w)^{1/2}$; θ refers to the momentum thickness.

Case	Re_τ	Re_θ	$10^3 C_f$	δ^*/δ	$10^2 \theta/\delta$	H	T_w/T_∞	M_τ	$\sqrt{\langle p'^2_w \rangle} / \tau_w$
DNS	583.9	2865.9	2.53	0.259	8.50	2.96	—	0.0712	—
LES-L1	541.0	2582.0	2.73	0.294	9.38	3.14	1.675	0.0740	3.01
LES-L2	599.4	2670.4	2.93	0.289	9.17	3.16	1.659	0.0767	3.46
LES-N2	599.2	2691.8	2.99	0.291	9.28	3.14	1.669	0.0773	3.43
LES-P2	590.7	2597.5	2.98	0.282	9.08	3.11	1.666	0.0773	3.34
LES-Q2	581.7	2565.5	2.89	0.279	8.99	3.11	1.666	0.0762	3.49
LES-R2	651.0	2669.6	3.19	0.266	8.79	3.02	1.661	0.0800	3.66
LES-S2	597.7	2388.7	2.99	0.251	8.26	3.04	1.666	0.0776	3.30

Table 3.3: Boundary layer properties for different grids using the CSM model.

Case	Line	Symbol
DNS		○
DSM	—	■
CSM	- -	▲
WALE	◆
ILES	· · ·	▼
LES-L1	—	■
LES-L2	- -	◆
LES-N2	▲
LES-P2	· · ·	◀
LES-Q2	· · · —	▼
LES-R2	· · · - -	▶
LES-S2	—	●

Table 3.4: Lines and symbols used in graphs' legends.

In the following, the legends are summarized in table 3.4.

3.2 Flow Organization

For subsonic, and subsequently supersonic flows, it is known that the very near-wall region is occupied by alternating streaks of high- and low-speed fluid. These streaks are presumed to derive from elongated, counter-rotating streamwise vortices near the wall. For the near-wall region $y^+ < 100$, those streaks are found to significantly contribute to the turbulence production, which occurs during the *bursting* process *i.e.* low-speed streaks would gradually lift up from the wall, oscillate, and then break up violently, ejecting fluid away from the wall and into the outer layer (Smits & Dussauge, 2006) [88].

In order to qualitatively assess the turbulent nature of the flow in the inner layer, wall-parallel slices of velocity and temperature fluctuations are plotted in Fig. 3.3 in a wall-parallel plane at $y^+ \simeq 10$. The data are obtained using the CSM model with the LES-L1 grid and are extracted from the station x_{res} . As reported by Duan *et al.* (2010) [23] and Pirozzoli & Bernardini (2011) [74], Fig. (3.3-a) shows typical alternating high- and low-speed streaks, which correspond to positive and negative velocity fluctuations, respectively. This alternative behavior is interpreted as the

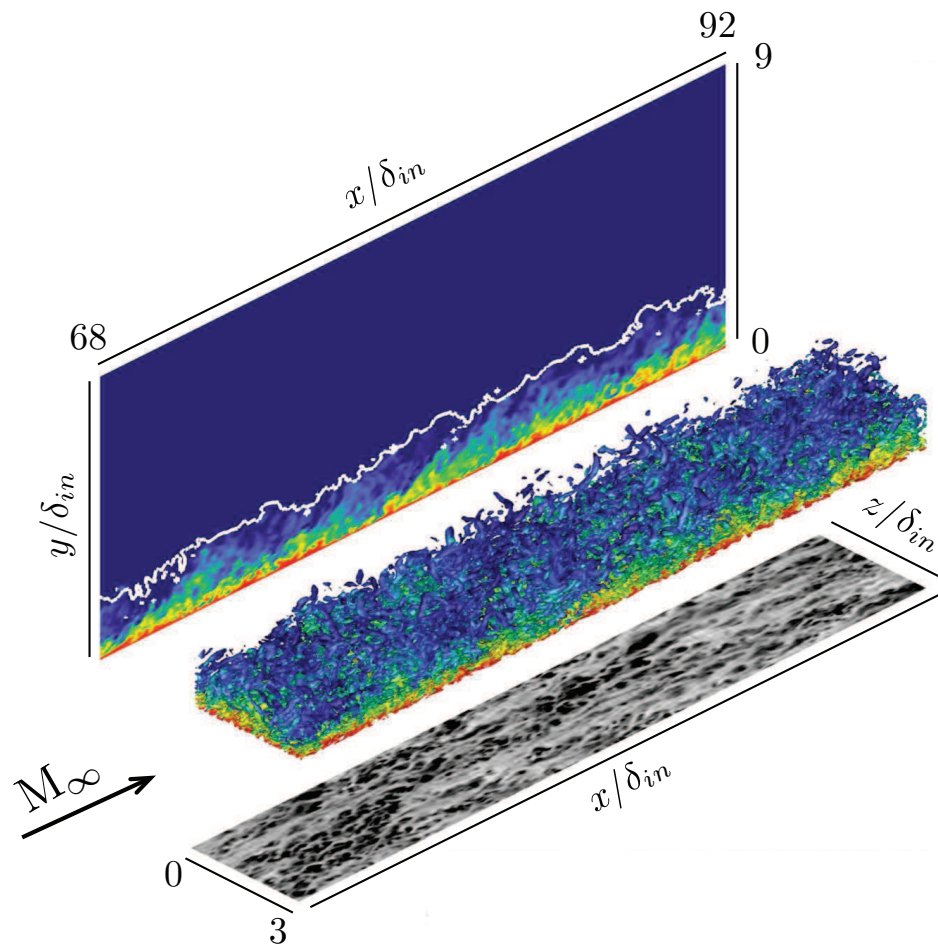


Figure 3.2: Instantaneous flow field for the LES-L1 grid with the CSM model: (center) Q-criterion iso-surface colored with the temperature field [25]; (top) Instantaneous temperature field in a x - y plane; (bottom) Temperature fluctuations field in the x - z plane at $y^+ \simeq 9$.

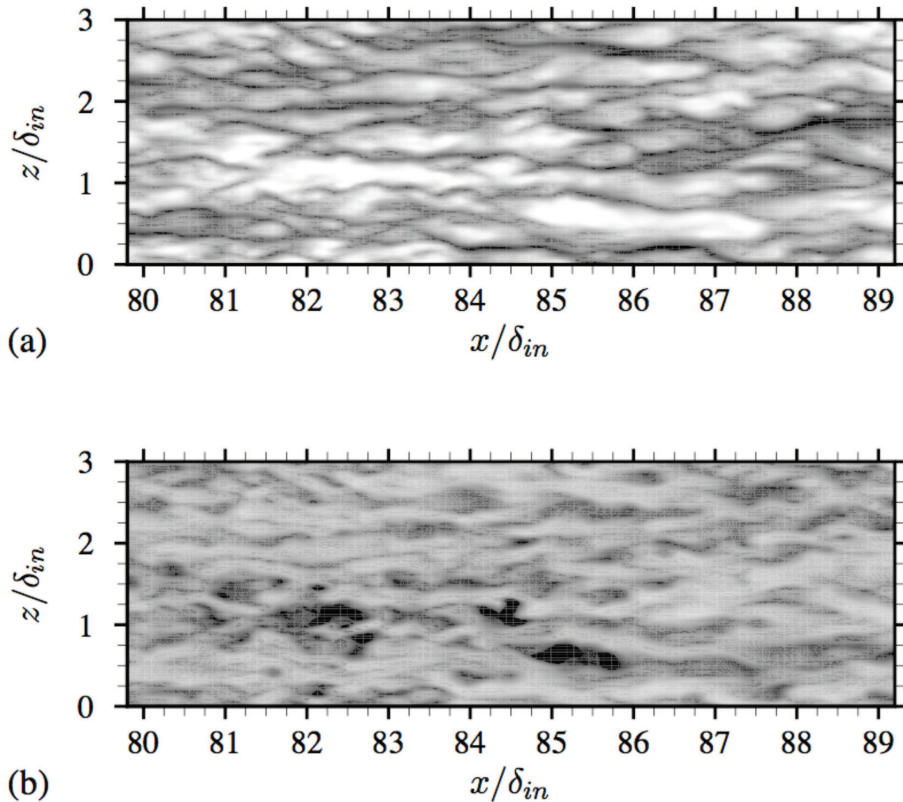


Figure 3.3: Instantaneous (a) velocity and (b) temperature fluctuation fields in the x - z plane at $y^+ \simeq 9$, for LES-L1 using the CSM model. Contour levels are shown for (a) $-0.2 \leq u'/u_\infty \leq 0.2$ and (b) $-0.2 \leq T'/T_\infty \leq 0.2$, from dark to light shades.

remnants of ‘sweep’ and ‘ejection’ events (Pirozzoli & Bernardini, 2011) [74].

For the temperature field, Fig. (3.3-b) shows the same structured pattern, with alternated dark and light shades. Pirozzoli & Bernardini (2011) [74] highlighted close correspondence of positive temperature fluctuations zones with low-speed streaks, and subsequently negative temperature fluctuations zones with high-speed streaks. This tendency is also observed in the present LES computation, and can be interpreted as the anti-correlated character that links the velocity and temperature fluctuations near solid walls.

One can also notice the number of streaks in the spanwise direction (z), which is an indicator of the width of the domain in the spanwise direction: a sufficient number of streaks means that the flow is not confined in spanwise direction, and that turbulence mechanisms are not inhibited by the domain extent (Jimenéz & Moin, 1991) [46].

In the outer layer, the flow is marked by the presence of a characteristic component, namely the large-scale turbulent *bulge*, also known as *Large Scale Motion*. Those structures are responsible for the large-scale transport of turbulence in the outer layer, and appear to play an important role in triggering instabilities in the near-wall region (Smits & Dussauge, 2006) [88]. Fig. (3.2) shows this turbulent structures, with a highly intermittent character, and inclined to the wall in the downstream direction.

3.3 Turbulence Statistics

3.3.1 Auto-Correlation Coefficients

To ensure that the computational domain is sufficiently wide in the spanwise direction, we analyzed the two-point correlations functions, defined by:

$$R_{\varphi' \varphi'}(r_z) = \sum_k^{Nz/2} \langle \varphi_k \varphi_{k+k_r} \rangle_H \quad k_r = 0, 1, \dots, N_z/2 \quad (3.1)$$

where $r_z = k_r \Delta_z$, φ' represents the fluctuations of flow variables, and the angled brackets $\langle \cdot \rangle_H$ represent an averaging operation over homogeneous directions.

As shown in Fig. (3.4), the auto-correlations distributions decrease to zero, which means that two points of the domain separated by $L_z/2$ are completely independent, and thus the domain is wide enough so that the principal turbulence mechanisms are not inhibited. This confirms the previous observation made on the streaks development in a x - z wall-parallel plane.

3.3.2 Wall properties

The boundary layer produces a drag on the plate due to the viscous stresses which are developed at the wall. To get an estimate of the velocity gradient near the wall, one can consider the skin-friction coefficient, which is defined as $C_f = 2\tau_w/\rho_\infty u_\infty^2$, where τ_w is the local wall-shear stress and u_∞ is the free-stream velocity.

Fig. (3.5) shows the incompressible skin-friction distribution, $C_{f_{inc}}$, as a function of the Reynolds number based on the incompressible momentum thickness, $Re_{\theta_{inc}}$, and is compared to formulas by Smits *et al.* (1983) [90], Blasius and Kármán-Schoenherr [41], as well as to DNS data

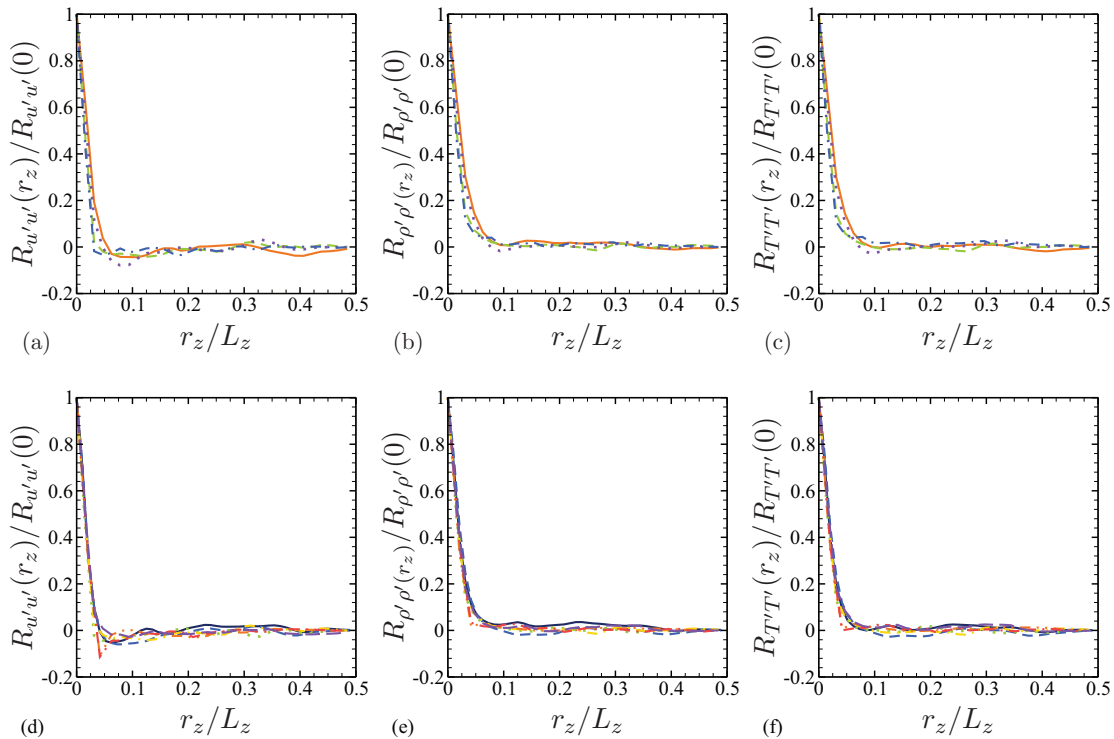


Figure 3.4: Instantaneous auto-correlation coefficients at $y^+ \simeq 9$. (a-c) SGS models study using LES-P2 grid; (d-f) Grid sensitivity study using CSM model. For legend, see table 3.4.

of Guarini *et al.* (2000) [38], Maeder *et al.* (2001) [63], Pirozzoli *et al.* (2004) [76] and Pirozzoli & Bernardini (2011) [74].

The skin-friction coefficient, $C_{f_{inc}}$, and the Reynolds number, $Re_{\theta_{inc}}$, are calculated using the van-Driest II theory for an adiabatic wall (Pirozzoli *et al.*, 2004; Pirozzoli & Bernardini, 2011), which is found to be a reliable transformation for collapsing data at different Mach regimes:

$$C_{f_{inc}} = F_c C_f \quad \text{and} \quad Re_{\theta_{inc}} = F_\theta Re_\theta \quad (3.2)$$

where the transformation functions F_c and F_θ are:

$$F_c = \frac{T_w/T_\infty - 1}{\arcsin^2 \alpha} \quad \text{and} \quad F_\theta = \frac{\mu_\infty}{\mu_w} \quad (3.3)$$

where

$$\alpha = \frac{T_w/T_\infty - 1}{\sqrt{T_w/T_\infty (T_w/T_\infty - 1)}} \quad (3.4)$$

The incompressible skin-friction coefficient correlations used in Fig. (3.5) are given by:

$$\begin{aligned} C_{f_{inc, B}} &= 0.026 Re_{\theta_{inc}}^{-1/4} \\ C_{f_{inc, S}} &= 0.024 Re_{\theta_{inc}}^{-1/4} \\ C_{f_{inc, KS}} &= \frac{1}{17.08 (\log_{10} Re_{\theta_{inc}})^2 + 25.11 (\log_{10} Re_{\theta_{inc}}) + 6.012} \end{aligned} \quad (3.5)$$

where the subscripts S, B and KS refer to the prediction laws of Smits *et al.* (1983) [90], Blasius and Kármán-Schoenherr (Hopkins & Inouye, 1971) [41], respectively.

Fig. (3.5) shows that the skin-friction coefficient, $C_{f_{inc}}$, is overall well reproduced by the present simulations. For the DSM model, $C_{f_{inc}}$ lies within the analytical Blasius' and Kármán Schoenherr's curves, while it is over-estimated by a maximum of 7% by the CSM model. The same trend is also observed for the different grid resolutions, where only the LES-L1 grid predicted a value of $C_{f_{inc}}$ that lies within the analytical curves, and all other cases over-predicted the skin-friction coefficient, the difference reaches a maximum of 18% for LES-R2 case. Note that the latter case contains two times less points in y and z directions than the reference case LES-P2.

Fig. (3.6) depicts the variation of the normalized *r.m.s.* wall-pressure fluctuations as a function

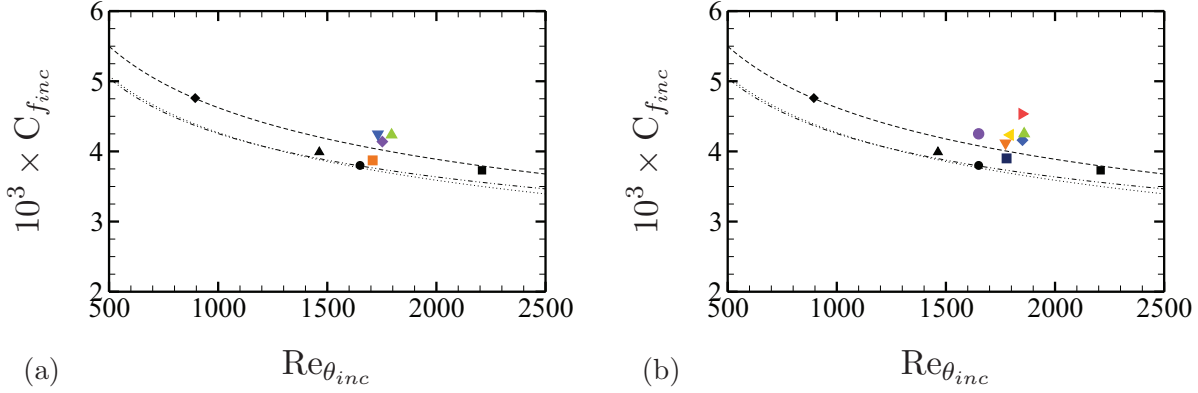


Figure 3.5: Incompressible skin-friction coefficient $C_{f,inc}$ as a function of Reynolds number based on incompressible momentum thickness $Re_{\theta_{inc}}$. (—) Blasius; (· – ·) Kármán Schoenherr; (··) Smits *et al.* (1983); ■ Pirozzoli *et al.* ($M=2.25$); ♦ Guarini *et al.* ($M=2.5$); ▲ Maeder *et al.* ($M=3$); ● Pirozzoli & Bernardini ($M=2$). (a) SGS models study using LES-P2 grid; (b) Grid sensitivity study using CSM model. For legend, see table 3.4.

of the friction Reynolds number, Re_τ . It is defined by Farabee & Casarella (1991) [28] as:

$$\frac{p_{rmsw}^2}{\tau_w^2} = \begin{cases} 6.5 + 1.86 \ln \left(\frac{Re_\tau}{333} \right) & Re_\tau > 333 \\ 6.5 & Re_\tau < 333 \end{cases} \quad (3.6)$$

Recently, Bernardini & Pirozzoli (2011) [9] proposed a curve fit for their DNS data at $M_\infty = 2$, which reads:

$$\frac{p_{rmsw}^2}{\tau_w^2} = 2.27 \ln Re_\tau - 7.36 \quad (3.7)$$

The distributions show over-prediction of p_{rmsw}/τ_w compared to the formula by Farabee & Casarella (1991) [28], where it is estimated by 6% for the DSM model, 13% for the WALE model, 22% for the CSM and 26% for the Implicit LES. Fig. (3.6-b) shows also the same behavior, where p_{rmsw}/τ_w monotonically increases when the grid is coarsen. Higher levels are reached for the coarsen grids in the spanwise direction (namely LES-Q2 and LES-R2 cases). This over-estimation shows again the impact of the spanwise grid-resolution on resolving the turbulence.

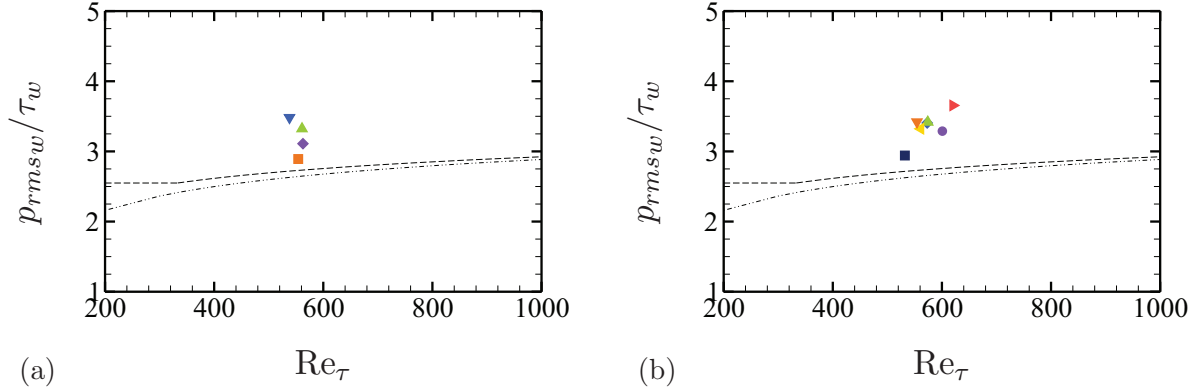


Figure 3.6: Normalized *r.m.s.* wall-pressure distribution p_{rmsw}/τ_w as a function of Reynolds number Re_τ . (—) Farabee & Casarella (1991) [28]; (· – ·) Bernardini & Pirozzoli (2011) [9]. (a) SGS models study using LES-P2 grid; (b) Grid sensitivity study using CSM model. For legend, see table 3.4.

3.3.3 First- and second-order statistics

In supersonic turbulent flows, compressibility effects are assumed to be weak for values of turbulent Mach number, M_t , that does not exceed 0.3 (Smits & Dussauge, 2006) [88]. Fig. (3.7) shows M_t as a function of y/δ . It can be seen that M_t doesn't vary much neither with SGS models nor with grid resolutions, and the peak value reaches $M_t^{max} \approx 0.325$ at $y/\delta \simeq 0.04$, except for LES-R2 grid where the peak of M_t attains almost 0.35. The compressibility effects are then supposed to be weak for the considered flow, and only variations of the thermodynamic quantities are supposed to vary across the boundary layer.

Distributions of the mean-averaged quantities as a function of y/δ are plotted in Fig. (3.8). The profiles collapse overall well with the DNS data, and the CSM model seems best estimating the averaged quantities. The normalized wall-temperature, T_w/T_∞ , is estimated by 1.717 for the DNS, 1.666 for the CSM model, 1.664 for the WALE model and 1.62 for the DSM model. $\langle \rho \rangle \langle u \rangle / \rho_\infty u_\infty$ is best estimated by the CSM model. The under-estimation of the wall-temperature by the DSM model could originates mainly from a too high damping of the turbulent fluctuations in this region, caused by a wrong prediction of the near wall asymptotic behavior of the SGS eddy viscosity μ_{sgs} . We also note that coarsening the grid seems to weakly affect the quantities (see Fig. 3.8-b).

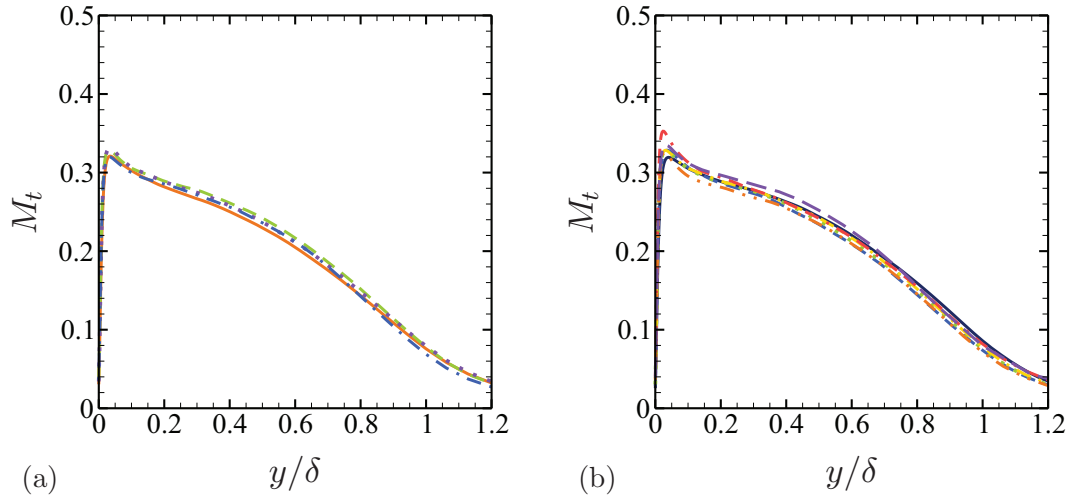


Figure 3.7: Turbulent Mach number, M_t , as a function of y/δ . (a) SGS models study using LES-P2 grid; (b) Grid sensitivity study using CSM model. For legend, see table 3.4.

The mean total temperature $\langle T_t \rangle$ is defined as:

$$\langle T_t \rangle = \langle T \rangle + \frac{1}{2} \frac{\gamma - 1}{\mathcal{R}\gamma} \left(\langle u_i^2 \rangle + \langle u'_i u'_i \rangle \right) \quad (3.8)$$

where \mathcal{R} is the specific gas constant, taken equal to $287.031 \text{ J.Kg}^{-1}\text{K}^{-1}$.

Since the mass flux and the total enthalpy are functions of y/δ only, integrating the total enthalpy equation across the boundary layer is independent of the streamwise location for adiabatic flows, which yields to:

$$\int_0^\infty \frac{\rho u}{\rho_\infty u_\infty} \left(1 - \frac{H_t}{H_{t_\infty}} \right) dy = 0 \quad (3.9)$$

Since the mass flux is always positive and $H_t/H_{t_\infty} < 1$ near the wall, there must be a region where $H_t/H_{t_\infty} > 1$, that is, there must be an overshoot in the total temperature distribution. In adiabatic flows, this overshoot is small so that it is difficult to measure it experimentally (less than 1% in supersonic turbulent boundary layer at $M = 2.3$ and $\text{Re}_\theta = 5500$ (Smits & Dussauge, 1996) [89].

Fig. (3.9) shows the normalized mean total temperature $\langle T_t \rangle / T_{t_\infty}$. As it can be seen, the total temperature is not constant throughout the layer. The overshoot of the total temperature is retrieved by all models and for different grid resolutions, and does not exceed 2% for all cases. This

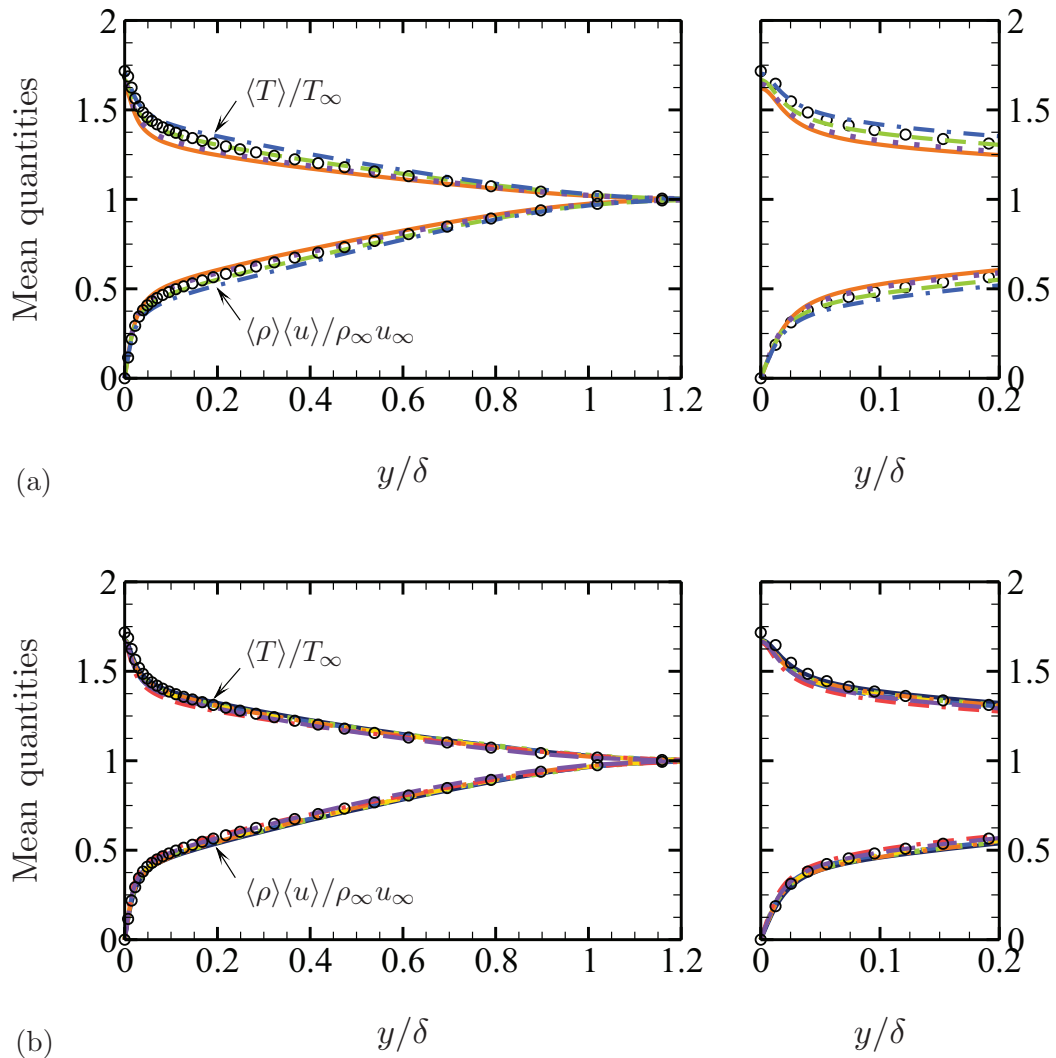


Figure 3.8: Distributions of the time-averaged mean quantities as a function of y/δ . (a) SGS models study using LES-P2 grid; (b) Grid sensitivity study using CSM model. For legend, see table 3.4.

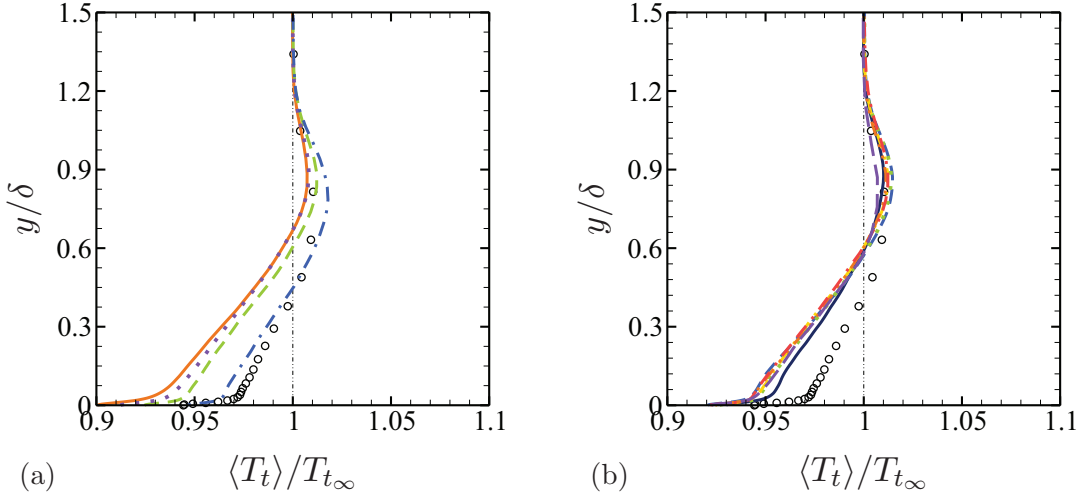


Figure 3.9: Distribution of the normalized time-averaged total temperature, $\langle T_t \rangle / T_{t_\infty}$, as a function of y/δ . ○ DNS Pirozzoli *et al.* (2004) [76] at $Re_\theta = 4260$. (a) SGS models study using LES-P2 grid; (b) Grid sensitivity study using CSM model. For legend, see table 3.4.

overshoot is expected to increase with positive heat flux, namely heated wall (Smits & Dussauge, 1996) [89].

The van-Driest transformed mean streamwise velocity $\langle u \rangle_{vd}^+$, which accounts for the variation of the mean flow properties aiming to collapse a compressible velocity profile with its incompressible counterpart, is defined as:

$$\langle u \rangle_{vd}^+ = \int_0^{u^+} \sqrt{\frac{\langle \rho \rangle}{\rho_w}} d\langle u \rangle^+ \quad (3.10)$$

The distribution of the van-Driest transformed mean streamwise velocity $\langle u \rangle_{vd}^+$ as a function of y^+ is reported in Fig. (3.10). Except a very good estimation of $\langle u \rangle_{vd}^+$ by the DSM model, the plot shows a slight under-estimation of $\langle u \rangle_{vd}^+$ in the Log-region compared to the DNS data, for the remaining SGS models (Fig. 3.10-a). In the viscous sub-layer and up to the buffer region ($y^+ < 30$), all models collapse well with the DNS. As expected for $y^+ < 5$, the velocity evolves linearly with regards to y^+ . As said before, a weak under-estimation of $\langle u \rangle_{vd}^+$ by the WALE and the CSM models (5% and 10%, respectively) in the logarithmic region ($C + 1/\kappa \log y^+$, with $C = 5.2$ and $\kappa = 0.41$) is observed in the region $30 < y^+ < 100$, even if the slope is well reproduced, and all models exhibit an under-estimation of u_{vd}^+ in the wake region and in the outer part of the boundary layer. In Fig.

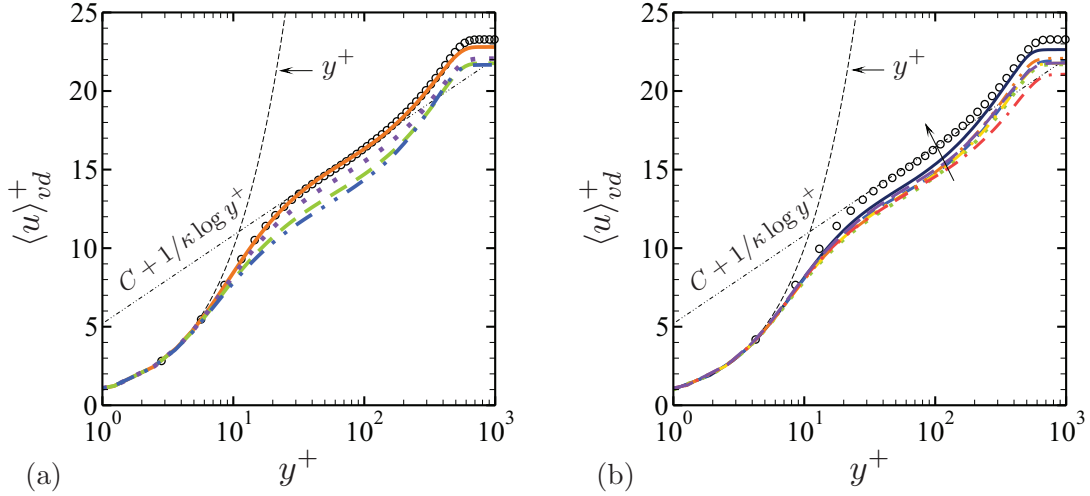


Figure 3.10: Distribution of the van-Driest transformed mean streamwise velocity $\langle u \rangle_{vd}^+$ as a function of y^+ . $C = 5.2$; $\kappa = 0.41$. (a) SGS models study using LES-P2 grid; (b) Grid sensitivity study using CSM model. For legend, see table 3.4.

(3.10-b), $\langle u \rangle_{vd}^+$ shows sensitivity to grid resolution, and the noted under-estimation decreases as the grid is refined. The spanwise resolution is found to influence more this under-estimation than the streamwise and the wall-normal resolutions.

Fig. (3.11) depicts the van-Driest transformed mean streamwise velocity deficit as a function of y/δ . All SGS models are found to exhibit overall acceptable results. While the CSM model fits well with the DNS, both the DSM and the WALE models under-estimate the velocity deficit, while the Implicit LES over-estimate it.

Figs. (3.12-a; 3.12-b) show the normalized velocity fluctuations as a function of y/δ and Figs. (3.12-c; 3.12-d) the velocity fluctuations in Morkovin's scaling as a function of y^+ . Except a good fitting in the near-wall region ($y/\delta < 0.05$ and $y^+ < 10$), all models present under-estimated magnitudes compared to the DNS, especially for the u_{rms}^+ component (5% for the DSM, 8% for the CSM and 10% for the WALE model). The location of the streamwise component peak is well estimated by all the models (0.02δ). It is also found that the wall-normal fluctuations, v_{rms}^+ , as well as the spanwise fluctuations, w_{rms}^+ , and the Reynolds shear stress $\langle u'v' \rangle^+$ are better estimated by the WALE and the CSM model. In Fig. (3.12-b), normalized velocity fluctuations are found to be weakly sensitive to the grid resolution. Fig. (3.12-e; 3.12-f) shows the normalized velocity fluctuations in Morkovin's scaling as a function of y^+ in Log-scale, where results, at $\text{Re}_{\delta_2} \approx 1800$

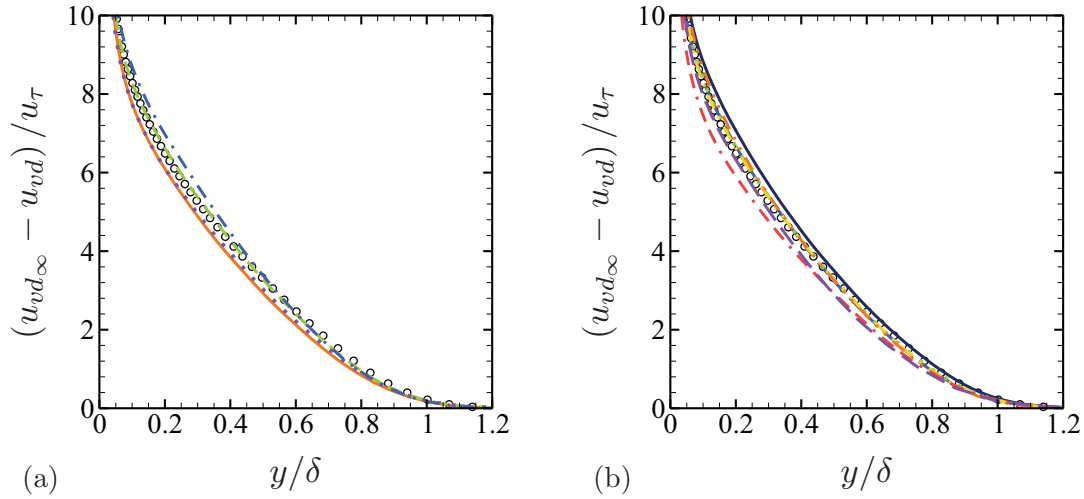


Figure 3.11: Normalized mean velocity deficit $u_{vd_\infty} - u_{vd}/u_\tau$ as a function of y/δ . (a) SGS models study using LES-P2 grid; (b) Grid sensitivity study using CSM model. For legend, see table 3.4.

in the region $50 < y^+ < 300$, are compared to:

- The curve fitting of DNS data (Pirozzoli *et al.*, 2004) [76] at $\text{Re}_{\delta_2} \approx 2400$, written:

$$\begin{aligned} \frac{\langle \rho \rangle}{\rho_w} \frac{\langle u'^2 \rangle}{u_\tau^2} &\approx 1.500 - 1.086 \log(y/\delta) - v(y^+) \\ \frac{\langle \rho \rangle}{\rho_w} \frac{\langle v'^2 \rangle}{u_\tau^2} &\approx 1.526 - v(y^+) \\ \frac{\langle \rho \rangle}{\rho_w} \frac{\langle w'^2 \rangle}{u_\tau^2} &\approx 1.243 - 0.510 \log(y/\delta) - v(y^+) \end{aligned} \quad (3.11)$$

- The subsonic experimental results by Perry & Li (1990) [70] at $\text{Re}_{\delta_2} = 5000$:

$$\frac{\langle u_i'^2 \rangle}{u_\tau^2} = B_i - A_i \log(y/\delta) - v(y^+) \quad (3.12)$$

where $B_1 = 2.39$, $A_1 = 1.03$, $B_2 = 1.6$, $A_2 = 0$, $B_3 = 1.20$, $A_3 = 0.475$. In both Eq. (3.11) and (3.12), $v(y^+)$ represents a correction of deviation from the logarithmic profile due to viscous action in the turbulent wall-region, that increases with y^+ , which is given by:

$$v(y^+) = 5.58y^{+1/2} - 22.4y^{+1} + 22.0y^{+5/4} - 5.62y^{+2} + 1.27y^{+11/4} \quad (3.13)$$

It can be seen from Fig. (3.12-e; 3.12-f) that even if the streamwise and the spanwise components

show an overall weak under-estimation in the considered region ($50 < y^+ < 300$), the slope is well reproduced for almost all considered cases. The wall-normal component collapses well with the curve-fitting, with regards to the slope as well as the magnitude. When refining the mesh, $u_{rms}^{+2}\langle\rho\rangle/\rho_w$ shows a small shift towards the reference, while the two other components remain unaffected by the grid refinement. It is also found that the results are more compatible with the DNS data rather than to the subsonic experimental results, which can be due to the Reynolds number effect.

The resolved turbulent kinetic energy, $K = \langle u'_i u'_i \rangle / 2$ for the SGS model study and for the grid sensitivity study is shown in Figs. (3.13-a) and (3.13-b), respectively, as well as the modeled part of the turbulent kinetic energy using the DSM model, $k_{sgs} = \tau_{kk}/(2\langle\rho\rangle)$, in Fig. (3.13-c). It is found that the peak position of K is overall well retrieved by all SGS models, and is located around $y^+ \approx 13$ for the DSM model and $y^+ \approx 12$ for the remaining models. This location is found to be weakly sensitive to the grid resolution, where it is $y^+ \approx 14$ for the LES-L1 grid, which constitutes a classical result.

For incompressible flows, the structure parameter is found to be constant, and lies between 0.14 and 0.17 (Smits & Dussauge, 2006) [88]. The structure parameter shows constant value ≈ 0.15 by all SGS models at $0.2 < y/\delta < 0.8$, and seems to be weakly sensitive to the grid resolution since all tested meshes exhibit values that lie between 0.14 and 0.17 (Fig. 3.14). Duan *et al.* (2011) [24] also showed in a DNS study that this parameter lies between 0.14 and 0.16 at $0.1 < y/\delta < 0.9$ when varying the Mach number from 3 to 5.

The distributions of the *r.m.s.* vorticity components as a function of y^+ are plotted in Fig. (3.15), where the i^{th} component of the *r.m.s.* of vorticity is defined as:

$$\Omega_i = \langle \omega_i'^2 \rangle^{1/2} \quad (3.14)$$

Both the CSM and the WALE models are seen to give better results compared to the DSM model, while in the near-wall region, the *r.m.s.* vorticity components are overall well estimated and fit well with the references ($y^+ \leq 10$), they are under-estimated away from the wall, especially for the streamwise component. As expected, the vorticity fluctuations are not isotropic for $y^+ \geq 30$, and only $\omega_2' \approx \omega_3'$ away from the wall.

Fig. (3.16) shows the different normalized shear stresses as a function of y^+ . The CSM and the

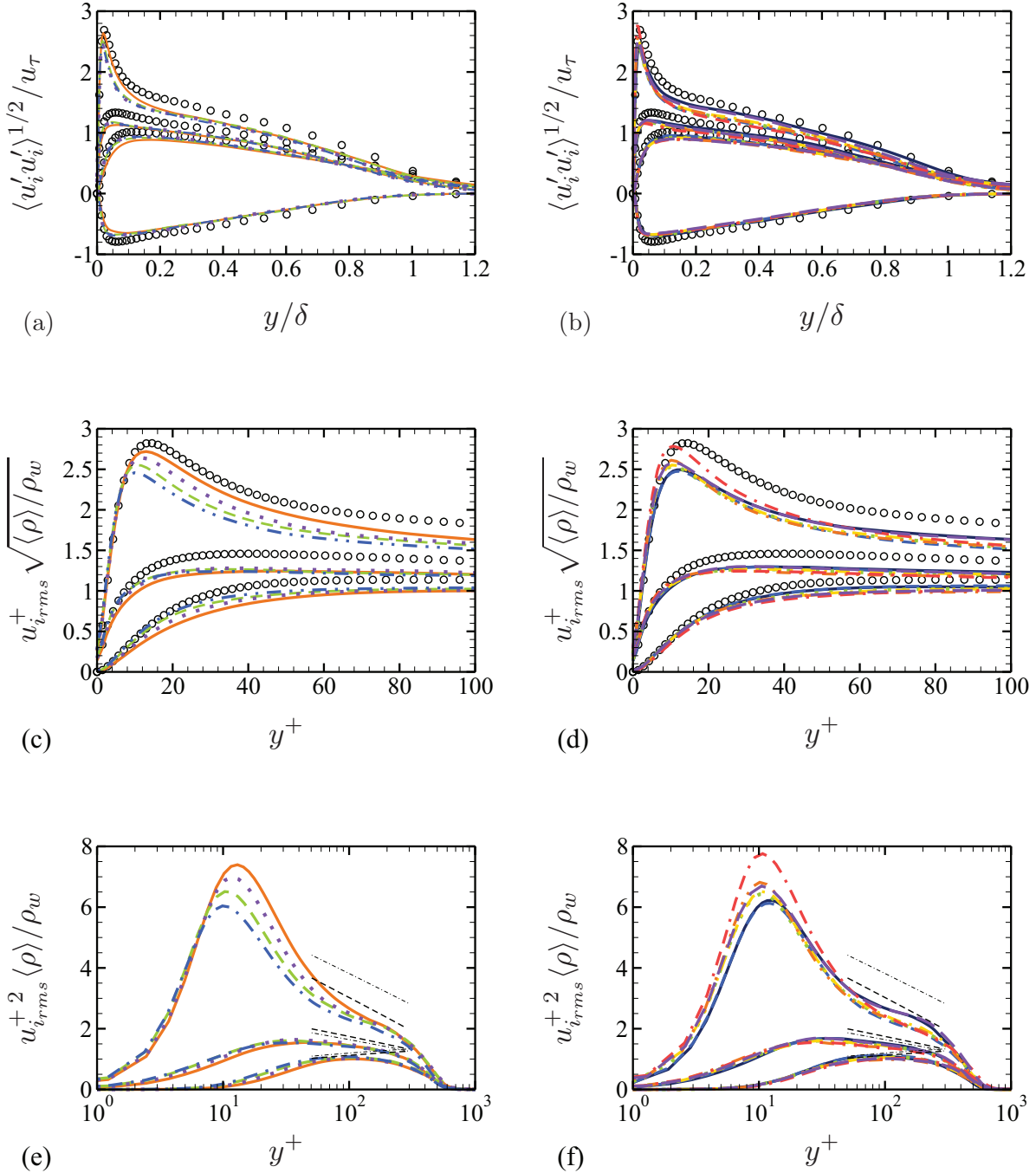


Figure 3.12: (a-b) r.m.s of velocity fluctuations components $u_i, rms/u_\tau$ as a function of y/δ ; (c-d) r.m.s velocity fluctuations in Morkovin's scaling as a function of y^+ ; (e-f) r.m.s velocity fluctuations in Morkovin's scaling as a function of y^+ in Log-scale. ($\cdot - \cdot$) Perry & Li (1990) [70] in Eq. 3.12. (---) Pirozzoli *et al.* (2004) [76] in Eq. 3.11. For legend, see table 3.4.

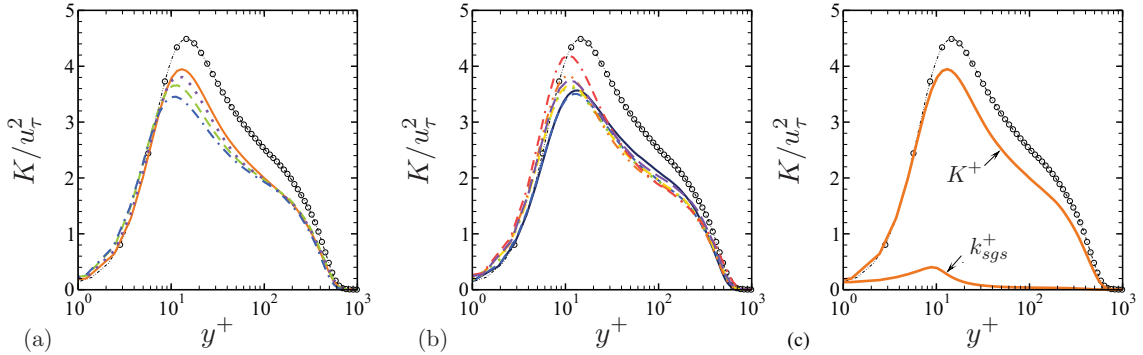


Figure 3.13: Normalized turbulent kinetic energy K/u_τ^2 as a function of y/δ . (a) SGS models study using LES-P2 grid; (b) Grid sensitivity study using CSM model; (c) Resolved turbulent kinetic energy K^+ and SGS turbulent kinetic energy k_{sgs}^+ for the LES-P2 grid using the DSM model as a function of y^+ . For legend, see table 3.4.

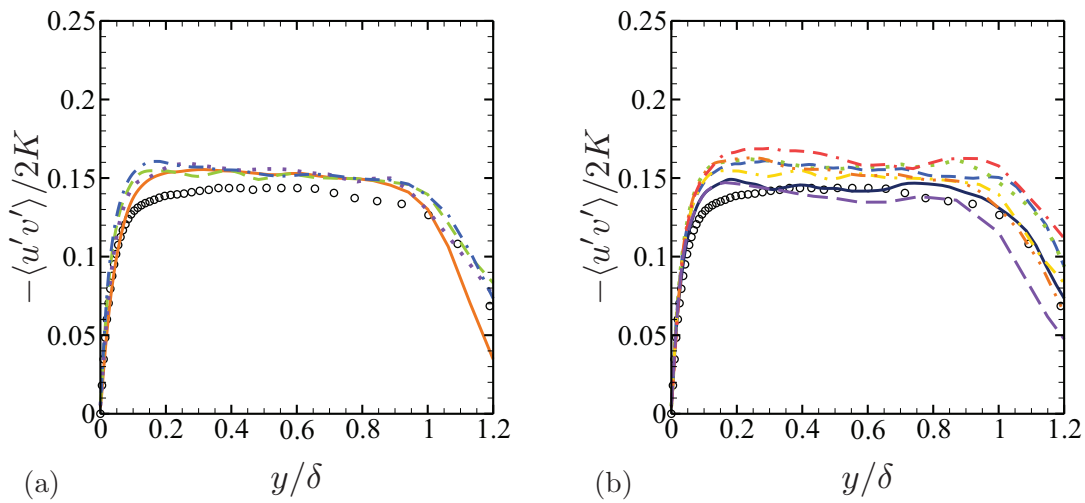


Figure 3.14: Structure parameter $-\langle u'v' \rangle / 2K$ as a function of y/δ . (a) SGS models study using LES-P2 grid; (b) Grid sensitivity study using CSM model. For legend, see table 3.4.

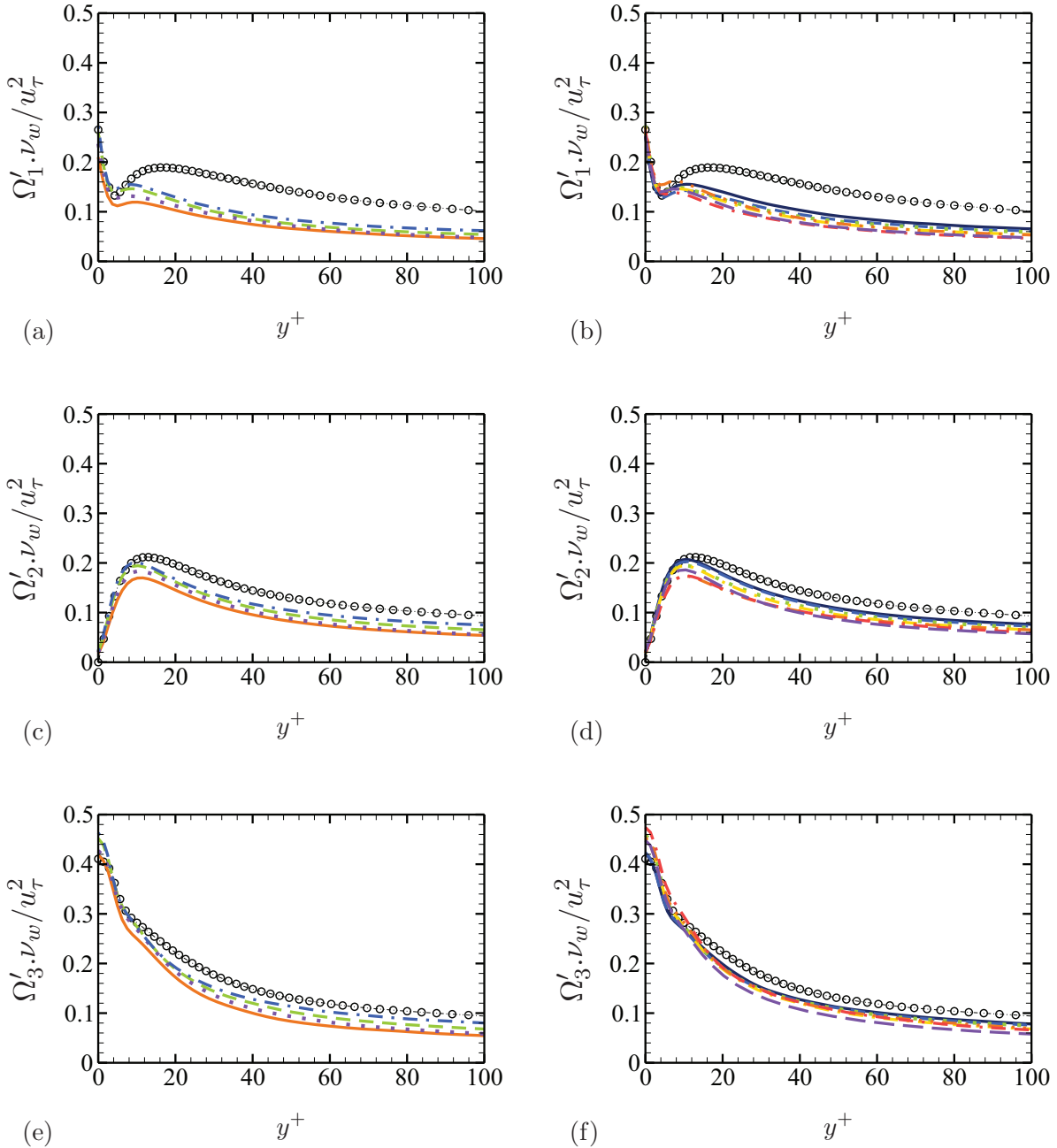


Figure 3.15: Distribution of r.m.s. vorticity components as a function of y^+ . (a) SGS models study using LES-P2 grid; (b) Grid sensitivity study using CSM model. For legend, see table 3.4.

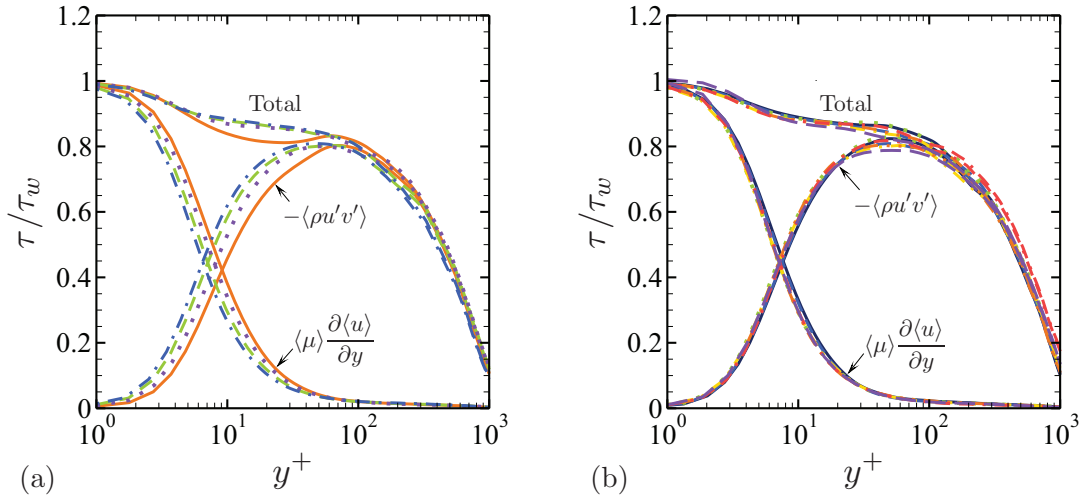


Figure 3.16: Turbulent shear stress $-\langle \rho u' v' \rangle$, mean viscous shear stress $\langle \mu \rangle \partial \langle u \rangle / \partial y$ and total shear stress $-\langle \rho u' v' \rangle + \langle \mu \rangle \partial \langle u \rangle / \partial y$ as a function of y^+ . (a) SGS models study using LES-P2 grid; (b) Grid sensitivity study using CSM model. For legend, see table 3.4.

WALE models show higher total shear stress compared to the DSM model (Fig. 3.16-a). Apart from the viscous sublayer, where viscous affects are dominant, the Reynolds shear stress accounts for almost all the total shear stress. As pointed out by Pirozzoli *et al.* (2004) [76], the Reynolds shear stress does not exceed unity for all SGS models. However, the total normalized shear stress is not constant throughout the viscous layer and in the lower part of the log-layer ($y^+ < 50$) as found by Pirozzoli *et al.* (2004) [76] and Duan *et al.* (2010) [23], and it decreases from 1 to 0.85 in the so-called region. Also, Fig. (3.16-b) shows that the different shear stresses are insensitive to the grid resolutions.

Fig. (3.17) depicts a comparison between the WENO-BWO scheme, the 4th order and the 6th order *split-centered* schemes, through the van-Driest transformed mean streamwise velocity, $\langle u \rangle_{vd}^+$, and the velocity fluctuations in Morkovin's scaling, as a function of y^+ . Except in the viscous sublayer, $\langle u \rangle_{vd}^+$ exhibits an over-estimation compared to the DNS data, which reaches a maximum of about 25% in the Log-region. The streamwise velocity fluctuations shows also the same tendency, where the peak is over-predicted by about 25% compared to the reference data. The wall-normal and the spanwise fluctuations components are however under-estimated. The observed trends are the footprint of an excessive numerical dissipation due to the WENO scheme. The 4th and the 6th order *split-centered* schemes show similar results, which are slightly under-estimated compared to

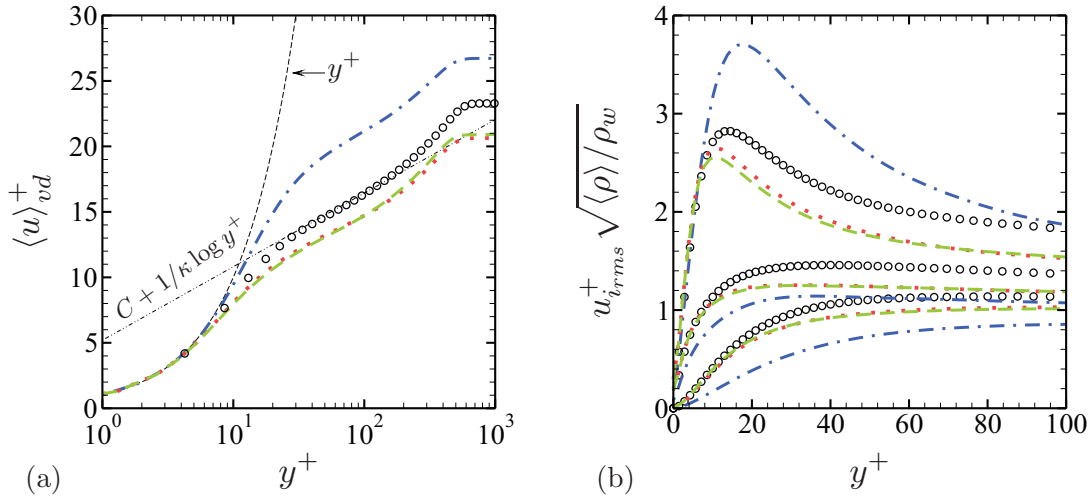


Figure 3.17: (a) Distribution of the van-Driest transformed mean streamwise velocity $\langle u \rangle_{vd}^+$ as a function of y^+ ; (b) r.m.s velocity fluctuations in Morkovin's scaling as a function of y^+ . (·—·) WENO-BWO scheme; (···) 4th split-centered; (- -) 6th split-centered.

the DNS data. However, the relative difference is much lower compared to the WENO scheme's result.

3.4 Subgrid scale analysis - On evaluating grid resolution

In LES, the accuracy of the resolved scales highly rely on the mesh size. A locally refined grid usually lead to more resolved turbulent energy but will definitely be more costly in terms of CPU time and memory requirements. The strategy in LES is then to make the best compromise between accuracy and computational cost. The SGS dissipation of a given SGS model may have originated, in different proportions, either from the resolved velocity fluctuations or from the mean-averaged velocity gradients. Before going onto the details of the flow physics, the objective here is first to assess the evaluation of the LES resolution by investigating the contribution of the SGS model to the turbulent energy dissipation.

3.4.1 Near-wall asymptotic behavior of the SGS viscosity

When modeling the subgrid terms, some constraints, physical as well as numerical, have to be set. Of primordial interest is the physical constraint, in a way that the modeled SGS terms must

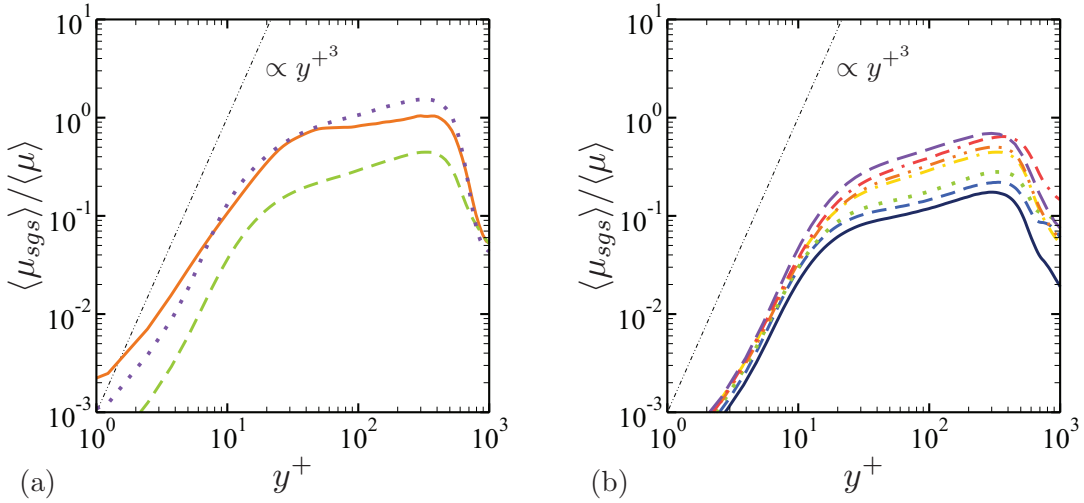


Figure 3.18: Normalized SGS viscosity, μ_{sgs}/μ , as a function of y^+ . (a) SGS models study using LES-P2 grid; (b) Grid sensitivity study using CSM model. For legend, see table 3.4.

be consistent with the properties of the studied phenomena. In an equilibrium boundary layer, and for a fine grid, the SGS model is supposed to exhibit the correct asymptotic behavior in the vicinity of a solid wall ($\mu_{sgs} \propto y^{+3}$). If this assumption does not hold for a given SGS model, it results in a too high damping of fluctuations in this region, and a wrong prediction of the skin friction (Garnier *et al.*, 2009) [32].

Fig. (3.18) shows the ratio of the SGS eddy viscosity to the molecular one $\langle \mu_{sgs} \rangle / \langle \mu \rangle$ as a function of y^+ . In Fig. (3.18-a), the DSM model does not exhibit the correct slope in the near-wall region, while it is well estimated by the CSM and the WALE models. Also, the DSM model seems not vanishing at the wall, although the flow is well resolved at this region ($\Delta y_{min}^+ \simeq 1$). However, the CSM model has a lower amount of μ_{sgs} , that monotonically increases when the grid is coarsened (Fig. 3.18-b). The CSM model is found to be less dissipative than the DSM model, but do preserve the good asymptotic behavior of the flow at the wall. For the DSM model, the combined effect of a weakly high SGS viscosity amount and a wrong asymptotic behavior near the wall can be a reason to its under-estimation of the temperature distribution, especially at the wall.

3.4.2 Ratio of turbulent kinetic energy

The parameter Γ , initially introduced by Pope (2004) [78] and used by Davidson (2009) [19], is defined as:

$$\Gamma = \frac{\langle K \rangle}{\langle k_{sgs} \rangle + \langle K \rangle} \quad (3.15)$$

where $\langle K \rangle$ is the resolved turbulent kinetic energy, $\langle k_{sgs} \rangle = \tau_{ii}/(2\rho)$ is the modeled part and u'_i is the i^{th} component of the resolved velocity fluctuation. It represents the ratio of the resolved turbulent kinetic energy $\langle K \rangle = \langle u'_i u'_i \rangle / 2$ to the total kinetic energy $\langle k_{sgs} \rangle + \langle K \rangle$. The isotropic part of the stress tensor is modeled according to Yoshizawa (1986) [108], where C_I is either retrieved using the dynamic procedure in the DSM model, or set constant for the CSM and the WALE models.

Based on the parameter given by Eq. (3.15), Pope (2004) [78] suggests that when 80% of the kinetic energy is accounted for, the LES can be considered as well-resolved.

In order to check this criterion, the parameter Γ is plotted as a function of y^+ , varying the SGS models (Fig. 3.19-a) and the grids resolution (Fig. 3.19-b). At the wall, the DSM model shows higher value of Γ than the CSM model, with 55% of the kinetic energy being resolved for the DSM model against 45% for the CSM model. However, one should remember that in the vicinity of the wall, the viscous effects are dominant, and the SGS model does not have significant effect on the turbulence structure. At the frontier of the viscous sublayer, this tendency is inverted, and up to $y^+ \simeq 100$, the CSM model better predicts Γ , until it reaches 1 for both SGS models. Fig. (3.19-b) shows that Γ is sensitive to the grid resolution at the wall, showing a monotone decrease while coarsening the grid, until reaching $\simeq 1$ at $y^+ \simeq 20$ for all grids. Apart from a small difference in a region very near from the wall, Γ reaches 1 quickly. However, because the SGS model is not supposed to act in the viscous sublayer where the grid is refined enough, and based on Pope's assumption, the parameter Γ seems not to be adapted to conclude for the present LES mesh quality.

3.4.3 Subgrid scale dissipation

In order to quantify the contribution of the SGS model to the production/destruction of turbulence, it is interesting to quantify the contribution of the SGS terms to turbulence, such as ε'_{sgs} and $\varepsilon_{\langle sgs \rangle}$, which are the production/destruction term of the resolved turbulent kinetic energy, $\langle K \rangle$,

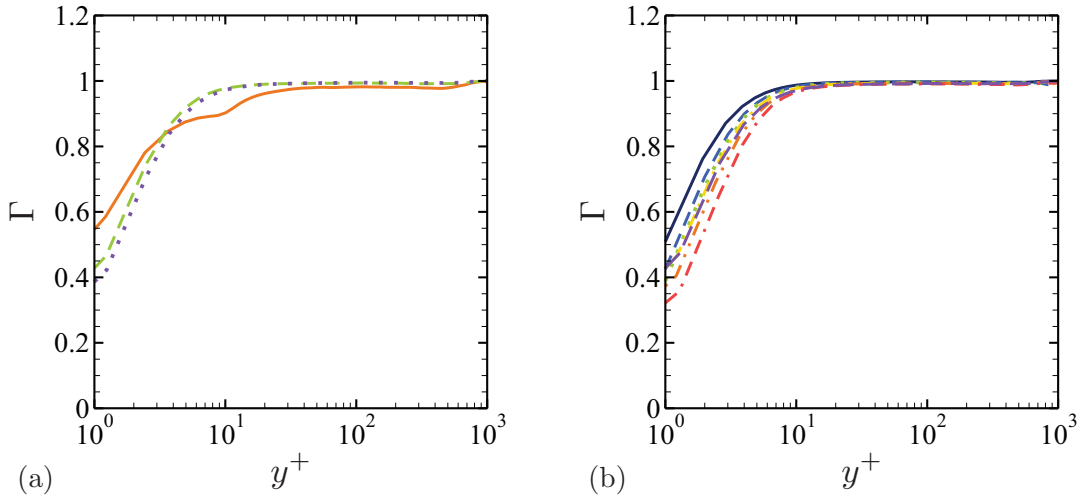


Figure 3.19: Ratio of the turbulent kinetic energy Γ as a function of y^+ . (a) SGS models study using LES-P2 grid; (b) Grid sensitivity study using CSM model. For legend, see table 3.4.

and the production/destruction term in the modeled turbulent kinetic energy, $\langle k_{sgs} \rangle$, respectively (Fig. 3.20).

The total SGS dissipation is then defined by:

$$\varepsilon_{sgs} = \varepsilon'_{sgs} + \varepsilon_{\langle sgs \rangle} \quad (3.16)$$

Following the developments by Davidson (2006) [20] for an incompressible flow, these terms can be explicitly formulated for the compressible case.

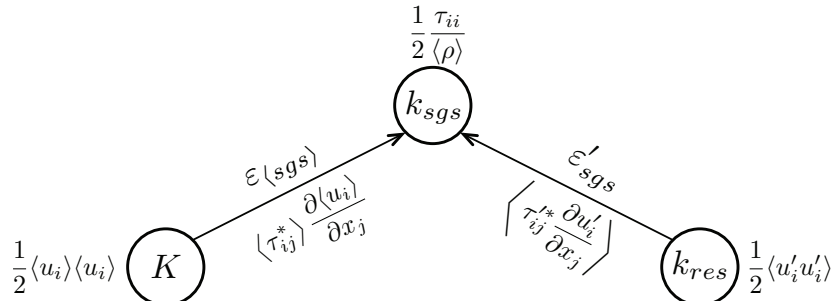


Figure 3.20: Contribution of the different SGS dissipation terms to turbulence.

Subgrid scale dissipation due to resolved fluctuations

The term of production/destruction of the resolved turbulent kinetic energy, $\langle K \rangle$, by SGS turbulence, which can also be interpreted as the SGS dissipation term due to the resolved fluctuations, was defined by Davidson (2006) [20] as:

$$\varepsilon'_{sgs} = \left\langle [\tau_{ij}^* - \langle \tau_{ij}^* \rangle] \frac{\partial u'_i}{\partial x_j} \right\rangle \quad (3.17)$$

where $\tau_{ij}^* = \tau_{ij} - \tau_{kk}\delta_{ij}/3$ is the modeled SGS stress tensor, and u'_i is the resolved fluctuations of the i^{th} component of the filtered velocity field. Simplifying the terms between the square-brackets, yields:

$$\begin{aligned} \tau_{ij}^* - \langle \tau_{ij}^* \rangle &= \tau'_{ij}^* = -2(\mu_{sgs} \tilde{s}_{ij}^* - \langle \mu_{sgs} \tilde{s}_{ij}^* \rangle) \\ &\simeq -2\mu_{sgs} s'_{ij}^* \end{aligned} \quad (3.18)$$

where $\tilde{s}_{ij}^* = \tilde{s}_{ij} - \tilde{s}_{kk}\delta_{ij}/3$ is the deviatoric part of the strain-rate tensor computed from the filtered velocity field, and s'_{ij}^* is the fluctuating tensor of \tilde{s}_{ij}^* :

$$\begin{aligned} \tilde{s}_{ij} &= \frac{1}{2} \left(\frac{\partial \tilde{u}_i}{\partial x_j} + \frac{\partial \tilde{u}_j}{\partial x_i} \right) \\ s'_{ij} &= \frac{1}{2} \left(\frac{\partial u'_i}{\partial x_j} + \frac{\partial u'_j}{\partial x_i} \right) \\ s'_{ij}^* &= s'_{ij} - \frac{1}{3} s'_{kk} \delta_{ij} \end{aligned} \quad (3.19)$$

Then, it follows:

$$\begin{aligned} \varepsilon'_{sgs} &= \left\langle \tau'_{ij}^* \frac{\partial u'_i}{\partial x_j} \right\rangle \simeq -2 \langle \mu_{sgs} s'_{ij}^* (s'_{ij} + \omega'_{ij}) \rangle \\ &\simeq -2 \langle \mu_{sgs} s'_{ij}^* s'_{ij} \rangle \end{aligned} \quad (3.20)$$

where $s'_{ij}^* \omega'_{ij}$ is equal to zero, since it is the product of a symmetric and anti-symmetric tensors,

$s'_{ij}\omega'_{ij}$:

$$\begin{aligned}\tilde{\omega}_{ij} &= \frac{1}{2} \left(\frac{\partial \tilde{u}_i}{\partial x_j} - \frac{\partial \tilde{u}_j}{\partial x_i} \right) \\ s'^*_{ij}\omega'_{ij} &= s'_{ij}\omega'_{ij} - \frac{1}{3}s'_{kk}\delta_{ij}\omega'_{ij} \\ &= s'_{ij}\omega'_{ij} - \frac{1}{3}s'_{kk}\omega'_{kk}\end{aligned}\quad (3.21)$$

It is interesting to quantify the ratio of the SGS dissipation term due to resolved velocity fluctuations in a wall-parallel plane $\varepsilon'_{sgs_{x+z}}$, since the streamwise and spanwise components of the SGS dissipation term make an important contribution to the total SGS dissipation (Davidson, 2009) [19]. It is defined as:

$$\begin{aligned}\varepsilon'_{sgs_{x+z}} &= -2 \left\langle \mu_{sgs} [s'^*_{ij}s'_{ij}]_{x+z} \right\rangle \\ &= -2 \left\langle \mu_{sgs} [s'^*_{11}s'_{11} + s'^*_{33}s'_{33} + 2s'^*_{13}s'_{13}] \right\rangle\end{aligned}\quad (3.22)$$

Subgrid scale dissipation due to time-averaged field

The production/destruction term, $\varepsilon_{\langle sgs \rangle}$, in the modeled turbulent kinetic energy $\langle k_{sgs} \rangle$, also interpreted as the SGS dissipation due to the time-averaged velocity field, is (Davidson, 2006) [20]:

$$\begin{aligned}\varepsilon_{\langle sgs \rangle} &= \langle \tau_{ij}^* \rangle \frac{\partial \langle \tilde{u}_i \rangle}{\partial x_j} = -2 \langle \mu_{sgs} \tilde{s}_{ij}^* \rangle (\langle \tilde{s}_{ij} \rangle + \langle \tilde{\omega}_{ij} \rangle) \\ &\simeq -2 \langle \mu_{sgs} \rangle \langle \tilde{s}_{ij}^* \rangle \langle \tilde{s}_{ij} \rangle\end{aligned}\quad (3.23)$$

where $\langle \tilde{s}_{ij}^* \rangle \langle \tilde{\omega}_{ij} \rangle$ is equal to zero, $\langle \tilde{u}_i \rangle$ is the time-averaged velocity field of the i^{th} component, and:

$$\begin{aligned}\langle \tilde{s}_{ij} \rangle &= \frac{1}{2} \left(\frac{\partial \langle \tilde{u}_i \rangle}{\partial x_j} + \frac{\partial \langle \tilde{u}_j \rangle}{\partial x_i} \right) \\ \langle \tilde{\omega}_{ij} \rangle &= \frac{1}{2} \left(\frac{\partial \langle \tilde{u}_i \rangle}{\partial x_j} - \frac{\partial \langle \tilde{u}_j \rangle}{\partial x_i} \right) \\ \langle \tilde{s}_{ij}^* \rangle &= \langle \tilde{s}_{ij} \rangle - \frac{1}{3} \langle \tilde{s}_{kk} \rangle \delta_{ij}\end{aligned}\quad (3.24)$$

Figs. (3.21-a) and (3.21-d) plot the ratio of the SGS dissipation due to the fluctuating flowfield to the total SGS dissipation, respectively varying the SGS model and the grid resolution. Davidson (2009) [19] showed that the higher resolution is, the higher is the $\varepsilon'_{sgs}/\varepsilon_{sgs}$ ratio. Fig. (3.21-a) shows

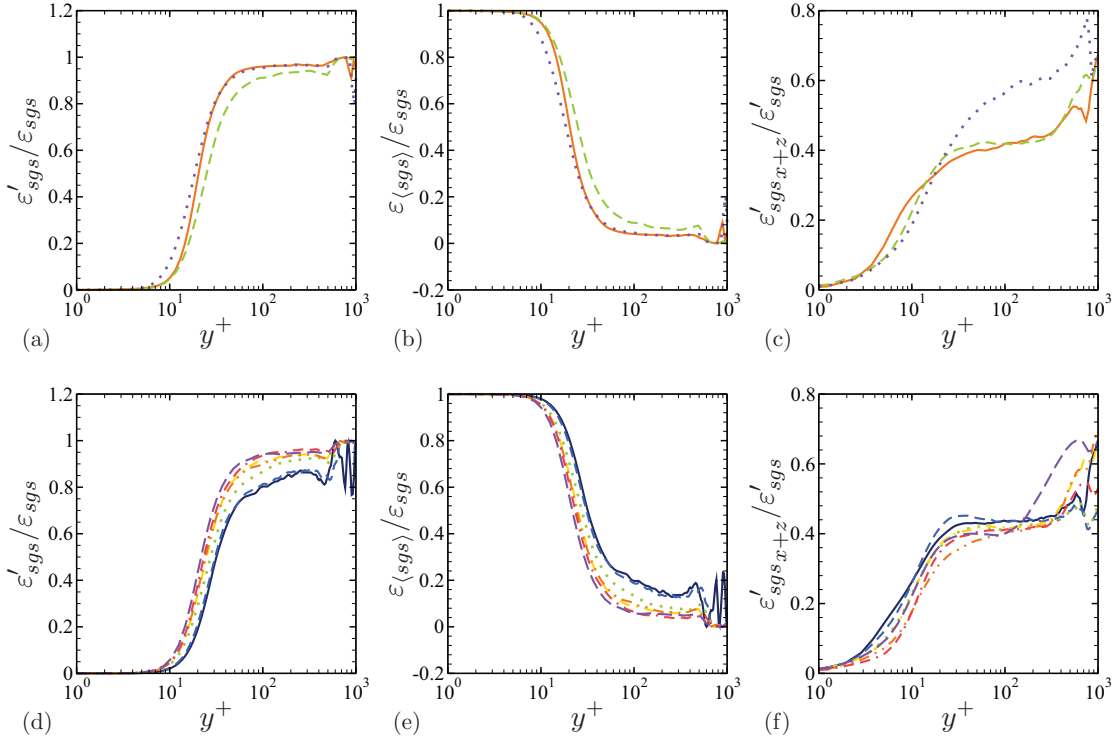


Figure 3.21: (a-d) Ratio of the SGS dissipation due to the fluctuating flowfield to the total SGS dissipation $\varepsilon'_{sgs}/\varepsilon_{sgs}$ as a function of y^+ ; (b-e) Ratio of the SGS dissipation due to the mean-averaged flowfield to the total SGS dissipation $\varepsilon_{\langle sgs \rangle}/\varepsilon_{sgs}$ as a function of y^+ ; (c-f) Ratio of the SGS dissipation due to the fluctuating flowfield in a wall-parallel plane to the total SGS dissipation due to the fluctuating flowfield $\varepsilon'_{sgs,x+z}/\varepsilon'_{sgs}$ as a function of y^+ . (a-b-c) SGS models study using LES-P2 grid; (d-e-f) Grid sensitivity study using CSM model. For legend, see table 3.4.

that, for the same given grid, the DSM model gives weakly better estimation of the ratio (barely 5%). $\varepsilon'_{sgs}/\varepsilon_{sgs}$ is very weak up to $y^+ \leq 10$ and increases steeply to reach its maximum at $y^+ \simeq 50$ for both models. However, it is shown in Fig. (3.21-d) that this ratio tends to monotonically increase when the grid is coarsen. For all the tested grids, the ratio varies between 0.85 and 0.95. In contrast to $\varepsilon'_{sgs}/\varepsilon_{sgs}$, $\varepsilon_{\langle sgs \rangle}/\varepsilon_{sgs}$ increases when coarsening the grid (Fig. 3.21-e).

Figs. (3.21-c) and (3.21-f) shows the ratio of the SGS dissipation due to the fluctuating flowfield in a wall-parallel plane $\varepsilon'_{sgs,x+z}$ to the total SGS dissipation due to the fluctuating flowfield ε'_{sgs} , respectively varying the SGS model and the grid resolution. The contribution of the resolved fluctuations in a wall-parallel plane varies between 0.4 for the CSM and the DSM models and 0.5 for the WALE model, in the outer region of the boundary layer. This contribution is also found

to be barely affected by the grid resolution. $\varepsilon'_{sgs,x+z}/\varepsilon'_{sgs}$ seems monotonically decreasing when the grid is coarsen, and the refinement in the spanwise direction is found to be more important.

3.4.4 Subgrid scale activity

The total SGS dissipation of a LES model, ε_{sgs} , is defined as the sum of both the SGS dissipation due to the fluctuating flowfield, ε'_{sgs} , and the one due to the mean-averaged flowfield, $\varepsilon_{\langle sgs \rangle}$.

The amount of turbulent dissipation is the central quantity used to assess the importance of the SGS model, i.e., to quantify the amount of modeling in a LES compared to a DNS (Geurts & Fröhlich, 2002) [35]. The SGS activity parameter is defined:

$$\varsigma = \frac{\varepsilon_{sgs}}{\varepsilon_{sgs} + \varepsilon} \quad (3.25)$$

where ε_{sgs} is the total SGS dissipation, defined as the sum of ε'_{sgs} and $\varepsilon_{\langle sgs \rangle}$, and ε is the molecular dissipation. It comes that $0 \leq \varsigma < 1$ by definition, with $\varsigma = 0$ corresponding to DNS and $\varsigma = 1$ to LES at infinite Reynolds number (Geurts & Fröhlich, 2002) [35].

Fig. (3.22) shows the SGS activity parameter ς as a function of y^+ , varying the SGS model (Figs. 3.22-a; 3.22-b; 3.22-c) and the grid resolution (Figs. 3.22-d; 3.22-e; 3.22-f). In the viscous sublayer and up to $y^+ \simeq 5$, SGS activity parameter ς is about 0.8 for all SGS models, and seems slightly over-predicted by the DSM model, compared to CSM and WALE models, reaching a maximum of 0.84 at the wall. In this region, ς seems weakly affected by the grid resolution, and all studied grids predict a value of 0.8 at the wall. In the transition region and up to $y^+ \simeq 300$, ς decreases otherwise for different SGS models, to reach a minimum of 0.5 for DSM for $y^+ \simeq 200$, 0.4 for the WALE model and 0.4 for the CSM model at $y^+ \simeq 300$. Same behavior is also observed for the different grids, where ς seems unaffected by the grid resolution. ς increases again in the outer region of the boundary layer, reaching a maximum of about 0.6 for the DSM model, 0.6 for the WALE model and 0.4 for the CSM model, to decrease again at the edge of the boundary layer. In this region, ς shows a monotone increase when coarsening the grid, with a maximum of 0.2 for LES-L1 grid to 0.5 for LES-S2 using the CSM model.

Fig. (3.22-b; 3.22-e) show the SGS activity parameter, ς'_{sgs} , due to the fluctuating flowfield and Figs. (3.22-c; 3.22-f) the SGS activity parameter $\varsigma_{\langle sgs \rangle}$ due to the mean-averaged flowfield, defined

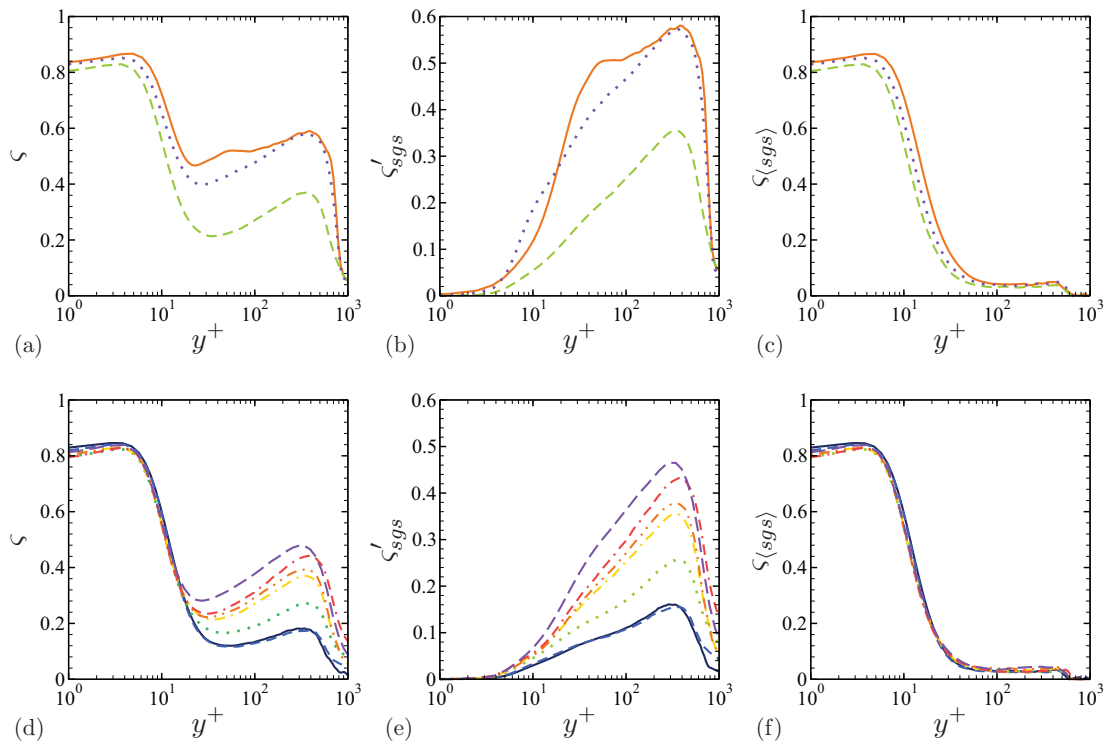


Figure 3.22: SGS Activity parameter ζ as a function of y^+ . (a-b-c) SGS models study using LES-P2 grid; (d-e-f) Grid sensitivity study using CSM model. For legend, see table 3.4.

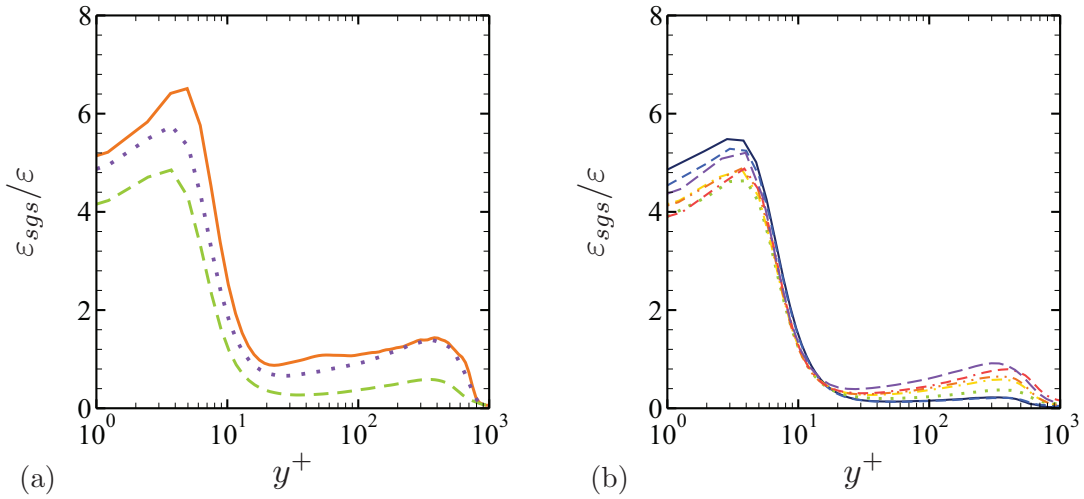


Figure 3.23: Ratio of the SGS dissipation to the viscous dissipation as a function of y^+ . (a) SGS models study using LES-P2 grid; (b) Grid sensitivity study using CSM model. For legend, see table 3.4.

by:

$$\begin{aligned}\varsigma_{(sgs)} &= \frac{\varepsilon_{(sgs)}}{\varepsilon_{(sgs)} + \varepsilon} \\ \varsigma'_{sgs} &= \frac{\varepsilon'_{sgs}}{\varepsilon'_{sgs} + \varepsilon}\end{aligned}\quad (3.26)$$

From Figs. (3.22-b; 3.22-e) and Figs. (3.22-c; 3.22-f), it can be deduced that the SGS dissipation is mainly driven by viscous effects in a near-wall region (up to $y^+ \simeq 10$), while the fluctuating flow-field mainly acts in the transition region and up to the edge of the boundary layer ($10 \leq y^+ \leq 1000$). From Figs. (3.22-a; 3.22-b; 3.22-c), it can be concluded that the DSM model seems more dissipative than both the CSM and the WALE models, especially in the outer region of the boundary layer, and referring to the definition of the SGS activity parameter, ς , the DSM model behaves better than the CSM model, in a way that it is higher for the same grid resolution. For the WALE model, ς'_{sgs} is very close to that of the DSM model throughout the layer.

A direct comparison of μ_{sgs} and μ can also be interesting. Davidson (2006) [20] suggested that, if $\mu_{sgs} \gg \mu$, the SGS dissipation is much larger than the viscous one, and if this is not the case, the grid is more likely to be a DNS grid. At $y^+ > 10$ (Fig. 3.23), the ratio of $\varepsilon_{sgs}/\varepsilon \leq 1$ in a wide range of the boundary layer, and thus $\mu_{sgs} \approx \mu$, which means that the considered grids are suitable for LES study.

3.5 Thermodynamic properties and Strong Reynolds Analogy

Figs. (3.24-a; 3.24-b; 3.24-c) shows the cross-stream distribution of the normalized *r.m.s* of some thermodynamic quantities with varying SGS models and Figs. (3.24-d; 3.24-e; 3.24-f) with varying the grid resolutions. Overall, the results show similar levels of these quantities when varying the SGS models. The *r.m.s* of temperature fluctuations, T_{rms} , exhibits a peak near the wall ($y/\delta \simeq 0.05$) where it reaches a maximum of 9% of T_∞ and decreases then up to a level of 2% of T_∞ outside the boundary layer. The same trend is also observed for the *r.m.s* of density fluctuations, ρ_{rms} , which exhibits a peak of $\approx 4.5\%$ of ρ_∞ in the same region, but continues to increase reaching a level of $\approx 5.5\%$ at $y/\delta \simeq 0.8$, to finally decrease to 2% of ρ_∞ outside the layer. At the wall, the *r.m.s* of the pressure fluctuations, p_{rms} , reaches a maximum of 3.75% of p_∞ for the Implicit LES, and decreases within the layer reaching 0.5% near the edge of the boundary layer. For the ILES, a bump of T_{rms} and ρ_{rms} is present in the outer region of the boundary layer $y/\delta > 0.2$, probably due to a lack of SGS energy dissipation in this region. All *r.m.s* quantities show a monotone increase when coarsening the grid. The observed bump was also found to be sensitive to the grid resolution, since it is also observed for the less y -direction refined grid (namely the LES-S2 grid), which can confirm an accumulation of non-dissipated energy in this region of the layer.

For an adiabatic supersonic turbulent boundary layer, it is commonly known that u' and T' are supposed to be perfectly anti-correlated and that the *Strong Reynolds Analogy* relation, linking the *r.m.s* of temperature and velocity fluctuations, is nearly equal to 1. By definition, the *r.m.s* of temperature fluctuations is defined by:

$$\langle T'T' \rangle = \left(\frac{\gamma - 1}{R\gamma} \right)^2 \langle u \rangle^2 \langle u'u' \rangle + 2\langle T'T'_t \rangle - \langle T'_t T'_t \rangle \quad (3.27)$$

where T'_t is the total temperature fluctuations.

If it is assumed that the following condition holds (Guarini *et al.*, 2000 [38]; Pirozzoli *et al.*, 2004 [76]):

$$\frac{\langle T'T' \rangle}{\langle T \rangle^2} \gg \frac{\langle T'_t T'_t \rangle - 2\langle T'T'_t \rangle}{\langle T \rangle^2} \quad (3.28)$$

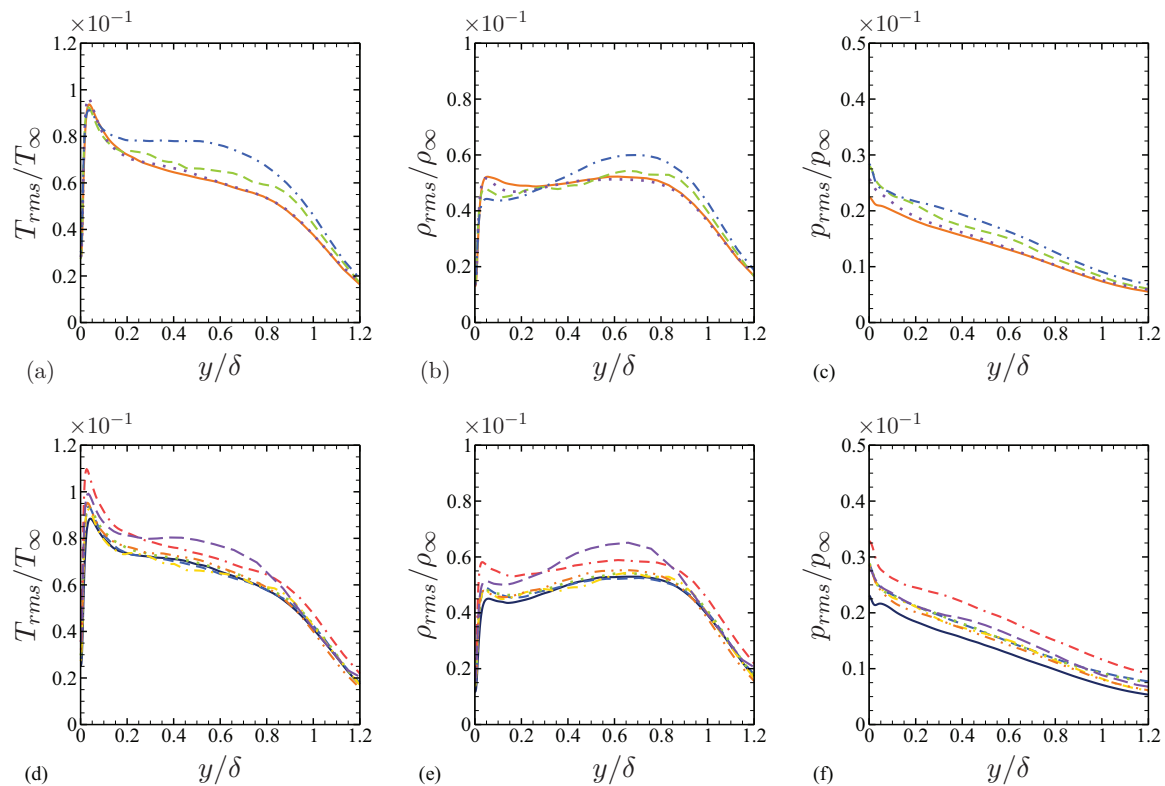


Figure 3.24: Normalized r.m.s. of the thermodynamic quantities as a function of y/δ . (a-b-c) SGS models study using LES-P2 grid; (d-e-f) Grid sensitivity study using CSM model. For legend, see table 3.4.

Eq. (3.27) is then written:

$$\langle T'T' \rangle^{1/2} \approx \frac{\gamma - 1}{\mathcal{R}\gamma} \langle u \rangle \langle u'u' \rangle^{1/2} \quad (3.29)$$

and the R_{uT} and R_{uv} correlations are written as:

$$R_{uT} = -1 + \frac{\langle T'_t T_t' \rangle}{2 \langle T'T' \rangle} \quad (3.30)$$

$$R_{uv} = -R_{vT} \left(1 - \frac{\langle v'T_t' \rangle}{\langle v'T' \rangle} \right) \quad (3.31)$$

Finally, if the total temperature is supposed uniform and the total temperature fluctuations are neglected (which is not necessary the case as shown in fig. 3.9), the SRA and the velocity-temperature correlation R_{uT} are then written:

$$\begin{aligned} \text{SRA} &= \frac{\sqrt{\langle T'T' \rangle} / \langle T \rangle}{(\gamma - 1) M_\infty^2 \sqrt{\langle u'u' \rangle} / \langle u \rangle} \approx 1 \\ R_{uT} &= \frac{\langle u'T' \rangle}{\sqrt{\langle u'u' \rangle} \sqrt{\langle T'T' \rangle}} \approx -1 \end{aligned} \quad (3.32)$$

where $\langle M \rangle = \langle u \rangle / \langle c \rangle$ is the local Mach number.

The SRA is found to be sensitive to the SGS model: for instance, the DSM and the WALE models under-predict the SRA (≈ 0.9 , while the Implicit LES over-predict it (≈ 1.1). The CSM model however estimates a value of $\text{SRA} \approx 1$ in almost all the boundary layer. The SRA is also found to be weakly sensitive to the grid resolution, with a slight increase of the value towards the coarser grid.

Previous reported computations predicted lower values of $-R_{uT}$, ranging between ≈ 0.55 and 0.8 (Pirozzoli *et al.*, 2004 [76]; Duan *et al.*, 2010 [23]; Pirozzoli & Bernardini, 2011 [74]). In the present simulations, $-R_{uT}$ lays between 0.5 and 0.6 at the outer region of the boundary layer $0.2 < y/\delta < 0.8$, and rises to 0.8 at $y/\delta \simeq 0.02$, where the models predict almost the same value. The velocity-temperature correlation $-R_{uT}$ is found to be slightly sensitive to the grid resolution, decreasing monotonically when coarsening the grid. At the vicinity of the boundary layer, $-R_{uT}$ drops rapidly, a feature that was not obvious in previous DNS studies, except in Guarini *et al.* (2000) [38] and Pirozzoli & Bernardini (2011) [74]. This weak anti-correlation between u' and T'

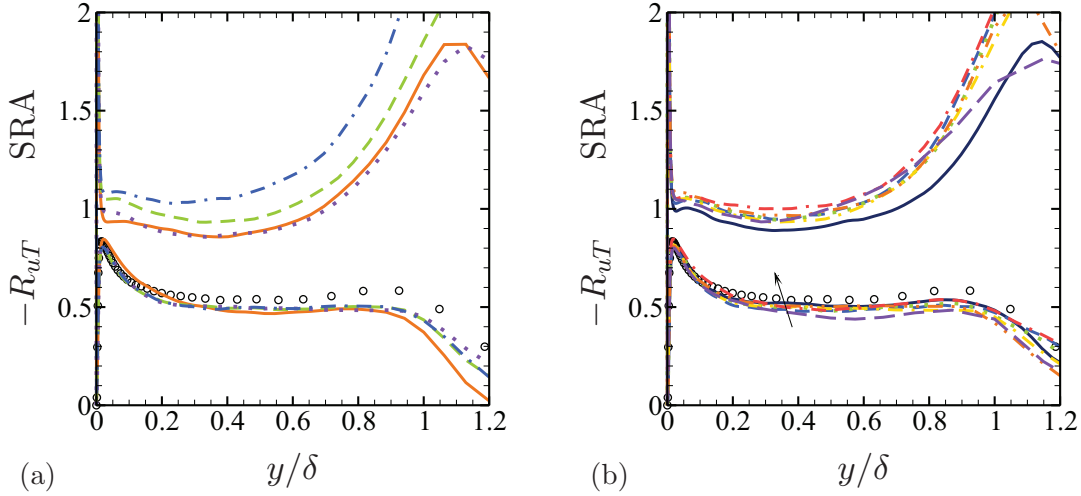


Figure 3.25: SRA and $-R_{uT}$ correlations as a function of y/δ . Circle: Pirozzoli *et al.* (2004) [76]. (a) SGS models study using LES-P2 grid; (b) Grid sensitivity study using CSM model. For legend, see table 3.4.

can be due to the non-negligible total-temperature fluctuations within the boundary layer (Pirozzoli *et al.*, 2004 [76]; Pirozzoli & Bernardini, 2011 [74]).

For isothermal supersonic turbulent boundary layers, an extended form of the SRA, which accounts for the heat flux at the wall, is available. The extended form of the SRA, proposed by Cebeci & Smith (1974) [13], is written as:

$$\text{ESRA} = \frac{\sqrt{\langle T' T' \rangle / \langle T \rangle}}{(\gamma - 1) M_\infty^2 \sqrt{\langle u' u' \rangle / \langle u \rangle}} \approx - \left(1 + \frac{T_w - T_{t\infty}}{\langle T \rangle} \frac{\langle u \rangle}{u_\infty} \right) \quad (3.33)$$

Other forms of SRA, proposed by Gaviglio (1987) [33] and Huang *et al.* (1995) [43], are also available, respectively named GSRA and HSRA. They write:

$$\frac{\sqrt{\langle T' T' \rangle / \langle T \rangle}}{(\gamma - 1) M_\infty^2 \sqrt{\langle u' u' \rangle / \langle u \rangle}} \approx \frac{1}{\beta} \left(1 - \frac{\partial \langle T_t \rangle}{\partial \langle T \rangle} \right)^{-1} \quad (3.34)$$

where $\beta = 1$ and $\beta = \text{Pr}_t$, respectively. One should note that $\text{Pr}_t = 0.9$ is used to plot this formula.

It is found that the classical SRA correlation better predicts the anti-correlation between u' and T' , compared to the modified forms, which predict a lower values of the SRA. It is quite reasonable since those relations are adapted to flows with significant heat exchanges.

Considering a polytropic behavior of the thermodynamic quantities (Lechner *et al.*, 2001) [57],

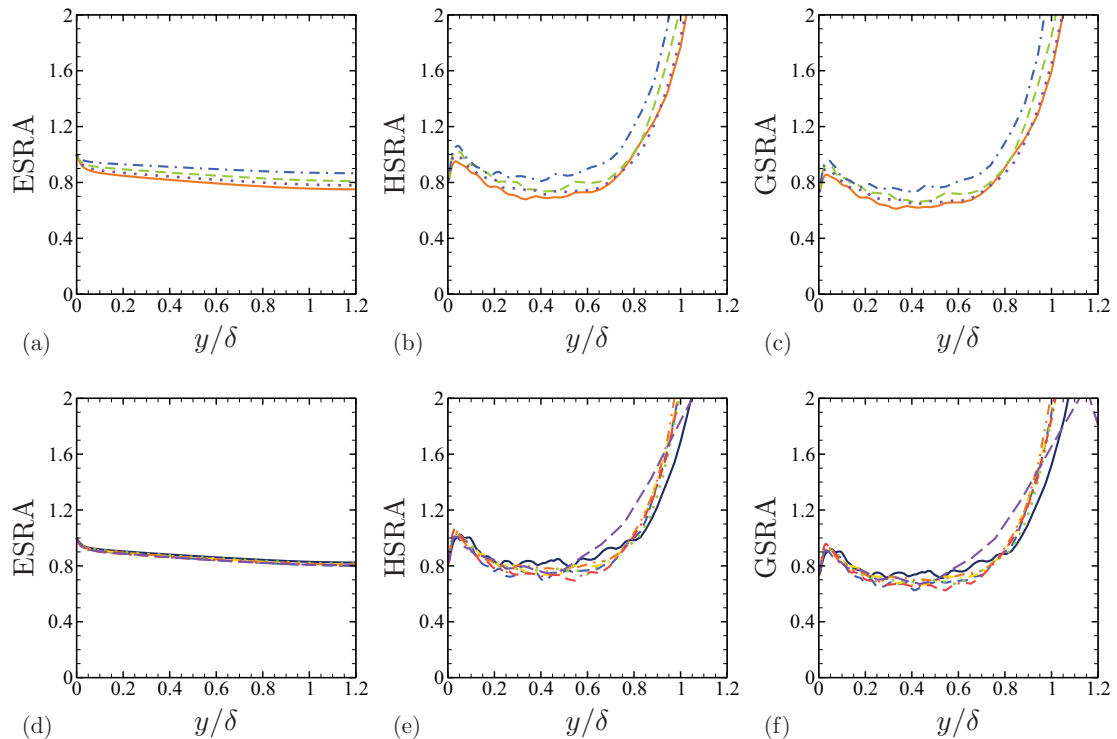


Figure 3.26: Modified SRA as a function of y/δ . (a, b, c) SGS models study using LES-P2 grid; (d, e, f) Grid sensitivity study using CSM model. For legend, see table 3.4.

the relationship between the density and the temperature fluctuations are as follows:

$$R_{\rho T} = \frac{\langle \rho' T' \rangle}{\sqrt{\langle \rho' \rho' \rangle} \sqrt{\langle T' T' \rangle}} \approx \frac{\sqrt{\langle \rho' \rho' \rangle} \langle T' \rangle}{\sqrt{\langle T' T' \rangle} \langle \rho' \rangle} = -1 \quad (3.35)$$

In a wide region of the boundary layer (see Fig. 3.27), ρ' and T' are anti-correlated, and $-R_{\rho T}$ weakly exceeds unity (≈ 1.1). The correlation $-R_{\rho T}$ is also found to be insensitive to the SGS models as well as to grid resolutions. The $-R_{uv}$ correlation's behavior (Fig. 3.27) is also consistent with theoretical observations: constant in the region $0.1 \leq y/\delta \leq 0.8$ and then decrease above this region (Spina *et al.*, 1994) [93]. At $0.2 < y/\delta < 0.8$, all models show trends, regardless of the grids ($0.45 < -R_{uv} < 0.5$). As it has been observed by Pirozzoli *et al.* (2004) [76], $-R_{uv}$ and R_{vT} are found to be fairly correlated, and nearly equal to ≈ 0.5 in the outer-region of the boundary layer ($0.2 < y/\delta < 0.8$). These results are also in good agreement with the subsonic experimental data of Klebanoff ($-R_{uv} \approx 0.5$). The influence of the mesh and the SGS model on R_{vT} in this region is weak.

The resolved turbulent Prandtl number Pr_t is defined as:

$$\begin{aligned} \text{Pr}_t &= \frac{\langle \rho u' v' \rangle \partial \langle T \rangle / \partial y}{\langle \rho v' T' \rangle \partial \langle u \rangle / \partial y} \\ &= \left(1 - \frac{\langle \rho v' T'_t \rangle}{\langle \rho v' T' \rangle} \right) \left(1 - \frac{\partial \langle T_t \rangle}{\partial \langle T \rangle} \right)^{-1} \end{aligned} \quad (3.36)$$

Assuming a uniform total temperature in Eq. (3.36) yields to $\text{Pr}_t = 1$. Fig. (3.28) shows that this assumption is not satisfied, where in a wide region of the boundary layer $y/\delta > 0.2$, $\text{Pr}_t < 0.8$. Pirozzoli & Bernardini (2011) [74] also found values of $\text{Pr}_t < 0.8$ at $y/\delta > 0.4$. This tendency is accentuated when coarsening the grid, where Pr_t shows a monotone decrease.

Pirozzoli *et al.* (2004) [76] proposed a curve fitting of their supersonic boundary layer DNS data at $\text{Re}_{\delta_2} \approx 2400$ in the region $0.2 < y/\delta < 0.8$:

$$\text{Pr}_t \approx 0.783 - 0.094 \left(\frac{y}{\delta} \right)^2 \quad (3.37)$$

It is found that the present results slightly under-estimate this curve-fitting with a maximum error of 12%. With refining the grid resolution, this error is minimized (LES-L1 grid).

Taking into account the fact that R_{uv} and R_{vT} are strongly anti-correlated, it is possible to

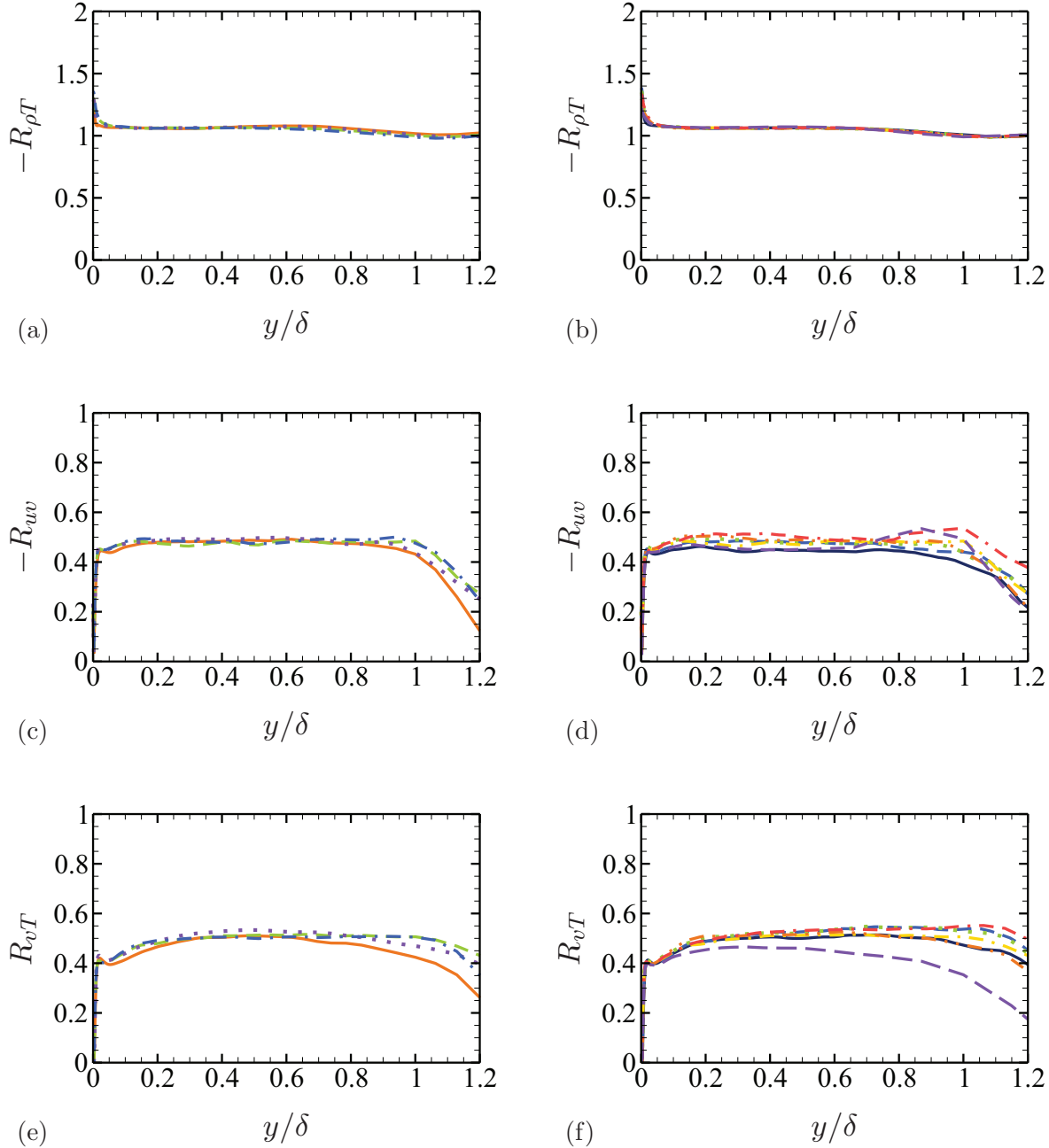


Figure 3.27: $-R_{\rho T}$, $-R_{uv}$ and R_{vT} correlations as a function of y/δ . (a, c, e) SGS models study using LES-P2 grid; (b, d, f) Grid sensitivity study using CSM model. For legend, see table 3.4.

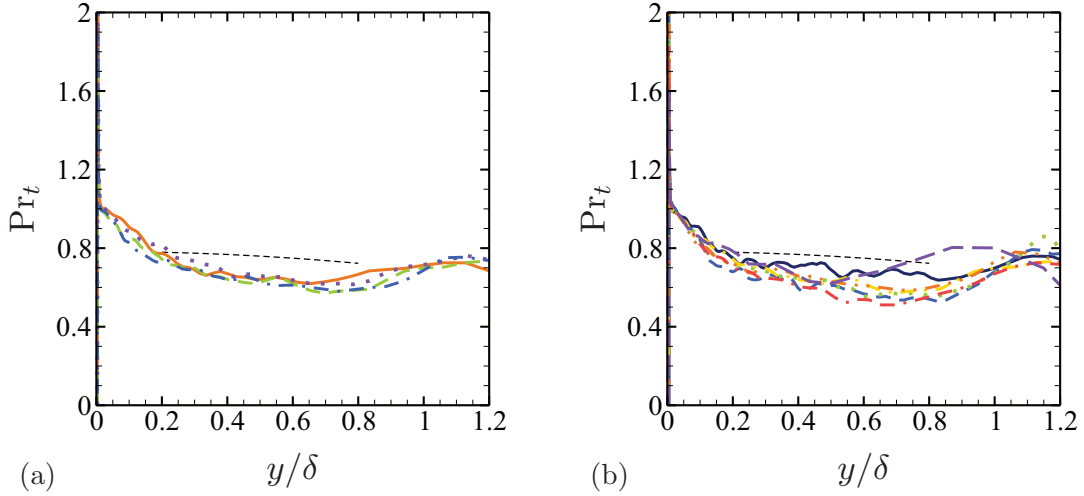


Figure 3.28: Resolved turbulent Prandtl number as a function of y/δ . (--) DNS curve-fitting in Eq. (3.37). (a) SGS models study using LES-P2 grid; (b) Grid sensitivity study using CSM model. For legend, see table 3.4.

write Pr_t as:

$$\text{Pr}_t \approx \left(1 - \frac{\partial \langle T_t \rangle}{\partial \langle T \rangle} \right)^{-1} \quad (3.38)$$

Eq. (3.38) is known as Huang's SRA relation (Huang *et al.*, 1995) [43].

Fig. (3.29) shows that this assumption is also not verified, except for the DSM model at $y/\delta < 0.3$ and the WALE model at $y/\delta < 0.2$, but that the maximum error does not exceed 15% for the CSM model at $y/\delta < 0.4$.

3.6 Instantaneous scatter plots

Scatter plots of fluctuating variables display fluctuations extracted each time-step at a given streamwise and wall-parallel position ($1 \times 1 \times 64$) of the computational domain. In the following, the analysis is made using the CSM-P2 test-case (see table 3.1).

The objective behind the analysis of the *Strong Reynolds Analogy* is to verify the applicability of the Morkovin's hypothesis. Reynolds Analogies in supersonic flows imply that the total temperature fluctuations are negligible and the turbulent Prandtl number is one. In particular, this yields to

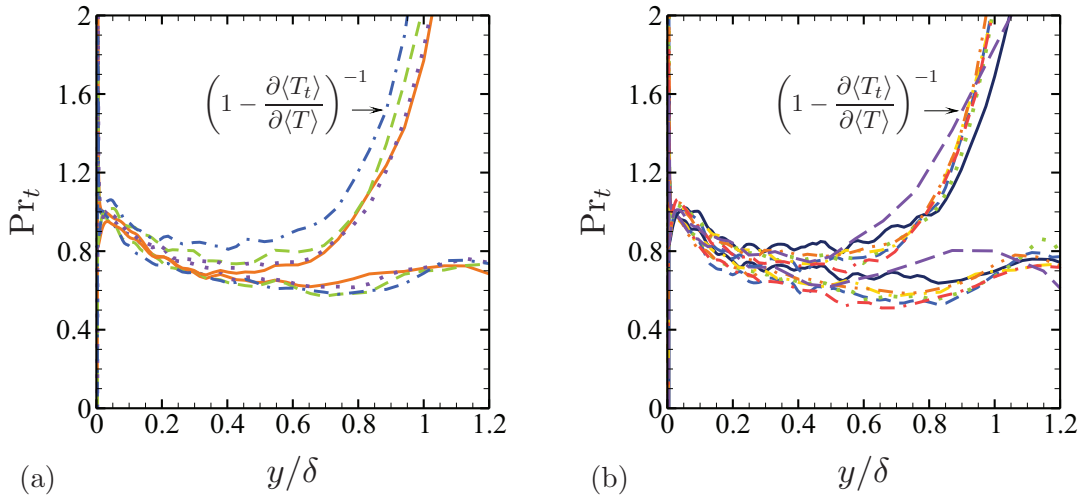


Figure 3.29: Resolved turbulent Prandtl number Pr_t and Huang's relation (Eq. 3.36) as a function of y/δ . (a) SGS models study using LES-P2 grid; (b) Grid sensitivity study using CSM model. For legend, see table 3.4.

the following relations:

$$\frac{\sqrt{\langle T' T' \rangle} / \langle T \rangle}{(\gamma - 1) M_\infty^2 \sqrt{\langle u' u' \rangle} / \langle u \rangle} \simeq 1, \quad -R_{uT} \simeq 1 \quad (3.39)$$

Note that Spina *et al.* (1994) [93] reported that the correlation coefficient $-R_{uT}$ is rather close to 0.8 or 0.9.

However, it is interesting to test the validity of the *strict* SRA assumption for the instantaneous quantities. For instance, the relation between the instantaneous temperature and velocity fluctuations is given by:

$$C_p T' + \langle u \rangle u' = 0 \quad (3.40)$$

This can be rewritten as:

$$\frac{T'}{\langle T \rangle} = -(\gamma - 1)\langle M \rangle^2 \frac{u'}{\langle u \rangle} \quad (3.41)$$

where $\langle M \rangle = \langle u \rangle / \langle c \rangle$ is the local Mach number.

Fig. (3.30) depicts scatter plots of the normalized temperature - velocity fluctuations. It shows

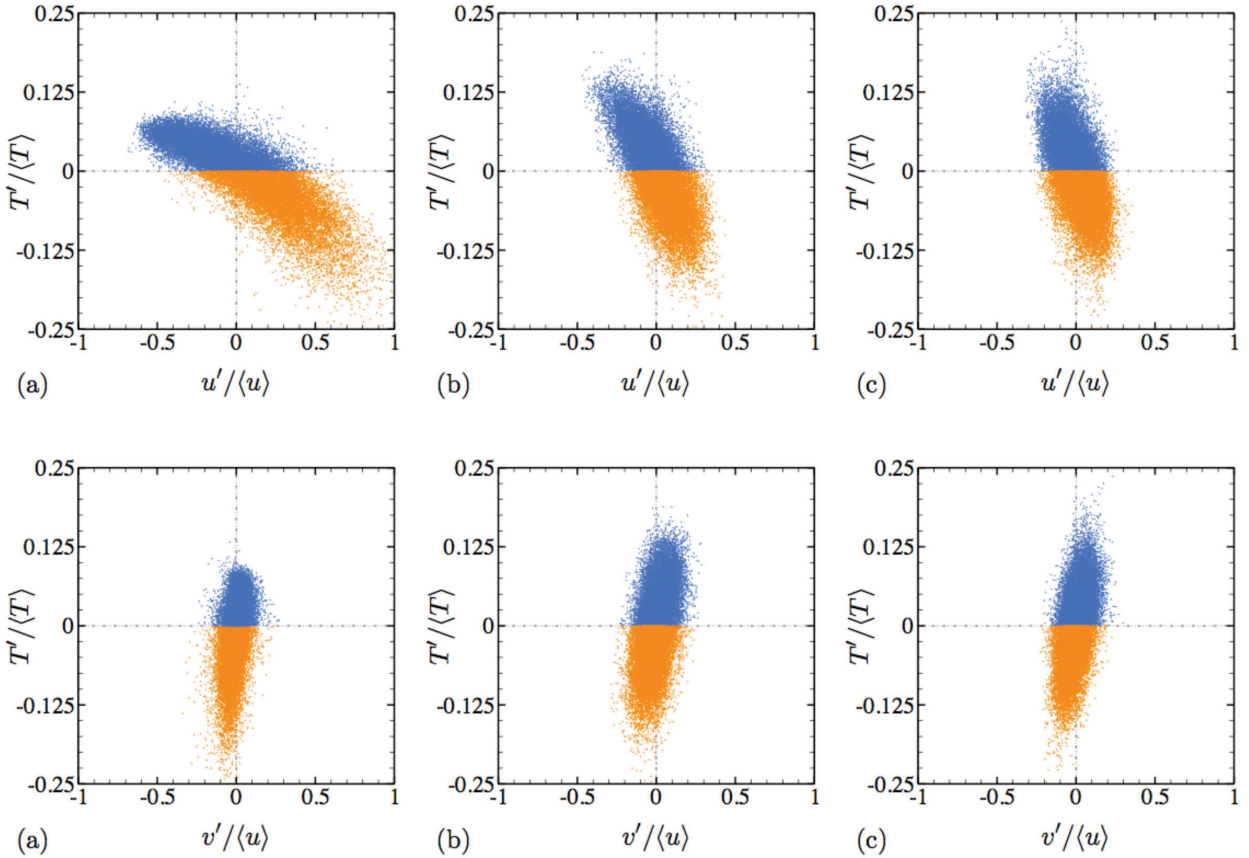


Figure 3.30: Scatter plots of (a-c) the normalized temperature - streamwise velocity fluctuations and (d-f) the normalized temperature - wall-normal velocity fluctuations in a wall-normal plane for the CSM-P2 case. (a, d) $y^+ \simeq 9$; (b, e) $y^+ \simeq 28$; (c, f) $y^+ \simeq 100$.

that the instantaneous temperature and streamwise velocity fluctuations are highly correlated, while a weak correlation links the instantaneous temperature and wall-normal velocity fluctuations.

As it can be seen in Fig. (3.31), the scatter plots of the Eq. (3.41) are found to barely hold for the *strict* SRA. A linear curve-fitting of the scatter plots shows a gradually decreasing from slope 0.86 close to the wall ($y^+ \simeq 9$) to 0.52 in the Log-region ($y^+ \simeq 100$).

Rubesin (1990) [79], Huang *et al.* (1995) [43] and Lechner *et al.* (2001) [57] assuming a polytropic behavior of the thermodynamic fluctuations, wrote:

$$\frac{p'}{\langle p \rangle} = n \frac{\rho'}{\langle \rho \rangle} = \frac{n}{n-1} \frac{\rho T'}{\langle \rho \rangle \langle T \rangle} \quad (3.42)$$

It follows that $(n-1)\rho'/\langle \rho \rangle \approx T'/\langle T \rangle$ and that $R_{\rho T} = -1$, where $n = 0$ is found to be an excellent

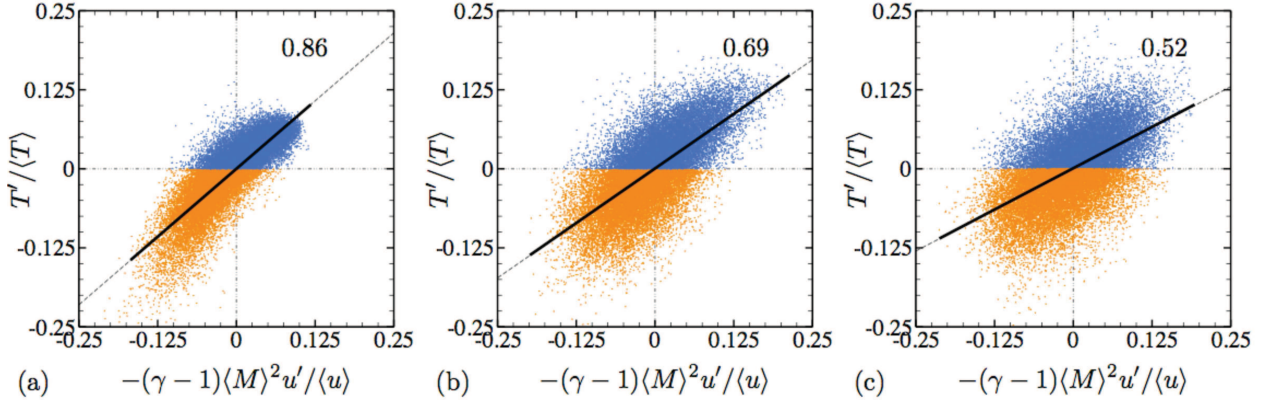


Figure 3.31: Scatter plots of the *strict* SRA in a wall-normal plane for the CSM-P2 case. (a) $y^+ \simeq 9$; (b) $y^+ \simeq 28$; (c) $y^+ \simeq 100$.

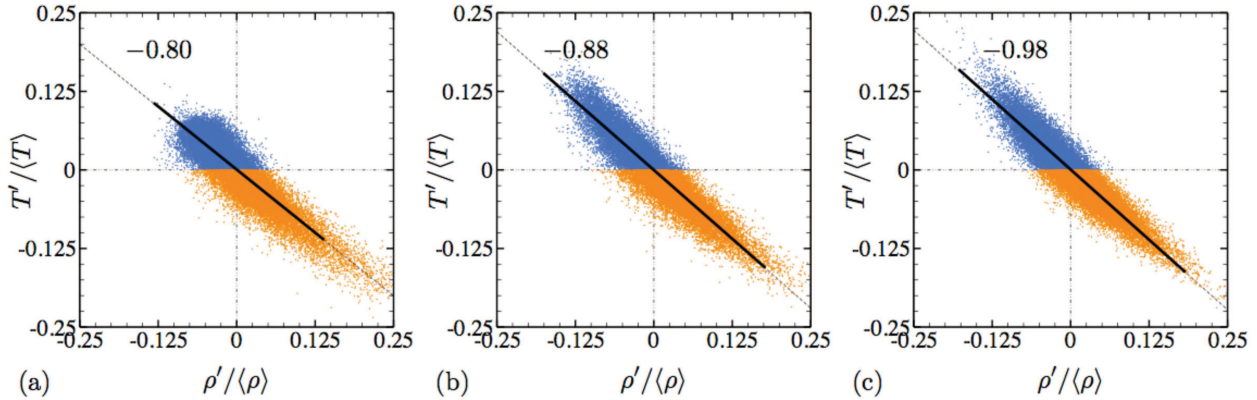


Figure 3.32: Scatter plots of the normalized temperature - density fluctuations in a wall-normal plane for CSM-P2 case. (a) $y^+ \simeq 9$. (b) $y^+ \simeq 28$. (c) $y^+ \simeq 100$.

agreement with the near-wall behavior of supersonic turbulent channel flows (Coleman *et al.*, 1995 [15]; Lechner *et al.*, 2001 [57]).

Fig. (3.32) shows scatter plots of normalized temperature fluctuations $T'/\langle T \rangle$ against normalized density fluctuations. At $y^+ \simeq 9$, $R_{\rho T}$ is found to be less than 1, and the relation $(n - 1)\rho' / \langle \rho \rangle \approx T' / \langle T \rangle$ seems better verified as the distance from the wall increases, reaching 0.98 at $y^+ \simeq 100$.

Fig. (3.33) shows that the pressure fluctuations are weakly unimportant compared to the density fluctuations, which confirm the validity of the Eq. (3.42) in the current study.

Using the entropy relation $s = C_v \log(p/\rho^\gamma)$ and assuming a linear relationship between the

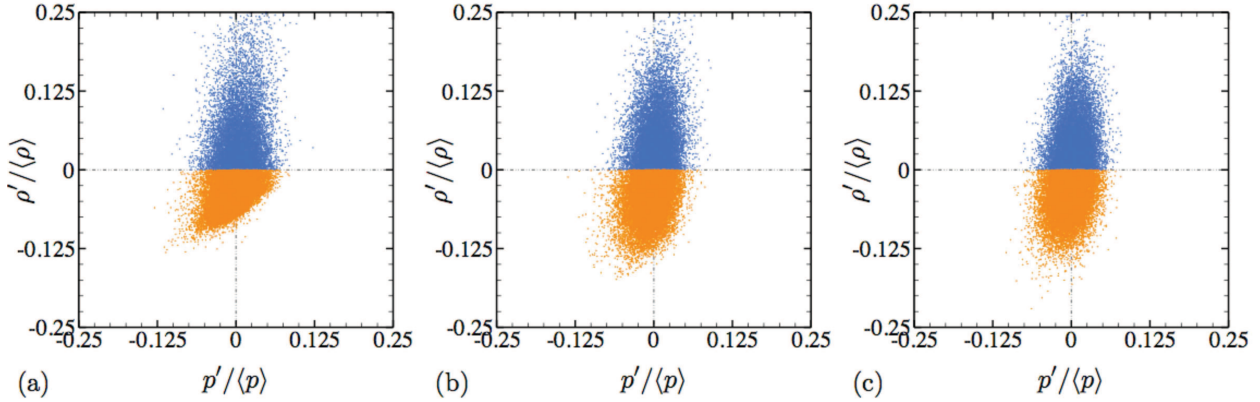


Figure 3.33: Scatter plots of the normalized density - pressure fluctuations in a wall-normal plane for CSM-P2 case. (a) $y^+ \approx 9$; (b) $y^+ \approx 28$; (c) $y^+ \approx 100$.

thermodynamic fluctuations, it comes that:

$$\frac{s'}{C_v} = -(\gamma - 1) \frac{\rho'}{\langle \rho \rangle} + \frac{T'}{\langle T \rangle} = -\gamma \frac{\rho'}{\langle \rho \rangle} + \frac{p'}{\langle p \rangle} = \gamma \frac{T'}{\langle T \rangle} - (\gamma - 1) \frac{p'}{\langle p \rangle} \quad (3.43)$$

If we neglect the pressure fluctuations in the near-wall region, we can write:

$$\frac{s'}{C_v} = -\gamma \frac{\rho'}{\langle \rho \rangle} = \gamma \frac{T'}{\langle T \rangle} \quad (3.44)$$

Scatter plots of the entropy fluctuations as a function of the density fluctuations Figs. (3.34-a; 3.34-b; 3.34-c) and pressure fluctuations Figs. (3.34-a; 3.34-b; 3.34-c) in a wall-normal plane are presented. A linear fitting of the values shows that the slope of the (s', ρ') scatter plot is -1.12 in a very near-wall region ($y^+ \approx 9$), and it increases until reaching -1.25 at $y^+ \approx 100$. The scatter plot relating the entropy fluctuations to the pressure fluctuations (3.34-d; 3.34-e; 3.34-f) shows also that the pressure fluctuations can weakly be neglected, which probably deviates the previous scatter plot from the theoretical slope ($\sim -\gamma$).

Scatter plots of the total temperature fluctuations as a function of the temperature and velocity fluctuations are presented in Fig. (3.35). It shows that an instantaneous quadratic relationship exists between the total and the static temperature fluctuations. Similar relation is also found with the streamwise velocity component.

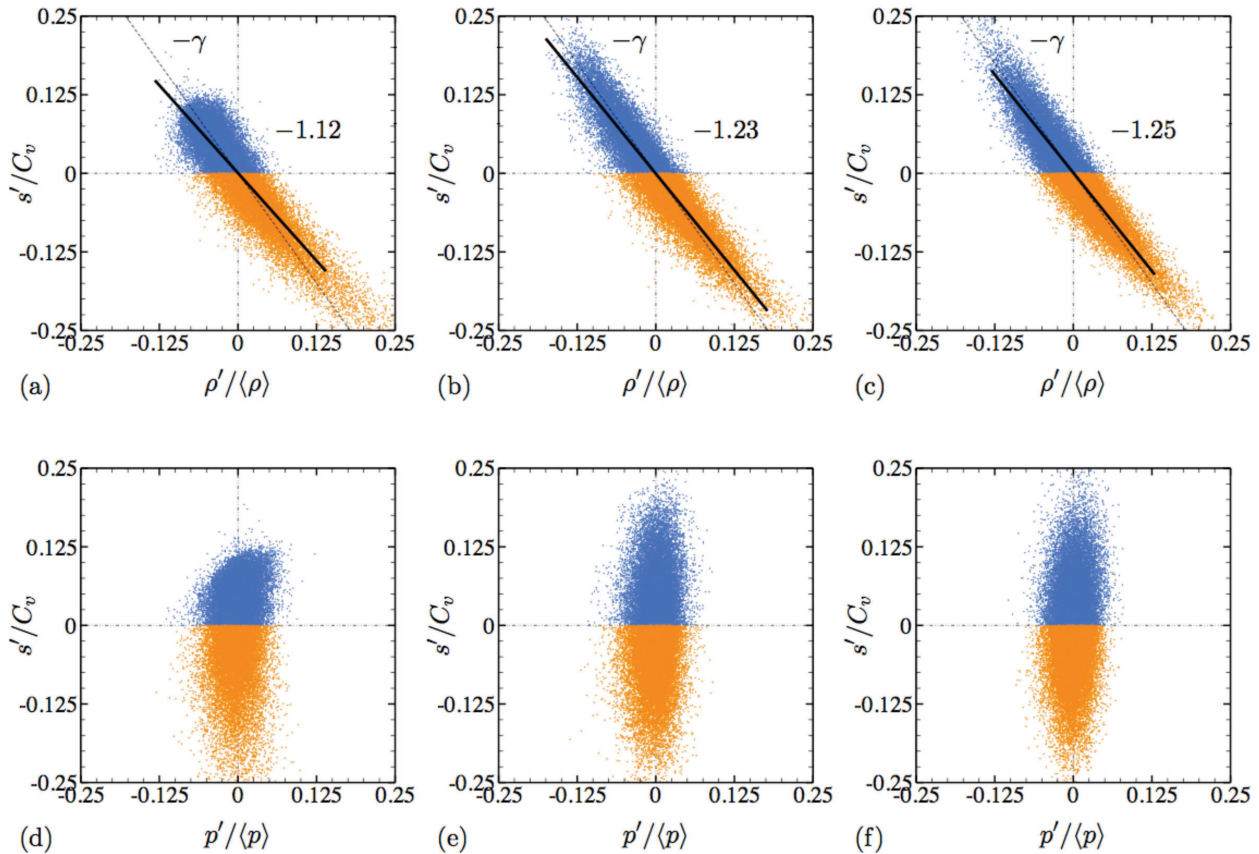


Figure 3.34: Scatter plots of (a-c) the normalized entropy-density fluctuations and (d-f) the normalized entropy-pressure fluctuations in a wall-normal plane for CSM-P2 case. (a, d) $y^+ \simeq 9$; (b, e) $y^+ \simeq 28$; (c, f) $y^+ \simeq 100$.

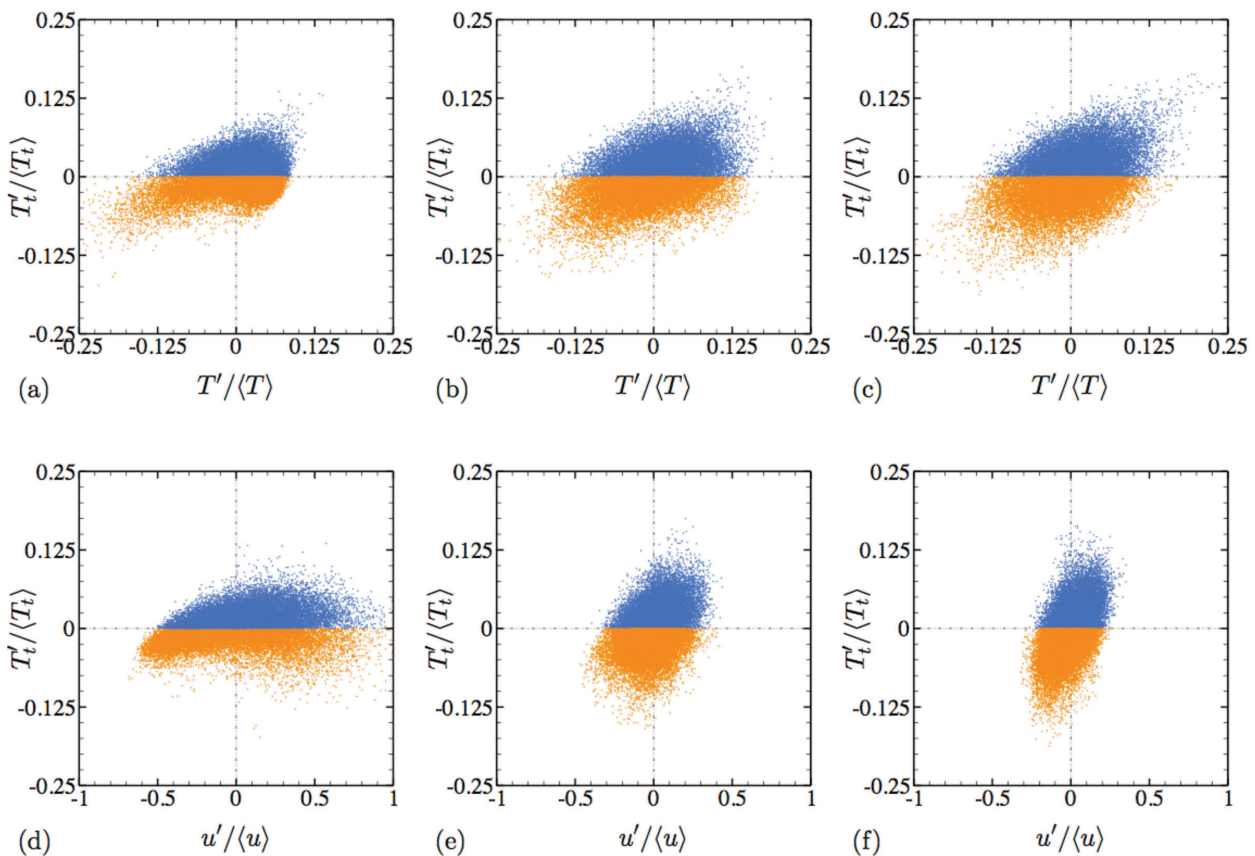


Figure 3.35: Scatter plots of (a-c) the normalized total-temperature - temperature fluctuations and (d-f) the normalized total temperature - velocity fluctuations in a wall-normal plane for the nearly-adiabatic CSM-P2 case. (a, d) $y^+ \simeq 9$; (b, e) $y^+ \simeq 28$; (c, f) $y^+ \simeq 100$.

3.7 Turbulence behavior

3.7.1 Anisotropy invariants map

The behavior of turbulent wall-bounded flows can be analyzed by examining the evolution of anisotropy through the turbulent stresses, $\langle u'_i u'_j \rangle$, which can be qualified using the anisotropy tensor, defined as $a_{ij} = \langle u'_i u'_j \rangle - 2K\delta_{ij}/3$, where δ_{ij} is the Kronecker tensor. The normalized anisotropy tensor, $b_{ij} = a_{ij}/2K$, is then simply defined:

$$b_{ij} = \frac{\langle u'_i u'_j \rangle}{2K} - \frac{1}{3}\delta_{ij} \quad (3.45)$$

The anisotropy tensor has three invariants, the first being simply the trace of the tensor and is zero by definition. Therefore, any turbulent state can be fully characterized by the second and the third invariants, given by:

$$\begin{aligned} \text{II} &= b_{ij}b_{ji} = \frac{1}{2}b_{ii}^2 \\ \text{III} &= b_{ij}b_{jk}b_{ki} = \frac{1}{3}b_{ii}^3 \end{aligned} \quad (3.46)$$

In the map shown in Fig. (3.36), point C_1 represents perfectly isotropic turbulence, where $\text{II} = \text{III} = 0$. Point C_2 is two-components isotropic turbulence limit, where $\text{II} = 1/12$ and $\text{III} = -1/108$, and C_3 is one-component turbulence limit, where $\text{II} = 1/3$ and $\text{III} = 2/27$. The upper boundary C_2C_3 represents two-dimensional turbulence, while the two lower bounds C_1C_2 and C_1C_3 correspond to axisymmetric compression and expansion turbulence, respectively.

According to Lumley (1978) [61], any realizable quantity associated with the fluctuating field must be within the anisotropy map or on its boundaries (C_1C_2 , C_1C_3 and C_2C_3). An analysis of the variation of these points and curves in the anisotropy-invariants map can help to highlight the change of the turbulence state.

As it can be seen from Fig. (3.37), the computed anisotropy maps for different models and grids lie inside the theoretical map, showing basically the same trends. Very close to the wall, the wall-normal fluctuation component, $\langle v'^2 \rangle$, is quickly vanishing compared to the other two components, $\langle u'^2 \rangle$ and $\langle w'^2 \rangle$, making the turbulence state approximately two-dimensional. Here, the two-dimensionality means a two-component flow because $\langle u'^2 \rangle$ and $\langle w'^2 \rangle$ vary in the y -direction

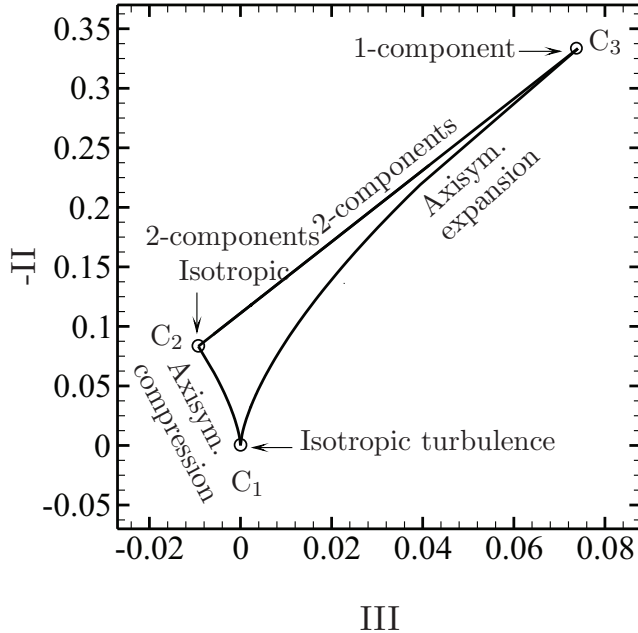


Figure 3.36: Anisotropy invariants map.

(Pope, 2000) [77]. Moving progressively inside the boundary layer, a state of an axisymmetric expansion is observed up to the outer edge of the boundary layer ($y \simeq \delta$), where the turbulence state is near-isotropic, and thus located near the origin of the map. This behavior of the turbulence is well reproduced by the current simulations in accordance with previous studies (Krogstad & Torbergse, 2000 [52]; Shahab *et al.*, 2011 [84]).

3.7.2 Skewness and flatness factors

Higher-order moments such as the skewness and the flatness factors of the velocity fluctuations can be analyzed for better understanding the turbulence nature from statistics view-point.

The skewness and flatness coefficients of a given velocity fluctuation are defined as:

$$\begin{aligned} S(u'_i) &= \frac{\langle u'_i^3 \rangle}{\langle u'_i^2 \rangle^{3/2}} \\ F(u'_i) &= \frac{\langle u'_i^4 \rangle}{\langle u'_i^2 \rangle^2} \end{aligned} \tag{3.47}$$

It is worth recalling that the skewness coefficient is a dimensionless quantity that measures the

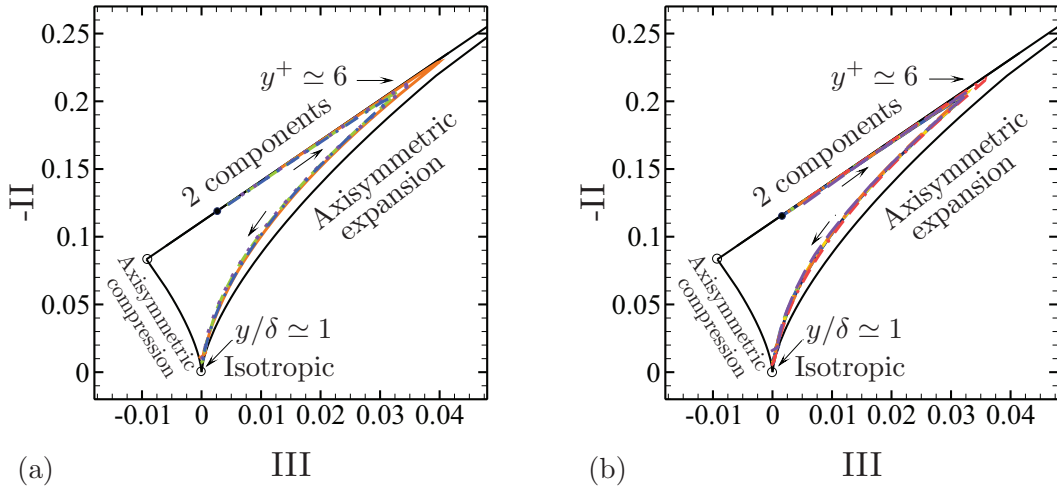


Figure 3.37: Anisotropy invariants maps. (a) SGS models study using LES-P2 grid; (b) Grid sensitivity study using CSM model. For legend, see table 3.4.

asymmetry of the *Probability Distribution Function* (PDF) of a given random field regarding its mean value. Unlike the variance, which is always positive, the skewness factor can be positive or negative. Quantitatively, a positive value of the skewness factor means that the PDF curve has a longer tail towards the positive axis and its shape is skewed to the negative axis. The opposite applies for a negative skewness. Zero skewness indicates perfectly symmetry with a normal distribution (Gaussian shape). The flatness (or kurtosis) coefficient is another dimensionless quantity that characterizes the relative deviation from a normal distribution. The latter has a flatness value of 3.

The distribution of the skewness and the flatness factors along the boundary layer are depicted in Fig.(3.38) for different LES models and grid resolutions. Apart from the near wall deviation of the skewness and flatness coefficients, the turbulence behavior is found to be nearly Gaussian, with $S(u') \approx 0$ (but negative) and $F(u') \approx 3$. This result is in good agreement with the DNS data. The peak position of both factors is correctly recovered by the LES models and with different grids, whereas their magnitudes are weakly over-estimated. For instance, $S(u')$ reaches a maximum of 2 for the ILES against a maximum of 1 for the DNS, and up to $y^+ \approx 100$, the CSM model and the ILES better predict it with $S(u') \approx -0.25$. On the other hand, $F(u')$ maximum attains 11 against a maximum of 4 for DNS, and up to $y^+ \approx 100$, all LES models succeed to predict the right value of the flatness factor with $F(u') \approx 3$.

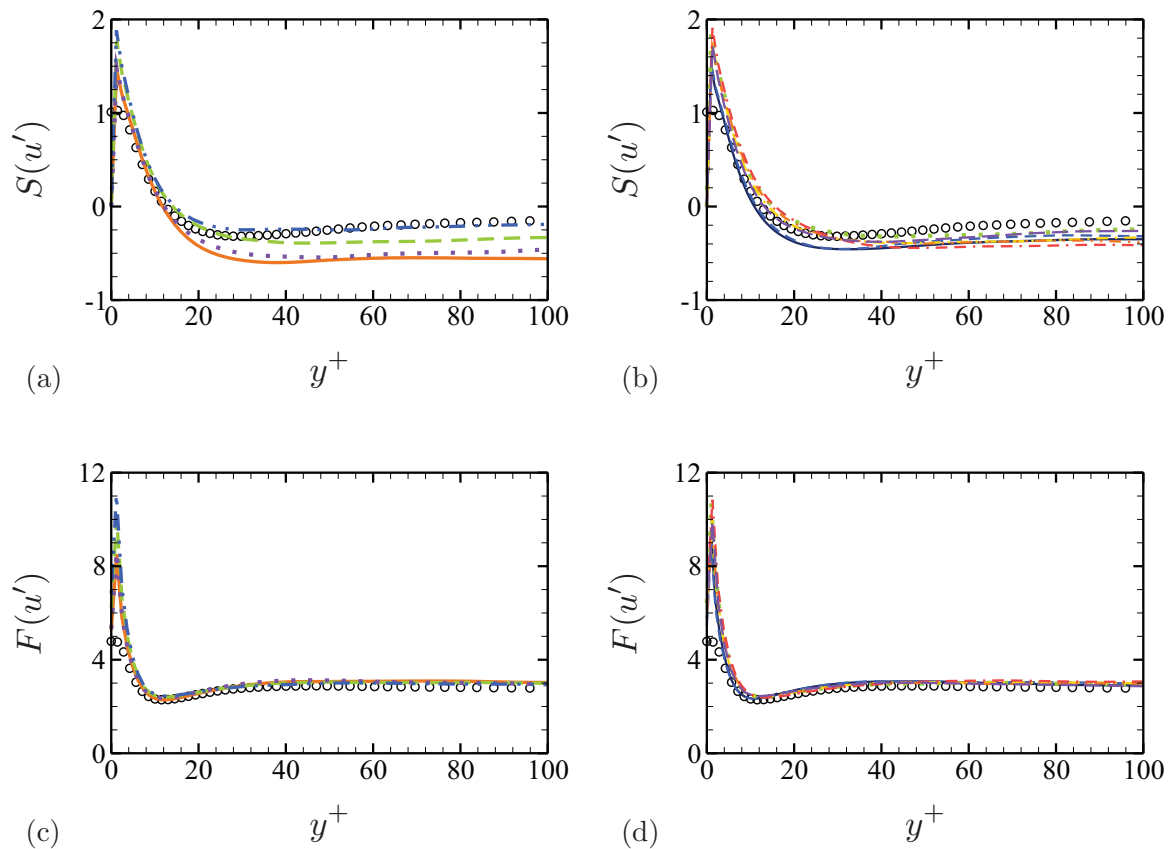


Figure 3.38: (a, b) Skewness and (c, d) Flatness factors as a function of y^+ . For legend, see table 3.4.

Case	u_{rms}^+	v_{rms}^+	w_{rms}^+	$-\langle u'v' \rangle^+$	K^+	ε^+	$-\langle v'T' \rangle$	T_{rms}	ρ_{rms}	p_{rms}
Compressible	1	1	1	2	2	0	1	0	0	0
Incompressible	1	2	1	3	2	0	2	0	—	0

Table 3.5: Power indices n of near-adiabatic-wall asymptotic behaviors.

3.7.3 Near-wall asymptotic behavior

By means of the continuity equation and the non-slip wall boundary conditions, Tamano (2002) [97] and Morinishi *et al.* (2004) [66] proposed a comparison of analytical adiabatic and isothermal near-wall asymptotic behaviors for compressible and incompressible turbulent channel flows, expressed as a power of y^+ .

In the following, we examine the near-adiabatic-wall asymptotic behaviors of the different turbulent quantities, namely the velocity fluctuations, the turbulent kinetic energy, the molecular dissipation and the fluctuations of thermodynamic quantities. The turbulent fluctuations ϕ' of a given quantity ϕ are expanded in terms of Taylor series of y^+ as follows:

$$\phi' = \xi_{1,\phi}(x, z, t) + \xi_{2,\phi}(x, z, t)y^+ + \xi_{3,\phi}(x, z, t)y^{+2} + \mathcal{O}(y^{+3}) \quad (3.48)$$

We can observe that the no-slip condition at the wall implies ξ_1 for all velocity fluctuating components are zero. For an incompressible flow, satisfying the continuity equation at the wall additionally yields $\xi_2 = 0$ for v' as $\partial v'/\partial y|_w = 0$ and thus $v_{rms} \propto y^{+2}$. On the other hand, $u_{rms} \propto y^+$ and $w_{rms} \propto y^+$. It follows that $K^+ \propto y^{+2}$ and $\langle u'v' \rangle \propto y^{+3}$.

The temperature and pressure distributions have a non-zero value at the wall, which implies that $T_{rms} \propto y^{+0}$ and $p_{rms} \propto y^{+0}$. Consequently, it yields $\langle v'T' \rangle \propto y^{+2}$.

For a compressible turbulent flow, the main difference with an incompressible one comes from the density variation with $\partial \rho / \partial t|_w \neq 0$ and ρ_{rms} presents a non-zero value asymptotic behavior, which yields $\partial u_i / \partial x_i|_w \neq 0$. According to Eq. (3.48), $\partial v'/\partial y|_w \neq 0$. It yields u_{rms} , v_{rms} and w_{rms} present asymptotes $\propto y$. It follows that $K \propto y^2$, $\langle u'v' \rangle \propto y^2$, and then $\langle v'T' \rangle \propto y^1$.

Table 3.5 summarizes the different power indices n ($\propto y^{+n}$) of near-adiabatic-wall asymptotic behavior of the different quantities.

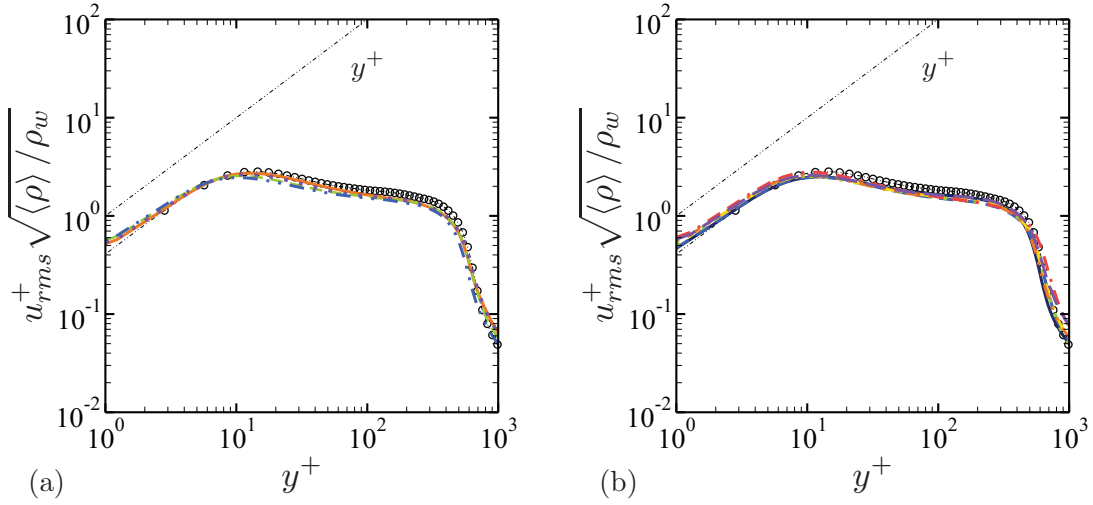


Figure 3.39: Near-wall asymptotic behavior of the streamwise velocity fluctuations u_{rms} in Morkovin's scaling as a function of y^+ . (a) SGS models study using LES-P2 grid; (b) Grid sensitivity study using CSM model. For legend, see table 3.4.

Figs. (3.39) to (3.45) plot the near-wall asymptotic behavior of the velocity fluctuations u_{rms}^+ , v_{rms}^+ , w_{rms}^+ according to the Morkovin's scaling, as well as the Reynolds shear stress $\langle u'v' \rangle^+$, the normalized kinetic energy K^+ , the turbulent heat flux $-\langle v'T' \rangle$, the temperature fluctuations T_{rms} and the density fluctuations ρ_{rms} as a function of y^+ in *log-log* coordinates.

Fig. (3.39; 3.41) show that, at the wall and up to the frontier of the viscous sublayer, u_{rms}^+ and w_{rms}^+ vary linearly with decreasing y^+ . All SGS models exhibit acceptable behavior for the different quantities, and all grid-resolution cases almost fairly compare with the near-wall required asymptotes, except at the wall region ($\Delta y_{min}^+ \approx 1$), due to the wall-grid LES requirement, where $\Delta y_{min}^+ \gtrsim 1$.

The difference in indices between the compressible and incompressible flows was mainly observed for v_{rms}^+ , $-\langle u'v' \rangle^+$ and $-\langle v'T' \rangle$. Those asymptotes are plotted in Fig. (3.40;3.42;3.44), and show that, up to the considered wall-region ($\Delta y^+ \gtrsim 1$), the near-wall asymptotic behavior of v_{rms}^+ , $-\langle u'v' \rangle^+$ and $\langle v'T' \rangle^+ = R_{vT}$ are better estimated using the incompressible indices ($\propto y^{+2}$, y^{+3} and y^{+2} , respectively), even if the Morkovin's scaling is not used for the Reynolds shear stress. In fact, according to Tamano (2002) [97], the theoretical compressible asymptotes of these quantities hold for the very near-wall region, *i.e.* at $0.1 \leq y^+ \leq 1$. However, since LES modeling requires a minimal wall-resolution $\Delta y_{min}^+ \gtrsim 1$, this region is not covered by this near-wall asymptotic behavior.

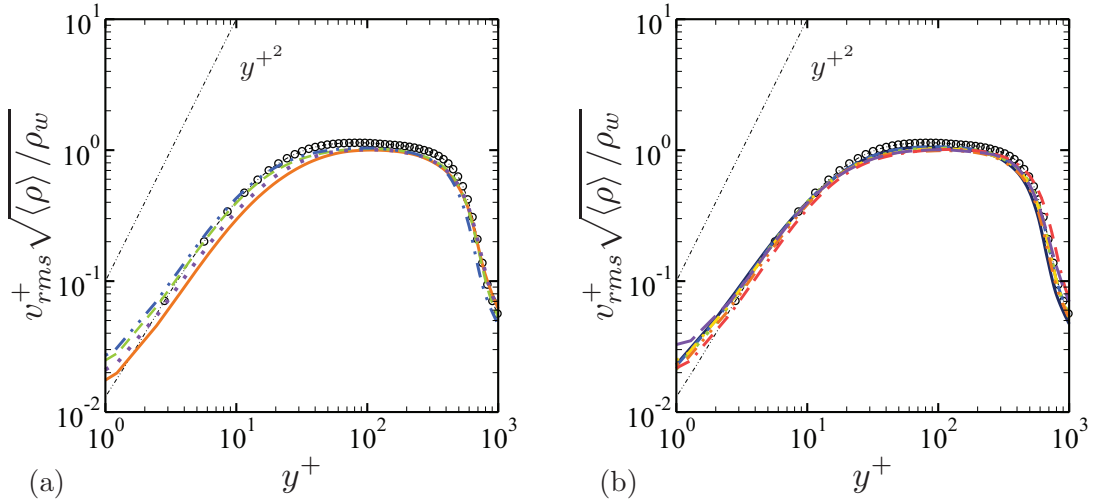


Figure 3.40: Near-wall asymptotic behavior of the wall-normal velocity fluctuations v_{rms} in Morkovin's scaling as a function of y^+ . (a) SGS models study using LES-P2 grid; (b) Grid sensitivity study using CSM model. For legend, see table 3.4.

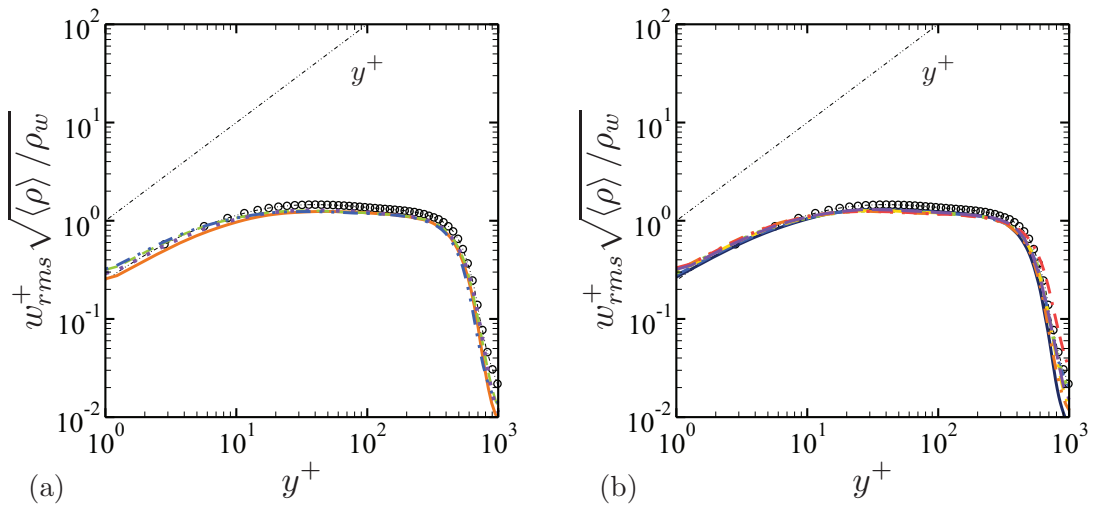


Figure 3.41: Near-wall asymptotic behavior of the spanwise velocity fluctuations w_{rms} in Morkovin's scaling as a function of y^+ . (a) SGS models study using LES-P2 grid; (b) Grid sensitivity study using CSM model. For legend, see table 3.4.

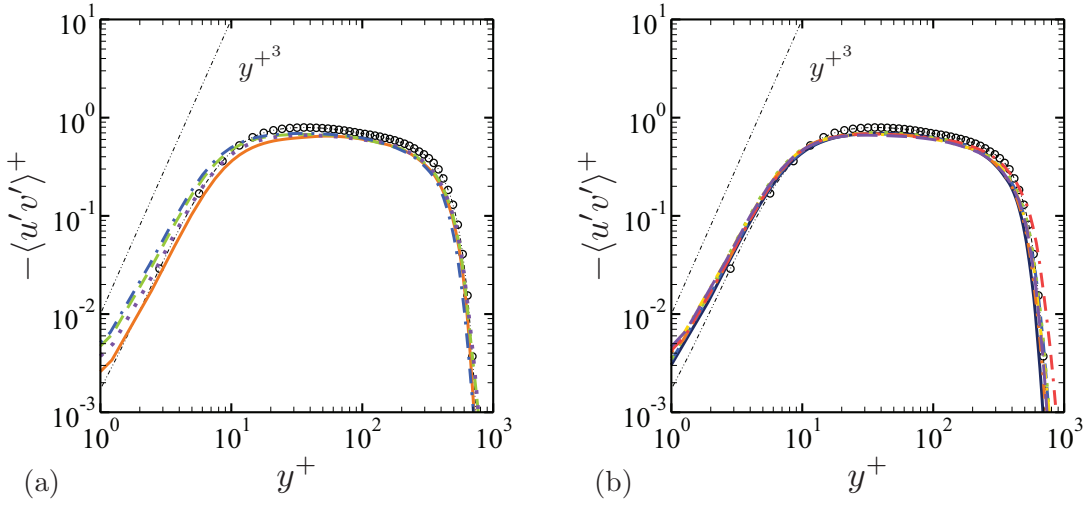


Figure 3.42: Near-wall asymptotic behavior of the normalized Reynolds shear stress $\langle u'v' \rangle^+$ as a function of y^+ . (a) SGS models study using LES-P2 grid; (b) Grid sensitivity study using CSM model. For legend, see table 3.4.

Considering the turbulent kinetic energy component K^+ , it varies linearly with decreasing y^{+2} , while the molecular dissipation ε exhibits a non-zero constant behavior near the wall (Fig. 3.43), tendency that was also confirmed by Morinishi *et al.* (2004) [66]. This behavior is found to be unaffected by varying the SGS model or the grid resolution.

Morinishi *et al.* (2004) [66] also reported that the near-adiabatic-wall behavior of the thermodynamic quantities T_{rms} , ρ_{rms} and p_{rms} for a compressible flow, have a constant non-zero value asymptote (y^{+0}) with decreasing y^+ . As it is shown in Fig. (3.45), T_{rms}/T_∞ , ρ_{rms}/ρ_∞ and p_{rms}/p_∞ exhibit an asymptote $\propto y^{+0}$ when decreasing y^+ . However, for a compressible flow near an isothermal wall, T_{rms} should vary linearly with decreasing y^+ , while ρ_{rms} and p_{rms} do conserve a constant non-zero value asymptote with the same boundary condition.

Hence, for a near-adiabatic-wall region ($1 \leq y^+ \leq 6$), all statistics showed overall good asymptotic behavior when compared to their incompressible flow counterparts discussed by Morinishi *et al.* (2004) [66]. $\langle u'v' \rangle^+$ and $\langle v'T' \rangle^+$ also showed acceptable behaviors compared to the incompressible asymptotes even if the variation in the mean density profile is not taken into account.

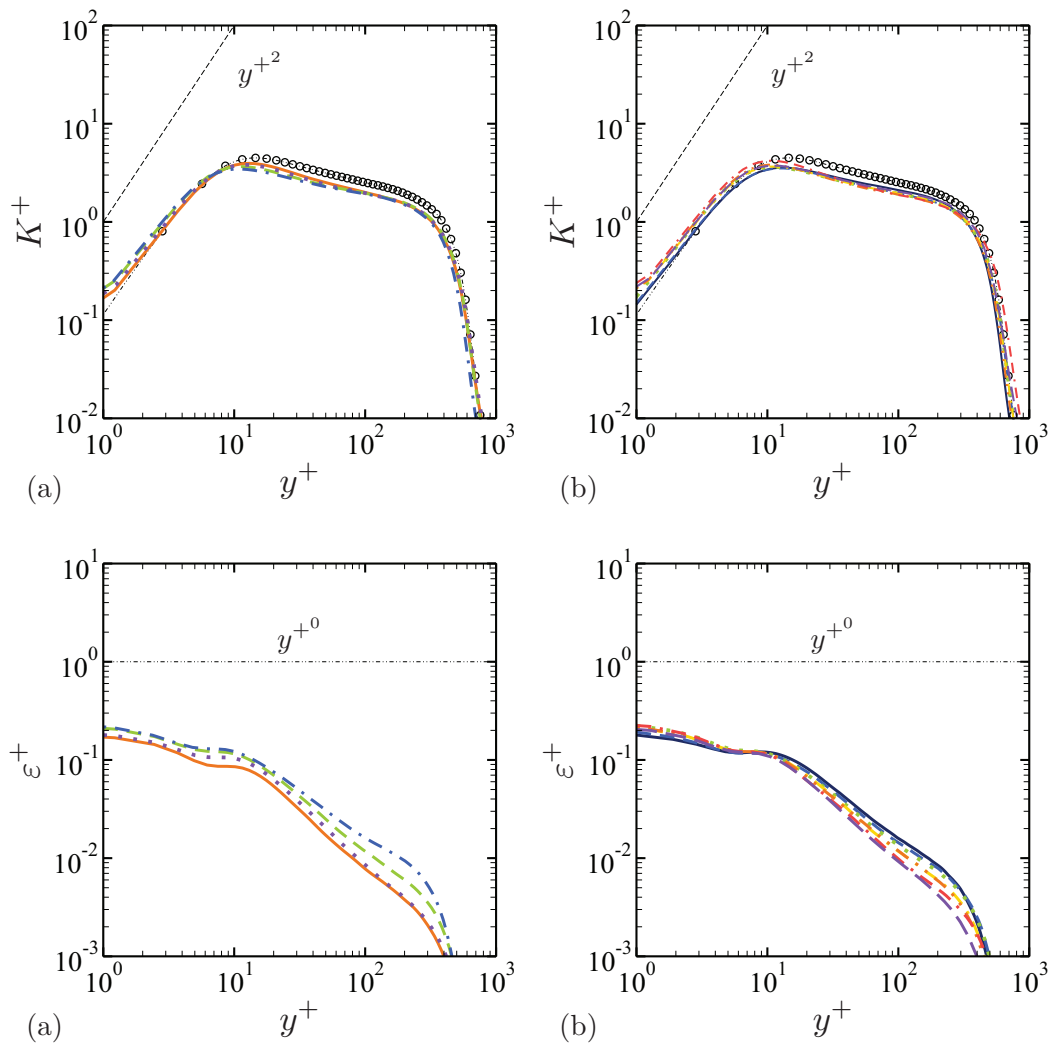


Figure 3.43: Near-wall asymptotic behavior of (a-b) the normalized kinetic Energy and (c-d) the normalized molecular dissipation as a function of y^+ . For legend, see table 3.4.

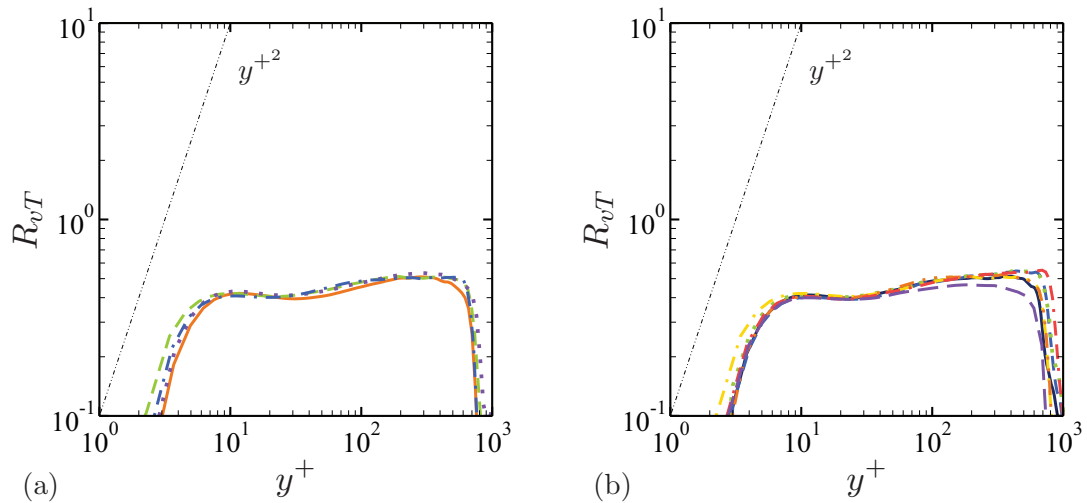


Figure 3.44: Near-wall asymptotic behavior of the normalized turbulent heat flux, R_{vT} , as a function of y^+ . (a) SGS models study using LES-P2 grid; (b) Grid sensitivity study using CSM model. For legend, see table 3.4.

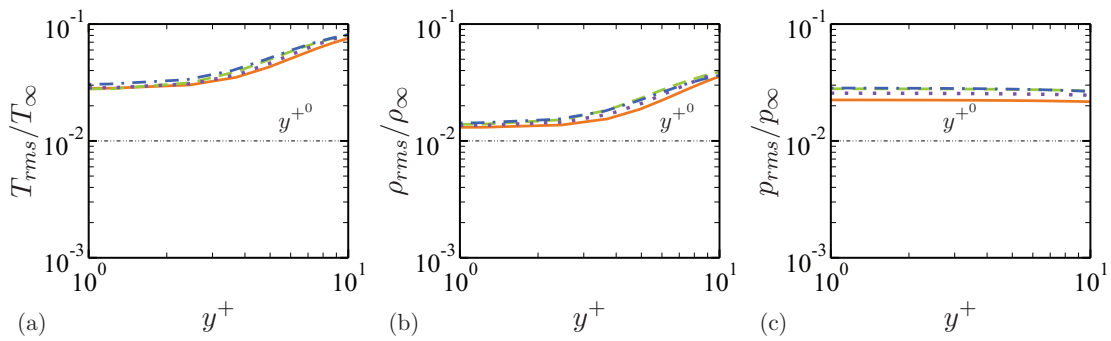


Figure 3.45: Near-wall asymptotic behavior of (a) the temperature, (b) the density and (c) the pressure fluctuations as a function of y^+ . For legend, see table 3.4.

3.8 Turbulent energy dissipation rate

In homogeneous compressible turbulence with constant viscosity, the turbulent energy dissipation is commonly written as the sum of two components, namely the solenoidal dissipation ε_s and the dilatational dissipation ε_d . However, in inhomogeneous turbulent flows, an inhomogeneous component of the dissipation, ε_I , is also expressed.

By definition, the turbulent energy dissipation ε is defined as:

$$\varepsilon \equiv \left\langle \tau'_{ik} \frac{\partial u'_i}{\partial x_k} \right\rangle \quad (3.49)$$

where τ'_{ik} is defined as (Huang *et al.*, 1995) [43]:

$$\begin{aligned} \tau'_{ik} = & \left[\mu' \left(\frac{\partial u'_i}{\partial x_k} + \frac{\partial u'_k}{\partial x_i} \right) - \frac{2}{3} \mu' \frac{\partial u'_l}{\partial x_l} \delta_{ik} \right] - \left[\left\langle \mu' \left(\frac{\partial u'_i}{\partial x_k} + \frac{\partial u'_k}{\partial x_i} \right) \right\rangle - \frac{2}{3} \left\langle \mu' \frac{\partial u'_l}{\partial x_l} \right\rangle \delta_{ik} \right] \\ & + \left[\langle \mu \rangle \left(\frac{\partial u'_i}{\partial x_k} + \frac{\partial u'_k}{\partial x_i} \right) - \frac{2}{3} \langle \mu \rangle \frac{\partial u'_l}{\partial x_l} \delta_{ik} \right] + \left[\mu' \left(\frac{\partial \langle u_i \rangle}{\partial x_k} + \frac{\partial \langle u_k \rangle}{\partial x_i} \right) - \frac{2}{3} \mu' \frac{\partial \langle u_l \rangle}{\partial x_l} \delta_{ik} \right] \end{aligned} \quad (3.50)$$

The total energy dissipation can be cast as the sum of three parts $\varepsilon = \varepsilon_1 + \varepsilon_2 + \varepsilon_3$, where:

$$\begin{aligned} \varepsilon_1 &= \langle \mu \rangle \left\langle \frac{\partial u'_i}{\partial x_k} \left(\frac{\partial u'_i}{\partial x_k} + \frac{\partial u'_k}{\partial x_i} \right) \right\rangle - \frac{2}{3} \langle \mu \rangle \left\langle \frac{\partial u'_i}{\partial x_k} \frac{\partial u'_l}{\partial x_l} \right\rangle \delta_{ik} \\ \varepsilon_2 &= \left\langle \mu' \frac{\partial u'_i}{\partial x_k} \left(\frac{\partial u'_i}{\partial x_k} + \frac{\partial u'_k}{\partial x_i} \right) \right\rangle - \frac{2}{3} \left\langle \mu' \frac{\partial u'_i}{\partial x_k} \frac{\partial u'_l}{\partial x_l} \right\rangle \delta_{ik} \\ \varepsilon_3 &= \left\langle \mu' \frac{\partial \langle u_i \rangle}{\partial x_k} \right\rangle \left(\frac{\partial \langle u_i \rangle}{\partial x_k} + \frac{\partial \langle u_k \rangle}{\partial x_i} \right) - \frac{2}{3} \left\langle \mu' \frac{\partial u'_i}{\partial x_k} \right\rangle \frac{\partial \langle u_l \rangle}{\partial x_l} \end{aligned} \quad (3.51)$$

The quantity $\varepsilon_1 = \varepsilon_s + \varepsilon_d + \varepsilon_I$ is also expressed as the sum of three contributions, namely, the solenoidal dissipation, ε_s , the dilatational dissipation, ε_d , and the inhomogeneous dissipation, ε_I , written:

$$\begin{aligned} \varepsilon_s &= 2\langle \mu \rangle \langle \omega'_{ij} \omega'_{ij} \rangle \\ \varepsilon_d &= \frac{4}{3} \langle \mu \rangle \left\langle \frac{\partial u'_l}{\partial x_l} \frac{\partial u'_k}{\partial x_k} \right\rangle \\ \varepsilon_I &= 2\langle \mu \rangle \left(\frac{\partial^2 \langle u'_i u'_j \rangle}{\partial x_i \partial x_j} - 2 \frac{\partial}{\partial x_i} \left\langle u'_i \frac{\partial u'_j}{\partial x_j} \right\rangle \right) \end{aligned} \quad (3.52)$$

Note that in our case, ε_s is simply deduced from $\varepsilon_s = \varepsilon_1 - \varepsilon_d - \varepsilon_I$.

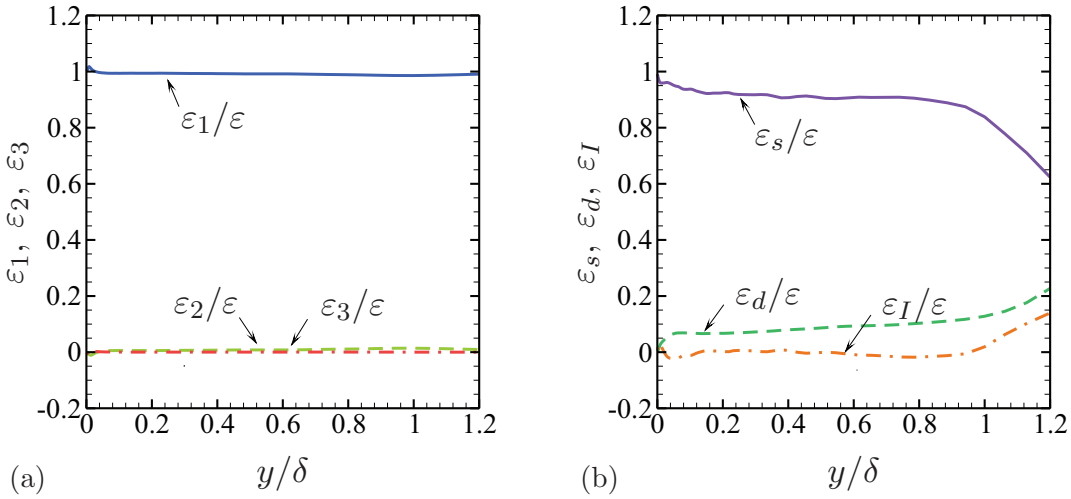


Figure 3.46: Ratios of the turbulent energy dissipation rate terms as a function of y/δ .

Fig. (3.46-a) shows the ratios of $\varepsilon_1/\varepsilon$, $\varepsilon_2/\varepsilon$ and $\varepsilon_3/\varepsilon$ as a function of y/δ . It is shown that ε_1 dominates the other contributions. This result is found to be a classical finding for an adiabatic turbulent boundary layer, since μ' is negligible for such a flow. Fig. (3.46-b) shows the ratios $\varepsilon_s/\varepsilon$, $\varepsilon_d/\varepsilon$ and $\varepsilon_I/\varepsilon$ as a function of y/δ , and shows that the inhomogeneous part of the dissipation is also negligible.

Fig. (3.47-a) shows the ratio of dilatational dissipation to solenoidal dissipation as a function of y/δ . The ratio is found to be constant throughout the boundary layer, reaching a level of 10%. Although, this result is in good concordance with the classical data of homogeneous shear flows (Sarkar *et al*, 1992) [81], a difference exists compared to the DNS data of Huang *et al.* (1995) [43], which shows a level of 3% in a turbulent channel flow. Fig. (3.47-b) shows the ratio $\varepsilon_d/\varepsilon_s$ as a function of the turbulent Mach number. As found by Huang *et al.* (1995) [43], the relationship between $\varepsilon_d/\varepsilon_s$ and M_t is not linear. Furthermore, this result shows that the Sarkar's dilatational dissipation model formulated for the problem of compressible shear layers growth rate is not applicable in our case.

3.9 Conclusion

In this chapter, large-eddy simulations of an adiabatic supersonic turbulent boundary layer at Mach number $M = 2$ and a Reynolds number up to $Re_\tau = 600$ are performed and compared to DNS and

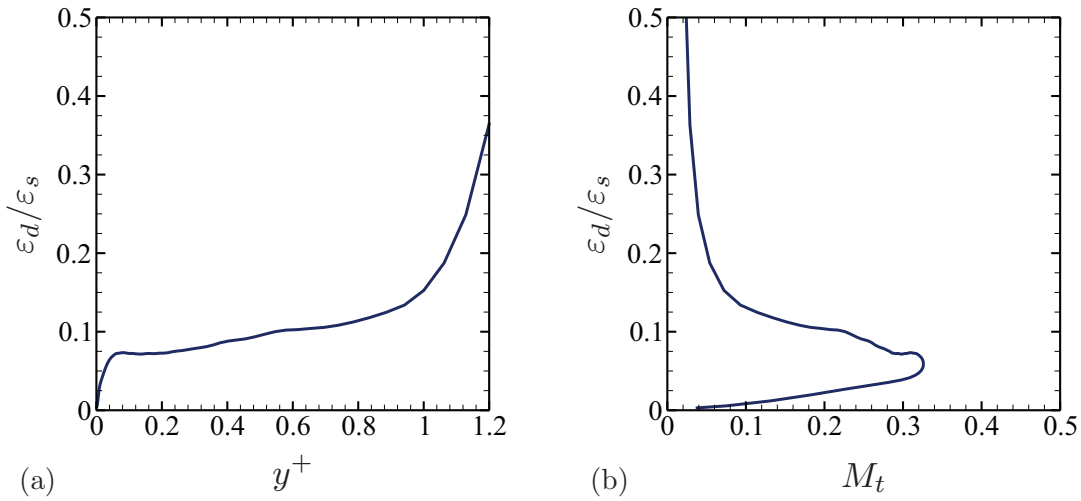


Figure 3.47: Ratio of the dilatational to the solenoidal dissipation as a function of (a) y/δ and (b) turbulent Mach number M_t .

experimental data.

For the three considered SGS models, the main statistical quantities show an overall acceptable agreement. As a first observation, the CSM and the WALE models show better results compared to the DSM. In fact, both models give the correct rate of decay as the wall is approached, which ensure that the SGS viscosity vanishes properly within the viscous sublayer. The results show that the DSM predicts the main statistical quantities with better accuracy, especially when estimating the peaks of the velocity fluctuations and the *r.m.s.* of the wall-pressure distribution. However, it shows less confidence in predicting the mean temperature profile especially at the wall, where the WALE and the CSM models perform better. The temperature and the velocity fluctuations are not perfectly anti-correlated, where R_{uT} is in a good agreement with the DNS, and attains 0.55 in a wide range of the boundary layer. Furthermore, it is found that the correlations linking the thermodynamic quantities derived from the SRA, such as $R_{\rho T}$ and R_{uv} , are in acceptable agreements compared to the theoretical references and DNS results. The use of an Implicit LES shows tendencies that do not vary much compared to the explicit LES models, but it seems that the lack of SGS dissipation affected some thermodynamic quantities, such as T_{rms} and ρ_{rms} , where a bump in the outer region of the boundary layer is observed. This bump can express an accumulation of non-dissipated energy that moved away from the wall.

By discussing the different components of the subgrid scale dissipation, an attempt to set a

criterion to evaluate the quality of LES grid resolutions have been made. By analyzing the different components of the turbulent energy dissipation rate, the present LES shows confidence to correctly predict the dissipation rate. In fact, it is found that the dissipation is mainly solenoidal throughout the boundary layer, which is a classical finding for the considered case. As expected for adiabatic flows, the inhomogeneous part is negligible, due to the weak value of μ' . Also, the dilatational dissipation ε_d does not exceed 10% of the solenoidal component ε_s .

Finally, it is worth mentioning that the CSM and the WALE models show similar computational performance in terms of CPU resources, using almost 1/4 less time than the DSM model.

Even though the WALE and CSM models give very similar results for most of the discussed quantities, it is considered that the CSM model will be used for the study of the isothermal supersonic turbulent boundary layer, due to its better performance for predicting the wall-temperature.

In following, only the CSM model will be used for the simulation of a cold-wall supersonic turbulent boundary layer.

Chapter 4

Isothermal Supersonic Turbulent Boundary Layer

This chapter is divided into two parts. First, a comparison is made between an isothermal wall with the theoretical adiabatic temperature (referred to as nearly-adiabatic) and an adiabatic-wall ($q_w = 0$) boundary layers. The objective of this study is to highlight the main differences resulting in varying the wall condition. The second part of the chapter is dedicated to the study of a cold-wall boundary layer, and the results are analyzed and compared to the adiabatic case.

4.1 Nearly-adiabatic wall Conditions

4.1.1 Flow conditions and simulation parameters

The isothermal nearly-adiabatic wall condition is achieved by imposing a fixed-wall temperature, given by the recovery temperature from the relation:

$$T_{aw} \simeq T_r = T_\infty \left(1 + r \frac{\gamma - 1}{2} M_\infty^2 \right) \quad (4.1)$$

where $r = 0.89$ is the recovery factor.

The test case is performed using the LES-P2 grid (see table 3.1). The turbulent inflow conditions as well as the mean velocity and the temperature profiles are the same as used in the adiabatic case. Series of $\approx 140 \tau_c$, (δ_{in}/u_∞) characteristic times is first achieved to sweep the initial transient flowfield. Turbulence statistics are then sampled and extracted each time-step from time series covering $\approx 300 \tau_c$.

Case	Re_τ	Re_θ	$10^3 C_f$	δ^*/δ	$10^2 \theta/\delta$	H	T_w/T_∞	M_τ
DNS	583.9	2865.9	2.53	0.259	8.50	2.96	1.717	0.0712
Adiabatic	590.7	2597.5	2.98	0.282	9.08	3.11	1.666	0.0773
Nearly-adiabatic	572.1	2560.8	2.94	0.297	9.03	3.29	1.75	0.0786

Table 4.1: Boundary layer properties of the wall boundary condition study using LES-P2 grid. $\text{Re}_\tau = \rho_w u_\tau \delta / \mu_w$; $\text{Re}_\theta = \rho_\infty u_\infty \theta / \mu_\infty$; $C_f = 2\tau_w / \rho_\infty u_\infty^2$; $H = \delta^*/\theta$; $M_\tau = u_\tau / (\gamma R T_w)^{1/2}$.

4.1.2 Wall properties

Table 4.1 compares the boundary layer properties with the DNS data.

Since T_w is imposed, the computed ratio T_w/T_∞ is found to be high compared to the adiabatic case and the DNS data (where a nearly-adiabatic wall condition is also used). This increase in T_w/T_∞ is due to a decrease in the freestream temperature T_∞ at the given station. If normalized with the inlet freestream temperature, $T_w/T_{\infty_{in}} \approx 1.712$, which is in very good agreement with the reference data.

Fig. (4.1-a) shows the skin-friction coefficient, $C_{f_{inc}}$, as a function of the Reynolds number, $\text{Re}_{\theta_{inc}}$. It is found that $C_{f_{inc}}$ gives similar results as the adiabatic case, where it is over-predicted by 6% compared to the Blasius curve, for both the adiabatic and the nearly-adiabatic cases. However, $\text{Re}_{\theta_{inc}}$ is found to decrease and moves towards the DNS data for the nearly-adiabatic boundary layer, due to the weak increase of the predicted wall-temperature. As seen in Fig (4.1-b), even if p_{rms_w}/τ_w is slightly over-predicted, it seems that the value moves towards the analytical and the DNS references data, probably due to an increase in the estimation of the friction velocity.

4.1.3 Near-wall asymptotic behavior

According to Tamano (2002) [97] and Morinishi *et al.* (2004) [66], the main difference between the near-wall asymptote of an adiabatic flow and that of an isothermal flow, is the T_{rms} asymptote, which is $\propto y^+$ for the isothermal case. As a consequence, the index n of the near-wall heat flux asymptote R_{vT} is supposed to increase. Since the near-adiabatic-wall asymptote of $R_{v'T'} \propto y^{+2}$, then the isothermal-case asymptote should be $\propto y^{+3}$.

Table 4.2 summarizes the different power indices n ($\propto y^{+n}$) of useful quantities. Fig. (4.2)

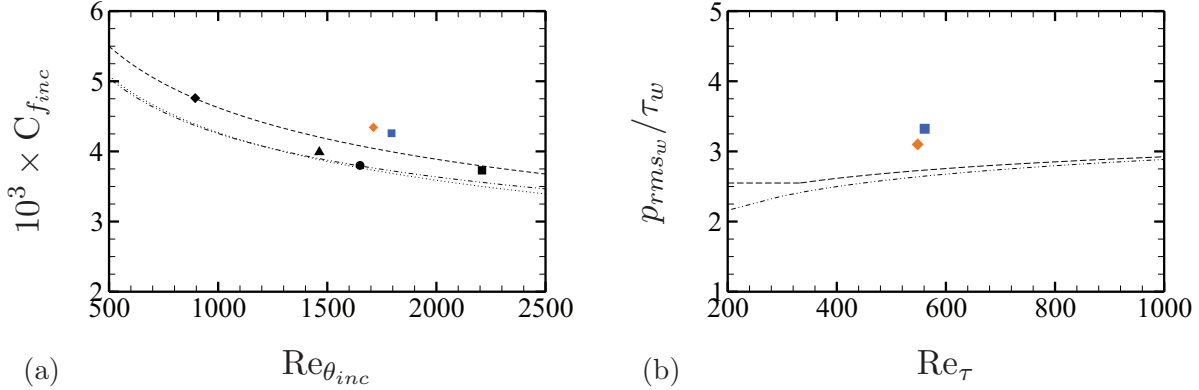


Figure 4.1: (a) Incompressible skin-friction coefficient $C_{f_{inc}}^f$ as a function of Reynolds number based on incompressible momentum thickness $Re_{\theta_{inc}}$. (b) Normalized r.m.s. wall-pressure distribution p_{rms_w}/τ_w as a function of the Reynolds number Re_τ . \blacklozenge Nearly-adiabatic condition; \blacksquare Adiabatic condition. For legend, see caption in Fig. (3.5).

Case	u_{rms}^+	v_{rms}^+	w_{rms}^+	$-\langle u'v' \rangle^+$	K^+	ε^+	$-\langle v'T' \rangle$	T_{rms}	ρ_{rms}	p_{rms}
Compressible	1	1	1	2	2	0	2	1	0	0
Incompressible	1	2	1	3	2	0	3	1	—	0

Table 4.2: Power indices n of near-adiabatic-wall asymptotic behaviors.

shows the near-wall asymptotic behaviors of K^+ and ε^+ , and shows that both of them exhibit the correct near-wall asymptotes, with $\propto y^{+2}$ and $\propto y^{+0}$, respectively.

Fig. (4.3-a) shows a comparison of the asymptotic behavior of T_{rms} for the adiabatic and nearly-adiabatic wall condition. As found by Morinishi *et al.* (2004) [66], T_{rms} follows y^+ for the nearly-adiabatic wall. The near-wall asymptotic behavior of R_{vT} compared to y^{+2} and y^{+3} is shown in Fig. (4.3-b). It shows that, in the considered wall-region ($y^+ \simeq 1$), y^{+2} is found to be a good asymptote of R_{vT} , which is in contrast with the theoretical compressible near-wall asymptote ($\propto y^{+3}$).

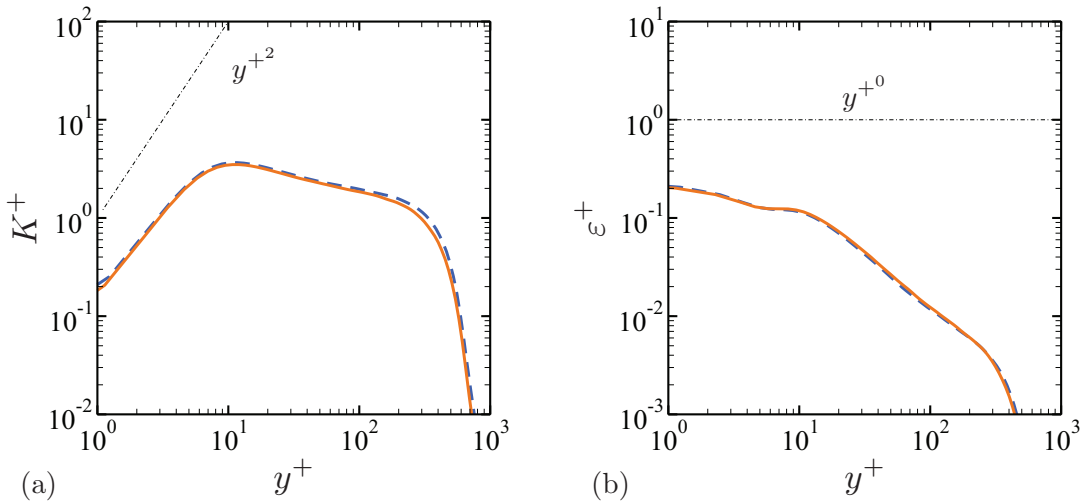


Figure 4.2: (a) Near-wall asymptotic behavior of the normalized turbulent kinetic energy and (b) the normalized dissipation rate as a function of y^+ . (—) Nearly-adiabatic condition; (- -) Adiabatic condition.

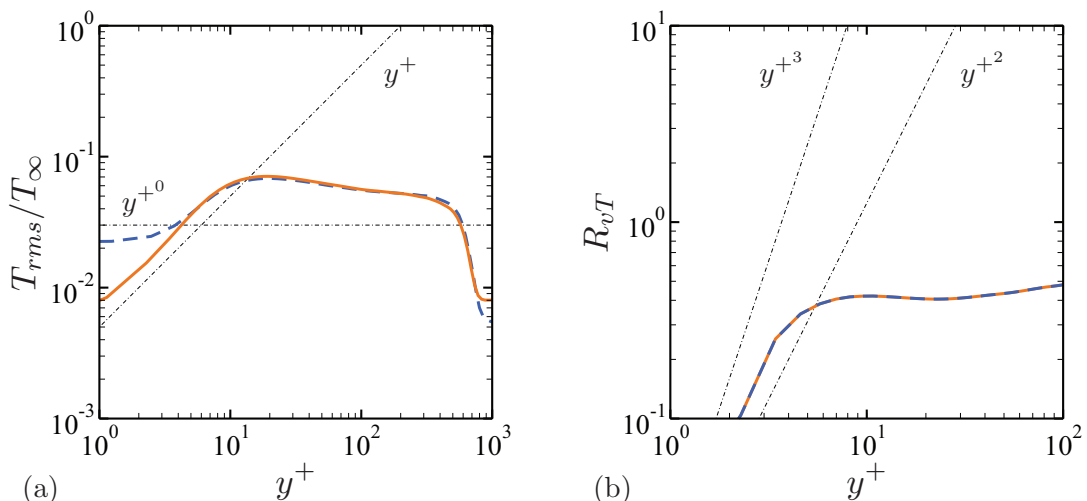


Figure 4.3: (a) Near-wall asymptotic behavior of the normalized r.m.s temperature fluctuations T_{rms}/T_∞ and (b) Near-wall asymptotic behavior of the normalized heat flux R_{vT} as a function of y^+ . (—) Nearly-adiabatic condition; (- -) Adiabatic condition.

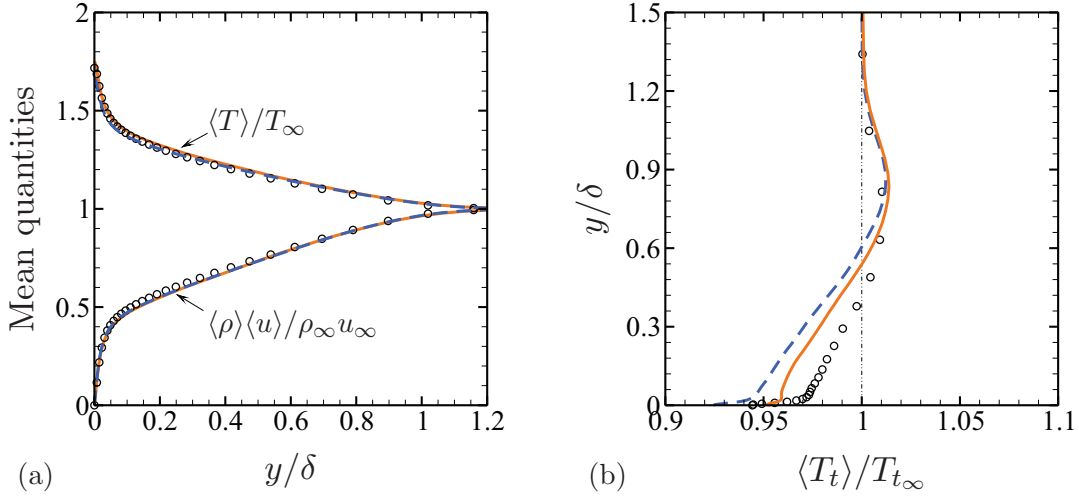


Figure 4.4: (a) Distributions of the time-averaged mean quantities as a function of y/δ . (b) Distribution of the normalized time-averaged total temperature $\langle T_t \rangle / T_{t\infty}$ as a function of y/δ . Circle: DNS Pirozzoli & Bernardini (2011) [74]. (—) Nearly-adiabatic condition; (---) Adiabatic condition.

4.1.4 Turbulence statistics

The time-averaged mean temperature distribution as well as the streamwise velocity component multiplied by the density ratio $\langle \rho \rangle / \rho_\infty$ are presented in Fig. (4.4-a). Although a small difference ($\approx 2\%$) in the temperature profile in the inner region of the boundary layer ($y/\delta < 0.2$), both quantities predict the same tendency. For the total temperature, however, a weak improvement of the profile is observed in the inner region of the boundary layer (Fig. 4.4-b).

Fig. (4.5-a) shows the van-Driest transformed mean streamwise velocity $\langle u \rangle_{vd}^+$ as a function of y^+ , where both results are found to almost perfectly collapse, excepting in the wake region, due to the weak decrease of the Reynolds number with the wall condition. The velocity fluctuations remain also unaffected by the wall condition (Fig. 4.5-b).

In Fig. (4.6) the normalized *r.m.s.* of the thermodynamic quantities as a function of y/δ are shown. Due to the imposed temperature condition, a small increase of the *r.m.s.* of the temperature fluctuations (Fig. 4.6-a), and subsequently the density fluctuations (Fig. 4.6-b), is observed in a wide region of the boundary layer (a maximum of 15% and 7% at peak values, respectively). However, the pressure fluctuations remains small (< 3% of p_∞) and unaffected by the wall-condition.

Fig. (4.7-a) shows the SRA and the R_{uT} correlation as a function of y/δ . It shows that u'

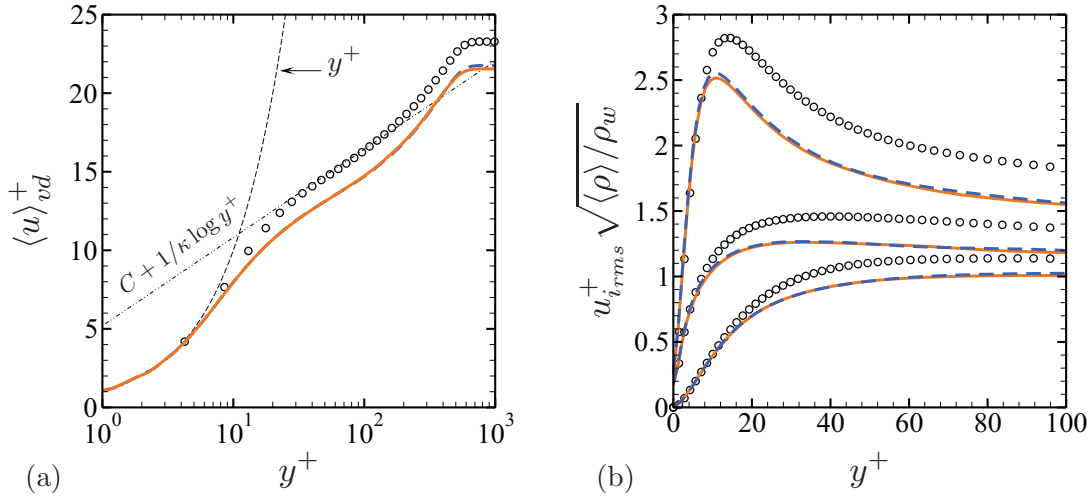


Figure 4.5: (a) Distribution of the van-Driest transformed mean streamwise velocity $\langle u \rangle_{vd}^+$ as a function of y^+ . (b) r.m.s velocity fluctuations in Morkovin's scaling as a function of y^+ . The two constants of the log-region profile are $C = 5.2$ and $\kappa = 0.41$. Circle: DNS Pirozzoli & Bernardini (2011) [74]. (—) Nearly-adiabatic condition; (---) Adiabatic condition.

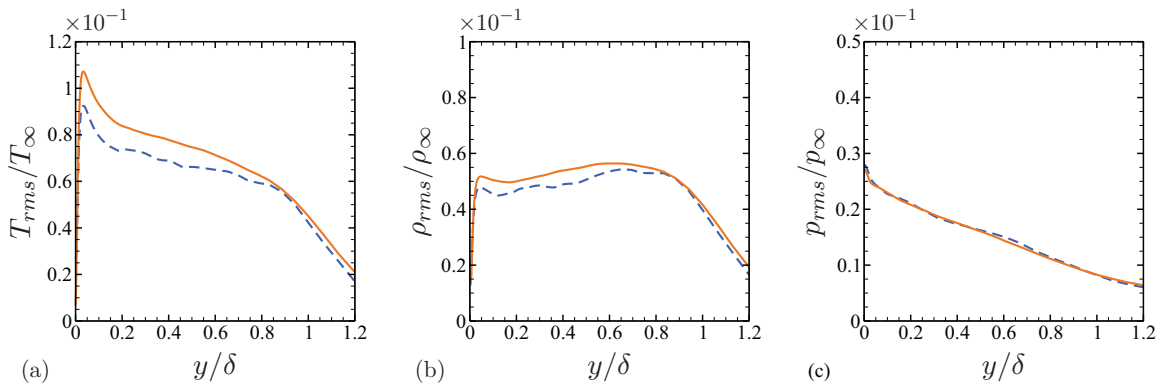


Figure 4.6: Normalized r.m.s. of the thermodynamic quantities as a function of y/δ . (—) Nearly-adiabatic condition; (---) Adiabatic condition.

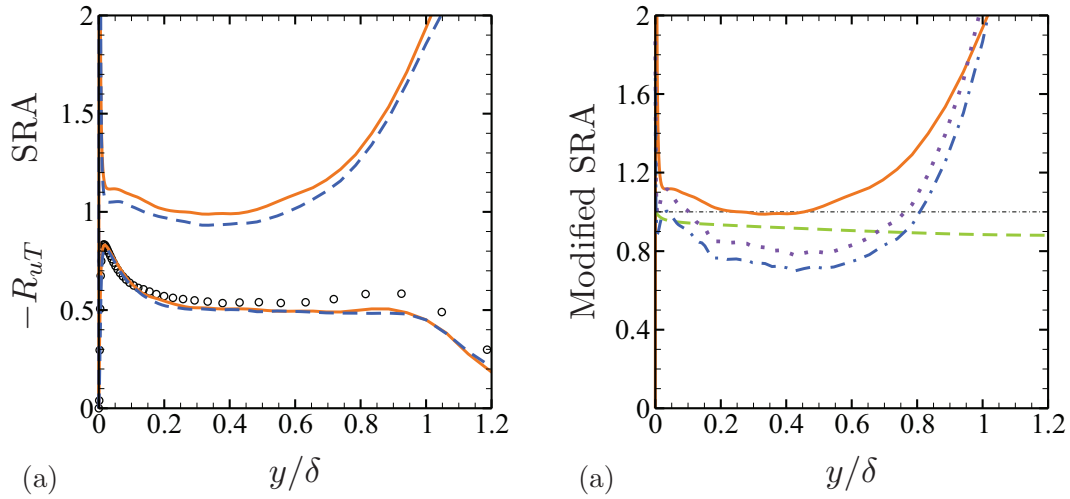


Figure 4.7: (a) SRA and $-R_{uT}$ correlations as a function of y/δ . (—) Nearly-adiabatic condition; (---) Adiabatic condition. (b) Modified SRA relations as a function of y/δ ; (—) SRA; (—) ESRA; (···) HSRA; (·—·) GSRA.

and T' conserve the same level of correlation since $-R_{uT}$ remains about the same as the adiabatic case. The SRA shows a weak increase of about 5% compared to the adiabatic reference case, and the nearly-adiabatic wall condition seems to better predict this analogy. Fig. (4.7-b) shows a comparison of the modified SRA relations. Again, it is found that the computed SRA relation provides a best fit. The ESRA predicts a lower value, where the mismatch reaches a maximum of $\approx 12\%$ below 1.

Fig. (4.8) shows the $-R_{uv}$, R_{vT} correlations as well as the structure parameter $-\langle u'v' \rangle / 2K$ as a function of y/δ . It can be seen that those correlations are very weakly sensitive to the wall condition.

4.1.5 Scatter plots

Fig. (4.9) shows the scatter plots of the instantaneous SRA correlation. As expected, the nearly-adiabatic wall-condition predicts higher correlation between u' and T' , where a linear-fitting of the SRA scatter is found to exhibit a slope $\propto 0.96$ and $\propto 0.59$ for the present case, at $y^+ \simeq 9$ and $y^+ \simeq 100$, respectively, while it only reaches 0.86 and 0.52 for the adiabatic case at the same wall-distance.

However, scatter plots of the temperature fluctuations as a function of the density fluctuations

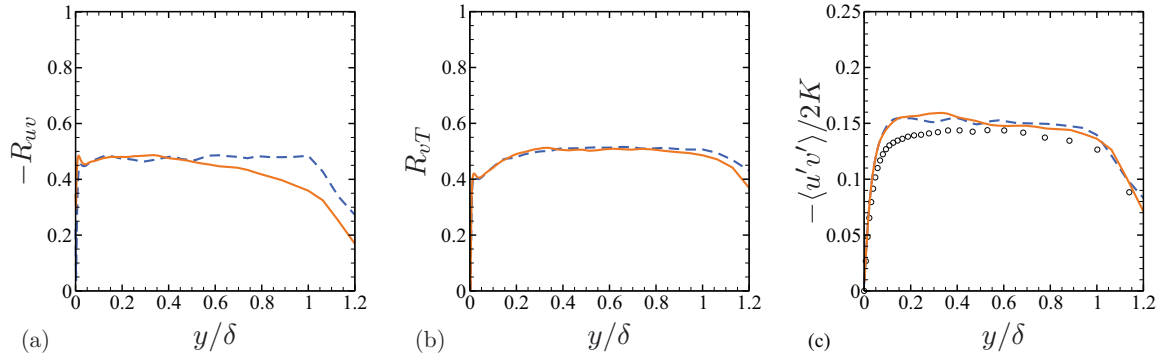


Figure 4.8: $-R_{uv}$, R_{vT} correlations and structure parameter $-\langle u'v' \rangle / 2K$ as a function of y/δ . (—) Nearly-adiabatic condition; (---) Adiabatic condition.

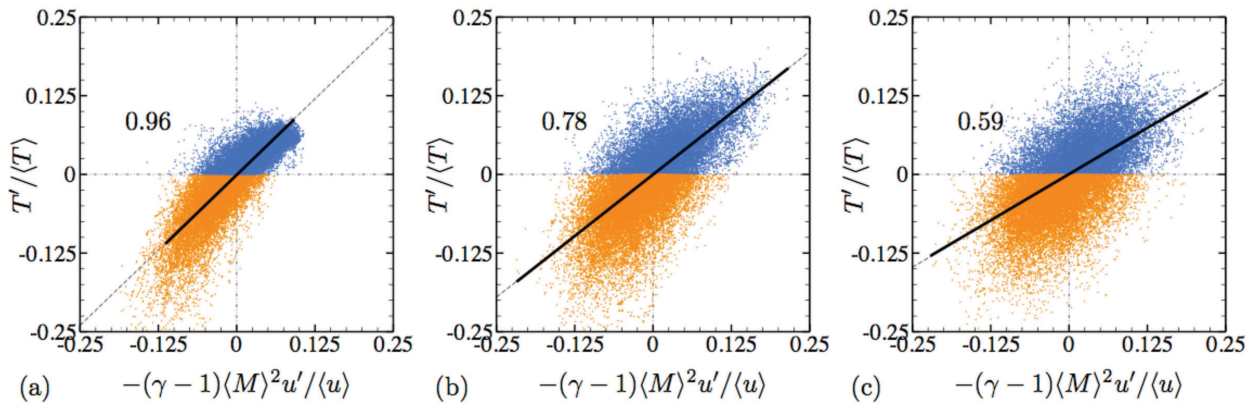


Figure 4.9: Scatter plots of the *strict* SRA in a wall-normal plane for the nearly-adiabatic CSM-P2 case. (a) $y^+ \approx 9$. (b) $y^+ \approx 28$. (c) $y^+ \approx 100$.

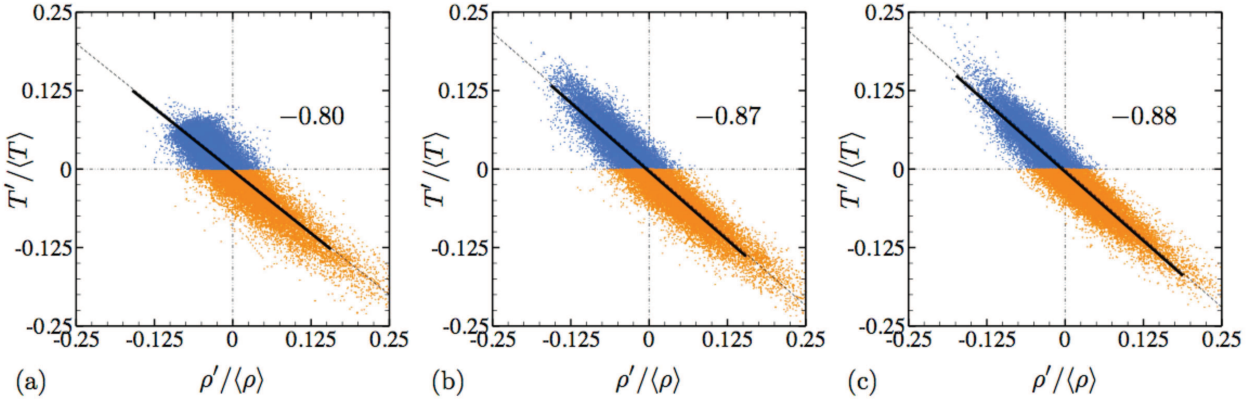


Figure 4.10: Scatter plots of the normalized temperature - density fluctuations in a wall-normal plane for CSM-P2 case. (a) $y^+ \approx 9$. (b) $y^+ \approx 28$. (c) $y^+ \approx 100$.

(Fig. 4.10) does not show a linear anti-correlation between ρ' and T' as expected for a polytropic flow. It exhibits a slope $\propto 0.8$ and 0.88 , at $y^+ \approx 9$ and $y^+ \approx 100$, respectively, against -0.8 and -0.98 at the same regions for the adiabatic case.

It can be concluded that the nearly-adiabatic boundary layer shows overall similar results compared to the adiabatic one. Because of the very weak increase of the wall-temperature due to the wall condition, the Reynolds number is found to weakly decrease, and thus the wall-shear, τ_w , to slightly increase. As suspected, the near-wall asymptotic behavior of T_{rms} and R_{vT} is modified compared to the adiabatic case. A small increase in the r.m.s of the temperature as well as the density fluctuations is also observed, while p_{rms} conserves its adiabatic low fluctuating level. Finally, the near-adiabatic wall condition is found to weakly improve the SRA relation.

4.2 LES of cold-wall supersonic turbulent boundary layer

In this section, the cold-wall supersonic turbulent boundary layer case is simulated. The considered domain has the same dimensions as the adiabatic case, *i.e.*, $L_x \times L_y \times L_z = 106\delta_{in} \times 9.13\delta_{in} \times 3.18\delta_{in}$ in the streamwise x , wall-normal y and spanwise z directions. Here δ_{in} , denotes the boundary layer thickness at the inflow plane, and is taken equal to its adiabatic counterpart. To discretize the physical domain, $N_x \times N_y \times N_z = 1536 \times 180 \times 120$ grid points are used. The corresponding mesh is uniformly spaced in the streamwise and spanwise directions, while it is clustered in the wall-normal direction ($\beta = 6.50$). The grid spacing, expressed in term of wall-units, gives $\Delta x^+ = 34.0$,

Case	Re_τ	Re_θ	Re_{δ_2}	Δx^+	Δy^+	Δz^+
Adiabatic	505-633	2038-2828	1408-1962	34.2-34.4	1.18-1.19	12.3-12.4
Cool	1004-1376	2348-3330	2649-3751	34.0-38.6	0.49-0.55	13.1-14.8

Table 4.3: Reynolds numbers ranges for the adiabatic and isothermal-wall boundary layers and wall-units grid spacing.

$\Delta y_{min}^+ \simeq 0.49$ and $\Delta z^+ = 13.1$, respectively in the streamwise, the wall-normal and the spanwise directions.

At the inlet, the Reynolds numbers characterizing the flow are $\text{Re}_\tau \simeq 498$ and $\text{Re}_\theta \simeq 1275$. The imposed wall-temperature is $T_w/T_{aw} = 0.5$, which gives $T_w/T_\infty \approx 0.85$. To prescribe fully turbulent inflow boundary condition, the recycling/rescaling procedure is used, where the velocity profile is defined using Eq. (2.65), while the temperature and the density profiles are defined by Eq. (2.66), according to the new wall-condition. As for the previous computations, the flowfield is initialized using the digital filter procedure using the isothermal mean velocity, density and temperature profiles. After sweeping the initial transient flow ($\approx 100\tau_c$), statistics are sampled each time step for a period covering only $30\tau_c$, where $\tau_c = \delta_{in}/u_\infty$. The simulation was performed over about 288 hours using 256 processors, for a total of 73720 CPU hours.

4.2.1 Flow properties

In order to study the unique effect of the wall-temperature on the flow dynamics, it is important to match a given Reynolds number for the different cases, namely the adiabatic and the cold-wall boundary layer cases. Based on the Fernholz and Finley (1980) [30] classification criterion, Duan *et al.* (2010) [23] suggested to match a given Reynolds number, Re_{δ_2} , while varying the wall-temperature ($\text{Re}_{\delta_2} = \text{Re}_\theta \mu_\infty / \mu_w$). They also reported that the same conclusions are drawn by matching Re_τ or Re_θ . Since the adiabatic boundary layer analysis was based on matching Re_τ for comparing the DNS and the LES data, it was agreed in the present study that the comparison of the adiabatic case with the present cold-wall case will be made by matching Re_τ . However, in the second-half of the domain, the Reynolds number based on the friction velocity, Re_τ , ranges from ≈ 1000 to ≈ 1380 (see table 4.4).

Case	Re_τ	Re_θ	$\text{Re}_{\theta, inc}$	$10^3 C_f$	δ^*/δ	$10^2 \theta/\delta$	H	T_w/T_∞	$10^2 M_\tau$
Adiabatic	557.2	2368.2	1640.0	3.05	0.280	8.90	3.14	1.66	7.818
Cool	1040.3	2366.9	2670.1	3.09	0.196	10.9	1.79	0.85	7.864

Table 4.4: Boundary layer properties of the isothermal boundary layers. C_{finc} and $\text{Re}_{\theta inc}$ are calculated using van-Driest II theory (Eq. 4.2).

Case	T_w/T_r	T_w/T_∞	$10^2 \beta_q$	$10^{-2} T_\tau$
Nearly-adiabatic	1	1.71	0.0	0.0
Cool	0.5	0.85	-5.55	0.141

Table 4.5: Boundary layer thermal properties of the isothermal boundary layers. $q_w = -\lambda_w \partial \langle T \rangle / \partial y|_w$; $\beta_q = q_w / C_p \rho_w u_\tau T_w$; $T_\tau = q_w / \rho_w C_p u_\tau$.

Failing to match Re_τ or Re_δ in the considered part of the domain, the following results are compared to the reference adiabatic case (CSM-P2) with matching Re_θ , taken equal to ≈ 2366 . The presented results are extracted at a station $x_{res} \simeq 53.8\delta_{in}$, which gives a Reynolds number $\text{Re}_\tau \approx 1040.3$.

The basic flow properties are reported in table 4.3, and the thermal flow properties of the cold-wall and the nearly-adiabatic-wall boundary layers are given in table 4.5.

For a cold-wall boundary layer, Hopkins & Inouye (1971) [41] and Cook & Richards (1977) [17] recommended the use of the van-Driest II theory transformation to predict C_{finc} . The transformed incompressible skin-friction coefficient, C_{finc} , and the incompressible Reynolds number based on momentum thickness, $\text{Re}_{\theta inc}$, are transformed according to $C_{finc} = F_c C_f$ and $\text{Re}_{\theta inc} = F_\theta \text{Re}_\theta$, respectively, where the transformation functions F_c and F_θ are defined by:

$$F_c = \frac{\vartheta_M}{(\arcsin \alpha + \arcsin \beta)^2} \quad \text{and} \quad F_\theta = \frac{\mu_\infty}{\mu_w} \quad (4.2)$$

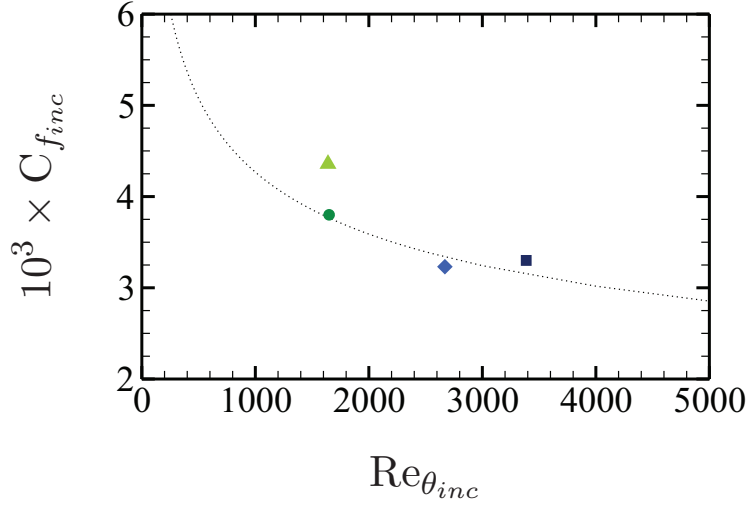


Figure 4.11: Incompressible skin-friction coefficient, $C_{f_{inc}}$, as a function of Reynolds number based on the incompressible momentum thickness, $\text{Re}_{\theta_{inc}}$. (···) Smits *et al.* (1983) [90]; ● Adiabatic DNS ($M=2$), Pirozzoli & Bernardini (2011) [74]; ■ Isothermal ($T_w/T_\infty \approx 0.6$, $M=0.06$), Back *et al.* (1970) [2]; ▲ Adiabatic LES ($M=2$); ◆ Isothermal LES ($T_w/T_\infty \approx 0.85$, $M=2$).

where

$$\begin{aligned} \vartheta_M &= 0.2rM_\infty^2 \\ \alpha &= \frac{2A^2 - B}{(4A^2 + B^2)^{1/2}} \quad \text{and} \quad \beta = \frac{B}{(4A^2 + B^2)^{1/2}} \\ A &= \left(\frac{\vartheta_M}{T_w/T_\infty} \right)^{1/2} \quad \text{and} \quad B = \frac{1 + \vartheta_M}{T_w/T_\infty} - 1 \end{aligned} \quad (4.3)$$

where r is the recovery factor, taken equal to 0.89. Note that according to this definition, $\text{Re}_{\theta_{inc}} = \text{Re}_{\delta_2}$.

Fig. (4.11) shows $C_{f_{inc}}$ as a function of $\text{Re}_{\theta_{inc}}$ compared to the analytical formula $C_{f_{inc},S} = 0.024\text{Re}_{\theta_{inc}}^{-1/4}$ by Smits *et al.* (1983) [90] and to the experiment by Back *et al.* (1970) [2] of a turbulent boundary layer at $M = 0.06$ over a cooled-wall with $T_w/T_\infty \approx 0.6$. The present isothermal boundary layer shows good agreement compared to the analytical formula, where it is slightly under-predicted by 3% compared to the theoretical curve.

4.2.2 Flow organization

Fig. (4.12-a) highlights the instantaneous velocity fluctuations field in a wall-parallel plane at $y^+ \simeq 9$. As it is observed in the adiabatic case, it shows an alternating high- and low-speed streaks, respectively corresponding to positive and negative velocity fluctuations, typical of a fully turbulent wall-bounded flow. However, the observed streaks are found to be smaller and more elongated than their adiabatic counterparts. This behavior was also observed by Coleman *et al.* (1995) [15] and Duan *et al.* (2010) [23]. The same streaky pattern is also visible in the instantaneous temperature fluctuations field (Fig. 4.12-b). However, the correspondence between high-speed streaks and low-value temperature fluctuations is not evident. Instead, a close structural matching between high-speed velocity fluctuations and high-value temperature fluctuations is formed in this region, which can be a footprint of a strong correlation between u' and T' in the very near-wall region.

Noting the number of the resolved streaks in the spanwise direction, it can be concluded that the adopted length, $L_z \approx 3\delta_{in}$, is suitable to fully resolve the most energetic turbulent scales.

4.2.3 Near-wall asymptotic behavior

The near-wall asymptotic behavior of the cold-wall case will follow the same asymptotes as the nearly-adiabatic-wall boundary layer, as reported in table 4.2. Fig. (4.13) shows the near-cold-wall asymptotic behaviors of T_{rms}/T_∞ and R_{vT} compared to the adiabatic case. It is found that the asymptote of T_{rms}/T_∞ weakly agree with the theoretical tendency $\propto y^+$, while R_{vT} agree well with y^{+3} decay.

4.2.4 Turbulence statistics

The anisotropy invariants map of the cold-wall boundary layer, presented in Fig. (4.14-a), shows the same turbulence state observed in the adiabatic-wall boundary layer. First, a two-components state in the near-wall region with a maximum anisotropy reached at $y^+ \simeq 8$ is observed, and then gradually switched to a state of axisymmetric expansion up to the edge of the boundary layer, where an isotropic turbulence behavior is reached. Compared to the adiabatic case, a weak shift of the map is observed along the two-components boundary. This behavior discussed by Shahab (2011) [83] can be explained by a strengthening of the streamwise fluctuating velocity component relative to the wall-normal component. The structure parameter (Fig. 4.14-b) is also found to weakly

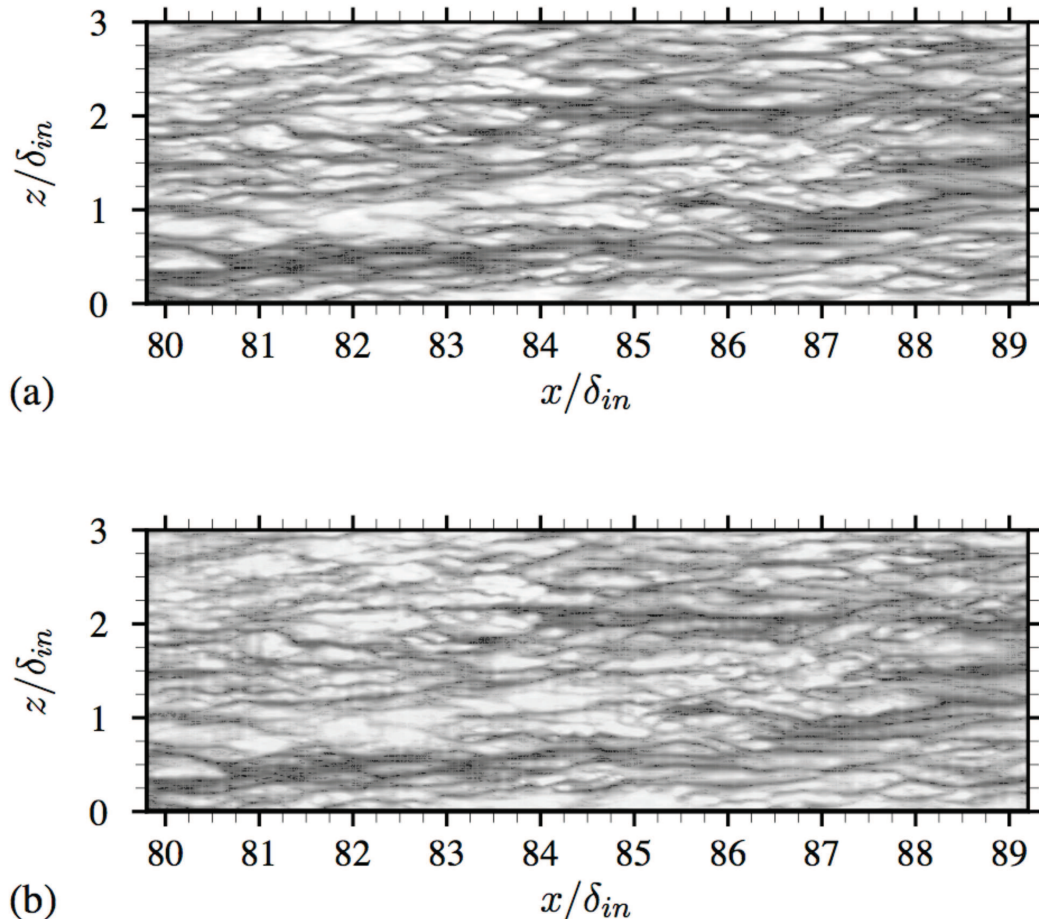


Figure 4.12: (a) Instantaneous velocity fluctuations field and (b) temperature fluctuations field in the x - z plane at $y^+ \simeq 9$. Contour levels are shown for $-0.25 \leq u'/u_\infty \leq 0.25$ and $-0.12 \leq T'/T_\infty \leq 0.12$, from dark to light shades.

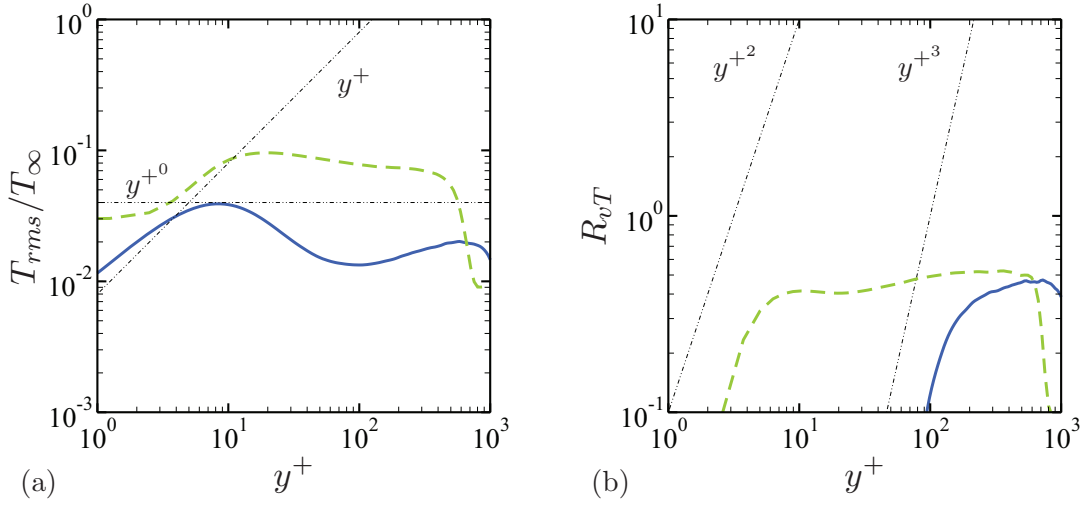


Figure 4.13: (a) Near-wall asymptotic behavior of the normalized *r.m.s* temperature fluctuations, T_{rms}/T_∞ and (b) Near-wall asymptotic behavior of the normalized heat flux, R_{vT} , as a function of y^+ . (—) Isothermal case; (---) Adiabatic case.

decrease compared to the adiabatic case, with a constant value of about 0.14 in a wide region of the layer ($0.1 \leq y/\delta \leq 0.8$).

It is known that the anisotropy coefficient v_{rms}^2/u_{rms}^2 decreases when moving towards the wall. A decrease in the ratio means that the wall seems to force the turbulence in favor of the streamwise direction compared to the wall-normal direction (Deleuze, 1995) [22]. Figs. (4.15-a; 4.15-b) show respectively the anisotropy ratios v_{rms}^2/u_{rms}^2 and w_{rms}^2/u_{rms}^2 as a function of y^+ . Both quantities are found to decrease throughout the layer when the wall is cooled, where in the very near-wall region, the relative difference is found to be more significant for w_{rms}^2/u_{rms}^2 . This indicates a decrease of the spanwise and the wall-normal intensity fluctuations compared to the streamwise one when cooling the wall. The same anisotropic behavior was also observed by Duan *et al.* (2010) [23], who concluded that, as a result to this decrease, a less mixing in the wall-normal and spanwise directions occurs, which yields a more elongated streaks compared to the adiabatic case, as observed in Fig. (4.12).

The turbulent Mach number for the isothermal boundary layer is shown in Fig. (4.16). M_t reaches a peak of 0.372 at $y/\delta \approx 0.026$, and is slightly higher than 0.3 up to $y/\delta \approx 0.38$. However, even if $M_t > 0.3$ in the inner region of the layer, the compressibility effects are suspected to be small, and can be taken into account via the variation of the mean density.

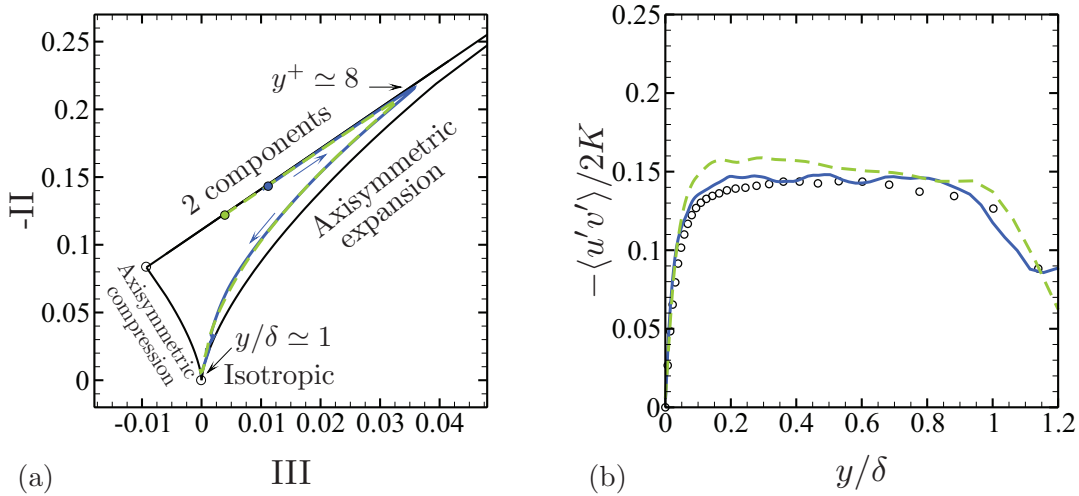


Figure 4.14: (a) Anisotropy invariants map. (b) Structure parameter as a function of y/δ . \circ DNS Pirozzoli & Bernardini (2011). (—) Isothermal case; (---) Adiabatic case.

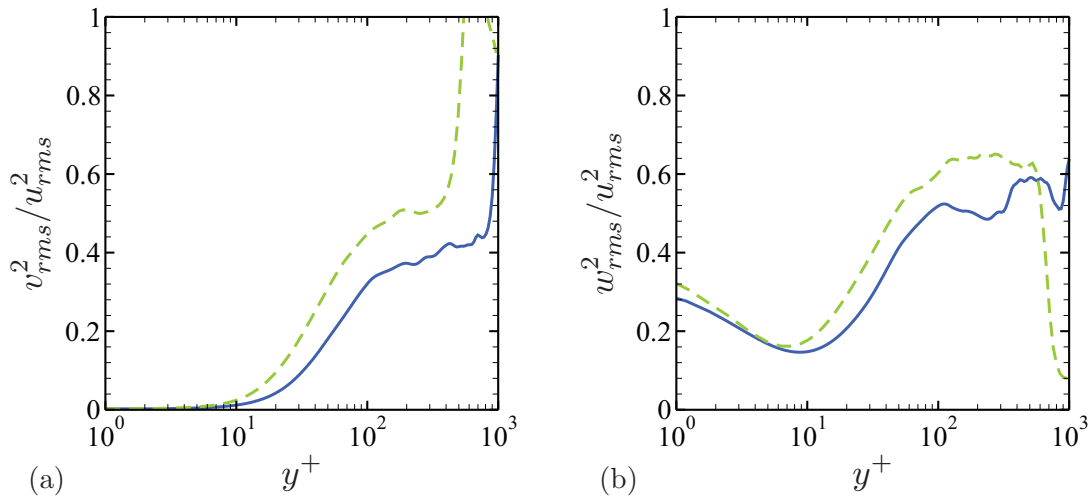


Figure 4.15: Anisotropy ratios as a function of y^+ . (a) v_{rms}^2/u_{rms}^2 ; (b) w_{rms}^2/u_{rms}^2 . (—) Isothermal case; (---) Adiabatic case.

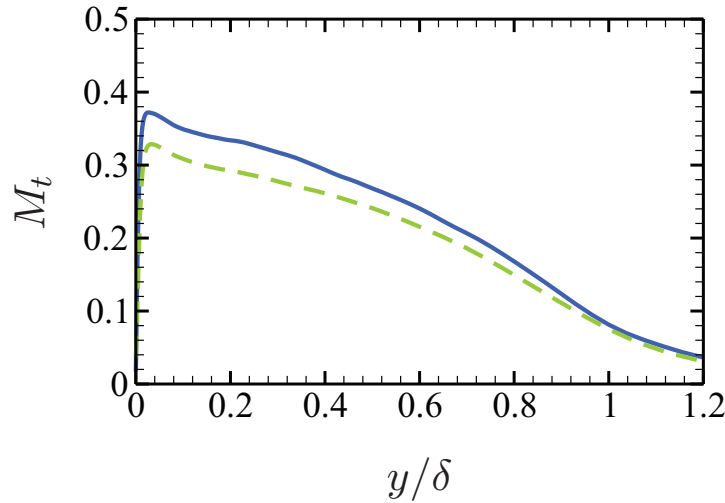


Figure 4.16: Turbulent Mach number, M_t , as a function of y/δ . (—) Isothermal case; (---) Adiabatic case.

The time-averaged mean quantities as a function of y/δ are depicted in Fig. (4.17-a). Compared to the adiabatic profile, $\langle \rho \rangle \langle u \rangle / \rho_\infty u_\infty$ shows an increase as a consequence of the increase in the mean density distribution. As expected, the temperature profile is found to deviate from its adiabatic value due to the strong cooling, where $T_w/T_\infty = 0.85$, and $\langle T \rangle$ is nearly constant throughout the layer.

Fig. (4.17-b) shows $\langle T \rangle / T_\infty$ as a function of $\langle u \rangle / u_\infty$. The computed $\langle T \rangle / T_\infty$ (lines) are found to well collapse with the Walz's (1969) [103] equation (symbols), which confirms the validity of this equation for predicting the temperature-velocity relationship for isothermal boundary layers, at least for the considered conditions. The Walz's (1969) [103] equation is defined:

$$\frac{\langle T \rangle}{T_\infty} = \frac{T_w}{T_\infty} + \frac{T_r - T_w}{T_\infty} \frac{\langle u \rangle}{u_\infty} + \frac{T_\infty - T_r}{T_\infty} \frac{\langle u \rangle^2}{u_\infty^2} \quad (4.4)$$

The streamwise and wall-normal velocity fluctuations as well as the Reynolds shear stress, shown in Morkovin's scaling, are shown in Fig. (4.18), and compared to the experimental results of Piponnaiu (2009) [71] (for adiabatic $M = 2.28$ supersonic turbulent boundary layer at $Re_\theta \approx 5070$). As reported by Coleman *et al.* (1995) [15] and Duan *et al.* (2010) [23], when the variation in the density distribution is taken into account, the present isothermal results are found to collapse

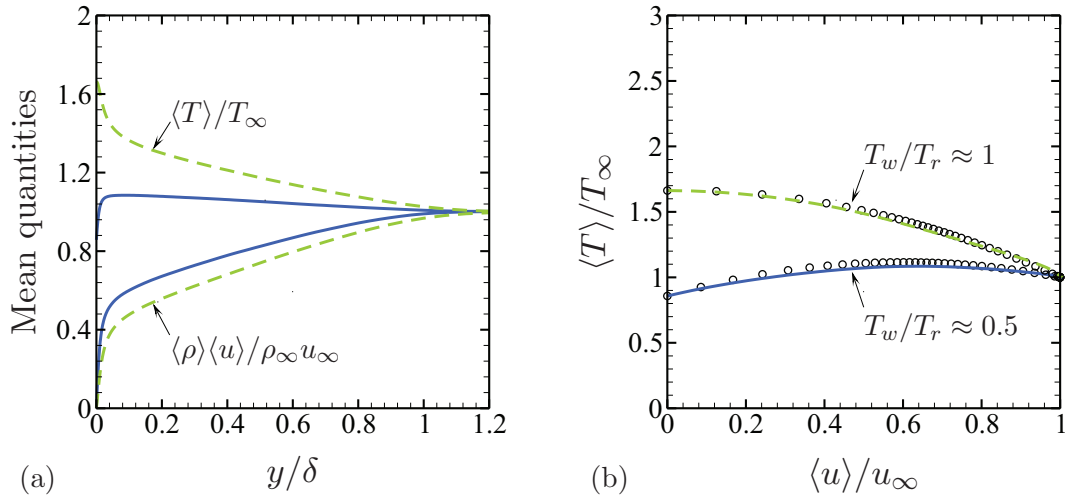


Figure 4.17: (a) Distributions of the time-averaged mean quantities as a function of y/δ . (b) Predicted Walz's equation. (—) Isothermal case; (- -) Adiabatic case.

with the adiabatic supersonic flow data, which were found to be in a good agreement with the incompressible data of Klebanoff ($M \simeq 0$). The weak over-prediction by LES of the wall-normal component is known to be due to an under-estimation of this value by experiments (Pirozzoli & Bernardini, 2011) [74].

The van-Driest transformed mean streamwise velocity $\langle u \rangle_{vd}^+$ is shown as a function of y^+ (Fig. 4.19-a). The cold-wall case shows a very good agreement throughout the layer, where it fits properly with the incompressible logarithmic law.

For isothermal boundary layers, it is possible to express the temperature profile $\langle T \rangle / T_w$ in a logarithmic form using a turbulent total temperature T_i , as defined by Debièvre *et al.* (1997) [21]:

$$T_i = T + \left(\frac{\text{Pr}_m}{2C_p} \right) u^2 \quad (4.5)$$

where $\text{Pr} =_m$ is the mixed Prandtl number, defined by (Smits & Dussauge, 2006) [88] and calculated as:

$$\text{Pr}_m = \frac{\mu + \langle \mu_{sgs} \rangle}{\mu / \text{Pr} + \langle \mu_t \rangle / \text{Pr}_{sgs}} \quad (4.6)$$

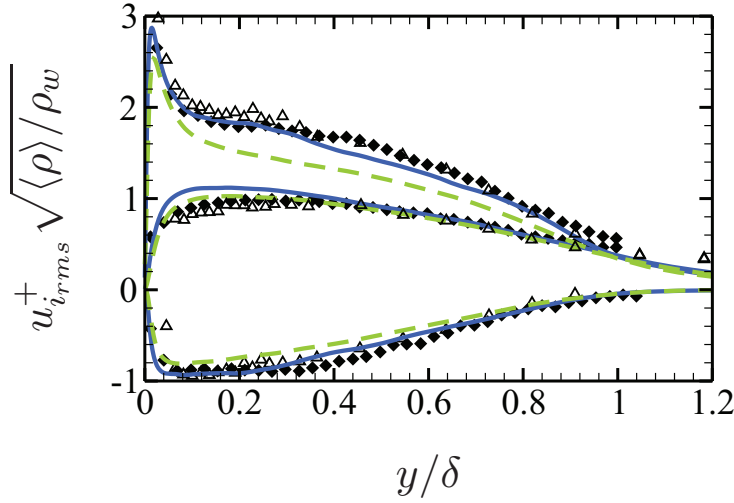


Figure 4.18: *r.m.s* velocity fluctuations in Morkovin's scaling as a function of y/δ . Symbols: Adiabatic ($M = 2.28$), Piponnau (2009) [71]; Diamond: PIV; Triangle: LDA. (—) Isothermal case; (---) Adiabatic case.

where $\text{Pr}_{sgs} = 0.9$. This leads to:

$$\frac{\langle T_i \rangle}{T_w} = 1 - \frac{\text{Pr}_m T_\tau}{T_w} \langle u \rangle^+ \quad (4.7)$$

where T_τ is the friction temperature defined using the wall-heat flux q_w , respectively written:

$$T_\tau = q_w / \rho_w C_p u_\tau, \quad q_w = -\lambda_w \partial \langle T \rangle / \partial y|_w \quad (4.8)$$

Finally, integrating through the layer, the transformed total temperature distribution gives:

$$\langle T_t \rangle^+ = \int_0^{T_i^+} \sqrt{\frac{T_w}{\langle T \rangle}} d\langle T_i \rangle^+ = C_T + \frac{1}{\kappa} \log y^+ \quad (4.9)$$

where $\langle T_i \rangle^+ = -\langle T_i \rangle / (T_\tau \text{Pr}_m)$.

Fig. (4.19-b) shows the transformed total temperature, $\langle T_t \rangle^+$, as a function of y^+ for the cold-wall case. It is found that the distribution follows the logarithmic-law slope $1/\kappa$, to a constant C_T , which depends on the Prandtl number and the ratio of the wall-temperature to the recovery temperature T_w/T_r (Debièvre *et al.*, 1997 [21]). In the present LES simulation, the logarithmic-law

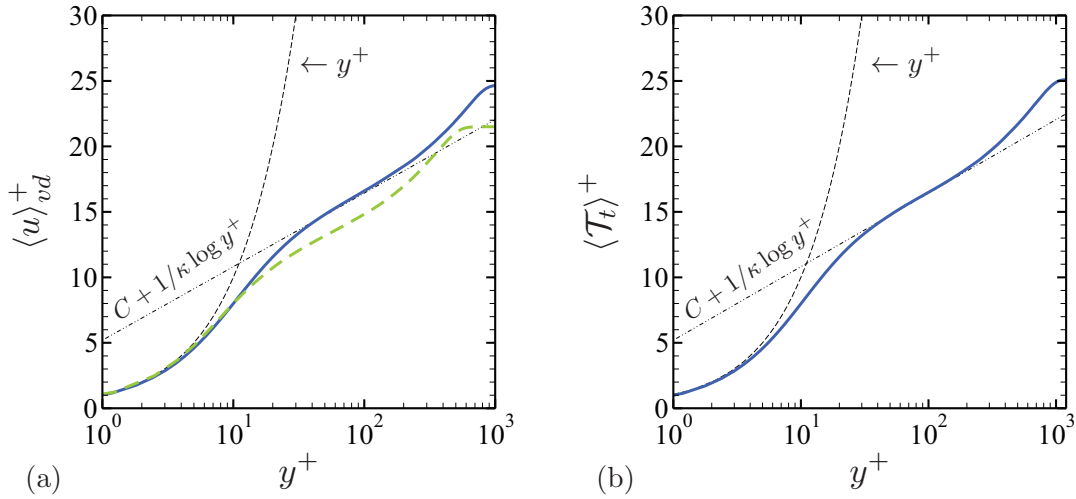


Figure 4.19: (a) Distribution of the van-Driest transformed mean streamwise velocity $\langle u \rangle_{vd}^+$ as a function of y^+ . (b) Distribution of the transformed total temperature $\langle T_t \rangle^+$ as a function of y^+ . $C = 5.2$; $\kappa = 0.41$. (—) Isothermal case; (---) Adiabatic case.

have a constant $C_T \simeq C = 5.2$.

Fig. (4.20) shows the different shear stresses as a function of y^+ for the cold-wall boundary layer, compared to the adiabatic LES case and DNS data by Pirozzoli *et al.* (2004) [76]. It is found that the computed shear stresses are better predicted in the isothermal case than in the adiabatic one, in a way that the cooled boundary layer results are closer to the DNS data. Indeed, it is shown that there is a region of constant total shear stress in the viscous sublayer and the lower part of the boundary layer (Pirozzoli *et al.*, 2004 [76]; Duan *et al.*, 2010 [23]).

The *r.m.s* of static temperature fluctuations are shown in Fig. (4.21). It shows that the temperature fluctuations drastically decrease with wall-cooling, where it attains a peak of 4% of T_∞ against $\approx 10\%$ for the adiabatic case.

Total temperature fluctuations $T_{t_{rms}}$ are shown in Fig. (4.22). In the inner layer, $T_{t_{rms}}$ reaches 6% of T_∞ for the wall-cooling case, while it is less than 4% for the adiabatic case. In the outer region, however, both cases exhibit nearly equal levels. When normalizing by $\langle T_t \rangle$, the peak of $T_{t_{rms}}$ is found to increase and reach $\approx 9\%$ of $\langle T_t \rangle$.

The correlation between the velocity and the temperature fluctuations, $-R_{uT}$, is shown in Fig. (4.23-a). As expected, u' and T' are not found to be anti-correlated as commonly assumed for adiabatic supersonic boundary layers, since the total temperature fluctuations are non-negligible.

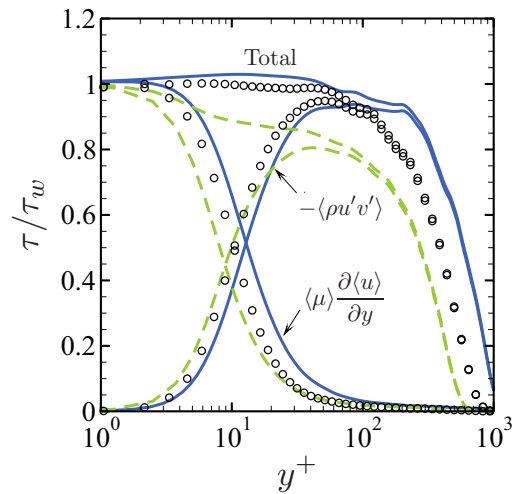


Figure 4.20: Reynolds stress $-\langle \rho u' v' \rangle$, mean viscous shear stress $(\mu) \partial \langle u \rangle / \partial y$ and total shear stress $-\langle \rho u' v' \rangle + (\mu) \partial \langle u \rangle / \partial y$ as a function of y^+ . (—) Isothermal case; (- -) Adiabatic case.

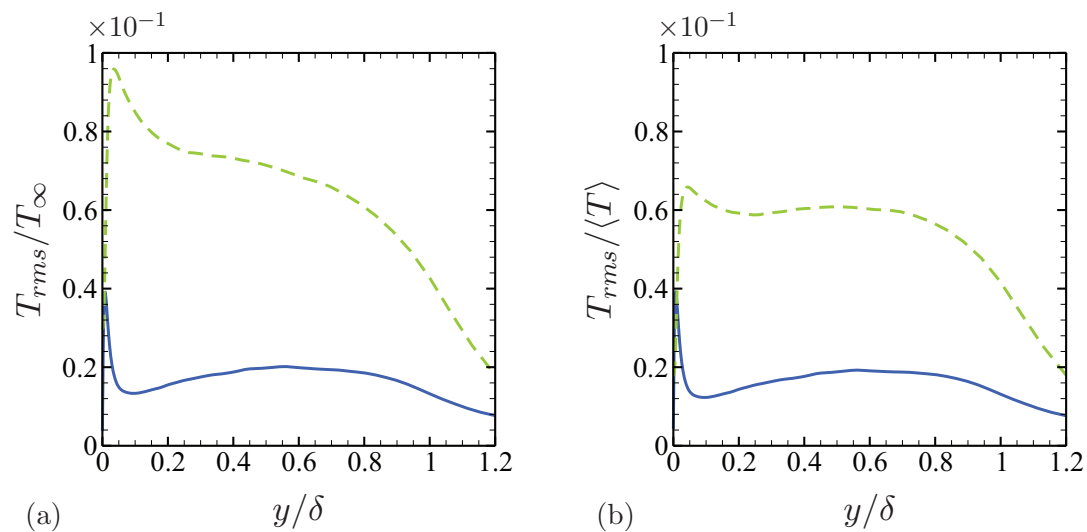


Figure 4.21: Normalized r.m.s. of the static temperature (a) T_{rms}/T_∞ and (b) $T_{rms}/\langle T \rangle$ as a function of y/δ . (—) Isothermal case; (- -) Adiabatic case.

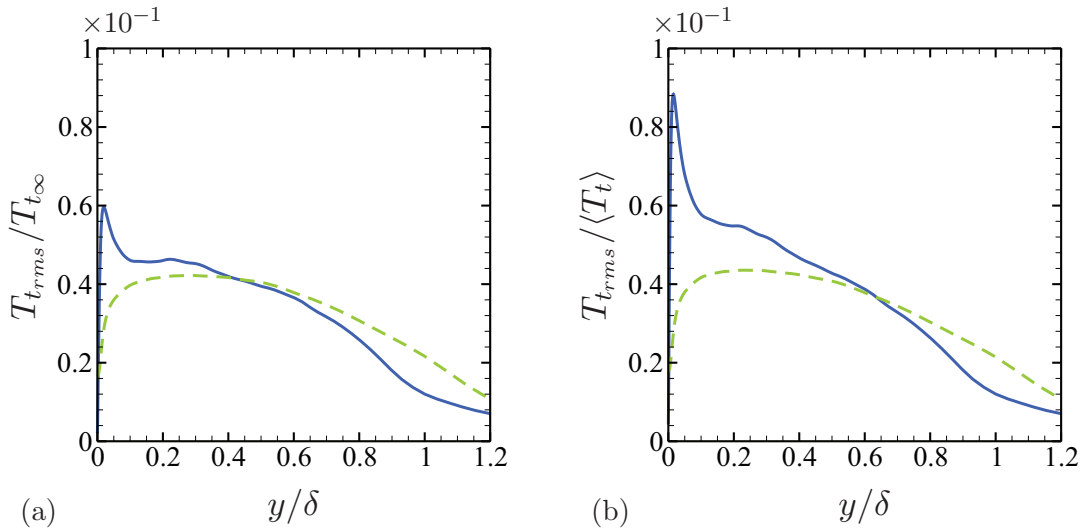


Figure 4.22: Normalized r.m.s. of the total temperature (a) $T_{trms}/T_{t\infty}$ and (b) $T_{trms}/\langle T_t \rangle$ as a function of y/δ . (—) Isothermal case; (---) Adiabatic case.

At the wall, $-R_{uT} \approx -1$, which means that u' and T' are perfectly correlated, feature that has also been reported by Coleman *et al.* (1995) [15] and Duan *et al.* (2010) [23]. This tendency confirms the observation made on the instantaneous velocity and temperature fluctuating fields (Fig. 4.12). When moving away from the wall, $-R_{uT}$ increases, and reaches a maximum of 0.49, a value that is nearly equal to the adiabatic-case result. The change in sign of R_{uT} is found to occur nearly at the location of the maximum temperature distribution. The same tendency has also been observed by Duan *et al.* (2010) [23]. When normalizing with the freestream quantities, the tendency confirms that the main difference with the adiabatic case is reached in a very-near wall region (Fig. 4.23-b), where $\langle u'T' \rangle$ are of opposite signs, a difference that seems to fade in the outer region of the boundary layer.

Fig. (4.24) shows the heat flux $\langle v'T' \rangle$ when normalized by the fluctuating r.m.s quantities (a) and by the free stream quantities (b). A significant decrease of R_{vT} and $\langle v'T' \rangle/u_\infty T_\infty$ is observed with wall-cooling. In a very-near wall region, R_{vT} is negative: equal to -0.35 at the wall, it continues to decrease and attains a peak of -0.45 at $y/\delta \approx 0.01$, where it starts to increase up to $y/\delta \approx 0.1$. At $y/\delta \approx 0.2$, it reaches 0.36 and remains constant (≈ 0.4) up to the edge of the boundary layer. The same tendency is observed with the freestream normalization $\langle v'T' \rangle/u_\infty T_\infty$. $\langle v'T' \rangle/u_\infty T_\infty$ is about 4 times larger in the adiabatic case than in the cold-wall case, with a maximum reached at $y/\delta \approx 0.2$.

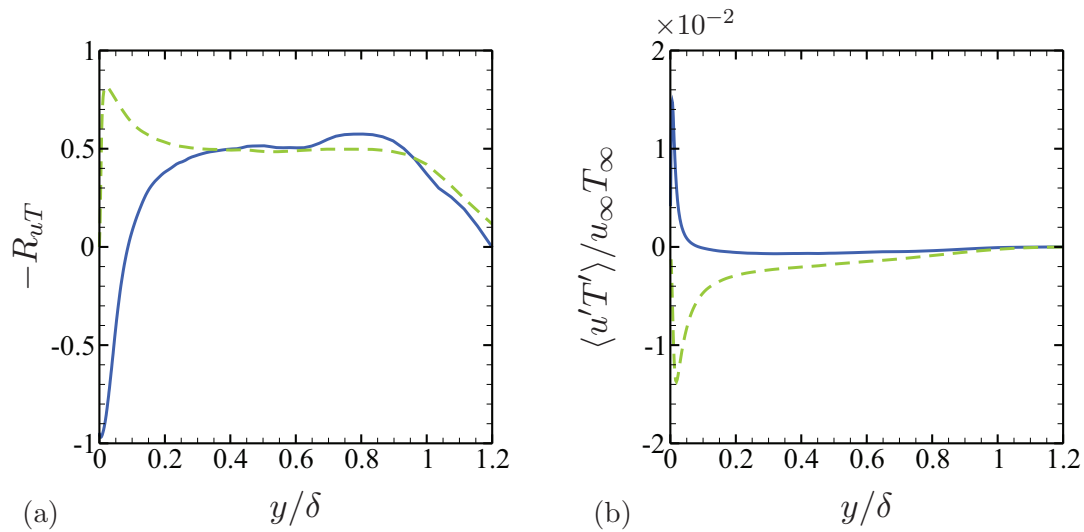


Figure 4.23: (a) $-R_{uT}$ correlation and (b) $\langle u'T' \rangle / u_\infty T_\infty$ heat flux as a function of y/δ . (—) Isothermal case; (- -) Adiabatic case.

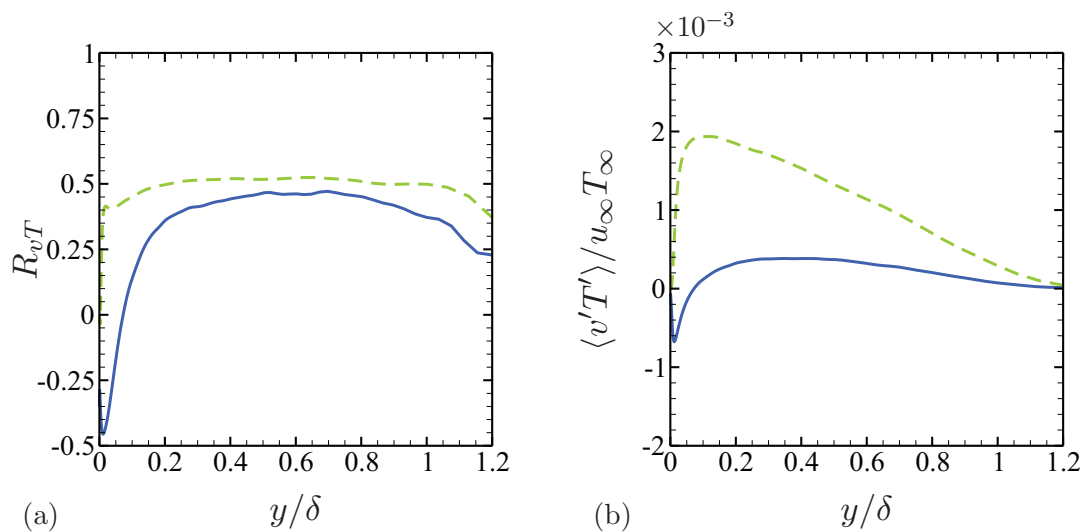


Figure 4.24: (a) R_{vT} correlation and (b) $\langle v'T' \rangle / u_\infty T_\infty$ heat flux as a function of y/δ . (—) Isothermal case; (- -) Adiabatic case.

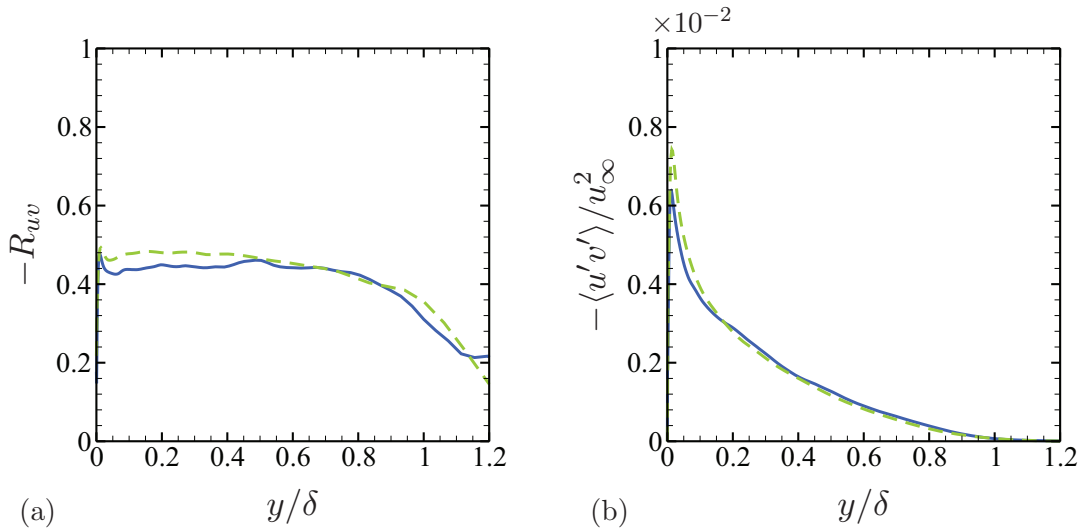


Figure 4.25: (a) $-R_{uv}$ correlation and (b) $\langle u'v' \rangle / u_\infty^2$ shear stress as a function of y/δ . (—) Isothermal case; (---) Adiabatic case.

Figs. (4.25-a) and (4.25-b) plot respectively $-R_{uv}$ correlation and the normalized shear stress $\langle u'v' \rangle / u_\infty^2$ as a function of y/δ . Except a weak decrease in a near-wall region, it is found that the cooling does not have a significant effect on both quantities throughout the layer, where $-R_{uv}$ exhibits its typical adiabatic-wall value ($\simeq 0.45$). Audiffren (1993) [1] showed that the wall heating has a weak influence on $\langle u'v' \rangle$, which seems also to be applicable in the case of wall cooling.

Counter to the adiabatic case, R_{vT} and $-R_{uv}$ are not correlated, at least in the inner region of the boundary layer, which was expected since the total temperature fluctuations are not negligible.

4.2.5 Scatter plots

Scatter plots of the fluctuating variables display fluctuations extracted each time-step at a given streamwise and wall-parallel position ($1 \times 1 \times 120$) of the computational domain.

Fig. (4.26) plot the scattered temperature fluctuations as a function of the streamwise velocity fluctuations (top). As expected, it is shown that the present results does not verify the Morkovin's hypothesis, where the correlation linking u' and T' is found to have a positive slope in the near-wall region, and tend to zero when moving away from the wall.

The modified SRA relations linking u' and T' are written:

$$\frac{T'/\langle T \rangle}{(\gamma - 1)M^2u'/\langle u \rangle} \approx \frac{1}{c(\partial\langle T_t \rangle / \partial\langle T \rangle - 1)} \quad (4.10)$$

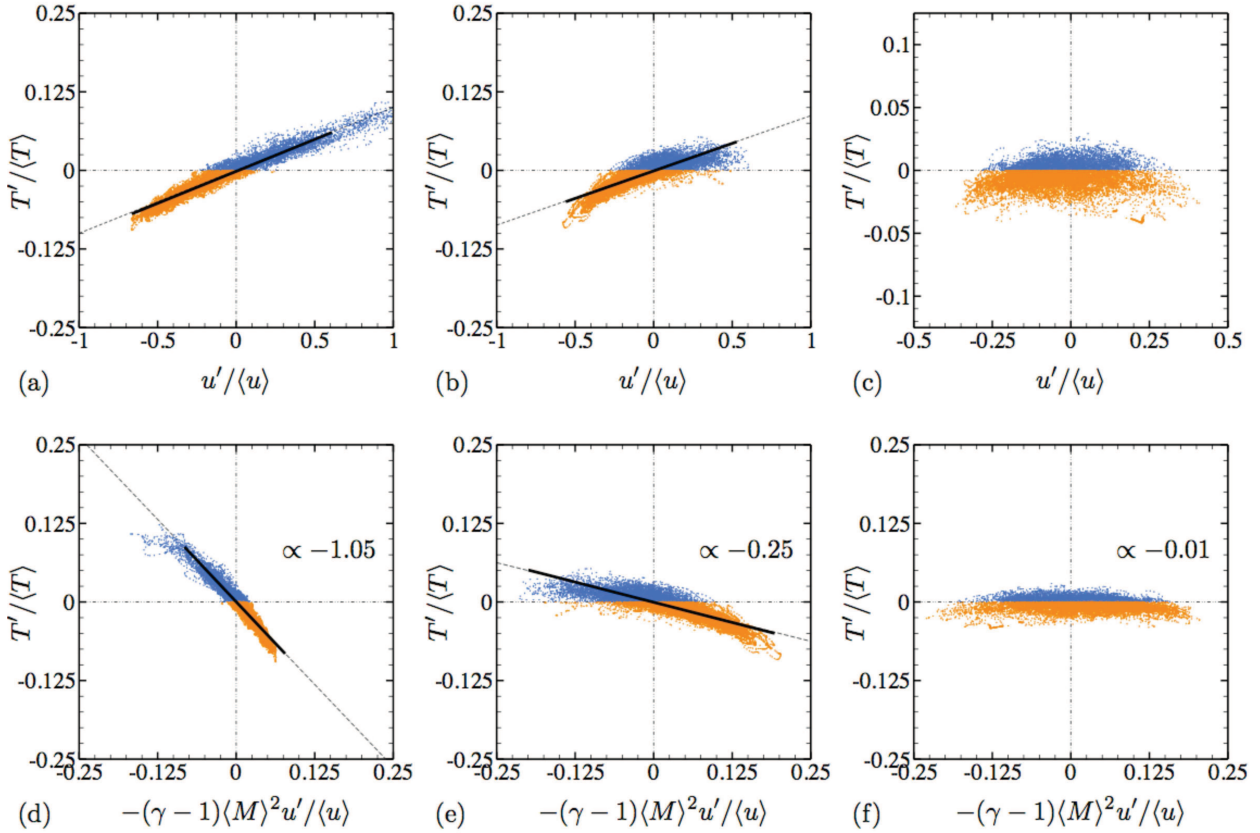


Figure 4.26: Scatter plots of (a-c) the normalized temperature - streamwise velocity fluctuations and (d-f) the *strict* SRA in a wall-normal plane for the cold-wall boundary layer. (a, d) $y^+ \simeq 9$; (b, e) $y^+ \simeq 28$; (c, f) $y^+ \simeq 100$.

where $c = 1$ by Gaviglio (1987) [33], $c = 1.34$ by Rubesin (1990) [79] and $c = \text{Pr}_t$ by Huang *et al.* (1995) [43]. For $c = 1$, the equation gives $\partial\langle T_t \rangle / \partial\langle T \rangle \simeq 1.95$ in a very near-wall region ($y^+ \simeq 9$). Lechner *et al.* (2001) [57] found similar results in a DNS of supersonic isothermal channel flow, where $\partial\langle T_t \rangle / \partial\langle T \rangle = 2.08$ gave a value of $c = 1.05$.

Assuming a polytropic behavior of the thermodynamic quantities, the fluctuations ρ' and T' are assumed to be perfectly correlated. This result is not verified in the present cold-wall boundary layer, where a linear-fitting slope of 0.65 is found in the near-wall region (Fig. 4.27).

As written for the adiabatic case, when neglecting the pressure fluctuations, the normalized entropy fluctuations, s'/C_v , should have a slope proportional to $-\gamma$ when shown against $\rho'/\langle \rho \rangle$. In a very near-wall region, this slope is found to be proportional to -0.91 , which can be explained by a non-negligible level of pressure fluctuations (Fig. 4.28).

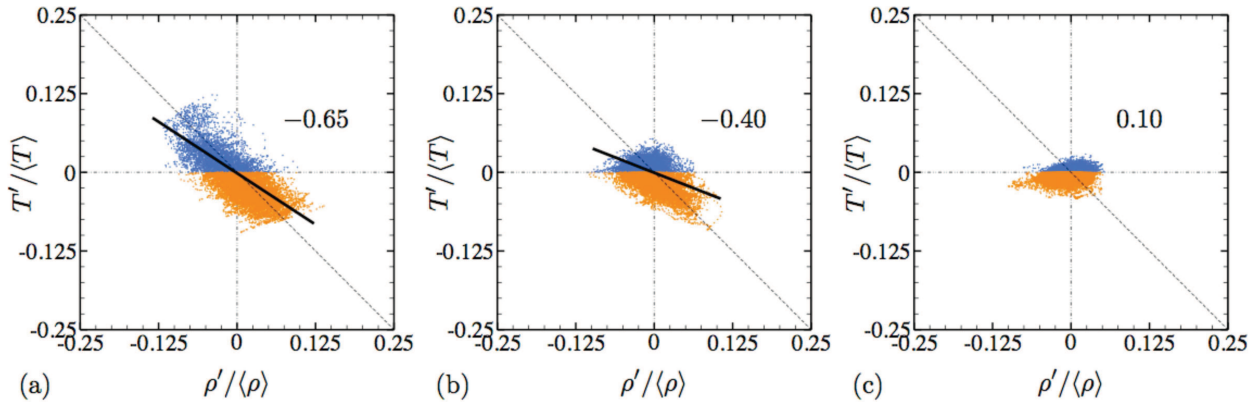


Figure 4.27: Scatter plots of the normalized temperature - density fluctuations in a wall-normal plane for the cold-wall boundary layer. (a) $y^+ \simeq 9$; (b) $y^+ \simeq 28$; (c) $y^+ \simeq 100$.

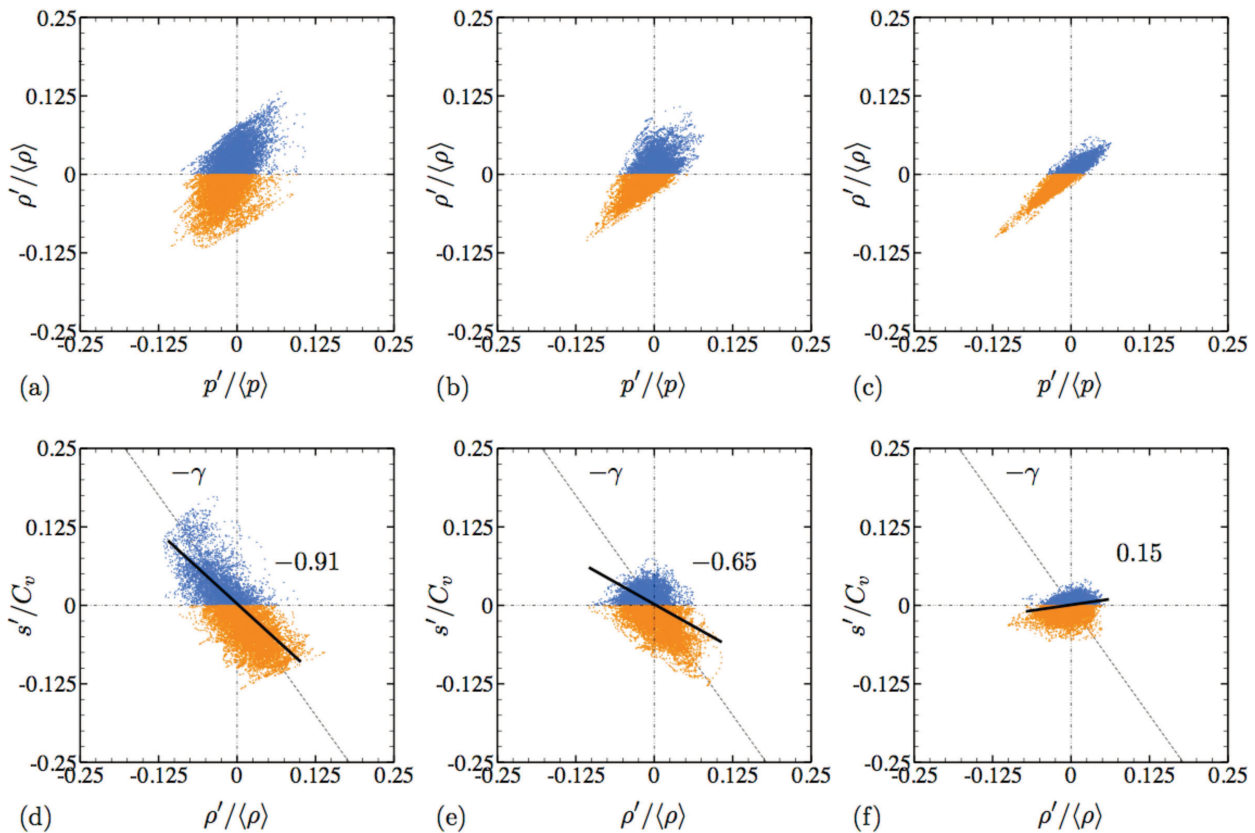


Figure 4.28: Scatter plots of (a-c) the normalized density - pressure fluctuations and (d-f) the normalized entropy - density fluctuations in a wall-normal plane for the cold-wall boundary layer. (a, d) $y^+ \simeq 9$; (b, e) $y^+ \simeq 28$; (c, f) $y^+ \simeq 100$.

The total temperature fluctuations is defined as (Lechner *et al.*, 2001) [57]:

$$T'_t \approx T' + \frac{1}{C_p} \left(\langle u \rangle u' + \frac{u'_i u'_i - \langle u'_i u'_i \rangle}{2} \right) \quad (4.11)$$

which can be expanded to:

$$\frac{T'_t}{\langle T_t \rangle} = \frac{\langle T \rangle}{\langle T_t \rangle} \left(\frac{T'}{\langle T \rangle} + (\gamma - 1) \langle M \rangle^2 \left(\frac{u'}{\langle u \rangle} + \frac{u'^2 - \langle u'^2 \rangle}{2 \langle u \rangle^2} \right) \right) \quad (4.12)$$

Fig. (4.29) shows the scattered total temperature fluctuations as a function of the temperature fluctuations, velocity fluctuations and kinetic energy fluctuations. As it was concluded by Lechner *et al.* (2001) [57], in the near-wall region, the contribution of the temperature, velocity and kinetic energy fluctuations is of the same order, and none of those quantities can be neglected ($(\gamma - 1) \langle M \rangle^2 \simeq 0.095$ and $\langle T \rangle / \langle T_t \rangle \simeq 0.96$).

To a first order, $T'_t / \langle T_t \rangle$ can be written:

$$\frac{T'_t}{\langle T_t \rangle} \approx (\gamma - 1) \langle M \rangle^2 \frac{T}{\langle T_t \rangle} \frac{u'}{\langle u \rangle} \quad (4.13)$$

Fig. (4.30) confirms that approximating $T'_t / \langle T_t \rangle$ as written in Eq. (4.13) does not hold for the near-wall region, and can only be adopted in a region sufficiently far from the wall ($y^+ \geq 100$).

4.2.6 Conclusion

In this chapter, basic properties and flow characteristics of isothermal supersonic turbulent boundary layers were investigated using LES. The nearly-adiabatic boundary layer statistics show overall comparable results with the adiabatic LES data. The only difference concerns the near-wall asymptotic behavior, where T_{rms} and $\langle v' T' \rangle$ admit respectively y^+ and y^{+3} as near-wall asymptotes. For the cold-wall supersonic turbulent boundary layer, first- as well as second-order statistics are analyzed. It is found that the compressibility effects are not enhanced due to the cooling, where the turbulent Mach number does not exceed 0.4 throughout the boundary layer. The velocity fluctuations scaled according to the Morkovin's hypothesis exhibit acceptable agreement with experimental data of an adiabatic supersonic turbulent boundary layer results. As expected, the total temperature fluctuations are found to be higher than that of the adiabatic case. As a consequence, the

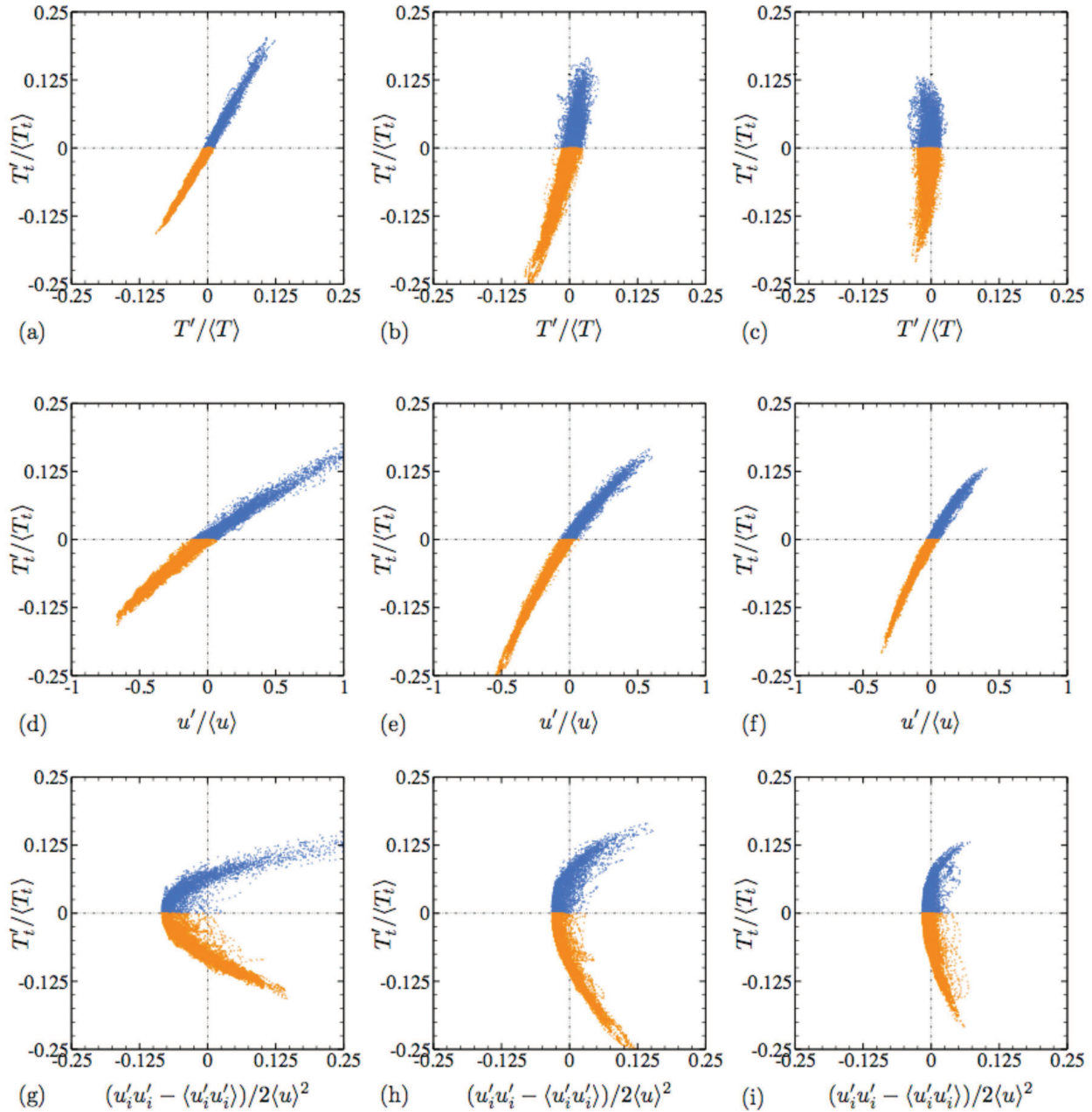


Figure 4.29: Scatter plots of (a-c) the normalized total-temperature - temperature fluctuations, (d-f) the normalized total-temperature - velocity fluctuations and (g-i) the normalized total-temperature kinetic energy fluctuations in a wall-normal plane for the cold-wall boundary layer. (a, d, g) $y^+ \simeq 9$; (b, e, h) $y^+ \simeq 28$; (c, f, i) $y^+ \simeq 100$.

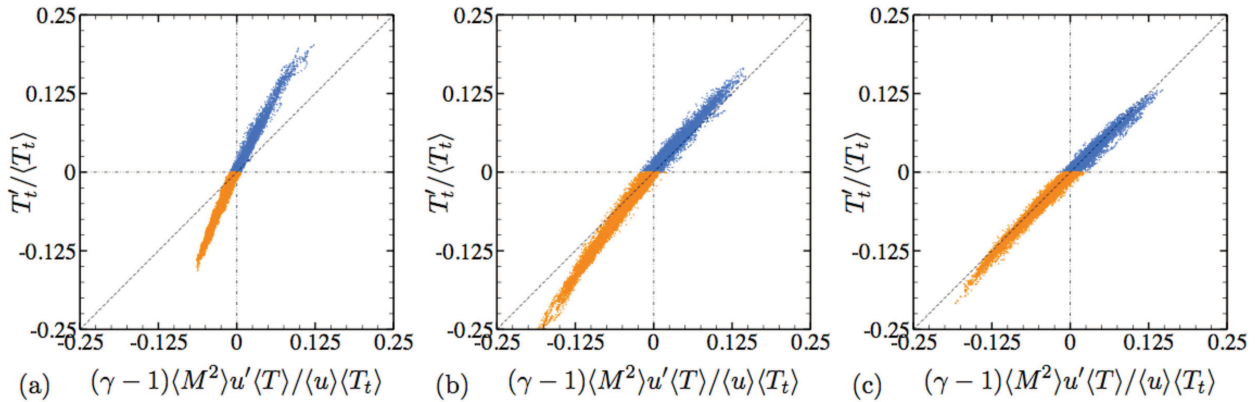


Figure 4.30: Scatter plots of the total-temperature - velocity fluctuations in a wall-normal plane for the cold-wall boundary layer. (a) $y^+ \approx 9$. (b) $y^+ \approx 28$. (c) $y^+ \approx 100$.

velocity and the temperature fluctuations are not anti-correlated, as concluded for adiabatic flows. Instead, a strong relationship between u' and T' exists in the near-wall region. These tendencies were also verified through instantaneous scatter plots.

Chapter 5

Conclusions & perspectives

This study, conducted within the ATAC¹ research program under the auspices of the French Space Agency², is a part of a large activity dedicated to experimental and numerical analysis of side-loads in rocket nozzles. The focus here is to study the dynamics of a supersonic boundary layer and its effect on heat transfer at solid walls. This configuration represents a basic element towards full characterization of complex unsteady turbulent flows in rocket nozzles.

The current investigation deals with high-fidelity numerical simulations of wall heat transfers in three-dimensional supersonic turbulent boundary layers (TBL). The use of three-dimensional direct- and large-eddy simulations of TBL was shown to well determine the physical mechanisms behind the turbulent transport/diffusion formation and the general properties of the boundary layer, which depends critically on the development of large-scale turbulent structures.

In this study, the equations governing the considered flows are solved using an in-house solver, named CHOC-WAVES, which is a three-dimensional multi-species solver with variable thermodynamic properties running on massively parallel computers with an Immersed Boundary Method, in order to handle complex geometries. The code is based on low-dissipation high-order accurate methods in finite difference formulation, typically fourth- or sixth-order in space and third order in time.

Our choice has been directed towards the use of a skew-symmetric *split-centered* conservative scheme for the convective fluxes. In terms of turbulence modeling, several subgrid scale models have been used to model the action of the small scale structures on the turbulence: the dynamic

¹Aérodynamique des Tuyères et Arrière-Corps.

²Centre National d'Études Spatiales, CNES

Smagorinsky model (DSM), the coherent structures model (CSM) and the WALE model, as well as an Implicit approach, in order to assess the contribution of the subgrid scale terms. For the considered subgrid scale models, the main statistical quantities showed an overall acceptable agreement compared to results available in the literature. Both the CSM and the WALE models showed good near-wall scaling and better prediction of the wall-properties. The use of an Implicit LES highlighted a lack of subgrid scale dissipation that affected some thermodynamic quantities, where a *bump* in *r.m.s* of the temperature fluctuations in the outer region of the boundary layer was observed, which could be due to the manifestation of an accumulation of non-dissipated energy in this region. Based on the different subgrid scale dissipation terms, an attempt was made to set a criterion for evaluating the quality of LES grid resolutions.

Based on this analysis, the CSM model was selected for the study of an isothermal supersonic turbulent boundary layer. The obtained results, corroborated by the state-of-the-art literature data, showed that the main conclusions made for wall-bounded turbulent shear flows incompressible adiabatic flows can be adopted for the case of adiabatic as well as isothermal supersonic flows, as long as the variations in the mean flow properties are taken into account, which is the basis of the well-known Morkovin's hypothesis. Strong compressibility effects were found to be negligible, and could be taken into account by density scaling. The temperature as well as the velocity fluctuating fields were found to be weakly correlated, and were linked through the *Strong Reynolds Analogy*. The second part of the study was dedicated to the analysis of basic properties and flow characteristics of LES of cold-wall supersonic turbulent boundary layer. The velocity fluctuations, which were scaled according to the Morkovin's hypothesis, showed acceptable agreement with the experimental results. As expected, the total temperature fluctuations were found to be higher when compared to the adiabatic case. Furthermore, the velocity and temperature fluctuations were not anti-correlated, since a strong correlation linked u' and T' in the near-wall region ($y^+ \simeq 9$). These tendencies were also verified through instantaneous scatter plots of the fluctuating quantities at different distances from the wall.

Based on the present work, and taking into account the current progress in numerical methods and high-performance computing, the large-eddy simulation is found to be a promising tool for studying such complex phenomena.

As an outlook, to further understand the near-wall dynamics in supersonic bounded flows, some future works can be addressed:

- Comparative study of strongly cooled/heated boundary layers at fixed wall-heat flux. This point will help to clarify the change in the large-scale structures dynamics, and will bring more light into the mechanisms of energy transfer between the different turbulent fluctuating components in case where energy is added/extracted from the fluid. Another important point is to highlight the stabilizing/destabilizing effects of turbulence under strong thermal constraints.
- Study of the dynamics and wall heat-transfer in a wall-jet blowing parallel along a wall in order to be closer to the case of film cooling in supersonic nozzles.

List of Figures

1.1	<i>Vulcain II</i> engine, at the P5 test bench in DLR Lampoldshausen, Germany (left); Nozzle geometry with the dump cooling design (right). (Suslov <i>et al.</i> , 2010) [96].	2
1.2	General diagram of a turbulent boundary layer on a flat plate (Schlichting, 1979 [82]).	7
2.1	Spectre d'énergie typique dans un écoulement turbulent homogène.	19
2.2	Spectre d'énergie de l'approche Dynamique du modèle de Smagorinsky.	22
2.3	Choix des stencils pour la reconstruction des flux dans le cas du schéma WENO du 5 ^{ème} ordre.	29
2.4	Choix des stencils pour la reconstruction des flux dans le cas du schéma WENO du 5 ^{ème} ordre à Large Bande optimisé.	30
2.5	Domaine de calcul et conditions aux limites de la configuration étudiée.	37
3.1	Computational domain size.	46
3.2	Instantaneous flow field for the LES-L1 grid with the CSM model: (center) Q-criterion iso-surface colored with the temperature field [25]; (top) Instantaneous temperature field in a x - y plane; (bottom) Temperature fluctuations field in the x - z plane at $y^+ \simeq 9$	49
3.3	Instantaneous (a) velocity and (b) temperature fluctuation fields in the x - z plane at $y^+ \simeq 9$, for LES-L1 using the CSM model. Contour levels are shown for (a) $-0.2 \leq u'/u_\infty \leq 0.2$ and (b) $-0.2 \leq T'/T_\infty \leq 0.2$, from dark to light shades.	50
3.4	Instantaneous auto-correlation coefficients at $y^+ \simeq 9$. (a-c) SGS models study using LES-P2 grid; (d-f) Grid sensitivity study using CSM model. For legend, see table 3.4.	52

3.5 Incompressible skin-friction coefficient $C_{f_{inc}}$ as a function of Reynolds number based on incompressible momentum thickness $\text{Re}_{\theta_{inc}}$. (—) Blasius; (·—·) Kármán Schoenherr; (···) Smits <i>et al.</i> (1983); ■ Pirozzoli <i>et al.</i> ($M=2.25$); ◆ Guarini <i>et al.</i> ($M=2.5$); ▲ Maeder <i>et al.</i> ($M=3$); ● Pirozzoli & Bernardini ($M=2$). (a) SGS models study using LES-P2 grid; (b) Grid sensitivity study using CSM model. For legend, see table 3.4.	54
3.6 Normalized <i>r.m.s.</i> wall-pressure distribution p_{rmsw}/τ_w as a function of Reynolds number Re_τ . (—) Farabee & Casarella (1991) [28]; (·—·) Bernardini & Pirozzoli (2011) [9]. (a) SGS models study using LES-P2 grid; (b) Grid sensitivity study using CSM model. For legend, see table 3.4.	55
3.7 Turbulent Mach number, M_t , as a function of y/δ . (a) SGS models study using LES-P2 grid; (b) Grid sensitivity study using CSM model. For legend, see table 3.4.	56
3.8 Distributions of the time-averaged mean quantities as a function of y/δ . (a) SGS models study using LES-P2 grid; (b) Grid sensitivity study using CSM model. For legend, see table 3.4.	57
3.9 Distribution of the normalized time-averaged total temperature, $\langle T_t \rangle / T_{t_\infty}$, as a function of y/δ . ○ DNS Pirozzoli <i>et al.</i> (2004) [76] at $\text{Re}_\theta = 4260$. (a) SGS models study using LES-P2 grid; (b) Grid sensitivity study using CSM model. For legend, see table 3.4.	58
3.10 Distribution of the van-Driest transformed mean streamwise velocity $\langle u \rangle_{vd}^+$ as a function of y^+ . $C = 5.2$; $\kappa = 0.41$. (a) SGS models study using LES-P2 grid; (b) Grid sensitivity study using CSM model. For legend, see table 3.4.	59
3.11 Normalized mean velocity deficit $u_{vd_\infty} - u_{vd}/u_\tau$ as a function of y/δ . (a) SGS models study using LES-P2 grid; (b) Grid sensitivity study using CSM model. For legend, see table 3.4. .	60
3.12 (a-b) <i>r.m.s</i> of velocity fluctuations components $u_{i,rms}/u_\tau$ as a function of y/δ ; (c-d) <i>r.m.s</i> velocity fluctuations in Morkovin's scaling as a function of y^+ ; (e-f) <i>r.m.s</i> velocity fluctuations in Morkovin's scaling as a function of y^+ in Log-scale. (·—·) Perry & Li (1990) [70] in Eq. 3.12. (—) Pirozzoli <i>et al.</i> (2004) [76] in Eq. 3.11. For legend, see table 3.4.	62
3.13 Normalized turbulent kinetic energy K/u_τ^2 as a function of y/δ . (a) SGS models study using LES-P2 grid; (b) Grid sensitivity study using CSM model; (c) Resolved turbulent kinetic energy K^+ and SGS turbulent kinetic energy k_{sgs}^+ for the LES-P2 grid using the DSM model as a function of y^+ . For legend, see table 3.4.	63

3.14 Structure parameter $-\langle u'v' \rangle / 2K$ as a function of y/δ . (a) SGS models study using LES-P2 grid; (b) Grid sensitivity study using CSM model. For legend, see table 3.4.	63
3.15 Distribution of <i>r.m.s.</i> vorticity components as a function of y^+ . (a) SGS models study using LES-P2 grid; (b) Grid sensitivity study using CSM model. For legend, see table 3.4.	64
3.16 Turbulent shear stress $-\langle \rho u'v' \rangle$, mean viscous shear stress $\langle \mu \rangle \partial \langle u \rangle / \partial y$ and total shear stress $-\langle \rho u'v' \rangle + \langle \mu \rangle \partial \langle u \rangle / \partial y$ as a function of y^+ . (a) SGS models study using LES-P2 grid; (b) Grid sensitivity study using CSM model. For legend, see table 3.4.	65
3.17 (a) Distribution of the van-Driest transformed mean streamwise velocity $\langle u \rangle_{vd}^+$ as a function of y^+ ; (b) <i>r.m.s</i> velocity fluctuations in Morkovin's scaling as a function of y^+ . ($\cdot - \cdot$) WENO-BWO scheme; (\cdots) 4 th split-centered; ($-\cdot-$) 6 th split-centered.	66
3.18 Normalized SGS viscosity, μ_{sgs}/μ , as a function of y^+ . (a) SGS models study using LES-P2 grid; (b) Grid sensitivity study using CSM model. For legend, see table 3.4.	67
3.19 Ratio of the turbulent kinetic energy Γ as a function of y^+ . (a) SGS models study using LES-P2 grid; (b) Grid sensitivity study using CSM model. For legend, see table 3.4.	69
3.20 Contribution of the different SGS dissipation terms to turbulence.	69
3.21 (a-d) Ratio of the SGS dissipation due to the fluctuating flowfield to the total SGS dissipation $\varepsilon'_{sgs}/\varepsilon_{sgs}$ as a function of y^+ ; (b-e) Ratio of the SGS dissipation due to the mean-averaged flowfield to the total SGS dissipation $\varepsilon_{\langle sgs \rangle}/\varepsilon_{sgs}$ as a function of y^+ ; (c-f) Ratio of the SGS dissipation due to the fluctuating flowfield in a wall-parallel plane to the total SGS dissipation due to the fluctuating flowfield $\varepsilon'_{sgs_{xz}}/\varepsilon'_{sgs}$ as a function of y^+ . (a-b-c) SGS models study using LES-P2 grid; (d-e-f) Grid sensitivity study using CSM model. For legend, see table 3.4.	72
3.22 SGS Activity parameter ς as a function of y^+ . (a-b-c) SGS models study using LES-P2 grid; (d-e-f) Grid sensitivity study using CSM model. For legend, see table 3.4.	74
3.23 Ratio of the SGS dissipation to the viscous dissipation as a function of y^+ . (a) SGS models study using LES-P2 grid; (b) Grid sensitivity study using CSM model. For legend, see table 3.4.	75
3.24 Normalized <i>r.m.s.</i> of the thermodynamic quantities as a function of y/δ . (a-b-c) SGS models study using LES-P2 grid; (d-e-f) Grid sensitivity study using CSM model. For legend, see table 3.4.	77

3.25 SRA and $-R_{uT}$ correlations as a function of y/δ . Circle: Pirozzoli <i>et al.</i> (2004) [76]. (a) SGS models study using LES-P2 grid; (b) Grid sensitivity study using CSM model. For legend, see table 3.4.	79
3.26 Modified SRA as a function of y/δ . (a, b, c) SGS models study using LES-P2 grid; (d, e, f) Grid sensitivity study using CSM model. For legend, see table 3.4.	80
3.27 $-R_{\rho T}$, $-R_{uv}$ and R_{vT} correlations as a function of y/δ . (a, c, e) SGS models study using LES-P2 grid; (b, d, f) Grid sensitivity study using CSM model. For legend, see table 3.4.	82
3.28 Resolved turbulent Prandtl number as a function of y/δ . (--) DNS curve-fitting in Eq. (3.37). (a) SGS models study using LES-P2 grid; (b) Grid sensitivity study using CSM model. For legend, see table 3.4.	83
3.29 Resolved turbulent Prandtl number Pr_t and Huang's relation (Eq. 3.36) as a function of y/δ . (a) SGS models study using LES-P2 grid; (b) Grid sensitivity study using CSM model. For legend, see table 3.4.	84
3.30 Scatter plots of (a-c) the normalized temperature - streamwise velocity fluctuations and (d-f) the normalized temperature - wall-normal velocity fluctuations in a wall-normal plane for the CSM-P2 case. (a, d) $y^+ \simeq 9$; (b, e) $y^+ \simeq 28$; (c, f) $y^+ \simeq 100$	85
3.31 Scatter plots of the <i>strict</i> SRA in a wall-normal plane for the CSM-P2 case. (a) $y^+ \simeq 9$; (b) $y^+ \simeq 28$; (c) $y^+ \simeq 100$	86
3.32 Scatter plots of the normalized temperature - density fluctuations in a wall-normal plane for CSM-P2 case. (a) $y^+ \simeq 9$. (b) $y^+ \simeq 28$. (c) $y^+ \simeq 100$	86
3.33 Scatter plots of the normalized density - pressure fluctuations in a wall-normal plane for CSM-P2 case. (a) $y^+ \simeq 9$; (b) $y^+ \simeq 28$; (c) $y^+ \simeq 100$	87
3.34 Scatter plots of (a-c) the normalized entropy-density fluctuations and (d-f) the normalized entropy-pressure fluctuations in a wall-normal plane for CSM-P2 case. (a, d) $y^+ \simeq 9$; (b, e) $y^+ \simeq 28$; (c, f) $y^+ \simeq 100$	88
3.35 Scatter plots of (a-c) the normalized total-temperature - temperature fluctuations and (d-f) the normalized total temperature - velocity fluctuations in a wall-normal plane for the nearly-adiabatic CSM-P2 case. (a, d) $y^+ \simeq 9$; (b, e) $y^+ \simeq 28$; (c, f) $y^+ \simeq 100$	89
3.36 Anisotropy invariants map.	91
3.37 Anisotropy invariants maps. (a) SGS models study using LES-P2 grid; (b) Grid sensitivity study using CSM model. For legend, see table 3.4.	92

3.38 (a, b) Skewness and (c, d) Flatness factors as a function of y^+ . For legend, see table 3.4.	93
3.39 Near-wall asymptotic behavior of the streamwise velocity fluctuations u_{rms} in Morkovin's scaling as a function of y^+ . (a) SGS models study using LES-P2 grid; (b) Grid sensitivity study using CSM model. For legend, see table 3.4.	95
3.40 Near-wall asymptotic behavior of the wall-normal velocity fluctuations v_{rms} in Morkovin's scaling as a function of y^+ . (a) SGS models study using LES-P2 grid; (b) Grid sensitivity study using CSM model. For legend, see table 3.4.	96
3.41 Near-wall asymptotic behavior of the spanwise velocity fluctuations w_{rms} in Morkovin's scaling as a function of y^+ . (a) SGS models study using LES-P2 grid; (b) Grid sensitivity study using CSM model. For legend, see table 3.4.	96
3.42 Near-wall asymptotic behavior of the normalized Reynolds shear stress $\langle u'v' \rangle^+$ as a function of y^+ . (a) SGS models study using LES-P2 grid; (b) Grid sensitivity study using CSM model. For legend, see table 3.4.	97
3.43 Near-wall asymptotic behavior of (a-b) the normalized kinetic Energy and (c-d) the normalized molecular dissipation as a function of y^+ . For legend, see table 3.4.	98
3.44 Near-wall asymptotic behavior of the normalized turbulent heat flux, R_{vT} , as a function of y^+ . (a) SGS models study using LES-P2 grid; (b) Grid sensitivity study using CSM model. For legend, see table 3.4.	99
3.45 Near-wall asymptotic behavior of (a) the temperature, (b) the density and (c) the pressure fluctuations as a function of y^+ . For legend, see table 3.4.	99
3.46 Ratios of the turbulent energy dissipation rate terms as a function of y/δ	101
3.47 Ratio of the dilatational to the solenoidal dissipation as a function of (a) y/δ and (b) turbulent Mach number M_t	102
4.1 (a) Incompressible skin-friction coefficient $C_{f_{inc}}$ as a function of Reynolds number based on incompressible momentum thickness $Re_{\theta_{inc}}$. (b) Normalized <i>r.m.s.</i> wall-pressure distribution p_{rms_w}/τ_w as a function of the Reynolds number Re_τ . \blacklozenge Nearly-adiabatic condition; \blacksquare Adiabatic condition. For legend, see caption in Fig. (3.5).	107
4.2 (a) Near-wall asymptotic behavior of the normalized turbulent kinetic energy and (b) the normalized dissipation rate as a function of y^+ . (—) Nearly-adiabatic condition; (- -) Adiabatic condition.	108

4.3 (a) Near-wall asymptotic behavior of the normalized <i>r.m.s</i> temperature fluctuations T_{rms}/T_∞ and (b) Near-wall asymptotic behavior of the normalized heat flux R_{vT} as a function of y^+ . (—) Nearly-adiabatic condition; (- -) Adiabatic condition.	108
4.4 (a) Distributions of the time-averaged mean quantities as a function of y/δ . (b) Distribution of the normalized time-averaged total temperature $\langle T_t \rangle / T_{t\infty}$ as a function of y/δ . Circle: DNS Pirozzoli & Bernardini (2011) [74]. (—) Nearly-adiabatic condition; (- -) Adiabatic condition.	109
4.5 (a) Distribution of the van-Driest transformed mean streamwise velocity $\langle u \rangle_{vd}^+$ as a function of y^+ . (b) <i>r.m.s</i> velocity fluctuations in Morkovin's scaling as a function of y^+ . The two constants of the log-region profile are $C = 5.2$ and $\kappa = 0.41$. Circle: DNS Pirozzoli & Bernardini (2011) [74]. (—) Nearly-adiabatic condition; (- -) Adiabatic condition.	110
4.6 Normalized <i>r.m.s.</i> of the thermodynamic quantities as a function of y/δ . (—) Nearly-adiabatic condition; (- -) Adiabatic condition.	110
4.7 (a) SRA and $-R_{uT}$ correlations as a function of y/δ . (—) Nearly-adiabatic condition; (- -) Adiabatic condition. (b) Modified SRA relations as a function of y/δ ; (—) SRA; (—) ESRA; (···) HSRA; (··) GSRA.	111
4.8 $-R_{uv}$, R_{vT} correlations and structure parameter $-\langle u'v' \rangle / 2K$ as a function of y/δ . (—) Nearly-adiabatic condition; (- -) Adiabatic condition.	112
4.9 Scatter plots of the <i>strict</i> SRA in a wall-normal plane for the nearly-adiabatic CSM-P2 case. (a) $y^+ \approx 9$. (b) $y^+ \approx 28$. (c) $y^+ \approx 100$	112
4.10 Scatter plots of the normalized temperature - density fluctuations in a wall-normal plane for CSM-P2 case. (a) $y^+ \approx 9$. (b) $y^+ \approx 28$. (c) $y^+ \approx 100$	113
4.11 Incompressible skin-friction coefficient, $C_{f_{inc}}$, as a function of Reynolds number based on the incompressible momentum thickness, $Re_{\theta_{inc}}$. (···) Smits <i>et al.</i> (1983) [90]; ● Adiabatic DNS ($M=2$), Pirozzoli & Bernardini (2011) [74]; ■ Isothermal ($T_w/T_\infty \approx 0.6$, $M=0.06$), Back <i>et al.</i> (1970) [2]; ▲ Adiabatic LES ($M=2$); ◆ Isothermal LES ($T_w/T_\infty \approx 0.85$, $M=2$).	116
4.12 (a) Instantaneous velocity fluctuations field and (b) temperature fluctuations field in the x - z plane at $y^+ \approx 9$. Contour levels are shown for $-0.25 \leq u'/u_\infty \leq 0.25$ and $-0.12 \leq T'/T_\infty \leq 0.12$, from dark to light shades.	118

4.13 (a) Near-wall asymptotic behavior of the normalized <i>r.m.s</i> temperature fluctuations, T_{rms}/T_∞ and (b) Near-wall asymptotic behavior of the normalized heat flux, R_{vT} , as a function of y^+ . (—) Isothermal case; (---) Adiabatic case.	119
4.14 (a) Anisotropy invariants map. (b) Structure parameter as a function of y/δ . \circ DNS Pirozzoli & Bernardini (2011). (—) Isothermal case; (---) Adiabatic case.	120
4.15 Anisotropy ratios as a function of y^+ . (a) v_{rms}^2/u_{rms}^2 ; (b) v_{rms}^2/u_{rms}^2 . (—) Isothermal case; (---) Adiabatic case.	120
4.16 Turbulent Mach number, M_t , as a function of y/δ . (—) Isothermal case; (---) Adiabatic case.	121
4.17 (a) Distributions of the time-averaged mean quantities as a function of y/δ . (b) Predicted Walz's equation. (—) Isothermal case; (---) Adiabatic case.	122
4.18 <i>r.m.s</i> velocity fluctuations in Morkovin's scaling as a function of y/δ . Symbols: Adiabatic ($M = 2.28$), Piponnaiu (2009) [71]; Diamond: PIV; Triangle: LDA. (—) Isothermal case; (---) Adiabatic case.	123
4.19 (a) Distribution of the van-Driest transformed mean streamwise velocity $\langle u \rangle_{vd}^+$ as a function of y^+ . (b) Distribution of the transformed total temperature $\langle T_t \rangle^+$ as a function of y^+ . $C = 5.2$; $\kappa = 0.41$. (—) Isothermal case; (---) Adiabatic case.	124
4.20 Reynolds stress $-\langle \rho u' v' \rangle$, mean viscous shear stress $\langle \mu \rangle \partial \langle u \rangle / \partial y$ and total shear stress $-\langle \rho u' v' \rangle + \langle \mu \rangle \partial \langle u \rangle / \partial y$ as a function of y^+ . (—) Isothermal case; (---) Adiabatic case.	125
4.21 Normalized <i>r.m.s.</i> of the static temperature (a) T_{rms}/T_∞ and (b) $T_{rms}/\langle T \rangle$ as a function of y/δ . (—) Isothermal case; (---) Adiabatic case.	125
4.22 Normalized <i>r.m.s.</i> of the total temperature (a) T_{rms}/T_∞ and (b) $T_{rms}/\langle T_t \rangle$ as a function of y/δ . (—) Isothermal case; (---) Adiabatic case.	126
4.23 (a) $-R_{uT}$ correlation and (b) $\langle u' T' \rangle / u_\infty T_\infty$ heat flux as a function of y/δ . (—) Isothermal case; (---) Adiabatic case.	127
4.24 (a) R_{vT} correlation and (b) $\langle v' T' \rangle / u_\infty T_\infty$ heat flux as a function of y/δ . (—) Isothermal case; (---) Adiabatic case.	127
4.25 (a) $-R_{uv}$ correlation and (b) $\langle u' v' \rangle / u_\infty^2$ shear stress as a function of y/δ . (—) Isothermal case; (---) Adiabatic case.	128
4.26 Scatter plots of (a-c) the normalized temperature - streamwise velocity fluctuations and (d-f) the <i>strict</i> SRA in a wall-normal plane for the cold-wall boundary layer. (a, d) $y^+ \simeq 9$; (b, e) $y^+ \simeq 28$; (c, f) $y^+ \simeq 100$	129

4.27 Scatter plots of the normalized temperature - density fluctuations in a wall-normal plane for the cold-wall boundary layer. (a) $y^+ \simeq 9$; (b) $y^+ \simeq 28$; (c) $y^+ \simeq 100$.	130
4.28 Scatter plots of (a-c) the normalized density - pressure fluctuations and (d-f) the normalized entropy - density fluctuations in a wall-normal plane for the cold-wall boundary layer. (a, d) $y^+ \simeq 9$; (b, e) $y^+ \simeq 28$; (c, f) $y^+ \simeq 100$.	130
4.29 Scatter plots of (a-c) the normalized total-temperature - temperature fluctuations, (d-f) the normalized total-temperature - velocity fluctuations and (g-i) the normalized total-temperature kinetic energy fluctuations in a wall-normal plane for the cold-wall boundary layer. (a, d, g) $y^+ \simeq 9$; (b, e, h) $y^+ \simeq 28$; (c, f, i) $y^+ \simeq 100$.	132
4.30 Scatter plots of the total-temperature - velocity fluctuations in a wall-normal plane for the cold-wall boundary layer. (a) $y^+ \simeq 9$. (b) $y^+ \simeq 28$. (c) $y^+ \simeq 100$.	133

List of Tables

2.1	Coefficients des schémas centrés du 2 ^{ème} au 8 ^{ème} ordre.	35
3.1	Grid resolution sensitivity study using the CSM model. Subscript (+) denotes the normalization by the friction velocity, with $y^+ = y\rho_w u_\tau / \mu_w$	47
3.2	Boundary layer properties using LES-P2 grid for different subgrid models. $\text{Re}_\tau = \rho_w u_\tau \delta / \mu_w$; $\text{Re}_\theta = \rho_\infty u_\infty \theta / \mu_\infty$; $C_f = 2\tau_w / \rho_\infty u_\infty^2$; $H = \delta^* / \theta$; $M_\tau = u_\tau / (\gamma R T_w)^{1/2}$; θ refers to the momentum thickness.	47
3.3	Boundary layer properties for different grids using the CSM model.	47
3.4	Lines and symbols used in graphes' legends.	48
3.5	Power indices n of near-adiabatic-wall asymptotic behaviors.	94
4.1	Boundary layer properties of the wall boundary condition study using LES-P2 grid. $\text{Re}_\tau = \rho_w u_\tau \delta / \mu_w$; $\text{Re}_\theta = \rho_\infty u_\infty \theta / \mu_\infty$; $C_f = 2\tau_w / \rho_\infty u_\infty^2$; $H = \delta^* / \theta$; $M_\tau = u_\tau / (\gamma R T_w)^{1/2}$. . .	106
4.2	Power indices n of near-adiabatic-wall asymptotic behaviors.	107
4.3	Reynolds numbers ranges for the adiabatic and isothermal-wall boundary layers and wall-units grid spacing.	114
4.4	Boundary layer properties of the isothermal boundary layers. $C_{f_{inc}}$ and $\text{Re}_{\theta_{inc}}$ are calculated using van-Direst II theory (Eq. 4.2).	115
4.5	Boundary layer thermal properties of the isothermal boundary layers. $q_w = -\lambda_w \partial \langle T \rangle / \partial y _w$; $\beta_q = q_w / C_p \rho_w u_\tau T_w$; $T_\tau = q_w / \rho_w C_p u_\tau$	115

Bibliography

- [1] N. Audiffren, Turbulence d'une couche limite soumise à une variation de densité due à une onde de choc ou un chauffage pariétal, *Ph-D thesis, Université Aix Marseille II*, France, 1993.
- [2] L. H. Back, R.F. Cuffel and P.F. Massier, Effect of wall cooling on the mean structure of a turbulent boundary layer in low-speed gas flow, *Int. J. Heat Mass Transfer*, 13, 1029-1047, 1970.
- [3] L. H. Back, P.F. Massier and R.F. Cuffel, Some observations on reduction of turbulent boundary-layer heat in nozzles, *AIAA J.*, 4 (12), 2226-2229, 1966.
- [4] L. H. Back, P.F. Massier and H. L. Gier, Convective heat transfer in convergent-divergent nozzle, *Int. J. Heat Mass Transfer*, 7, 549-568, 1964.
- [5] L. H. Back, P.F. Massier and R.F. Cuffel, Flow phenomena and convective heat transfer in a conical supersonic nozzle, *J. Spacecraft*, 4 (8), 1040-1047, 1967.
- [6] L. H. Back, P.F. Massier and R.F. Cuffel, Heat-transfer measurements in the shock-induced flow separation region in a supersonic nozzle, *AIAA J. Technical Notes*, 6 (5), 923-925, 1968.
- [7] D. R. Bartz, Turbulent boundary layer heat transfer from rapidly accelerating flow of rocket combustion gazes and of heated air, *Technical report, Jet Propulsion Laboratory*, 1963.
- [8] M. Bernardini, Direct numerical simulation of transonic shock wave/boundary layer interaction, *Ph-D thesis, Università di Roma, La Sapienza*, Italy, 2009.
- [9] M. Bernardini and S. Pirozzoli, Wall pressure fluctuations beneath supersonic turbulent boundary layers, *Phys. Fluids*, 23 (8), 2011.

- [10] D. R. Boldman, J. F. Schmidt and A. Fortini, Turbulence heat-transfer and boundary layer measurements in a canonical nozzle with a controlled inlet velocity profile, *NASA, Technical Notes, TN D-3221*, 1966.
- [11] P. Bradshaw, Compressible turbulent shear layers, *Annu. Rev. Fluid Mech.*, 9, 33-54, 1977.
- [12] C. Brun, M. P. Boiarcicu, M. Haberkorn and P. Comte, Large-eddy simulation of compressible channel flow, *Theor. Comput. Fluid Dyn.*, 22, 189-212, 2008.
- [13] T. Cebeci and A. M. O. Smith, Analysis of turbulent boundary layers. *New York, Academic Press, Inc. Applied Mathematics and Mechanics, N° 15*, 1974.
- [14] A. Chaudhuri, A. Hadjadj, A. Chinnayya and S. Palerm, Numerical study of compressible mixing layers using high-order WENO schemes. *J. Sci. Computing*, 47 (2), 170-197, 2011.
- [15] G. N. Coleman, J. Kim and R. D. Moser, A numerical study of turbulent supersonic isothermal wall channel flow, *J. Fluid Mech.*, 305, 159-183, 1995.
- [16] D. Coles, The turbulent boundary layer in a compressible fluid, *Phys. Fluids*, 7 (9), 1403-1423, 1961.
- [17] W. J. Cook and D. E. Richards, Heat transfer for highly cooled supersonic turbulent boundary layers, *AIAA J. Technical Notes*, 15 (9), 1335-1337, 1977.
- [18] L. Davidson, How to estimate the resolution of an LES of recirculating flow, *Quality and Reliability of Large Eddy Simulations II*, 16, 269-286, 2010.
- [19] L. Davidson, Large eddy simulations: How to evaluate resolution, *Int. J. Heat Fluid Flow*, 30, 1016-1025, 2009.
- [20] L. Davidson, Transport equations in incompressible URANS and LES, *Publication 2006/01*, Chalmers University of Technology, May 2006.
- [21] J. F. Debièvre, P. Dupont, D. R. Smith and A. J. Smits, Supersonic turbulent boundary layer subjected to step changes in wall temperature, *AIAA J.*, 35 (1), 51-57, 1997.
- [22] J. Deleuze, Structure d'une couche limite turbulente soumise à une onde de choc incidente, *Ph-D thesis, Université Aix-Marseille II*, 1995.

- [23] L. Duan, I. Beekman and M. P. Martin, Direct numerical simulation of hypersonic turbulent boundary layers. Part 2. Effect of wall temperature, *J. Fluid Mech.*, 655, 419-445, 2010.
- [24] L. Duan, I. Beekman and M. P. Martin, Direct numerical simulation of hypersonic turbulent boundary layers. Part 3. Effect of Mach number, *J. Fluid Mech.*, 672, 245-267, 2011.
- [25] Y. Dubief and F. Delcayre, On coherent-vortex identification in turbulence, *J. Turb.*, 1 (1), 11-33, 2000.
- [26] P. Dupont, Etude expérimentale des champs turbulents dans une couche limite supersonique fortement chauffée, *Ph-D thesis, Université d'Aix-Marseille II*, France, 1990.
- [27] T. M. Eidson, Numerical simulation of the turbulent Rayleigh-Bénard problem using subgrid modeling, *J. Fluid Mech.*, 158, 245-268, 1985.
- [28] T. Farabee and M. J. Casarella, Spectral features of wall pressure fluctuations beneath turbulent boundary layers, *Phys. Fluids*, 3 (10), 2410-2420, 1991.
- [29] H. H. Farnholtz and P. J. Finley, A critical compilation of compressible turbulent boundary layer data, *AGARDograph*, 223 (7402), 1977.
- [30] H. H. Farnholtz and P. J. Finley, A critical commentary on mean flow data for two-dimensional compressible boundary layers, *AGARDograph*, 253, 1980.
- [31] H. Foysi, S. Sarkar and R. Friedrich, Compressibility effects and turbulence scaling in supersonic channel flow, *J. Fluid Mech.*, 509, 207-216, 2004.
- [32] E. Garnier, N. Adams and P. Sagaut, Large eddy simulation for compressible flows, *Scientific computation, Springer Science*, 2009.
- [33] J. Gaviglio, Reynolds analogies and experimental study of heat transfer in the supersonic boundary layer, *Int. J. Heat Mass Transfer*, 30 (5), 911-926, 1987.
- [34] M. Germano, U. Piomelli, P. Moin and W. H. Cabot, A dynamic subgrid-scale eddy viscosity model, *Phys. Fluids A*, 3 (7), 1991.
- [35] B. Geurts and J. Frölich, A framework for predicting accuracy limitations in large-eddy simulation, *Phys. Fluids*, 14 (6), 41-44, 2002.

- [36] S. Ghosh, Direct and large-eddy simulation of supersonic turbulent flow in pipes, nozzles and diffusers, *Ph-D, thesis, Technische Universität München*, Germany, 2008.
- [37] R. L. Gran, J.E. Lewis and T. Kubota, The effect of wall cooling on a compressible turbulent boundary layer, *J. Fluid Mech.*, 66 (3), 507-528, 1974.
- [38] S. E. Guarini, R. D. Moser, K. S. Shariff and A. Wray, Direct numerical simulation of a supersonic turbulent boundary layer at Mach 2.5, *J. Fluid Mech.*, 414, 1-33, 2000.
- [39] A. Hadjadj and A. Kudryavtsev, Computation and flow visualization in high speed aerodynamics, *J. Turb.*, 6 (16) 33-81, 2005.
- [40] A. K. Henrick, T. D. Aslam and J. M. Powers, Mapped weighted essentially non-oscillatory schemes: Achieving optimal order near critical points, *J. Comp. Phys.*, 207, 542-567, 2005.
- [41] E. J. Hopkins and M. Inouye, An evaluation of theories for predicting turbulent skin friction and heat transfer on flat plates at supersonic and hypersonic Mach numbers, *AIAA J.*, 9 (6), 993-1003, 1971.
- [42] P. G. Huang, P. Bradshaw and T. J. Coakley, Skin friction and velocity profile family for compressible turbulent boundary layers, *AIAA J.*, 31 (9), 1600-1604, 1993.
- [43] P. G. Huang, G. N. Coleman and P. Bradshaw, Compressible turbulent channel flows: DNS results and modeling, *J. Fluid Mech.*, 305, 185-218, 1995.
- [44] N. Jarrin, J. C. Uribe, R. Prosser and D. Laurence, Synthetic Inflow Boundary Conditions for Wall Bounded Flows, *Advances in hybrid RANS-LES modelling*, 97, 77-86, 2008.
- [45] G. Jiang and C.W. Shu, Efficient implementation of weighted ENO schemes, *J. Comp. Phys.*, 126, 202-228, 1996.
- [46] J. Jiménez and P. Moin, The minimal flow unit in near-wall turbulence, *J. Fluid Mech.*, 225, 213-240, 1991.
- [47] P. Klebanoff, Characteristics of turbulence in a boundary layer with zero pressure gradient. *Tech. Rep.*, 1954.

- [48] M . Klein, A. Sadiki and J. Janicka, A digital filter based generation of inflow data for spatially developing direct numerical or large eddy simulation, *J. Comp. Phys.*, 186, 652-665, 2003.
- [49] H. Kobayashi, High spatial correlation SGS model for engineering turbulence, *Proceedings: 8th International symposium on engineering turbulence modeling and measurements - ETMM8*, 564-596, 2010.
- [50] H. Kobayashi, The subgrid-scale models based on coherent structures for rotating homogeneous turbulence and turbulent channel flow, *Phys. Fluids*, 17, 045104, 2005.
- [51] H. Kobayashi, F. Ham and X. Wu, Application of a local SGS model based on coherent structures to complex geometries, *Int. J. Heat Fluid Flow*, 29, 640-653, 2008.
- [52] P. A. Krogstad and L. E. Torbergson, Invariant analysis of turbulent pipe flow, *Flow, Turbulence and Combustion*, 64, 161-181, 2000.
- [53] A. J. Ladberman, Effect of wall temperature on a supersonic turbulent boundary layer, *AIAA J.*, 16 (7), 723-729, 1978.
- [54] A. J. Ladberman and A. Demetriades, Turbulent shear stresses in compressible boundary layers, *AIAA J.*, 17 (7), 736-744, 1979.
- [55] M. Lagha, J. Kim, J. D. Eldredge and X. Zhong, Near-wall dynamics of compressible boundary layers, *Phys. Fluids*, 23, 2011.
- [56] H. Laurent, Turbulence d'une interaction onde de choc/couche limite sur une paroi plane adiabatique ou chauffée, *Ph-D thesis, Université Aix-Marseille II*, 1996.
- [57] R. Lechner, J. Sesterhenn and R. Friedrich, Turbulent supersonic channel flow, *J. Turb.*, 2, 2001.
- [58] S. K. Lele, Compressibility effects on turbulence, *Annu. Rev. Fluid Mech.*, 26, 211-254, 1994.
- [59] D. K. Lilly, A proposed modification of the Germano subgrid-scale closure method, *Phys. Fluids A*, 4 (3), 633-635, 1992.
- [60] K. Liu and R. H. Pletcher, Compressibility and variable density effects in turbulent boundary layers, *J. Heat Transfer*, 129, 441-448, 2007.

- [61] J. L. Lumley, Computational modeling of turbulent flows, *Adv. Applied Mach.*, 18, 123-176, 1978.
- [62] T. S. Lund, X. Wu and K.D. Squires, Generation of turbulent inflow data for spatially-developing boundary layer simulations, *J. Comput. Phys.*, 140, 233-258, 1998.
- [63] T. Maeder, N. A. Adams and L. Kleiser, Direct simulation of turbulent supersonic boundary layers by an extended temporal approach, *J. Fluid Mech.*, 429, 187-216, 2001.
- [64] M. P. Martin, E. M. Taylor, M. Wu and V. G. Weirs, A bandwidth-optimized WENO scheme for the effective direct numerical simulation of compressible turbulence, *J. Comp. Phys.*, 220, 270-289, 2006.
- [65] P. Moin, K. Squires, W. Cabot and S. Lele, A dynamic subgrid-scale model for compressible turbulence and scalar transport, *Phys. Fluids A*, 3 (11), 2746-2757, 1991.
- [66] Y. Morinishi, S. Tamano and K. Nakabayashi, Direct numerical simulation of compressible turbulent channel flow between adiabatic and isothermal walls, *J. Fluid Mech.*, 502, 273-308, 2004.
- [67] M. V. Morkovin, Effect of compressibility on turbulent flows, *Mécanique de la Turbulence*, edited by A. Favre, 1961.
- [68] F. Nicoud and F. Ducros, Subgrid-scale stress modelling based on the square of the velocity gradient tensor, *Flow, Turbulence and Combustion*, 62, 183-200, 1999.
- [69] N. Onodera, T. Aoki and H. Kobayashi, Large-eddy simulation of turbulent channel flows with conservative ISO scheme, *J. Comp. Phys.*, 230, 5787-5805, 2011.
- [70] A. F. Perry and J.D. Li, Experimental support for the attached-eddy hypothesis in zero-pressure gradient turbulent boundary layers, *J. Fluid Mech.*, 218, 1, 1990.
- [71] S. Piponnai, Instantanéités dans les décollements compressibles : cas des couches limites soumises à ondes de choc, *Ph-D thesis*, Université de Provence Aix Marseille I, France, 2009.
- [72] S. Pirozzoli, Generalized conservative approximations of split convective derivative operators, *J. Comp. Phys.*, 229 (19), 7180-7190, 2010.

- [73] S. Pirozzoli, Numerical methods for high-speed flows, *Annual Review of Fluid Mechanics*, 43, 163-194, 2011.
- [74] S. Pirozzoli and M. Bernardini, Turbulence in supersonic boundary layers at moderate Reynolds number, *J. Fluid Mech.*, 688, 1-46, 2011.
- [75] S. Pirozzoli, M. Bernardini and F. Grasso, Direct numerical simulation of transonic shock/boundary layer interaction under conditions of incipient separation, *J. Fluid Mech.*, 657, 361-393, 2010.
- [76] S. Pirozzoli, F. Grasso and T. B. Gatski, Direct numerical simulation and analysis of a spatially evolving supersonic turbulent boundary layer at $M=2.25$, *Phys. Fluids*, 16 (3), 530-545, 2004.
- [77] S. B. Pope, *Turbulent flows*, Cambridge Univ. Press, 2000.
- [78] S. B. Pope, Ten questions concerning the large-eddy simulation of turbulent flows, *New J. Phys.*, 35 (6), 2004.
- [79] M. W. Rubesin, Extra compressibility terms for Favre-averaged two-equation models of inhomogeneous turbulent flows, *NASA, CR 177556*, 1990.
- [80] P. Sagaut, E. Garnier, E. Tromeur, L. Larchevêque and E. Labourasse, Turbulent inflow conditions for LES of subsonic and supersonic wall-bounded flows. *AIAA J.*, 42 (3), 469-478, 2004.
- [81] S. Sarkar, G. Erlebacher M. Y. Husaini, Compressible homogeneous shear: simulation and modeling. In *turbulent shear flows*, 8, (ed. F. Durst *et al.*), Springer, 1992.
- [82] H. Schlichting, Boundary-layer theory, 6th Ed., New York: McGraw-Hill, 1979.
- [83] M. F. Shahab, Numerical investigation of the influence of an impinging shock wave and heat transfer on a developing turbulent boundary layer, *Ph-D thesis, Ecole Nationale Supérieure de Mécanique et d'Aérotechnique*, France, 2011.
- [84] M. F. Shahab, G. Lehnash, T. B. Gatski and P. Comte, Statistical characteristics of an isothermal supersonic developing boundary layer flow from DNS data, *Flow, Turbulence and Combustion*, 86, 369-397, 2011.

- [85] A. J. Simonson and P. A. Krogstad, Turbulent stress invariant analysis: Clarification of existing terminology, *Phys. Fluids*, 17, 2005.
- [86] J. Smagorinsky, General circulation experiments with the primitives equations, *Mon. Weather Rev.*, 61, 99-164, 1963.
- [87] M. W. Smith and A. J. Smits, Visualization of the structure of supersonic turbulent boundary layers. *Experiments in Fluids*, 18, 288-302, 1995.
- [88] A. J. Smits and J. P. Dussauge, Turbulent shear layers in supersonic flow, *American Institute of Physics, New York, 2nd edition*, 2006.
- [89] A. J. Smits and J. P. Dussauge, Turbulent shear layers in supersonic flow, *American Institute of Physics*, 1996.
- [90] A. J. Smits, N. Matheson and P. N. Joubert, Low-Reynolds number turbulent boundary layers in zero and favorable pressure gradients, *J. Ship. Res.*, 147-157, 1983.
- [91] S. C. Sommer and B. J. Short, Free-flight measurements of turbulent boundary-layer skin-friction in the presence of severe aerodynamic heating at Mach numbers from 2.8 to 7.0, *Journal of the Aeronautical Sciences*, 23 (6), 536-542, 1956.
- [92] D. B. Spalding and S. W. Chi, The drag of a compressible turbulent boundary layer on a smooth flat-plate with and without heat transfer, *J. Fluid Mech.*, 18, 117-143, 1964.
- [93] E. F. Spina, A. J. Smits and S. K. Robinson, The physics of supersonic turbulent boundary layers, *Annu. Rev. Fluid Mech.*, 26, 287-319, 1994.
- [94] E. T. Spyropoulos and G. A. Braisdell, Large-eddy simulation of a spatially evolving supersonic turbulent boundary layer flow, *AIAA J.*, 36 (11), 1983-1990, 1998.
- [95] S. Stolz and N.A. Adams, Large-eddy simulation of high Reynolds number supersonic boundary layers using the approximate deconvolution model and a rescaling and recycling technique, *Phys. Fluids*, 15, 2398-2412, 2003.
- [96] D.I. Suslov R. Arnold and O.J. Haidn, Convective and film cooled nozzle extension for a high pressure rocket subscale combustion chamber, *Inproceedings: 48th AIAA Aerospace Sciences Meeting Including the New Horizons Forum and Aerospace Exposition*, AIAA 2010-1150, 2010.

- [97] S. Tamano, Direct Numerical Simulation of Wall-Bounded Compressible Turbulent Flow, *Nagoya Institute of Technology*, Japan, 2002.
- [98] S. Tamano and Y. Morinishi, Effect of different thermal wall boundary conditions on compressible turbulent channel flow at $M=1.5$, *J. Fluid Mech.*, 548, 361-373, 2006.
- [99] E. Touber, Unsteadiness in shock-wave/boundary-layer interactions, *Ph-D thesis, University of Southampton*, United Kingdom, 2010.
- [100] G. Urbin and D. Knight, Compressible large eddy simulation using unstructured grid: supersonic boundary layer, *2nd AFOSR Conference on DNS/LES, Kluwer Academic Publishers, Rutgers University*, 443-458, 1999.
- [101] E. R. Van Driest, Turbulent boundary layer in compressible fluids. *J. Aero. Sci.*, 18, 145-160, 1951.
- [102] E. R. Van Driest, Problem of Aerodynamic Heating, *Aeronautical Engineering Review*, 15 (10), 26-41, 1956.
- [103] A. Walz, Boundary layers of flow and temperature, *MIT Press*, 1969.
- [104] W. P. Wang and R. H. Pletcher, On the large eddy simulation of a turbulent channel flow with significant heat transfer, *Phys. Fluids*, 8 (12), 3354-3366, 1996.
- [105] F. M. White, Viscous fluid flow, *McGraw-Hill, Second edition*, 1991.
- [106] Z. T. Xie and I.P. Castro, Efficient generation of inflow conditions for large-eddy simulation of street-scale flows, *Flow, Turbulence and Combustion*, 81 (3), 449-470, 2008.
- [107] H. Yan, D. Knight and A. A. Zheltovodov, Large-eddy simulation of supersonic flat-plate boundary layers using the monotonically integrated large-eddy simulation MILES technique, *J. Fluids Eng.*, 124, 868-875, 2002.
- [108] A. Yoshizawa, Statistical theory for compressible turbulent shear flows with the application to subgrid modeling, *Phys. Fluids*, 7, 2152-2164, 1986.

